Biological regulation of Earth's early atmosphere : metal isotope constraints on Neoarchaean methane cycling
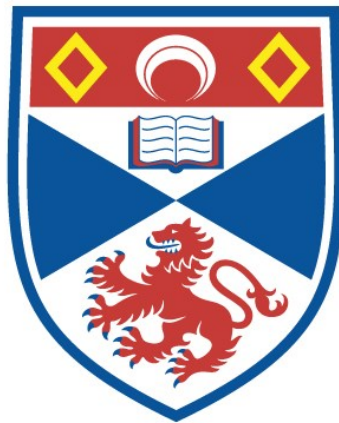
Natalya Andryivna Vladimirovna Zavina-James

A thesis submitted for the degree of PhD
at the
University of St Andrews

2022

Candidate's declaration

I, Natalya Andryivna Vladimirovna Zavina-James, do hereby certify that this thesis, submitted for the degree of PhD, which is approximately 45,000 words in length, has been written by me, and that it is the record of work carried out by me, or principally by myself in collaboration with others as acknowledged, and that it has not been submitted in any previous application for any degree. I confirm that any appendices included in my thesis contain only material permitted by the 'Assessment of Postgraduate Research Students' policy.

I was admitted as a research student at the University of St Andrews in September 2016.

I received funding from an organisation or institution and have acknowledged the funder(s) in the full text of my thesis.

Date   18-09-21   Signature of candidate

Supervisor's declaration

I hereby certify that the candidate has fulfilled the conditions of the Resolution and Regulations appropriate for the degree of PhD in the University of St Andrews and that the candidate is qualified to submit this thesis in application for that degree. I confirm that any appendices included in the thesis contain only material permitted by the 'Assessment of Postgraduate Research Students' policy.

Date   19-09-21   Signature of supervisor

Permission for publication

In submitting this thesis to the University of St Andrews we understand that we are giving permission for it to be made available for use in accordance with the regulations of the University Library for the time being in force, subject to any copyright vested in the work not being affected thereby. We also understand, unless exempt by an award of an embargo as requested below, that the title and the abstract will be published, and that a copy of the work may be made and supplied to any bona fide library or research worker, that this thesis will be electronically accessible for personal or research use and that the library has the right to migrate this thesis into new electronic forms as required to ensure continued access to the thesis.

I, Natalya Andryivna Vladimirovna Zavina-James, confirm that my thesis does not contain any third-party material that requires copyright clearance.

The following is an agreed request by candidate and supervisor regarding the publication of this thesis:

Printed copy

No embargo on print copy.

Electronic copy

Embargo on all of electronic copy for a period of 1 year on the following ground(s):

- Publication would preclude future publication

Supporting statement for electronic embargo request

Two papers based on this work are planned for publication over the course of the next year.

Title and Abstract

- I agree to the title and abstract being published.

Date   18-09-21   Signature of candidate

Date   19-09-21   Signature of supervisor

Underpinning Research Data or Digital Outputs

Candidate's declaration

I, Natalya Andryivna Vladimirovna Zavina-James, hereby certify that no requirements to deposit original research data or digital outputs apply to this thesis and that, where appropriate, secondary data used have been referenced in the full text of my thesis.

Date   18-09-21   Signature of candidate

Abstract

The Great Oxidation Event (GOE, c.2.43 Ga) marks a fundamental change in the interaction between the biosphere, atmosphere, and Earth's surface environment. Recent studies suggest that Earth's anoxic pre-GOE atmosphere was also heavily influenced by biological feedbacks. Notably, recent geochemical records (carbon and sulphur isotopes) suggest that a hydrocarbon-rich haze periodically formed as a result of enhanced methane fluxes, termed periodic haze events, from the biosphere. The extent to which the biosphere mediated these haze events is under-constrained, yet hypothesised to result from enhanced biological methane cycling. Copper and nickel are both bioessential trace metals utilised by aerobic methanotrophic bacteria and methanogenic archaea respectively, and it has been already demonstrated that methanogenic archaea fractionate Ni isotopes during metabolic uptake. This thesis applies these metal isotope systems to two well-preserved Archaean rock cores; the 2.5 Ga core GKF01 from the Griqualand West Basin, South Africa, and the 2.7 Ga core SV1 from the Hamersley Basin, Western Australia. Both cores exhibit carbon isotope evidence consistent with methane cycling, but reflect contrasting Archaean environments. In Chapter 3, a high-resolution copper isotope record measured in a suite of marine shales and carbonates from core GKF01 is presented. The data show a 0.8‰ range in copper isotope composition and a negative excursion that predates the onset of a pre-identified haze event. Examined alongside previously published carbon and sulphur isotope records, these data demonstrate a clear role for aearobic methanotrophy in the incorporation of methane into Late Archaean sediments. In Chapter 4, a similar high-resolution copper isotope record is analysed in sediments from core SV1, and copper isotope cycling in considered within the context of a mildly oxygenated, high pH lacustrine setting. A Copper isotope record reflecting approximate crustal average (*c.* 0.05‰) is reported, indicating either (1) a system in which no processes fractionate copper isotopes, (2) sedimentary phase homogenisation and/or overprinting of primary copper isotope signals by volcanic detrital input, or (3) complete consumption of copper by a copper-dependent process, however it is most likely that the record reflects process (2). Finally, Chapter 5 presents a high-resolution record of nickel isotopes in core GKF01 which reflects previously reported values of

euxinic sediment and black shales (*c.* 0.28‰). The data presented in this thesis demonstrate the clear potential for these isotope systems to be applied as biomarkers for the investigation of deep time biological methane cycling, and recommendations for future studies are also explored.

Acknowledgements

throughout this time, despite the distance. To Krisy Mahome, for welcoming me so warmly to Bloomington and providing me with a home away from home. You have all been entirely wonderful.

To my dad and Mellie, for all of the welcome breaks in Deutschland and unconditional support. To my grandparents, for everything. To Christopher Henry, who from the tender age of seven has always been there to comfort me when my academic pursuits go haywire, and to Evelyn Lily, my favourite lillasyster: your tenacity, bravery, and resilience is unmatched.

To my mum, моя мамачка и мой лучший друг. Огромное человеческое спасибо.

Finally, to David Evans. I don't think I could even begin to describe the many ways in which your constant and unconditional support, love, and patience has made any and all of this possible. Thank you for everything.

Contents

List of Figures

List of tables

Chapter 1

1. Introduction

1.1 Background

1.1.1 Earth's early atmospheric evolution

Since the origin of life at c. 3.7 – 4.3 Ga (Dodd et al., 2017), biology has exerted a primary influence over the basic composition of Earth's atmosphere (e.g., Margulis and Lovelock, 1974; Kasting and Siefert, 2002). This influence is perhaps most vividly illustrated by the Great Oxidation Event, or GOE, which was triggered by the evolution of oxidative photosynthesis and led to the pervasive and irreversible accumulation of oxygen in Earth's atmosphere at c. 2.43 Ga (e.g., Canfield, 2005; Farquhar et al., 2010; Luo et al., 2016). Prior to the GOE, the relationship between biology and atmospheric composition has remained speculative, largely due to the lack of geochemical evidence pertaining to Hadean and Archaean atmospheric compositions. It has been suggested that the early development of an atmosphere on Earth was likely catalysed by the moon-forming impact (*c.* 4.5 Ga; Kleine et al., 2002) and subsequent impacts, which devolatilised Earth's primitive mantle and led to a sequential repartitioning of volatiles, ultimately resulting in an atmosphere dominated by CO, CO_2, and possibly H_2O throughout the Hadean (Zahnle et al., 2010). Alternatively, passive degassing through high degrees of volcanism due to a hotter mantle potential temperature is also cited as a possible reason for atmosphere development, without the need to invoke impacts (Kasting, 1993). Up to this point, it is considered unlikely that any life could have survived long enough to propagate. Into the Archaean (spanning ~4 – 2.5 Ga), the earliest evidence of life is observed at *c.* 3.95 Ga (Eoarchaean) in the form of carbon isotope values consistent with autotrophy (Tashiro et al., 2017), likely via the acetyl-CoA pathway. This pathway is favoured for the Last

Universal Common Ancestor (LUCA) as it utilises CO_2 and H_2 and is prevalent across both methanogens (domain *archaea*) and acetogens (domain *bacteria*) (Weiss et al., 2016). However, it should be made clear that some of the earliest biosignatures found in the rock record remain controversial. It has been established that methanogens diverged from Euryarchaeaota by 3.15 Ga (the Palaeoarchaean) (Wolfe and Fournier, 2018), although the prevalence of this metabolic pathway across Euryarchaeaota, along with the phylogenetic evidence for the acetyl-CoA pathway in LUCA, strongly suggests that the methanogenic metabolism established itself as early as 1 Ga before this. While there is limited direct evidence for this, methane-bearing fluid inclusions from ~3.46 Ga hydrothermal precipitates are corroborative to some level and certainly indicate a degree of climatic impact by methane production at this time (Ueno et al., 2006). In addition, recent C isotope ($\delta^{13}C$) data from the Western Australian Pilbara Craton provide similar evidence for early methane cycling at 3.4-3.5 Ga (Shopf et al., 2018; Flannery et al., 2018). Given the environmental needs of these primitive organisms, it can be inferred that Earth's early Archaean atmosphere was an anoxic greenhouse rich in biologically derived CO_2 and CH_4 (e.g., Karecha et al., 2005; Nisbet and Fowler, 2011).

These atmospheric conditions persisted throughout the mid-Archaean (evidenced by mass-independent fractionation of sulphur isotopes (S-MIF), Farquhar and Wing, 2003), by which time anoxygenic photosynthesing metabolisms had evolved (~3.2 – 3.5 Ga; e.g. Blankenship, 2010), demonstrated by the abundant stromatolitic and photosynthetic microbial mats found in Australia and South Africa (e.g. Buick, 1992). By the late Archaean (*c.* 2.9 Ga), CO_2 levels had decreased enough to facilitate the emergence of carbonate reefs in shallow marine environments which, by implication, suggests a rise in seawater pH and locally oxidised water columns, driven by the emergence of oxygenic photosynthesis (Nisbet and Fowler, 2011). Free oxygen remained absent from Earth's atmosphere until approximately 2.45 Ga (e.g., Lyons et al., 2014), but did not accumulate to levels similar to that of today until ~2.3 Ga (e.g., Luo et al., 2016).

While the above overview (summarised in Figure 1, which summarises the important steps in the evolution of life, as well as the dominant atmospheric gasses) presents an evolving but generally stable atmospheric chemistry (in terms of its major constituents)

throughout the Archaean, the details surrounding the specific interplay between oxygen, methane and other reducing gasses (i.e., H_2) towards the end of the Eon remains speculative. It has been proposed that Earth's surface environments experienced transient, localised oxygen fluxes prior to the GOE (Anbar et al., 2007) and this has been substantiated by multiproxy (most notably Fe speciation, C, N, Mo, and Cr isotope) evidence suggesting the presence of oxygenic oases during this time (e.g., Planavsky et al., 2014; Yang et al., 2019; Crowe et al., 2013).

Alongside oxygen, there is compelling evidence for increased CH_4 fluxes during the late Archaean. Multiple S isotope analyses of 2.71 Ga pyritic shales from Ontario have suggested that Earth's atmosphere experienced heightened fluxes of CH_4, leading to the formation of organic-rich hazes (Kurzweil et al., 2013). More recently, robust multi-proxy (coupled C and S isotope data) evidence for enhanced CH_4 cycling has also been identified in late Archaean sediments from South Africa (e.g., Fischer et al., 2009; Zerkle et al., 2012; Izon et al., 2015; Izon et al., 2017). These findings, along with theoretical predictions based on climate models (e.g., Kasting et al., 2001) and photochemical models (e.g. Claire et al., 2014) provide the basis for the methane haze hypothesis. This hypothesis proposes that prior to the GOE, and from *c.* 2.7 – 2.5 Ga, Earth experienced Periodic Haze Events (PHEs), during which the atmosphere was dominated by a CH_4 rich haze (similar to that of Titan (Zerkle et al., 2012).
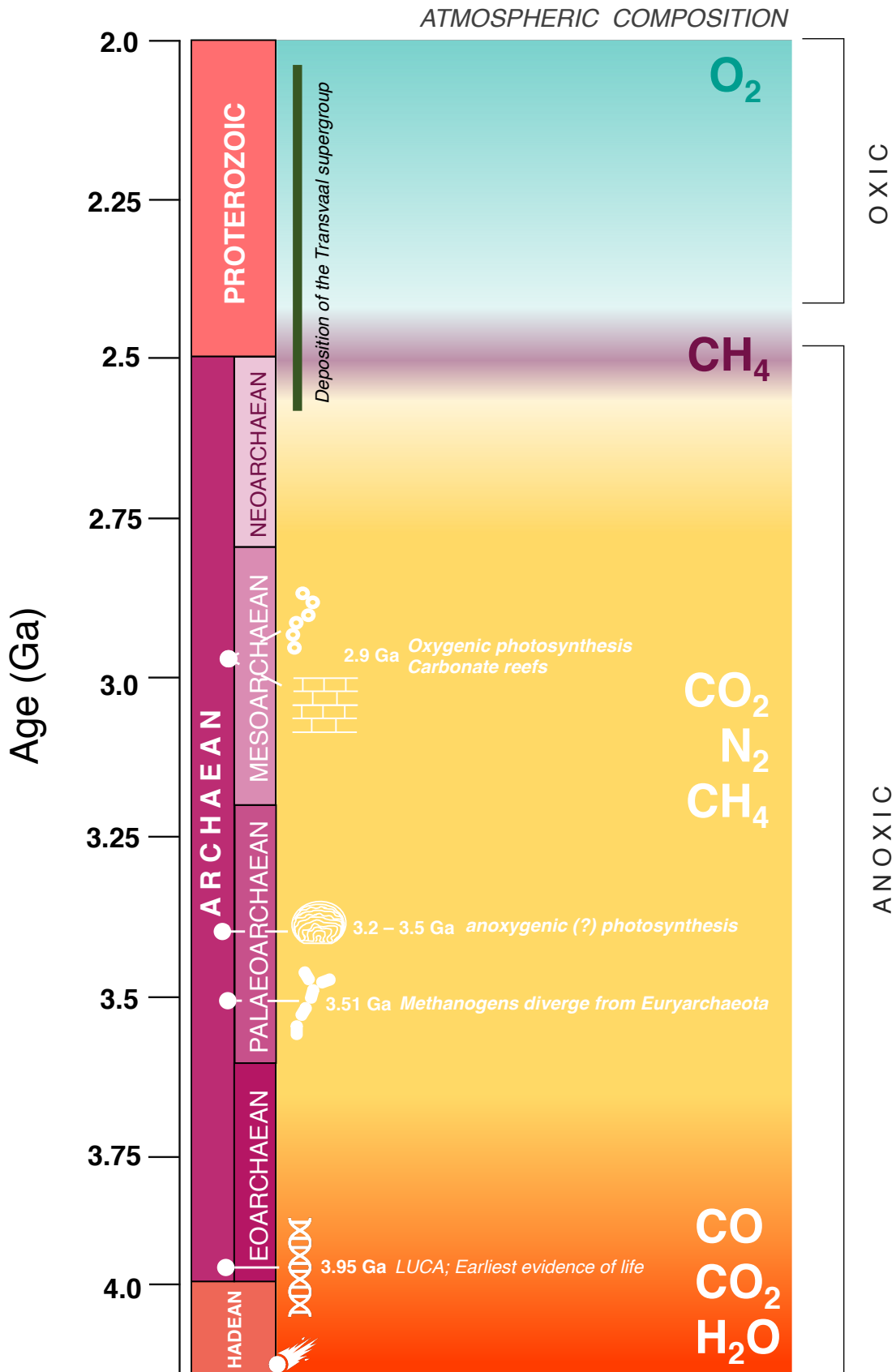
Figure 1: A schematic overview of Earth's atmospheric-biospheric evolution from the Hadean through to the Proterozoic. Gas composition changes reflect notable shifts rather than absolute abundance; it should be acknowledged that N_2 and CO_2 would have been present throughout the entire timescale presented (please refer to main text for references).

1.1.2 Periodic haze events

The observed correspondences between mass-independently fractionated S isotope ratio changes (S-MIF; $\Delta^{33}S$ and $\Delta^{36}S$) and extremely negative $\delta^{13}C_{org}$ excursions (collectively termed C-S anomalies) are of fundamental importance to the haze hypothesis and PHE formation (Izon et al., 2017). Organic $\delta^{13}C$ excursions are generally considered to represent the extensive assimilation of ^{13}C-depleted substrates (i.e., CH_4) into sedimentary organic matter by both aerobic and anaerobic methane oxidising bacteria (e.g., Summons et al., 1998; Orphan et al., 2002), and are therefore considered as robust biomarkers for methane incorporation in the geological record.

Mass-independent fractionation of sulphur isotopes (S-MIF) is a characteristic signature in pre-GOE (i.e., older than *c.* 2.43 Ga; Warke et al., 2020) sedimentary rocks and provides the strongest evidence for a reducing atmosphere with O_2 levels $< 10^{-5}$ present atmospheric levels (PAL) throughout the Archaean (e.g., Farquhar et al., 2000a). Experimental constraints and atmospheric models indicate that S-MIF formation may occur through atmospheric sulphur transformations involving UV photochemistry (e.g., Pavlov and Kasting, 2002; Claire et al., 2014). In the modern atmosphere, S-MIF formation is inhibited by the presence of O_2 and O_3, which absorb the UV radiation before it is able to photolyse tropospheric SO_2. Therefore, the presence of S-MIF during the Archaean provides potential evidence for an atmosphere with little to no O_2 (Pavlov and Kasting, 2002). However, other mechanisms for S-MIF formation have been demonstrated. Isotope fractionation during sulphur chain formation, which occurs when elemental S forms a gaseous phase, has been shown to generate S-MIF (Harman et al., 2018), as has atmospheric pressure-dependent SO_2 photolysis, where Archaean-like S-MIF signatures only occur under low atmospheric pressure (Endo et al., 2019).

Other Photochemical models predict that periodic changes in the S-MIF $\Delta^{33}S/\Delta^{36}S$ ratio throughout the Neoarchaean (in tandem with $\delta^{13}C_{org}$ excursions) could represent transitions between two anoxic atmospheric states: one with a $CH_4:CO_2$ ratio of <0.1 (haze-free, where SO_2 photolysis is the major source of S-MIF as there is no haze to inhibit such effects), and one with a $CH_4:CO_2$ ratio of ~0.2 (where an opaque organic haze decreases photolysis rates in the lower atmosphere and slows the rate of atmospheric S

cycling) (Izon et al., 2015). Alternative interpretations of this ratio switch include that it reflects a change in total pressure of SO_2 and/or volcanic input (i.e., Endo et al., 2019).
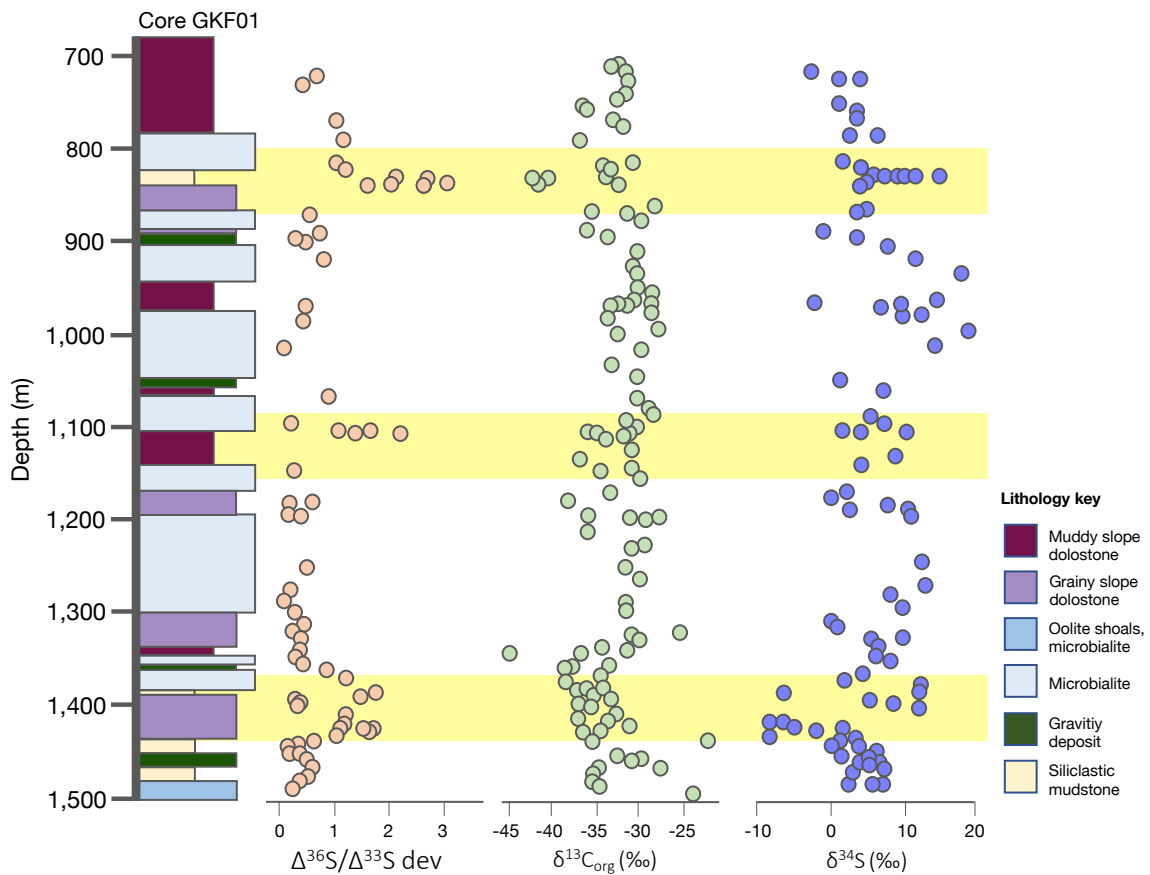
Figure 2: A stratigraphic log of core GKF01 illustrating the co-variance of S-MIF ratio deviations and carbon isotope excursions across three identified C-S anomalies/PHEs (highlighted in yellow) (Zerkle et al., 2012 and references therein).

Evidence for PHEs during the Neoarchaean principally derive from two drill cores obtained from the Archaean-Palaeoproterozoic Transvaal Supergroup: core GKF01 records three C-S anomalies (Figure 2; Zerkle et al., 2012), and core BH1-sacha records two anomalies (Izon et al., 2015). Recent work by Izon et al. (2017) has provided the first high resolution study of core GKF01 which focuses on the youngest PHE identified by Zerkle et al. (2012) and which reveals the sustained covariance of C and S sulphur isotopes throughout the stratigraphic section. Coupled with photochemical models, this high-resolution study strongly points towards a biological origin for atmospheric CH_4 hazes, where the relative availability of C and S to the biosphere mediated CH_4 flux.

1.1.3 Methane cycling and carbon isotope excursions

Methane (CH_4) is a potent greenhouse gas produced either via the thermochemical breakdown of organic matter or through biological processes (e.g., Canfield et al., 2005). These processes are associated with pronounced $\delta^{13}C_{org}$ excursions in the geological record; large negative isotopic fractionations occur during both the production and consumption of CH_4 (Hayes, 1993). In the modern system, 70% of annual global CH_4 emissions are derived from biological production, however only 40% of the total methane produced by methanogenic microorganisms reaches the atmosphere (e.g., Reebough, 2007). Aerobic and anaerobic methanotrophic bacteria and archaea oxidise a high proportion of all biologically-derived CH_4 (Lyu et al., 2018); anaerobic oxidation of methane (AOM) alone oxidises an estimated 80% of all CH_4 from marine sediments (Reebough, 2007).

Methanogens are prokaryotes belonging to Kingdom Archaea, and the majority are found within phyla Euryarchaeota and Crenarchaeota. They are obligate anaerobes and are found in abundance in extreme environments (such as that of early Earth) as well as soils and seawater (e.g., Borja and Rincón, 2011). In modern systems, various species of methanogenic archaea convert compounds such as $H_2 + CO_2$, formate, methanol, methylamines, and acetate to CH_4 (e.g., Blaut, 1994). However, methanogenic archaea also played a prominent role in early Earth's ecosystem; phylogenetic analyses, evidence from C isotope measurements of sedimentary rocks, and the abundance of H_2 and CO as electron donors during the Archaean are all suggestive of an environment dominated by H_2 -based methanogens, CO-based autotrophic acetogens, and methanogenic acetotrophs (Sauterey et al., 2020). The generation of significant amounts of methane in the environment likely encouraged the evolution of AOM, a process coupled to microbial sulphate reduction (MSR) where CH_4 and SO_2^{4-} are consumed by the methanotroph and sulphate reducer, producing HCO_3^- and HS^- (Moran et al. 2007), or to NO_3, Fe^{3+} or Mn^{4+} reduction (e.g., Taupp et al., 2010). The development of symbiosis within the CH_4 cycle coupled to MSR likely maintained relatively low levels of biological CH_4 flux to the atmosphere throughout the early- to mid-Archaean.

Anaerobic oxidation of methane occurs in anoxic marine and freshwater sediments and is mediated by anaerobic methanotrophic archaea (ANME) which form consortia with sulphate-reducing bacteria (SRB) in order to metabolise CH_4. Anaerobic methanotrophic archaea are related to methanogenic archaea; notably some ANME are also able to produce CH_4 in certain circumstances. There are three model pathways for AOM which depend on the availability of electron acceptors. Of relevance to the Archaean Earth is sulphate-dependent anaerobic methane oxidation (S-DAMO) and possibly metal ion (Mn^{4+} and Fe^{3+})-dependent anaerobic methane oxidation (M-DAMO) (e.g., Cui et al., 2014). Metabolically, it is though that ANME utilise the reverse-methanogenesis pathway under anoxic conditions (Hoehler et al., 1994), a hypothesis supported by numerous other studies involving the extraction of Ni proteins from microbial mats (e.g., Kruger et al., 2003; Scheller et al., 2010) (see section 1.1.4.1 for a description of Ni usage by ANME). Prior to localised and/or widespread O_2 availability on early Earth, AOM was likely the dominant C-burial pathway within the ecosystem, and has long been used to explain the extremely depleted C_{org} isotope signatures found in Archaean rocks (e.g., Eigenbrode and Freeman, 2006). However, anoxygenic phototrophy, methanogeneis, sulphate and sulphur reduction, and iron reduction metabolisms were also likely prolific (e.g., Canfield et al., 2006).

Aerobic methane oxidation is an oxidative metabolism ubiquitous in the modern environment. It is carried out by aerobic methane oxidising bacteria, of which there are three types. Type I methanotrophs belong to class (gamma) γ-proteobacteria and assimilate C compounds via the Ribulose Monophosphate (RuMP) cycle. These bacteria have stacked membranes which harbour the Cu-based particulate methane monooxygenase (pMMO), the enzyme involved in the primary step of the CH_4 oxidation pathway (see section 1.1.4.2). Type II methanotrophs belong to class (alpha) α-proteobacteria, use the Serine cycle to oxidise CH_4, and contain rings of pMMO-bearing membranes. These bacteria also may contain soluble (s) Fe-dependent MMO (sMMO) and are able to switch between the two enzymes depending on the nutrient availability of the system (e.g. Chistoserdova et al., 2005; Semrau et al., 2011). Finally type X methanotrophs, which belong to genus *methylcoccus* (γ-proteobacteria), combine features from both type I and type II methanotrophs; they possess stacked membranes

and the RuMP cycle, however they also contain elements of the serine cycle and express sMMO (Chistoserdova et al., 2005). Moreover, AMO has also been suggested as the C-assimilation pathway responsible for depleted C_{org} isotope signatures found in *c.* 2.7 Ga sedimentary rocks from Western Australia (e.g. Hayes, 1993; Eigenbrode and Freeman, 2006).

Carbon isotope signatures are extensively used as geochemical proxies for biological processes: stable isotope ratios of C in the majority of natural samples possess C isotope values ranging from -100‰ to +10‰, including marine carbonates, marine bicarbonates, mantle carbon, modern atmospheric CO_2, modern dissolved CO_2 (all broadly ranging between -10‰ to +10‰), and land plants, eukaryotic algae, cyanobacteria, anoxygenic photosynthetic bacteria, methanogenic bacteria, methanotrophic bacteria, and organic compound formed by serpentinization reactions (ranging between -5‰ to -85‰). Figure 3 summarises the range in C isotope values of organic and inorganic carbon compounds, highlighting the variety of processes which fractionate C isotopes (Planavsky et al., 2011). Isotopic fractionation during C assimilation results from a kinetic isotope effect which is inherent to irreversible enzymatic CO_2 fixation carried out by, for example, methanogenic bacteria (via the reductive acetyl-CoA/methanogenese or acetogenese pathway, leading to a fractionation of 15-58‰ between the biomass and the substrate), cyanobacteria (via the Calvin cycle/Rubisco(II) pathway, leading to a fractionation factor of 19.5-22‰ between the biomass and the substrate), and plants and algae (via the Calvin cycle/Rubisco(I) pathway, leading to a fractionation of 17-30‰ between the biomass and the substrate). Carbon isotopic fractionation for microbes utilising the reductive acetyl-CoA pathway (i.e. sulphate reducing bacteria) are similar to those of methanogenic bacteria (16-39‰), and are comparatively heavier for anoxygenic photoautotrophic bacteria using the 3-hydroxyprorionate cycle or the reductive citric acid cycle (0-13‰) (Hayes, 2001). The production of CH_4 by methanogenic bacteria via the acetyl-CoA pathway is thought to fractionate C isotopes to the highest degree (i.e. up to 58‰), producing the lightest isotopic C values in the sedimentary record when analysed in the organic C phase (i.e. Freeman et al., 1990).
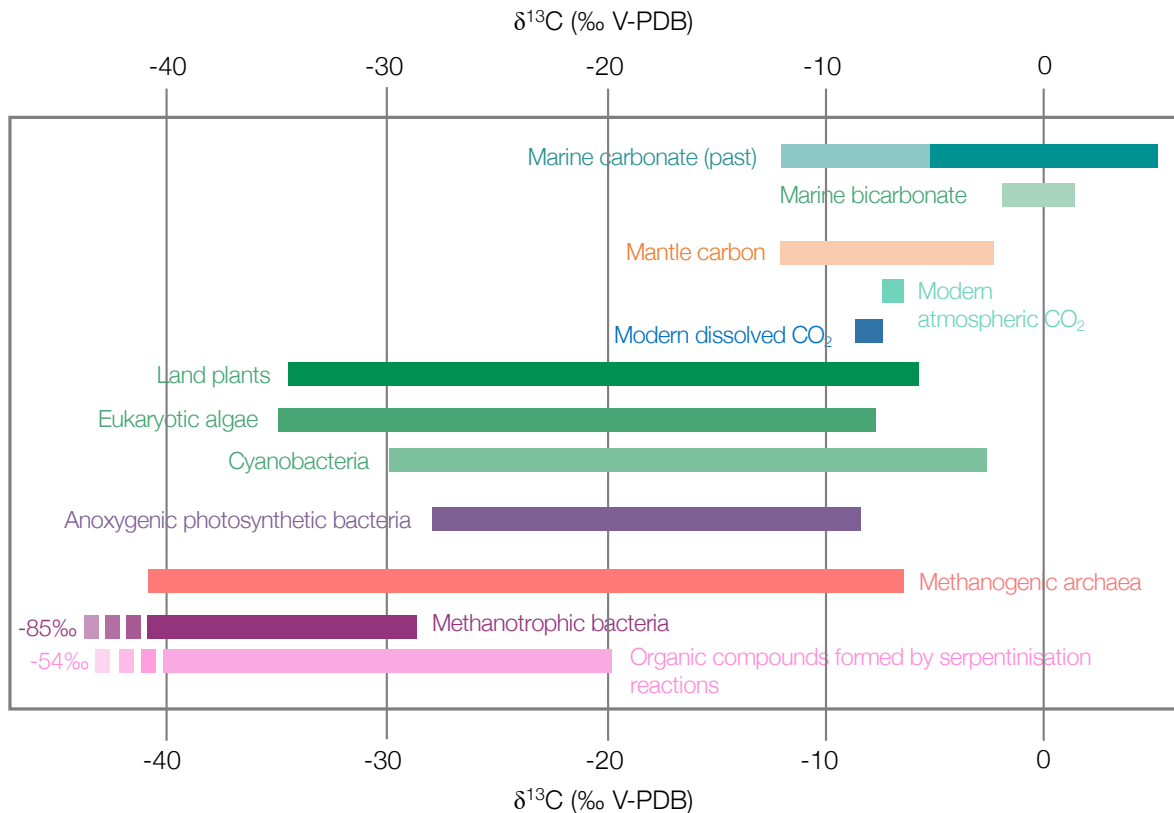
Figure 3: Carbon isotope values for inorganic and biological carbon compounds (modified from Planavsky et al., 2011 and references therin).

When searching for methanotrophic biosignatures in ancient rocks, differentiating between anaerobic and aerobic methane assimilation pathways has proven challenging, and complementary proxies are often sought. For example, the covariance of low $\delta^{13}C_{org}$ and low $\delta^{34}S_{pyrite}$ in rocks from the Belingwe belt (Zimbabwe) is used to suggest that local sulphate concentrations were high enough to sustain AOM coupled to MSR, and thus the low $^{13}C_{org}$ signal represents CH_4 oxidation by ANME (i.e., Grassineau et al., 2002). The lack of co-variation between $\delta^{34}S_{pyrite}$ and the low $\delta^{13}C_{org}$ in rocks of the Transvaal supergroup could, by contrast, suggest CH_4 oxidation by aerobic methane oxdation, as supressed sulphate levels are not conducive to the AOM-MSR coupling. Certainly, the low sulphate and O levels would have spatially restricted both AOM and aerobic methane oxidation, enabling high volumes of CH_4 to escape to the atmosphere (e.g., Izon et al., 2017). Organic C isotope signatures in late Archaean (2.7 – 2.5 Ga) sedimentary rocks from South Africa and Western Australia possess notably low $\delta^{13}C_{org}$ values (-45 to -60‰) which are considered to represent enhanced CH_4 cycling mediated by aerobic

10

methanotrophy in an environment which also exhibits low sulphate conditions (e.g. Izon et al., 2017; Eigenbrode and Freeman, 2006; Stueken et al., 2017).

1.2. Metal usage by methane-related metabolisms

As described above, several of these early metabolic pathways depend on metal ligands; Cu within the pMMO enzyme, Fe within the sMMO enzyme and, further to this, Ni within methyl-coenzyme M reductase (MCR), the enzyme responsible for CH_4 synthesis and anaerobic CH_4 oxidation (Wongnate and Ragsdale, 2015). Given the importance of these metal centres to their respective metabolisms, the critical aspect of this thesis is the exploration of Ni and Cu isotopes as potential biomarkers for methane cycling in Archaean sedimentary rocks. Recently, the use of metal stable isotopes as novel geochemical tracers has grown in popularity; Fe isotopes (for redox and biological uptake), Zn (biological uptake), and Mo (redox) have all been previously utilised in studies investigating deep-time environmental processes (Wiederhold, 2015). In comparison, Ni and Cu have received less attention in geological materials (Cameron et al., 2009; Chi-Fru et al., 2016).

1.2.1 Nickel isotopes and methanogenesis

Nickel is a bioessential trace metal utilised by methanogens during the production of methane (e.g., Silva and Williams, 2009). Broadly, the process by which CO_2 is reduced to CH_4 (methanogenesis) is as follows:

$$CO_2 \rightarrow R\text{-}CH\text{=}O \rightarrow CH_2 \rightarrow CH_3 \rightarrow CH_4$$
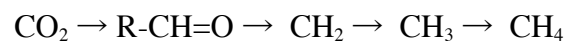
where a series of enzymes strip oxygen atoms from C and add H. Importantly, the last reaction (methyl to methane) is performed by methyl-coenzyme M reductase (MCR), which utilises a Ni-containing cofactor (Madigan and Martinko, 2015).

Nickel has five stable isotopes: ^{58}Ni, ^{60}Ni, ^{61}Ni, ^{62}Ni, and ^{64}Ni with relative abundances of 68%, 26%, 1%, 3% and 0.9% respectively (Elliott and Steele, 2017). Recent work on the stable isotopes of Ni in the Earth sciences reveals potential for this isotope system to be

developed as a biomarker in geological materials. Cameron et al. (2009) presented Ni stable isotope data for abiotic terrestrial samples, stony and Fe-meteorite samples, and pure cultures of three methanogenic archaea. They demonstrate that there is little demonstrable variation in the Ni isotopic composition in abiotic terrestrial samples and meteorites (0.08 – 0.27‰) (Figure 4). This implies that even under a wide variety of redox states and temperature gradients, isotopes of Ni fall within a ~0.2‰ range. Contrastingly, the methanogen cultures produce a considerable fractionation of Ni isotopes, which was not shown in the control cultures, establishing the unique role of methanogenic uptake in biotic Ni isotope fractionation (Figure 4). As such, Ni isotopes provide a seemingly robust isotope system with which to investigate early Earth CH_4 cycling, and the application of this isotope system in high-resolution to a suite of rocks which record enhanced CH_4 cycling could prove a method by which to test the applicability of this proxy.
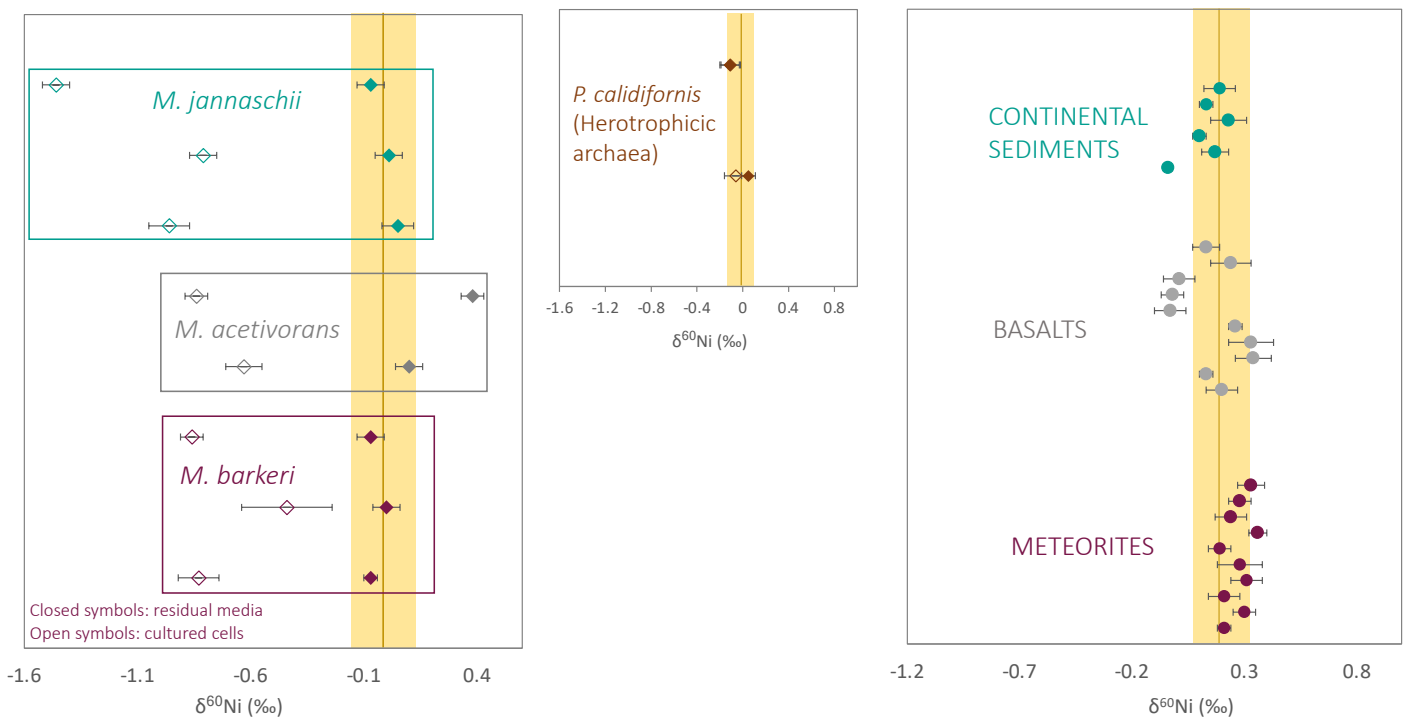
Figure 4: Nickel isotope fractionations for cultured methanogenic archaea, one heterotrophic archaea, and Ni isotope values for a variety of abiotic terrestrial samples and meteorites. The dark yellow line reflects the average, while the shaded yellow boxes reflet 1SD either side of this average (redrawn from Cameron et al., 2009).

1.2.2 Copper isotopes and aerobic methanotrophy

Like Ni, Cu is a bioessential trace metal and key element used to regulate the activity of the enzyme used to regulate the activity of the enzyme Methane monooxygenase (MMO) in particulate (pMMO) form. Methane monooxygenase is an integral protein located in the plasma layer of most aerobic methanotrophs and catalyses the oxidation of methane to methanol as described above (Madigan et al., 2015; Semrau et al., 2010). A simplified schematic of the methane oxidation process is shown below:

$$CH_4 \rightarrow CH_3OH \rightarrow CH_2O \rightarrow HCOO^- \rightarrow CH_2$$
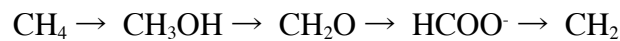
It is hypothesised in this thesis that this process will produce a fractionation in Cu, similar to that observed with Ni. Copper has two stable isotopes: ^{63}Cu and ^{65}Cu, with relative abundances of 69.15% and 30.85% respectively. To date, much work has focussed on the high temperature geochemistry of the Cu isotope system, with fewer studies investigating low temperature Earth surface processes (Moynier et al., 2017), and the Cu isotope variation in unaltered igneous rocks shows very little variability ($\delta^{65}Cu$ = ~0.10‰, n=287). The average Cu isotope signatures of sediments that have undergone minimal biogeochemical processing (i.e. river, lake, and ocean sediment, aerosols, and dust) have average Cu isotope signatures which are almost identical to those of high-temperature igneous rocks ($\delta^{65}Cu$ = ~0.08‰, n=48) (Figure 5a). However, supergene Cu ore minerals which have undergone (potentially multiple) oxidation and redox cycles show significant Cu isotope variability (up to 20‰ (Moynier et al., 2017).

Of specific interest here are the environmental samples which have experienced higher biogeochemical processing and which record an approximate Cu isotope range of ~2.5‰ (Figure 5b). Experimental constraints on Cu isotope fractionation propose four main mechanisms by which this 2.5‰ variation can occur. There are: (i) Equlibrium isotope distributions between different oxidation states (i.e. Cu(I), Cu(II), Cu(III); (ii) Equilibrium isotope distributions between dissolved aqueous species; (iii) Equilibrium and kinetic effects caused by interactions between (both biotic and abiotic) solids and aqueous solutions (i.e. sorption and precipitation); and (iv) the equilibrium and kinetic

effects related to cellular uptake (both in microbes and higher plants) (Moynier et al., 2017 and references therein).
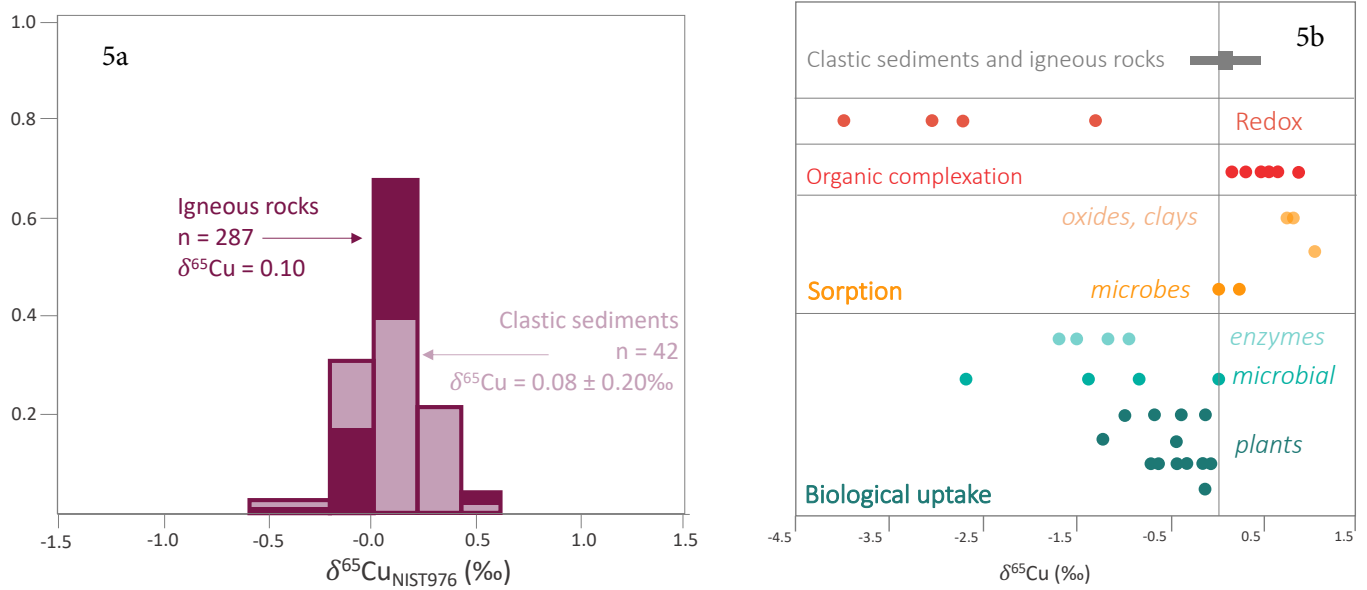
Figure 5a: The distribution of $\delta^{65}Cu$ values across igneous rocks and clastic sediments (modified from Moynier et al., 2017); figure 5b: Copper isotope fractionation induced by low-temperature biogeochemical processes (Moynier et al., 2017), defining Δ as $\Delta_{A-B} = \delta_A - \delta_B$;redox refers to abiotic redox reactions between aqueous Cu(II) and solid Cu(I) precipitates $\Delta_{reduced-oxidised}$ (Zhu et al., 2002, Ehrlich et al., 2004; Mathur et al, 2005); biological uptake: $\Delta_{organism-external}$; microbial sorption: $\Delta_{sorbed-solution}$; abiotic sorption (oxides, clays): $\Delta_{sorbed-free\ ion}$; organic complexation: $\Delta_{complexed-free\ ion}$.

Differentiating between these mechanisms when interpreting low-temperature Cu isotope signals within the context of biological uptake, however, remains difficult. For example, experiments undertaken by Navarrete et al. (2010) suggest that live bacterial cells preferentially take up the lighter Cu isotope (^{63}Cu), while the heavier isotope of Cu (^{65}Cu) sorbes to the dead microbial surfaces in a processes hypothesised to involve both mechanism iv (active cellular transport) and i (in this case, the reduction of Cu(II) to Cu(I). Mechanism i has also been noted during the incorporation of Cu(II) into proteins synthesised by bacteria and yeast (e.g. Zhu et al., 2002). Experiments investigating the sorption of Cu to bacterial and diatom surfaces reveal no Cu isotope fractionation upon sorption to bacterial cells at circumneutral pH, however at low pH (1.8 – 3.3) isotopically light Cu is found to be sorbed to the bacterial surface (Pokrovsky et al., 2008). During sorption of Cu to abiotic surfaces, aqueous Cu concentrations are noted to decrease as a function of increasing pH, as ^{65}Cu sorbs to ferrihydrite minerals leaving the residual water

column isotopically light (Balistrieri et al., 2008). As all metals sorb to the external surfaces of microbial cells, mechanism (iii) may also be relevant, however this is dependent on the size of the available free metal ion pool (Moynier et al., 2017).

Limited information is available pertaining to the fractionation of Cu by methanotrophic bacteria. Chi Fru (2014) showed that cells fractionate Cu isotopes during methane oxidation in experiments involving methanotrophic bacterial growth on various Cu-doped ferrihydrite minerals; lighter Cu isotopes are associated with biomass and heavy Cu isotopes are associated with the residual minerals. It was proposed that these patterns were proportional to growth and methane oxidations rates, however there is no published data to substantiate these results. Applications of Cu isotope geochemistry to deep-time geological materials are also limited, and as such there is little data on Cu isotopes in sedimentary rocks. One study, which analysed Cu isotopes in black shales and BIFs across the Archaean-Palaeoproterozoic transition (i.e., the GOE), found a shift from predominantly heavier to permanently lighter Cu isotopes (Chi-Fru et al., 2016). This has been interpreted to ultimately reflect increased oxidative weathering and a progressive increase in sulphate and sulphide availability during the GOE; in ferruginous (pre-GOE) waters, ^{65}Cu would have preferentially adsorbed to Fe-oxides deposited as BIFs, leading to ^{63}Cu enriched biomass and therefore ^{63}Cu enriched shales. Post-GOE oxidative weathering would have supplied the oceans with isotopically heavy Cu-Fe sulphides, which, along with waning BIF formation, would have led to ^{65}Cu enriched biomass/shales (Chi-Fru et al., 2016). Oxidative weathering results in dissolved riverine Cu with a heavy isotopic composition due to the controls that redox exerts on Cu isotope fractionation (namely equilibrium isotope distributions between the different oxidation states of Cu; e.g., Fujii et al., 2013)

Within the context of this thesis, Cu isotopes provide a potential proxy for aerobic methanotrophy in deep time. While there is currently no direct evidence to show that Cu isotopes are fractionated during uptake by aerobic methanotrophs, there is evidence for isotopic fractionation during uptake by other microbes, suggesting that processes

ubiquitous to biological metal uptake have the potential to fractionate the isotopes of said metals.

1.3 Aims and objectives

1.3.1 Research question

The aim of this thesis is the answer the broad research question:

How do Cu and Ni isotopes respond to enhanced methane cycling in deep time?

This thesis takes a geochemical approach, applying Cu and Ni isotopes to the ancient rock record in order to further understand the role of CH_4 cycling throughout the late Archaean. The aim of this thesis is thus to apply the novel metal stable isotope systems of Cu and Ni isotopes to ancient sedimentary rocks, to generate a high-resolution dataset, and to use these data to better understand the role of methanogenesis, anaerobic methanotrophy, and aerobic methanotrophy in the formation of PHEs.

Of particular significance to this study is the relative significant of aerobic vs anaerobic methanotrophy in the ancient system, and whether metal stable isotopes can serve as complementary or stand-alone proxies for enhanced methane cycling in conjunction with sedimentary records characterised by light carbon isotopic compositions. Core GKF01 from the *c.* 2.5 Ga Upper Nauga formation (Transvaal Supergroup, South Africa) has been selected as the primary lithological unit to investigate these potential metal isotope proxies. These rocks have previously been subjected to a successful high-resolution C-S-Fe speciation study (Izon et al., 2017) and provides the most compelling evidence for a period of enhanced CH_4 cycling in the geological record (see Figure 2, section 1.1.2 for all of GKF01, see Figure 2, Chapter 3 for the data from Izon et al., 2017). In addition to this, it represents a shallow marine setting with possible small-scale localised oxygenation events, providing a nuanced environment in which to study the possibility of aerobic methanotrophy. Alongside this, a complementary study of Cu isotopes in a *c.* 2.7 Ga core from Western Australia (Hamersley province, core SV1) will

further test the applicability of these isotope systems to similar rocks; it has already been proposed that aerobic methanotrophy was occurring in this environment, and previous C isotope analyses of these rocks have yielded some of the lightest $\delta^{13}C_{org}$ values in geological history (~ -50‰; Eigenbrode and Freeman., 2006). In contrast to GKF01, core SV1 represents a shallow environment with frequent input of volcanic detrital material (Stueken et al., 2015; 2017), and is hypothesised to reflect a closed, evaporitic, and alkaline lake system (e.g., Buick, 1992; Coffey et al., 2013; Stueken et al., 2017). This contrasting environment, which was deposited approximately 2 million years before the Upper Nauga formation, will provide the opportunity to compare Cu (isotope) cycling in two different late Archaean depositional environments.

The ultimate trigger for late Archaean atmospheric hydrocarbon haze formation, along with any biological controls, remains unknown. In this thesis, it is hypothesised that the CH_4 hazes thought to be recorded in GKF01 formed as the result of increased CH_4 fluxes from the biosphere, triggered by enhanced continental weathering; however, this remains untested. Figure 6 illustrates the proposed mechanism by which PHEs could have formed, based on the work of Izon et al. (2017) along with potential isotope systems suitable to test this hypothesis. In this schematic, the unknown trigger (which is hypothesised to be enhanced continental weathering) stimulates heightened primary productivity via additional nutrient delivery to the surface ocean. The subsequent higher availability of C_{org} then leads to increased methanogenesis, causing CH_4 to accumulate in the atmosphere and create a haze (evidenced by the $\Delta^{33}S/\Delta^{36}S$ ratio changes). An increase in methanogenic activity also impacts other biological processes. Methanotrophy is of particular interest; the $^{13}C_{org}$ record is representative of low C assimilation into substrate via CH_4 oxidation, thus the $^{13}C_{org}$ excursions observed during PHEs are likely the result of enhanced methanotrophy.
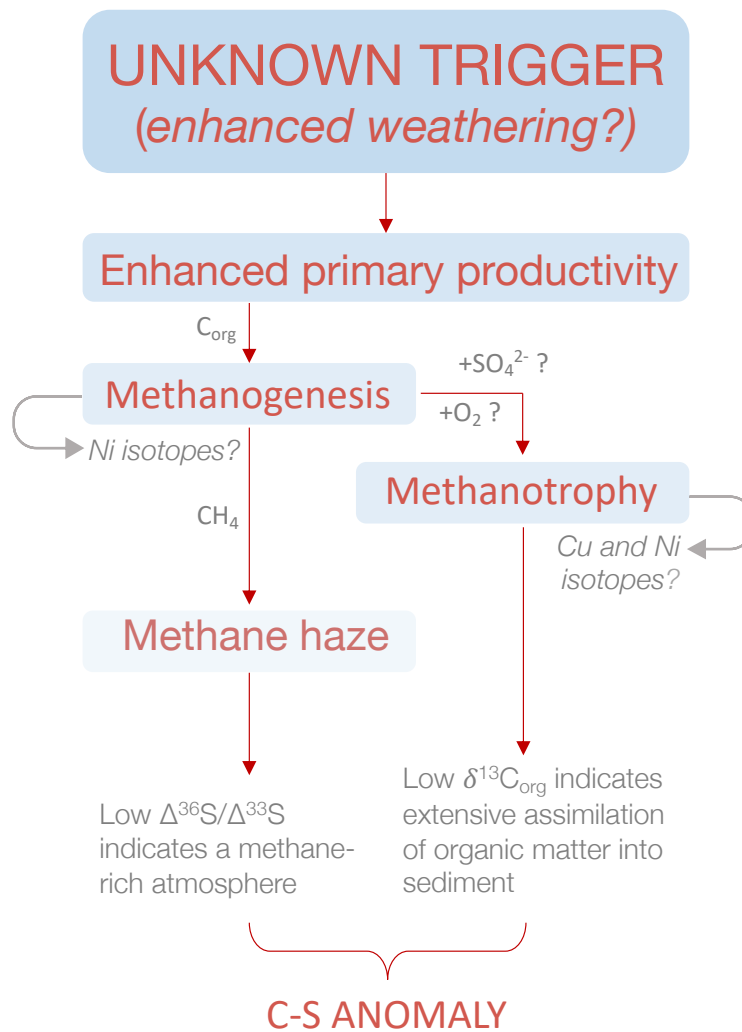
Figure 6: A schematic depiction of the processes leading to late Archaean organic haze formation. Potential isotope proxies are labelled by their respective metabolisms.

The overarching research aim above can be addressed by a number of objectives, which have been framed as Research Questions, given in Table 1. In order to address these questions, this thesis exploits core GKF01, an exceptionally preserved 2.65 – 2.5 Ga drill core from the Transvaal Supergroup, South Africa (Zerkle et al., 2012; Fischer et al., 2009) and core SV1, an exceptionally preserved *c.* 2.7 Ga drill core from the Tumbiana formation, Western Australia (e.g., Eigenbrode and Freeman, 2006).

	Research Question	Chapter
1	How can isotopic analysis of Cu and Ni contribute to our understanding of historic methane cycling behaviour in ancient lakes and oceans?	3, 4, 5
2	To what extent can Cu isotopes provide constraints on aerobic methane oxidation in deep time?	3, 4
3	In what way was methane oxidation a contributing factor to the extremely low $\delta^{13}C_{org}$ measured in core GKF01?	3, 5
4	Is there evidence of this in older rocks from Western Australia which possess similar $\delta^{13}C_{org}$ signatures to those in GKF01 in a contrasting environment?	4
5	To what extent can Ni isotopes provide constraints on methanogenesis in deep time?	5

Table 1: Research questions addressed in this thesis.

1.4 Thesis structure and author contributions

Chapter 2 of this thesis details the geological history of core GKF01, along with the analytical methods employed for the acquisition of the Cu isotope data for this thesis. Nickel isotope methods are discussed separately in Chapter 5.

Chapter 3 examines Cu isotopes in core GKF01 within the context of the C-S anomaly data produced by Izon et al. (2017). The aim of this chapter is to understand the marine biospheric response to enhanced CH_4 cycling and to test the efficacy of Cu isotopes as potential biomarkers in Archaean sedimentary rocks. Chapter 3 addresses questions 1, 2, and 3 listed above.

Chapter 4 applies Cu isotopes to core SV1, a core older than GKF01 which exhibits some of the lowest $\delta^{13}C_{org}$ values in geological history. Questions 1, 2, and 4 are addressed in this chapter, which examines a high-resolution Cu isotope record alongside Cu speciation models in order to further test the applicability of Cu isotopes as a deep-time biomarker and to investigate how basin size and pH may have impacted Cu (isotope) cycling at this time.

Chapter 5 answers research questions 1 and 3, and focuses on expanding the development of Ni isotope analyses in core GKF01 in order to apply them to the ancient rock record. The preliminary Ni isotope data are analysed alongside existing C-S data for this core and provide a starting point from which to further develop this proxy in ancient sedimentary rocks.

The impact of this study, main findings, and the outlook for future work is summarised in **Chapter 6.** This chapter provides a concluding discussion of the implications of this research by updating the knowledge gap.

A manuscript based on Chapter 3 is currently under review with Precambrian Research. N.A.V. Zavina-James, A.L. Zerkle, M.R. Warke, R.C.J. Steele, P.S. Savage (*in review)*. A copper isotope investigation of methane cycling in the Late Archaean, *Precambrian Research.*

All written work presented in this thesis is my own. In addition to guidance and technical support from my supervisors, a number of collaborators were established while undertaking the research presented in this thesis. Listed in order of appearance, these are:

- Dr Matthew Warke (University of St Andrews), who assisted in REY_{SN} anomaly (namely Eu_{SN}) data analysis of the GKF01 carbonate-rich sediments in Chapter 3.

- Dr Laura Wasylenki (Indiana University, Bloomington, USA; now Northern Arizona University, USA) and Professor Shuijiong Wang (Indiana University, Bloomington, USA; now China University of Geosciences) who granted me access to their Ni isotope biogeochemistry lab, provided the reagents with which I was able to undertake Ni column chemistry, and who operated the mass spectrometer during the analysis of the Ni isotope data presented in Chapter 5.

Chapter 2

Materials and methodology

2.1 Materials

2.1.1 Core GKF01: Geological history

While the absolute reconstruction of Archaean continental configuration remains speculative, geological and palaeomagnetic data point to the existence of the Kenorland supercontinent by the late Archaean (*c.* 2.7 – 2.6 Ga), which included the Karelian, Kaapvaal, Pilbara, and Superior cratons (Lubina and Slabunov, 2011; 2017). Alongside this, there are numerous lines of quantitative evidence to suggest the Kaapvaal and Pilbara cratons in particular were connected, forming the supercraton 'Vaalbara' between *c.* 2.78 – 2.70 Ga (e.g. de Kock et al., 2009). Much of this thesis uses samples from the Transvaal Supergroup, South Africa (Kapvaal craton) in order to investigate the role of enhanced CH_4 cycling in the late Archaean. In chapter 4, the same methodology is applied to an older core from the Tumbiana Formation, Western Australia (Pilbara craton). Please see Chapter 4 for a detailed description of the geological setting of the Tumbiana Formation. The Transvaal Supergroup represents a ~15 km thick succession of carbonates, iron formations, clastics, glacial deposits, and volcanics that were deposited on the Kaapvaal Craton between *c.* 2.65 ± 0.08 to 2.06 Ga (Neoarchaean to Palaeoproterozoic) (e.g. Fischer et al., 2009; Erikson et al., 2006). The rocks of the Transvaal Supergroup are preserved across three basins: Griqualand West, Kanye, and Transvaal (see Figure 1). The geology of these basins is dominated by the thick (~1500 – 1700 m) Neoarchaean Campbellrand-Malmani carbonate platform, which formed through a combination of microbial and

abiotic processes (e.g. Sumner and Grotzinger, 2004; Beukes, 1987). The deposition of this carbonate platform occurred over ~65 Ma, beginning at *c.* 2.58 and ending at *c.* 2.52 Ga, based on U-Pb dating of zircons from a volcanic ash bed (Sumner and Bowring, 1996), and records the formation of a carbonate ramp and the establishment of a carbonate shelf which was ultimately flooded during a major transgressive event (Beukes, 1987).
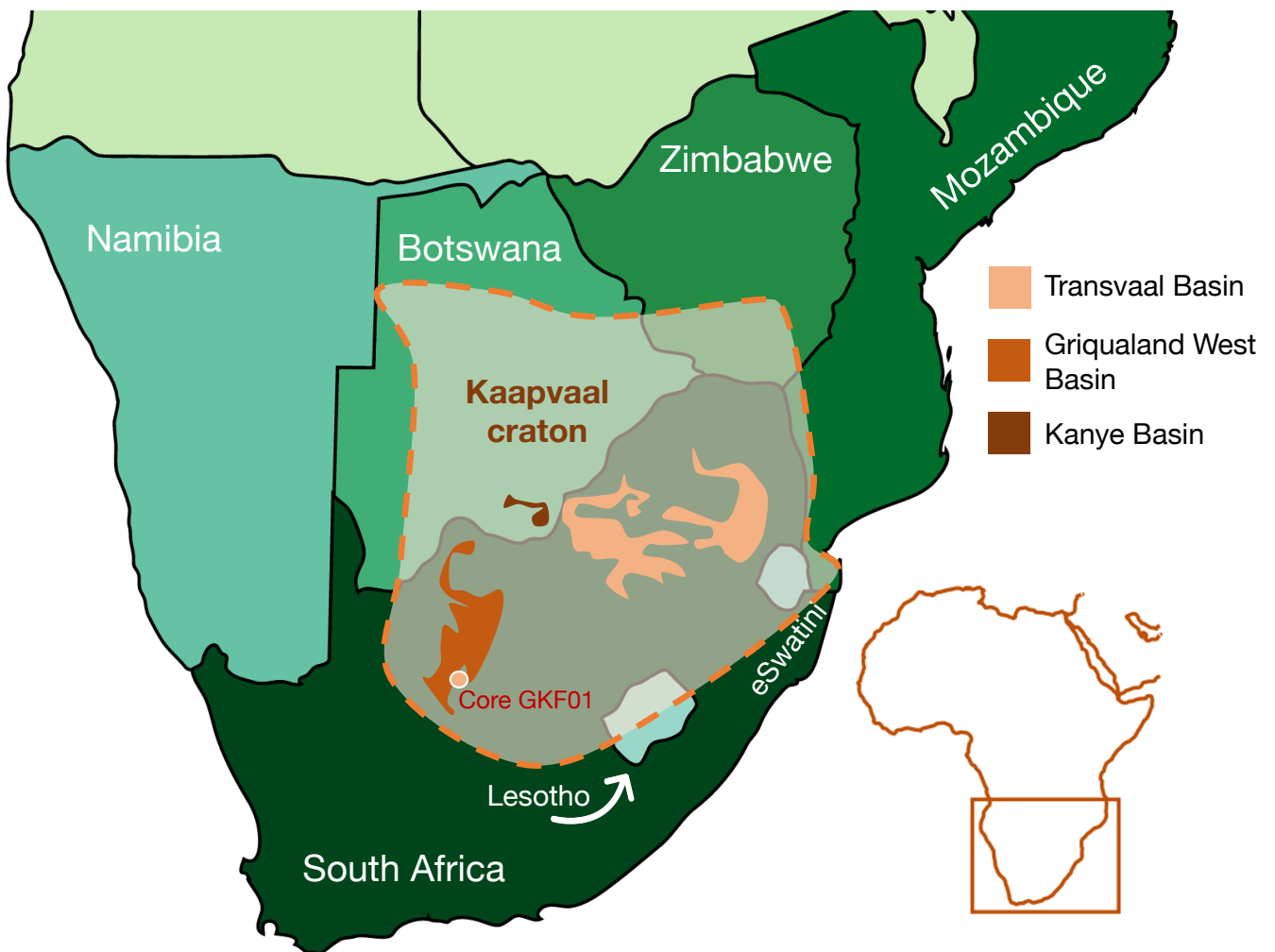
Figure 1: A map showing the regional geography of the Kaapvaal craton within the context of Southern Africa. Within the Kaapvaal craton, the Transvaal, Griqualand West, and Kanye basins are marked. Core GKF01 is taken from the South Griqualand West Basin (e.g. Wright et al., 2004).

The geology of this core has been extensively described by Schroder et al (2006). This section provides a summary of this description, focussed on core GKF01. Core GKF01 was drilled by the Agouron Insitute through the carbonate-dominated Campbellrand Subgroup (Figure 2) of the Transvaal Supergroup (Griqualand West basin, Figures 1 & 2) and comprises approximately 1,330 m of late Archaean sedimentary rocks. It represents a proximal transect through the latter half of the Schmidtsdrif Subgroup, the Campbellrand-Malmani carbonate platform, and the beginning of the Asbestos Hills Subgroup. Age constraints from U-Pb analyses of zircons place the base of the core at 2.65 ± 0.08 Gyr and the top at 2.5 Gyr (Zerkle et al., 2012; Fischer et al., 2009). Please refer to Figure 3 for a stratigraphic log transecting core GKF01.

The base of the core, within the Boomplaas formation of the Schmidtsdrif Subgroup, comprises approximately 21 m of cross-bedded to massive oolitic dolostones with local-scale stromatolitic structures. Along with this, a noted decrease in siliciclastic material up-section indicates a shallow subtidal environment. The Boomplaas Formation represents the establishment of a shallow-water carbonate ramp. Above this, the Lokammona Formation persists for 50 m and contains siliciclastic mudstones, pyritic siliciclastic conglomerates, and oolitic dolostones.
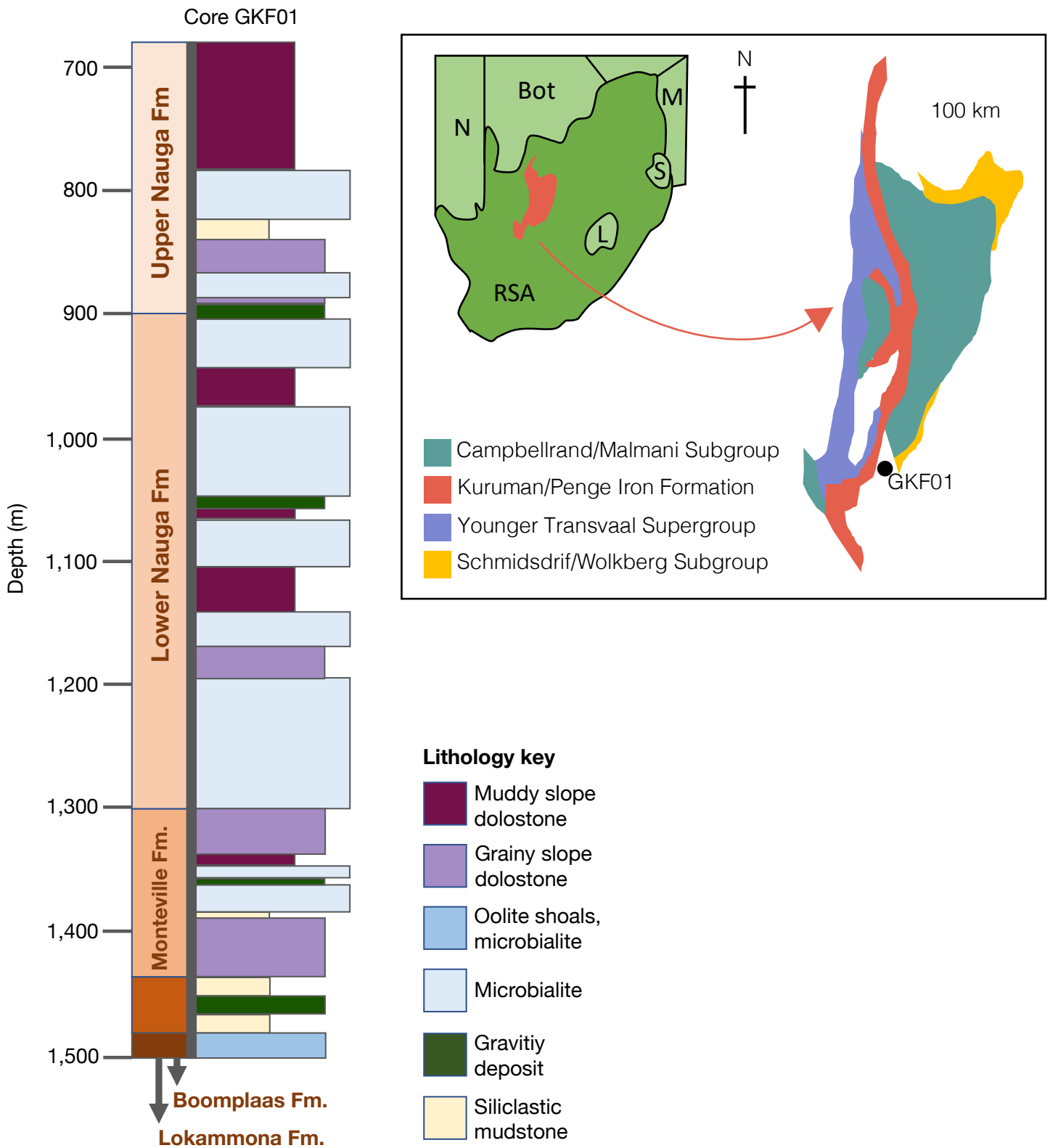
Figure 2: A schematic stratigraphic log of core GKF01, modified from Schroder et al. (2006) and Zerkle et al. (2012). Box widths indicate relative grain size. Inset: A schematic map showing the regional context of Core GK01 (redrawn from Izon et al., 2017).

The Nauga Formation, which has a sharp and conformable boundary with the Monteville Formation, has been informally subdivided into the Upper and Lower Nauga formations. These formations are separated by the Kamden Iron Formation, a pervasive marker that allows for stratigraphic correlation across cores (see Figure 3). The Lower Nauga Formation, like the Monteville Formation, was deposited in a sub-wave base slope environment. It persists for 404 m in core GKF01 and comprises well developed microbial facies, cherts, and cyclical microbialte-slope dolostone units. Local thin banded iron formation (BIF) beds are also present. The Upper Nauga Formation, from which the samples analysed for this thesis were obtained, begins above the Kamden Iron Formation. It continues for 581 m, making it the thickest formation in the core. It is composed of muddy and grainy slope dolostones, which occur in equal fractions. A prominent feature of this section is the cyclicity between microbialites and slope dolostones; the 'patchy' distribution of the microbialites have been inferred as a signal of variable local sediment input. Towards the top of the formation, there is a marked increase in intraclastic and peloidal turbiditic dolomite lithofacies. The Upper Nauga Formation retains the slope depositional environment of the Lower Nauga Formation, however the increasing presence of siliclastic mudstones unaccompanied by storm deposits suggests an increase in the volume of detrital input. A more detailed description of the Upper Nauga Formation, including the 100 m section analysed for this thesis can be found in section 1.1.2 below.

Overlying the Nauga formations, the Klein Naute Formation (84 m) presents massive and laminated siliclastic mudstones with abundance pyrite and chert nodules. The prevalence of mudstones and absence of detrital carbonates is suggestive of a low-energy deep water environment of deposition, well below the storm wave base. Interspersed with the low energy deposits are some dolarenite beds and cherts, the former of which indicates occasional high-energy depositional events. These low energy and deepening conditions are also reflected in the overlying Kuruman Formation (39 m), which presents a gradational increase in chert over siliclastic mudstone, along with episodes of BIF deposition.

Core GKF01 therefore provides a transect of a platform-to-basin transition. Beginning with a shallow sub-tidal carbonate ramp (Boomplaas Formation), flooding led to an increase in depth and the formation of a slope environment. The sub-wave base slope depositional environment then persisted throughout the Monteville and Nauga formations, before further deepening (i.e. Kleine Naute and Kuruman formations). Geochemical analyses of siliciclastic mudstones throughout this core are broadly concurrent with established major and trace element values of Archaean Continental Crust (ACC) and are thus reflective of Archaean crustal composition. However, these geochemical data also indicate that between the deposition of the Monteville and Nauga formations, a change in the provenance of the siliciclastic material took place. This is associated with tectonic changes, a major drop in sea level, and a noted major depositional hiatus (Schroder et al., 2006).

2.1.2   Core GKF01: Upper Nauga Formation and UN-HR

This thesis focuses on a high resolution 100m section (hereon referred to as UN-HR (Upper Nauga high resolution) of core GKF01 which transects the lower portion Upper Nauga formation (see Figure 3). UN-HR has already been subjected to one high resolution study, establishing the presence of a periodic haze event (PHE; Izon et al., 2017), providing a robust geochemical framework for further study. Due to its position almost directly above the Kamden Iron Formation (a pervasive stratigraphic marker throughout the Transvaal Supergroup), UN-HR can also be directly compared and traced within other cores. On a 10-m scale, the lithologies measured for this thesis come from three different lithological units: mudstone (approximately 50% of samples), mudstone-boundstone, and calcareous mudstone (the latter two making up the remaining 50% of samples). As the studied transect does not comprise uniform lithologies, nuances between lithologies must be considered and accounted for throughout sample preparation and analysis. For example, high abundances of Na and Mg can impact the efficacy of Ni column separations (please refer to Chapter 5 for detailed discussion on this). Figure 4 shows average major element distributions per lithological unit, higher concentrations of trace metals are found within the mudstone units (i.e. Zerkle et al., 2020; this study)

however, once normalised to TOC, they do not appear to be anomalous. Facies changes are therefore unlikely to impact any trace metal isotopic signatures throughout UN-HR.
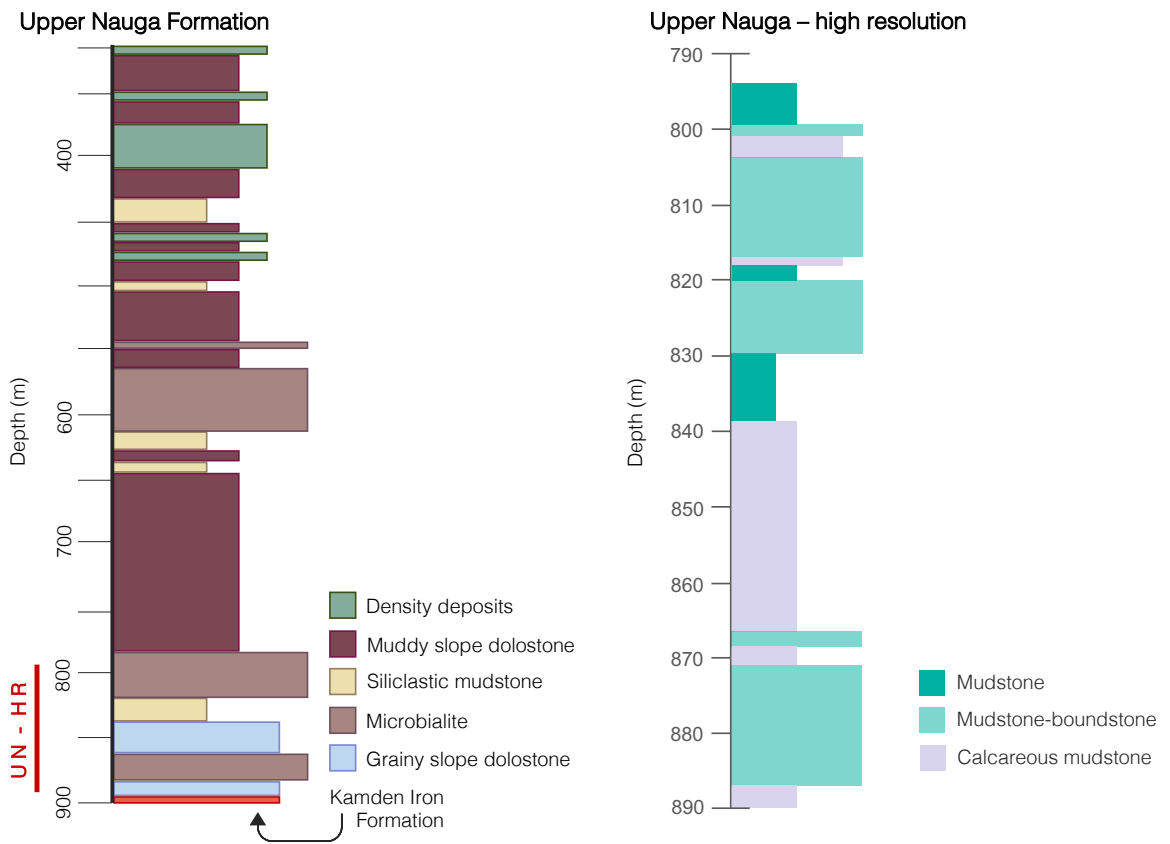
Figure 3: Stratigraphic log of the Upper Naugua Formation (redrawn from Schroder et al., 2006) and the UN-HR section (modified from Izon et al., 2017). Bar width indicates relative grain size.
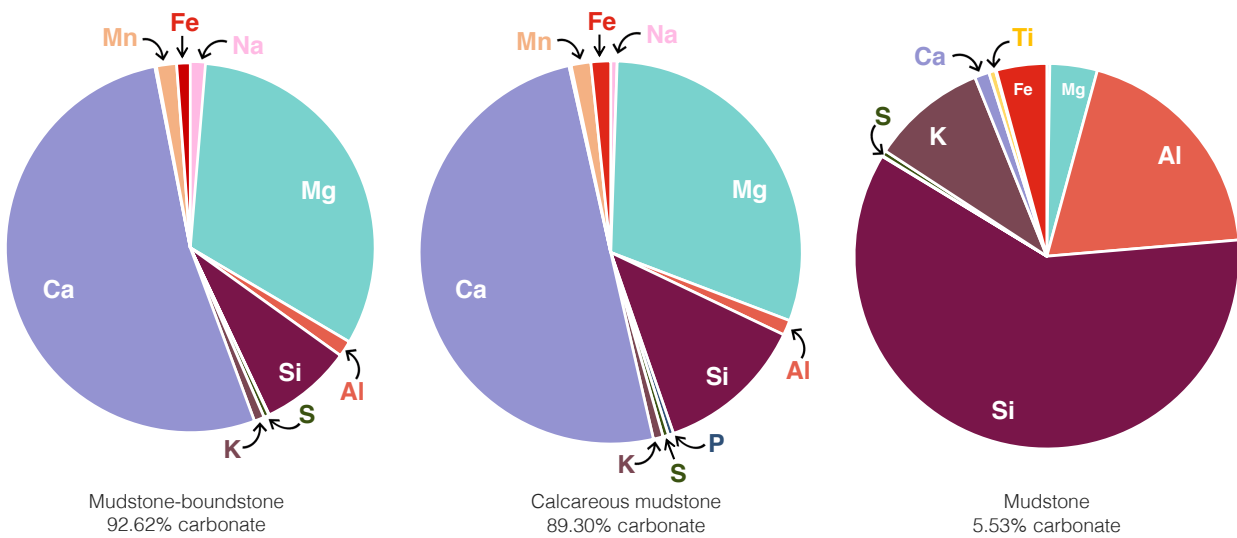
Figure 4: Average major element distributions per UN-HR lithological units.

2.1.3 Major and trace element analysis of core GKF01

Initial major and trace element abundances of core GKF01 were undertaken by Dr. Gareth Izon.

Major elemental abundances were determined by X-Ray Fluorescence (XRF) at the University of St Andrews. Samples were fused using a mixed lithium tetraborate (20%) and lithium metaborate (80%) flux, with ammonium iodide as a releasing agent. Samples were weighed before and after the preparation of fusion discs to determine loss on ignition (LOI). Fused samples were analysed on a Spectro Xepos HE instrument with a 50 W end-window X-ray tube to excite the samples and a 30 mm2 Peltier cooled silicon-drift detector, which provides a spectral resolution (full-width at half-maximum) of ≤155 eV at Mn Kα. These data, along with measured % carbonate, are reported in Appendix B.

Trace element analyses for Chapter 3 were performed at the University of St. Andrews via fusion-enhanced dissolution followed by inductively-coupled mass spectrometry (ICP MS). Approximately 0.25g of sample was weighed into platinum crucibles and roasted at 1000°C, overnight, to remove the volatile component. These pre-combusted residues were then then mixed and fused with 1.25g of a 50:50 mixture of lithium metaborate and lithium tetraborate flux, using a trace amount of ammonium iodide to produce a free homogeneous glass-bead. The resultant glass-bead, after dissolution in 5 % (vol/vol) ultra-pure nitric acid, was prepared for analysis using a Thermo X series2 ICP-MS. Standardisation was achieved via matrix-matched synthetic standards, while drift was corrected by internal normalisation following Re, Ge and Rh doping. Alongside unknowns, various international standards (GSR1–6, SBC-1, OU-8, OU-6 and SD0-1) were processed in an identical manner, producing data typically better than 10 % of certified values.

2.1.4 Core SV1 & the Tumbiana Formation

The Tumbiana Formation was deposited on the Pilbara Craton, Western Australia. Please refer to Chapter 4 for a detailed description discussion of Core SV1 and it's geological setting.

2.2 Methods

2.2.1 Scanning electron microscopy (SEM-EDS)

In order to determine the dominant Cu- and Ni-containing phases within the samples, a subset of hand specimens representing the three different lithological units (mudstone, calcareous mudstone, mudstone-boundstone) were selected for scanning electron microscope (SEM-EDS) analysis. Specimens were analysed at the Analysis and Characterisation facility of the ACEMAC Facility of the University of Aberdeen, using a Carl Zeiss GeminiSEM 300 high resolution Field Emission Scanning Electron Microscope with secondary electron, backscattered electron, and cathodoluminescence detectors. Specimens were cut, polished, and carbon-coated prior to SEM-EDS analysis. Please refer to Appendix A for an SEM image and spectra. The low Cu and Ni abundances in both the calcareous mudstone (Appendix A Figures 2a and 2b) and the mudstone-boundstone specimens (Appendix A Figures 3a – 3d) meant that no discernible Cu or Ni -bearing phases above the detection limit could be identified and as such, no images were captured for these samples. Low but identifiable Cu and Ni concentrations were only seen in the sulphide phases of the mudstone specimens (please see Appendix A Figures 1a – 1i). Nevertheless, while it was not possible to assess the phases hosting Cu and Ni within the mudstone-boundstone and calcareous mudstone unites with 100% accuracy, we hypothesise that, similarly to the mudstones, they are likely hosted in small sulphide phases.

2.2.2 Sample dissolution

Elemental and isotopic analysis of rocks requires complete decomposition of the lithological sample into solution, ensuring that all elements are mobilised and not bound or complexed. The UN-HR sample set analysed in this thesis can, most broadly, be split into two categories; approximately 50% of the samples are organic rich (TOC range 0.62 – 3.26 Wt %) alumnosilicates (Figure 3), and the other 50% are almost pure dolomites, with total carbonate ($CaCO_3$ wt%) ranging from 5.5% - 99.61%; total average 87.26%) (Figure 3). Given this, and that Cu and Ni are assumed to be hosted within sulphides, samples were dissolved via open-vessel acid digestion. This method is simple and effective when applied to samples that do not contain refractory minerals such as zircon. The SV sample set, though predominantly phyllosilicate, followed the same process, despite the lithological changes not being as nuanced. For Cu isotope analysis, samples were digested with ammonium bifluoride (NH_4HF_2) rather than concentrated hydrofluoric acid (HF) following the method developed by Zhang et al. (2012). As Ni isotope analyses are far more susceptible to contamination, samples for Ni isotope analysis were digested following the standard method for organic-rich geological materials, involving concentrated HF. All dissolutions were conducted within trace metal clean (ISO 5 hoods) laboratory conditions at the University of St Andrews.

Reagents:

- Milli-Q ultrapure water, 18.0 MΩ/cm resistivity, obtained from a Milli-Q water purification system (EMD Millipore, MA, USA).

- Hydrofluoric acid (HF UpA, 47-51%, ROMIL Ltd, UK).

- Ammonium bifluoride (NH_4HF_2, 99.999% trace metals basis, Sigma-Aldrich, MO, USA).

- Commercially available nitric acid (HNO_3, 68%, reagent grade (RG)) and hydrochloric acid (HCl, 37%, RG grade) was purified in a sub-boiling distillation system (Savillex, MN, USA).

All teflon and plasticware (pipette tips, centrifuge tubes, crucibles) was pre-cleaned via acid leaching. Plasticware was leached in 1 M distilled HCl for 24 hours at room temperature and then triple-rinsed with Milli-Q water. Teflon was cleaned by acetone, followed by 24 hours of leaching in hot RG HNO_3, 24 hours of leaching in in hot aqua regia, 24 hours of leaching in hot RG HCl, and then triple-rinsed with Milli-Q water. The dissolution method for Cu is described below. For the dissolution method employed for Ni isotope analyses, please refer to Chapter 5.

2.2.2.1 Dissolution methods for Cu and Ni

Sample digestions for Cu isotope analyses were undertaken using the digestion reagent NH_4HF_2, allowing us to avoid the extensive usage of concentrated HF, a corrosive and toxic acid. The utilisation of NH_4HF_2 as a digestion reagent for geological samples has been demonstrated to be an effective and comparatively safe and fast dissolution method (Zhang et al., 2012). Additionally, when compared to samples digested via HF for Ni analysis, we found that it is more effective at destroying refractory organic carbon particulates.

Approximately 50 mg (± 5 mg) of sample powder was weighed into pre-cleaned 7 mL Savillex PTFE vials using a Mettler-Toledo analytical balance (Mettler Toledo, UK), followed by 200 mg of NH_4HF_2. A mass ratio of 4:1 (NH_4HF_2 : sample) is required for the effective recovery of elements in lithological samples (Wilson, 1998), although Zhang et al (2012) found that 200 mg of NH_4HF_2 was effective in digesting sample masses of up to 200 mg. Vials were capped tightly and heated in an electric oven set to 230°C for 3 hours in order to obtain even and consistent heating. Ammonium bifluoride has a boiling point of ~140°C, although it can begin to partially decompose to form ammonia and HF vapours at temperatures of around 120°C and becomes molten at ~125-126.5°C. The reaction between the decomposition products on SiO_2 produce fluorosilicates which sequentially evolve to produce the highly volatile silicon tetrafluoride (SiF_4) upon the addition of HNO_3 and the application of heat (e.g. O'Hara et al., 2017). After oven heating, the samples were left to cool at room temperature. Once cooled, 2 mL of concentrated (~15.8 M), distilled HNO_3 was added and the vials were capped and placed on a hot plate at 160°C. This procedure effectively removes Si and liberates metals bound within the

silicate structure (e.g. Chao and Sanzolone, 1992). Nitric acid is also a strong oxidising agent that is commonly used to decomposes sulphides, carbonates, and organic material. The digests were then dried down overnight on a hot plate set to 160°C. Once dry, 2 mL of concentrated (~11.7 M), distilled HCl was added. Hydrochloric acid enables the further dissolution of carbonates, phosphates, sulphates, and sulphides (e.g. Chao and Sanzolone, 1992). and also serves to destroy any fluoride complexes which can form due to the use of F in the dissolution process. Finally, this final addition of concentrated HCl ensures that no traces of HNO_3, which can distrupt the efficacy of the column chemistry, remain in solution prior to ion exchange chromatography. After fluxing for 24 hours on a hot plate at 160°C, the digests were evaporated at 120°C. The final sample residues were taken up in 1 mL 7 M HCl + 0.001 % H_2O_2 (trace analysis grade) for ion exchange chromatography. Hydrogen peroxide is added to ensure that Cu is oxidised prior to ion exchange chromatography. The process is summarised in table 1 below.

Step	Action
1	weigh 50 mg sample powder
2	weigh 200 mg NH_4HF_2
3	Oven @ 230°C for 3 hours
4	add 2 mL concentrated HNO3
5	reflux 24 hours
6	dry down 24 hours
7	add 1 mL concentrated HCL
8	reflux 24 hours
9	dry down 24 hours
10	add 1 mL column acid

Table 1: Summary of the digestion procedure utilised in the dissolution of core GKF01 samples for Cu isotope analysis.

Sample dissolutions for Ni used trace metal grade, concentrated HF rather than NH_4HF_2 and the procedure is summarised in table 2. Powders were weighed to ensure that each sample contained between 1.5 – 2 µg of Ni; low Ni samples were weighed at 570 mg while higher Ni samples were weighed at 50 mg. For clarity, differing volumes and masses will be written as X aa, (Y aa) (e.g. 50 mg (570 mg) as samples with larger starting masses required larger volumes of acid reagents. After weighing, samples were initially treated with 0.5 mL (1 mL) of concentrated and distilled HNO_3 to avoid the formation of insoluble fluorides upon the addition of HF. As HNO_3 is a powerful oxidant, the addition

of concentrated HNO₃ to samples containing a high organic content can cause it to react vigorously. Therefore, following the addition of HNO₃, samples were left in a fume hood to react for ~10 minutes, after which 2 mL (4 mL) concentrated HF was added. The samples were left on a hot plate set to 160°C for 48 hours, dried down at a low (120°C) temperature for 24 hours, and then treated with 2 mL (4 mL) of aqua regia (1.125 mL (2.25 mL) concentrated HNO3, 0.5 mL (1 mL) concentrated HCl, 0.37 mL (0.75 mL) MilliQ). Aqua regia effectively releases trace metals from shales and can dissolved trace metals from some silicates (e.g. Xu et al., 2012). Following this addition, samples were refluxed for 24 hours on a hot plate set to 160°C and then dried down for 24 hours. This process was sequentially repeated with concentrated distilled HCl and HNO₃.

Step	Action
1	weigh 50 -570 mg sample powder
2	add 0.5 mL conc HNO3 (1 mL for larger samples)
3	add 2 mL conc HF (4 mL for larger samples)
4	hot plate @ 160°C for 48 hours
4	dry down 24 hours
5	add 2 mL aqua regia (4 mL for larger samples)
6	reflux 24 hours
7	dry down 24 hours
8	add 2 mL conc HCl (4 mL for larger samples)
9	reflux 24 hours
10	dry down 24 hours
11	add 2 mL conc HNO3 (4 mL for larger samples)
12	reflux 24 hours
13	dry down 24 hours
14	add 1 mL column acid

Table 2: Summary of the digrestion procedure utilised in the dissolution of Core GKF01 samples for Ni isotope analyses.

2.2.3 Trace metal analysis of core SV1

Digests were analysed for their trace element concentrations using an Agilent 7500a inductively coupled mass spectrometer (ICPMS). Samples were diluted 1:100 in weak (0.1 M) HNO_3 to given an approximate concentration of 20 ppb Cu and analysed for the following masses: ^{51}V, ^{53}Cr, ^{55}Mn, ^{57}Fe, ^{59}Co, ^{60}Ni, ^{63}Cu, ^{66}Zn, ^{75}As, ^{107}Ag. Blank and standard measurements were performed every 20th sample. Raw counts were converted into elemental concentrations by blank subtraction and standardisation using a multielement solution (IV-ICPMC-71A, Inorganic Ventures). Sample measurements were repeated 3 times and the resulting values represent the average of these three measurements. The standard deviation of these replicates was typically less than 3% for Cu, 4% for Ni, and 5% for the other elements reported here. Accuracy was assessed by dissolution of reference materials SCO-1 (marine shale) and GSP-2 (granite), which have reported Cu concentrations of ~28.7-29 ppm and ~43ppm respectively. Based on three replicate measurements, a an average value of 27.68±2 ppm for SCO-1 and 48±2 ppm for GSP-2 was measured. These data are presented in Chapter 4.

2.2.4 Ion exchange chromatography

Please refer to Chapter 5 for a detailed description and discussion of the ion exchange chromatography procedure for Ni.

For this thesis, Cu was concentrated and purified using a double-pass single column anion exchange chromatographic technique. Column chromatography is a method of element separation involving two phases: a mobile phase (liquid eluant) and a stationary phase (a porous matrix, e.g. ion exchange resin). When the mobile phase is passed through the stationary phase, elements are exchanged. Different affinities between elements contained in the liquid phase and stationary phase mean that elements travel at different speeds down the column length. The variable speeds of different elements can be exploited in order to chemically separate elements from each other (e.g Alberède, 2013). Factors such as resin size and type, as well as pH and acid medium, control the speed and efficacy of the separation procedure. Ion exchange resins can vary in terms of charge (anion; positively charged or cation; negatively charged), strength (strong ion exchange resins retain selectivity over a wide range of pH conditions, while weak ion exchange resins are pH-dependent), and resin particle size and porosity.

The method for the separation of transition metals on strongly basic anion exchange resins in a HCl media was first demonstrated by Kraus and Moore (1953) and Köster (1973). While successful, this procedure did not enable quantitative elimination of matrix elements as the standard BioRad AG1 resin employed does not efficiently retain Cu, resulting in Cu elution alongside matrix elements (Marechal et al., 1999). This problem has since been resolved by the use of a macroporous form of the AG1 resin (AG MP-1) which has significantly higher distribution coefficients for Cu(II), Fe(III), and Zn(II) (Van der Welt et al., 1985), broadly meaning that it can retain more of these elements per unit volume of the stationary phase (Ettre, 1992). The macroporous resin AG MP-1 (100-200 mesh, chloride form) such as the one employed for the samples analysed for this thesis) is made from chips rather than beads, increasing pore space but making it very fragile. Before use, the resin was cleaned by agitation in alternating Milli-Q and 0.5 N

HNO₃ rinses, after which the finest particles still in solution were discarded. The resin was then left in 6N HCl over night, rinsed three times in Milli-Q, and stored in Milli-Q.

For this thesis, all column chemistry was performed on bespoke shrink-fit Teflon columns containing a 15 mL reservoir and a 1.8 mL resin bed (6 mm diameter). The columns were loaded with 1.8 mL of cleaned Bio-Rad AG MP-1 anion resin (after Marechal et al., 1999) and stored in 0.5 M HNO₃. Before each set of column chemistries, the resin was gently backwashed in 5 mL of MilliQ in order to decompact the resin bed and to eliminate air bubbles that may interfere with elution speeds. Prior to the analysis of samples, the separation method was calibrated to ensure that the procedure effectively removed all ions contained within organic-carbon rich shale matrices. Two USGS standards were selected (the granite SGR-1B and the shale SCO-1) for this calibration. Sample powders were digested via the method used for Ni analyses (i.e. via HF rather than NH_4HF_2) and sequentially loaded and eluted in 1 mL aliquots following the separation procedure outlined in table 3. Elution curves for both standards are show in Figure 5. Copper in both standards was successfully separated between 12 – 26 mL, meaning that no modifications to this method were required.

Separation stage	Solution matrix	Volume (mL)
Pre-cleaning	MilliQ	10
Pre-cleaning	0.5 N HNO₃	10
Pre-cleaning	MilliQ	7
Pre-cleaning	0.5 N HNO₃	7
Pre-cleaning	MilliQ	5
Pre-cleaning	0.5 N HNO₃	5
Pre-cleaning	MilliQ	7
Conditioning	7 N HCl + 0.001 % H_2O_2	7
Sample load*	digested sample in 7 N HCl + 0.001 % H_2O_2	1
Matrix elution ‡	7 N HCl + 0.001 % H_2O_2	7
Copper elution†	7 N HCl + 0.001 % H_2O_2	20

*loaded in two aliquots of 0.5 mL

‡ acid added as 1, 1, and 5 mL

†acid added as 1, 1, 5, 5, 5, 2.5, and 0.5 mL

Table 3: Separation scheme for Cu employed in this thesis. Performed using BioRad AG MP-1 loaded onto a 1.8 mL resin bed (modified from Marechal et al., 1999).
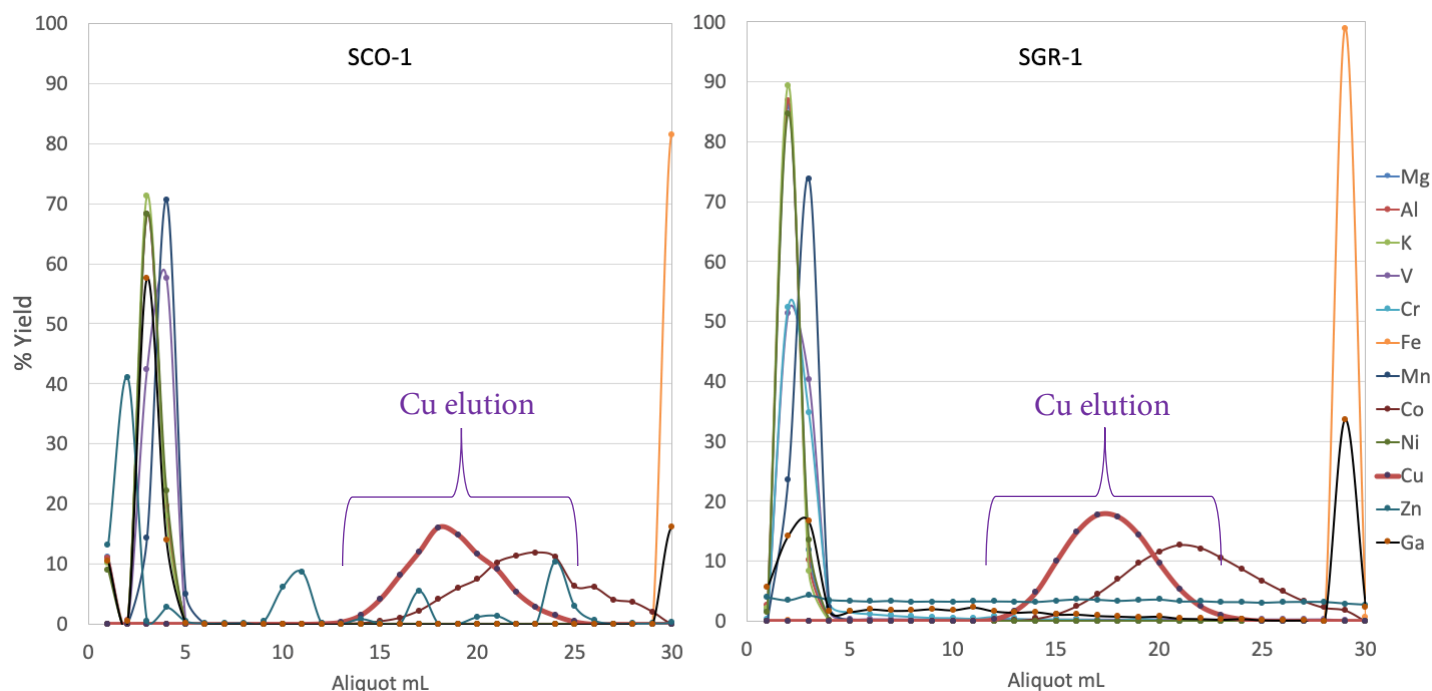
Figure 5: Elution curves for the standards (SCO-1 and SGR-1) used to calibrate the column method employed in this thesis. All element aliquots are plotted as percentage of total yield relative to the total sum of each element. The Cu elution curve is plotted as a thick red line with black cirlces. This column method does not separate Cu and Co, however a number of studies have shown that Co presence in solution does not impact the measured isotope ratio. These profiles were generated from a single column pass and include the final HNO_3 'wash' elution, which washes out Fe and Ga; each purification repeats the column step to further purify the sample.

Before samples were loaded, the columns were cleaned with alternating flushes of MilliQ and 0.5 M HNO_3. The resin was then conditioned with 6 mL of the column acid: 7 M HCl +0.001 % H_2O_2. As mentioned, H_2O_2 is added to ensure all metals in solution are oxidised and existing as ions, rather than as complexes. After conditioning, 1 mL of sample was loaded onto the resin in 2 0.5 mL aliquots. The matrix was then eluted in 7 M HCl + 0.001 % H_2O_2. Copper was eluted in 25 mL of 7 M HCl + 0.001 % H_2O_2. Samples containing the isolated Cu were dried down on a hot plate overnight, and the column chemistry was repeated once more to further purify Cu. Final Cu cuts were dissolved in 0.1 M HNO_3 for analysis. The total procedural blank (TPB) from these methods is around 16ng total Cu, or 1% compared to the average sample concentration of 1250ng Cu.

2.2.5 Mass spectrometry

Please refer to chapter 5 for information regarding Ni isotope analyses.

2.2.5.1. Principles of mass spectrometry

The method for the high-precision analysis of Cu isotopes by inductively coupled plasma-source multi-collector mass spectrometry (MC-ICP-MS) was first described by Maréchal et al. (1999). This was the first study to utilise MC-ICP-MS to detect small variations in Cu isotope ratios; previous attempts using Thermal Ionisation Mass Spectrometry (TIMS) were only able to detect large δ^{65}Cu variations (i.e. Walker et al., 1958; Shields et al., 1965).

Single collector ICP-MS uses one detector to measure a single mass at any given time (or more precisely, charged ions of a single mass/charge ratio), resulting in lower precision due to unavoidable plasma flicker and (e.g.) small variations in sample uptake velocity, which ultimately contribute to beam instability. Statistical methods can be applied to correct for this in order to achieve precision for elemental mass fractions of up to around 1%, however in many cases isotope ratio measurements cannot be made with the required precision on single collector instruments. To avoid this issue, multi-collector ICP-MS instruments use simultaneous collection of several masses in order to obtain high-precision isotope ratio measurements, due to the increased number of mounted detectors, wherein taking the ratio of simultaneously collected beam voltages cances out the inherent sample introduction and plasma instabilities. In the following section the basic principles of these instruments, including the sample introduction systems, are described. This section will begin with a discussion of features which are relevant to to both single and multi-collector ICP-MS, followed by detection, and then a description of the procedure used to produce the data presented in this thesis.

Broadly, mass spectrometry follows the process of vaporisation, ionisation, acceleration, deflection, and detection. All ICP-MS techniques comprise three essential parts of instrumentation: 1) an ion source, where ions are produced, accelerated, and focussed

into a beam; 2) the mass spectrometer, where ions which have the same approximate energy can be separated as a function of their mass-to-charge ratios and; 3) a detection system which converts the ion beam into a measurable electrical signal (eg. Van Haecke, 2012). See Figure 6 for a schematic view of a MC-ICP-MS.
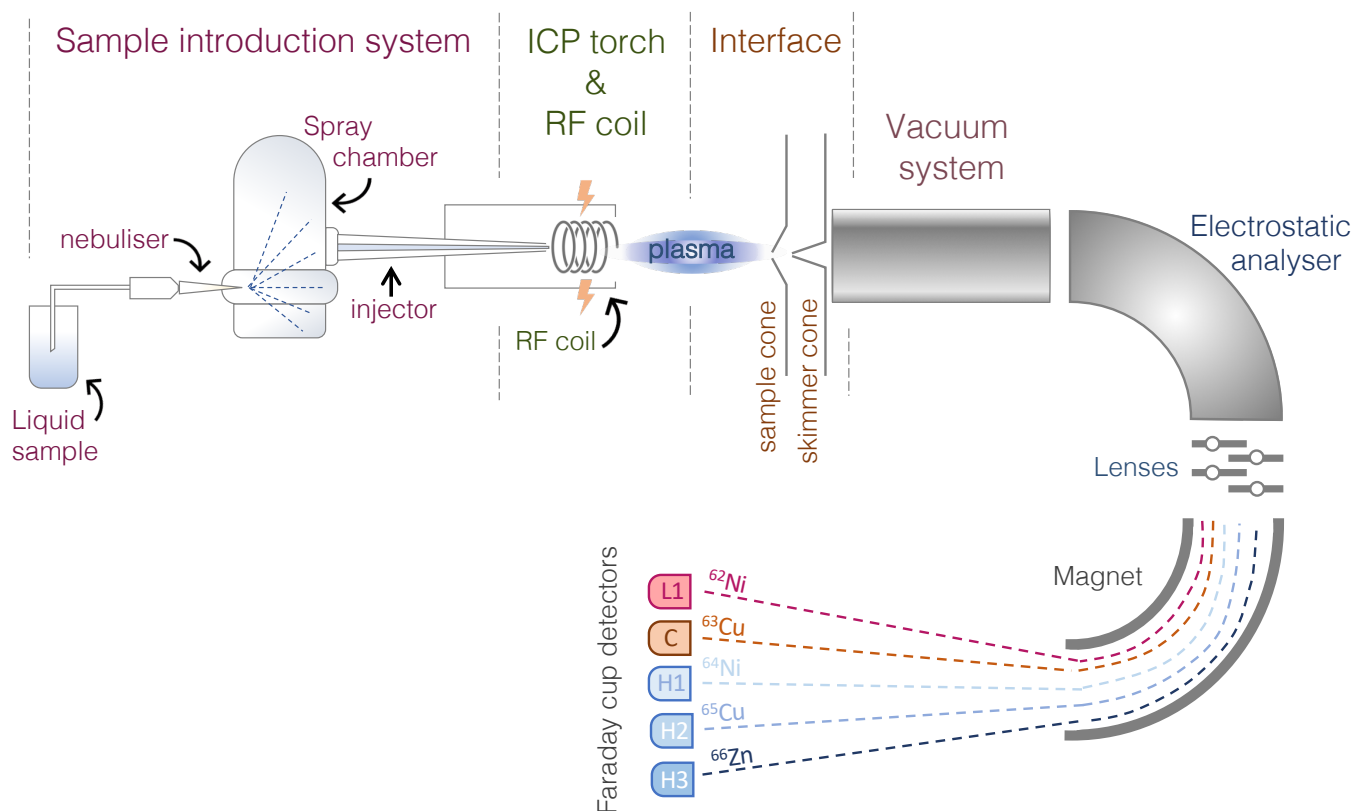
Figure 6: A schematic overview of an MC-ICP-MS, such as the Thermo Scientific (Bremen, Germany) Neptune+ High Resolution MC-ICP-MS used in this thesis. Here, a microflow nebuliser attachd to a thermo SIS spay chamber are used for sample introduction. The cup configurations used for Cu isotope analyses are also depicted.

i) Sample introduction.

In the case of solution ICP techniques, samples are typically introduced into the instrument as an aerosol. The aerosol is generated via a two-stage processes during which the nebuliser takes up the sample solution (sample + solvent, which is usually a weak acid) and aspirates it into a spray chamber. The spray chamber (which is sometimes heated), enabling the solvent to evaporate and leave a fine and pure aerosol of the analyte. The function of the spray chamber is chiefly to ensure that the flux of aerosol to the plasma is steady and constant, and to ensure that larger aerosol droplets do not enter the plasma.

This step is imperative; large variances in particle size can affect plasma behaviour and beam stability. For wet plasma introduction (i.e. when the sample + solvent aerosol is introduced directly to the plasma without the use of a desolvation system), the nebuliser and especially the spray chamber design have a large influence on the size and nature of the aerosol.

Pneumatic nebulisers are the most widely used type of nebuliser, relying on a gas flow (usually argon) to generate aerosolised sample. There are three main types of pneumatic nebuliser: concentric, microflow, and crossflow. Concentric nebulisers, which provide high sensitivity and stability, involve introducing the sample solution through a capillary tube to a low-pressure region via rapid gas flow which runs parallel to the capillary tube. The combination of low pressure and high-speed gas flow force the solution to aerosolise. Due to the small diameter of the capillary, blockages are a common issue when analysing matrix-heavy samples, and thus concentric nebulisers are best used with 'clean' solutions in which one is certain that everything is dissolved. Crossflow nebulisers, on the other hand, are better equipped to handle sample with complex matrices. They possess capillaries with larger diameters, and the Ar gas is directed a right-angles to the tip of the capillary tube. The contact between the high-speed gas and the liquid stream causes the liquid to aerosolise. While the larger capillary reduces the risk of blockage, the ability of the crossflow nebuliser to produce consistently fine aerosol particles is reduced. Both concentric and crossflow nebulisers are typically made of glass or various polymers (the latter being useful for the analysis of corrosive materials), rely on rapid gas flow (uptake rate = ~1 mL/min), and require fairly large volumes of sample. Lastly, microflow nebulisers, which are based on the same principles as concentric nebulisers, produce fine and consistent aerosols while providing much greater efficiency; they require lower sample flow (uptake rate = ~0.1 mL/min) and operate at higher gas pressure, leading to lower volumes of sample being used during analysis. They are generally made from PTFE, which reduces contamination. However, due to their narrow capillaries, microflow nebulisers are prone to blockages and, due to their high efficiency, introduce the entire sample into the plasma (leading to potential matrix suppression problems). They are therefore most highly suited to the analyses of samples with very low levels of dissolved

solids (Thomas, 2004). For this thesis, an ESI PFA microflow nebuliser (75 μl min^{-1}) was used.

Spray chambers, into which the nebuliser injects, have two designs: the Double-Pass and the Cyclonic. Double-pass spray chambers are usually made of PTFE and operate by directing the nebulised aerosol into a central tube, selecting the smaller droplets. The larger droplets, due to their weight, drain from the tube which is kept at positive pressure in order to force back the smaller droplets into the sample injector. Cyclonic spray chambers are usually made of glass and rely on centrifugal force, where a vortex produced via tangential flow of the sample aerosol and Ar gas inside the chamber sorts droplets according to size; larger droplets are forced to the walls of the chamber and eventually exit via gravity drainage, while the smaller droplets are carried with the gas stream into the plasma. Cyclonic spray chambers, when compared to double-pass spray chambers, have a higher sampling efficiency and thus enable higher sensitivity and lower detection limits. They are therefore most commonly utilised by MC-ICP-MS instruments. However, due to the droplet size distribution the double-pass spray chamber may, on occasion, be preferable (Thomas, 2004). For the Cu isotope analyses performed in this thesis, a cyclonic Thermo SIS glass spray chamber was used.

There are some instances where it is preferable to dry the sample solution prior to ionisation and, in doing so, separate the sample matrix from the analyte itself. This results in less complex material reaching the plasma which increases ionisation efficiency, resulting in greater sensitivity, reduced molecular interferences, and a lower required detection limit. This is especially useful for samples which have high trace element to matrix ratios or for samples in which the element of interest is only available in very low quantities, such as rare earth elements (REEs). In order to dry the sample solution for this purpose, a desolvating system is usually required. Desolvating systems negate the requirement for a separate spray chamber as they contain their own, and work by passing the sample aerosol through a (either heated or room-temperature) membrane which separates the solvent from the analyte. While desolvation devices are useful in providing greater sensitivity, there is the potential that the desolvation system might introduce unpredictable mass bias, volatile analyte loss within the desolvation unit and/or decreased plasma stability (e.g. Dauphas et al., 2009).

ii)   Ion source

The inductively coupled plasma (ICP) torch generates an argon plasma, which is defined as a gas mixture at high temperature which contains ions, electrons, and neutral particles. It is these particles which enable energy transfer into the plasma. The plasma is generated by passing a radio frequency current field (~27.12 or ~40.68 MHz) through a coil, generating a magnetic field. This magnetic field then causes electrons within the plasma to accelerate and move in a spiral fashion, acquiring high kinetic energy as they do so. The energy which these atoms attain mean that, when they collide with Ar atoms from the source gas, electron impact ionisation occurs and the plasma is thus sustained while Ar is supplied to the system. This process is initially stimulated by a high-voltage spark, which introduces 'seed electrons' into the spiral, as Ar does not possess any free electrons in its outer shell. The energy required to generate and maintain the plasma leads to maximum plasma electron temperatures of 5000-6000 K (Van Haecke, 2012). Argon is used due to the fact that it is inert and therefore has a very high ionisation potential, meaning that it takes more energy to ionise argon that most other elements, thus ensuring that most elements contained within typical dissolved samples are completely ionised when they enter the plasma. When the analyte enters the plasma, the aerosol is vaporised, atomised, and then ionised, ideally taking on a single charge.

iii)   Ion mean acceleration and focussing

The ions created in the plasma are directed into the mass spectrometer via a vacuum-maintained interface. The interface provides a link between the ICP ion source (which exists at close to atmospheric pressure) and the mass spectrometer (within which the efficient transmission and detection of ions requires a high vacuum) and consists of two cones: a sample cone, which samples the centre of the plasma, and a skimmer cone, which provides another barrier to leakage of the atmospheric pressure gas on the plasma side. This results in a two-set reduction in the pressure between the plasma and the beam acceleration/focussing lenses. The vacuum system also provides the instrument with the correct operating pressure, which prevents ions generated by the plasma from interacting with molecules, as this could cause them to lose their charge or become deflected before

they reach the detector (e.g. gas molecules). Beyond the interface, a series of electrostatic lenses (ion optics) direct and focus the ion beam towards the mass analyser, which separates ions by mass.

iv)   The mass analyser

In an ICP-MS, there are generally three types of mass analyser (mass spectrometer): a quadrupole filter, a magnetic sector, and a time-of-flight analyser. Broadly, all three of these analysers function by separating ions based on their mass-to-charge (m/z) ratio and filtering out interferences. Quadrople and magnetic sector mass spectrometers are described below.

a) *Quadrupole mass spectrometry*

A quadrupole comprises four parallel conductive rods which are arranged as two diametrically opposed 'pairs', with one pair recieveing a DC current, and one pair receiving an AC current. These respective currents create an oscillating electrical field when a voltage is applied, in which only ions of a certain (i.e. a specified) m/z ratio have a stable trajectory and are able to pass through to the detector. Ions with an m/z ratio outside of the specified window are removed from the ion beam (Van Haecke, 2012). Quadrupole filters are only used by single collector intruments, largely due to two reasos: (1) their principle of operation makes multi-collection impossible; the entire ion beam enters the quadrupole, however the electric field is such that only one m/z ratio is stable and can pass through the aperture to the detector at any given time (for example, if set to filter for ^{63}Cu only, the path of ^{65}Cu would not be stable and therefore not possible to detect), and (2) broadly, magnets have a better mass resolving power (resolution). While high-resolution quadrupoles have been designed, typical resolution for a quadruople is ~300 (where resolution is defined in equation (1)) comparised to ~ 1000 for a magnetic instrument in low resolution.

(1)

$$R = \frac{M}{\Delta M}$$

Equation (1): The equation for resolution, where ΔM = resolving power and M = mass of the (second) peak. Thus, resolution is mass-dependent. For example, if separating ^{238}U

from ^{239}Am (thus 238/(239-238) = a resolution of 238 is required, and if separating ^{56}Fe (mass 55.935) from $^{40}Ar^{16}O$ (mass 55.957), a mass resolution greater than 2545 would be required in order to separate Fe from the interference. In this latter instance, a quadrupole would not be capable of resolving this.

As such, quadrupoles are often used for concentration measurements where, typically, reproducibility of ~% is required. Isotope measurements have been made on quadrupole instruments, but this is only successful when isotope ratios vary by a large amount such as when the sample has been spiked (e.g. $^{135/138}$Ba spiked with ^{135}Ba, Evans et al., 2016).

(b) Magnetic sector mass spectrometry

For MC-ICP-MS, a double-focusing sector field mass spectrometer is used in order to achieve mass-independent resolution, enabling homogenous analytical selectivity across an entire mass range. When the ion beam enters the magnetic field, it is deflected; lighter masses are highly deflected, while heavier mass are less deflected. Thus, ions are separated by their m/z ratio. This occurs as the ions introduced into the magnetic field are focued to move along a circular path with a radius definied by the respective m/z ratio. Equation (2) defines the Lorentz force equation, where a charged particule (q) moving through a magnetic field with force (B) with velocity (v) will feel a Lorentz force with a magnitude of:

(2)

$$F = qvB \sin \theta$$

Where θ is the angle between velocity of the particle and the magnetic field. Centripedal force is defined as:

(3)

$$F = \frac{mv^2}{r}$$

When these two equations are set as equal to each other, the centripedal force required to move along a circular path can be expressed:

(4)

$$F = \frac{mv^2}{r} = qvB$$

When this is rearranged for r:

$$r = \frac{mv}{qB}$$

The radius that an ion follows through a magnetic field is thus equal to it's m/z ratio (m/q) multiplied by V/B (velocity over magnetic field strength). Given a constant velocity and a constant magnetic field, the radius of a singly charged particle's path is defined by it's mass. In order for this to effectively separate masses, all ions of the same mass must have the same velocity, as variation in velocities would result in different radii. In addition to this, the kinetic energy of the ions msut be the same. As such, before the ions can enter the magnetic field, they must all possess identical kinetic energies to ensure consistent velocity. This requires an electrostatic analyser (ESA) energy filter, which works on a similar principle to the magnetic sector; a charged ion beam is passed between two curved metal plates with a voltage applied to each (one positively charged and one negatively charged). Ions of a given energy will pass through via a cicular path, and those with too little or too much energy will be deflected towards the plates. The centripedal force required for the ions to move along a circular path is given by the force exerted by the electrical field on the ion (equation 6; Van Haecke, 2012):

$$F = \frac{mv^2}{r} = qE$$

Where E is equal to the electrical field strength. As such, the ion's kinetic energy controls the radius of the circular path:

$$r = \frac{mv^2}{qE} = \frac{2E_{kin}}{qE}$$

With single charged ions, equation (7) demonstrates that ions are dispersed as a function of their kinetic energy (Van Haecke, 2012).

v)   Detection

Once the ion beam has been deflected (either via quadrupole mass separation or via double-focused ESA and magnetic sector separation) the beams are measured by detectors. Detectors convert ions into electrical pulses, which can then be counted (Thomas, 2004). Single-collector ICP-MS instruments (such as quadrupoles) possess once detector, however MC-ICP-MS instruments (like the one used to produce the Cu isotope data anlaysed in this thesis) possess multiple detectors. This enables the measurement of several beams simultaneous, allowing for accurate isotopic calculations. In general, there are two typles of detector: Faraday cups and electron multipliers. Faraday cups are chiefly used in magnetic sector instruments, especially where the determination of high-precision isotope ratios is required, as they are robus and stable under variable temperatures and humidities (i.e. external variables). They are conductive cups capable of 'catching' ions in a vacuum. When the ion contacts the cup, the charge from the ion is transferred to the Faraday Cup, and the resulting current is converted to a voltage by a current-to-voltage converter (electrometer amplifier). In order for this to work, the resistance (R) of the current amplifier needs to be high (R = 10^{-10} to 10^{-16} Ohms) (Pfeiffer, 2020).

Electron multipliers function in a similar way to Faraday Cups, however they are significantly more sensitive. They operate based on the principes of dynodes (an electon in a vacuum which emits electrons when it collides with an ion) and secondary emission (the process by which electrons are emitted). Electron multipliers are effectively a series of connected dynodes that enable the process of secondary emission to occur repeatedly. E.g. a positively charged ion contacts the first dynode (which has a high negative voltage), resulting in the emission of several electrons which strike the next dynode. This repeats, resulting in the exponential amplification of electrons which create a signal large enough to be measured as an ion count (Wilschefski and Baxter, 2019).

2.2.4.2. Copper isotope analysis

For this thesis, Cu isotopes were analysed on a Thermo Neptune Plus MC-ICP-MS at the University of St Andrews. The instrument can be run in either low-, medium-, or high-resolution mode depending on the specific interreferences, if any, of the analytes of

interest (see section iv and equation (1) for resolution). As there are no isobaric interferences on either mass ^{63}Cu or ^{65}Cu, the instrument was operated in low resolution mode (ion currents ranging from 15-36 pA) with a wet plasma. Low resolution mode enables a higher level of sensitivity, which leads to better overall precision. It should be noted that some elements have the potential to create molecular spectral interferences for Cu analysis by forming argides and oxides. Titanium (^{47}Ti^{16}O) and Na (^{23}Na^{40}Ar) can interfere on ^{63}Cu and Mg (^{25}Mg^{40}Ar) and Ti (^{47}Ti^{18}O) on ^{65}Cu (Liu et al., 2014a). To avoid this, an aliquot of each sample was analysed for Cu relative to the concentrations of Mg, Na, and Ti. Ion chromatography was repeated if these elements were present in significant quantities in the aliquot (ratios of Mg, Ca, Fe, Na, Mn to Cu > 0.001; Ti/Cu > 0.3) (Liu et al., 2014a). For samples with high Cu concentrations (e.g. > 20 ppm Cu), the instrument was operated with an ion beam voltage of 3.6 V, analysing 63Cu concentrations of ~ 75 ppb. For samples with low Cu concentrations (< 20 ppm Cu), the instrument ran in low resolution mode with an ion beam voltage of 1.5 V analysing ^{63}Cu concentrations of 25 ppb. Ion beams were collected in Faraday cups connected to amplifiers using 10^{11} ohm resistors. The collector array was configured to collect the two Cu isotopes (L1: ^{62}Ni, H1: ^{64}Ni; H2: ^{65}Cu; H3: ^{66}Zn and C collecting ^{63}Cu. The instrument was tuned to maximise sensitivity and to optimise peak shape. Symmetrical, flat-topped peaks indicated maximum beam stability as instrumental drift (i.e. due to temperature changes) will not affect isotope ratio measurements.

Each measurement of samples and standards consisted of 22 cycles of 8.389 second integrations. Samples were bracketed by standard measurements of the Cu standard ERM AE633 and repeated 3 times. Lower concentration runs did not result in poorer precision; 2SE of high Cu (> 20 ppm) averages at 0.05‰ while 2SE for low Cu (< 20 ppm) averages at 0.06‰. Copper isotope ratios were calculated using sample-standard bracketing by comparison to ERM AE633 (calibrated as 0‰ to NIST SRM 976; Moeller et al., 2012) and are reported relative to this standard in delta (‰) notation:

$$\delta^{65}\text{Cu} = \left[\frac{\left({^{65}Cu}/{_{63}Cu} \right)_{sample}}{\left({^{65}Cu}/{_{63}Cu} \right)_{NIST976}} - 1 \right] x\ 1000$$

Analytical accuracy and precision

In order to examine and assess analytical accuracy and internal precision, 1 in every 12 samples was repeated as a total procedural repeat, i.e., from digestion through to isotope measurement. Further to this, isotope measurements were also made alongside reference material (BHVO-2a; 0.08‰ ± 0.05‰ (2SD; n=9), this thesis. Our measurements of various USGS reference standards (BIR-1, BHVO-2, SCO-1, SDC-1, GSP-2 and SDO-1) are statistically indistinguishable from published values (table 4).

Standard	Average (‰)	2SD (‰)	Recommended (‰)
BIR-1	0.09 (n = 3)	0.06	0.02 ± 0.06[1]
BHVO-2	0.07 (n = 9)	0.1	0.12 ± 0.02[1]
GSP-2	0.37 (n = 9)	0.09	0.29 ± 0.05[2-7]
SCO-1	-0.13 (n = 15)	0.05	-0.16[8]
SDC-1	0.09 (n = 3)	0.10	N/A
SDO-1	-0.19 (n = 3)	0.03	N/A

Table 4: Reference materials analysed alongside samples in this thesis; [1] Moynier et al., 2017; [2-7] Wang et al., 2019; Huang et al., 2017; Hou et al., 2016; Liu et al., 2014b; Bigalke et al., 2010a; Bigalke et al., 2010b; [8] Sossi et al., 2015. Repeats are based on individual measurements.

Figure 7 plots BHVO-2, GSP-2, and SCO-1 (i.e., all standards analysed on multiple Cu isotope analytical runs) linearly, where '*n*' refers to the analytical session.
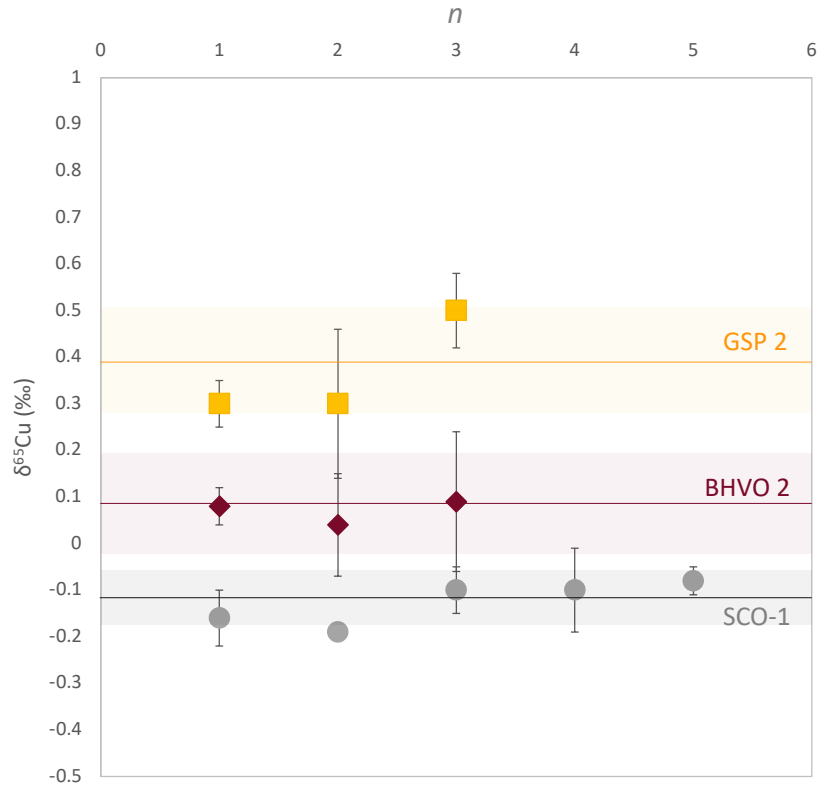
Figure 7: Standard data (for standards analysed for more than one analytical session). Each datapoint represents 3 repeat measurements. Dark lines represent the overall average and shaded bars represent average error (2SD) as reported in table 4.

Based on replicate analyses of natural samples and synthetic solutions, the long-term reproducibility for $\delta^{65}Cu$ measurements were conservatively estimated at 0.000‰ ± 0.11‰ (2SD; n=98). This is based on a grand dataset created by normalising every measurement and subtracting the mean from each sample measurement to redistribute them around zero (Figure 8) (after Steele et al., 2011; Kenney and Keeping 1951).
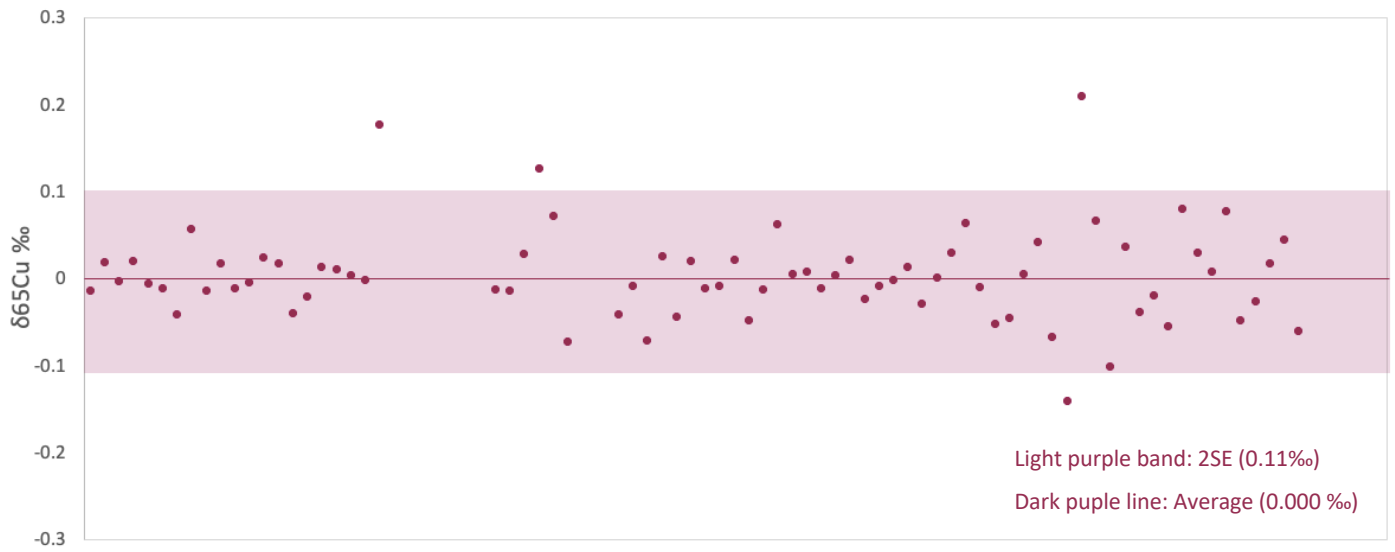
Figure 8: Long-term reproducibility for δ^{65}Cu analysis at St Andrews, based on all data analysed for this thesis (i.e. samples and standards).

Chapter 3

Copper isotope evidence for aerobic methanotrophy in the late Archaean.

This is an expanded version of:

N.A.V. Zavina-James, A.L. Zerkle, M.R. Warke, R.C.J. Steele, P.S. Savage (in review). A copper isotope investigation of methane cycling in the Late Archaean, Precambrian Research.
Data analysed and manuscript written by N.A.V. Zavina-James

3.1. Introduction

The Great Oxidation Event (GOE, c. 2.3 Ga) provides the first compelling evidence that biology can play a significant role in altering the atmospheric composition and Earth's surface environment. The rise of oxygenic photosynthesising cyanobacteria, which triggered the pervasive oxygenation of Earth's oceans and atmosphere, is considered to be one of the most important evolutionary steps in Earth's history, eventually enabling the development of complex multicellular life (e.g., Canfield, 2005; Farquhar et al., 2010). More recently, the simple narrative of an irreversible rise in atmospheric oxygen has been contested, with arguments for earlier accumulation(s) of oxygen (e.g., Anbar et al., 2007; Garvin et al., 2009), as well as proposals suggesting that Earth's pre-GOE atmosphere experienced periodic haze events (PHEs), during which it was dominated by a methane-rich haze (Zerkle et al., 2012).

The presence of S-MIF (Δ^{33}S and Δ^{36}S; Farquhar and Wing, 2003) is a characteristic signature in pre-GOE sedimentary rocks and provides the strongest evidence for a reducing atmosphere with extremely low oxygen levels throughout the Archaean, since low oxygen levels are required for the production and preservation of S-MIF signals (<10⁻

[5] present atmospheric levels; Pavlov and Kasting, 2002). Variability in Δ^{33}S- Δ^{36}S dynamics have been forwarded as novel proxies that are capable of resolving subtle changes in the chemical composition of the atmosphere (e.g., Claire et al., 2014; Endo et al., 2016). Of relevance here, the broad correlations between low Δ^{36}S/Δ^{33}S values and extremely negative organic carbon isotope values (δ^{13}C$_{org}$), termed C-S anomalies, have formed the primary evidence for the development of PHEs during the Neoarchaean (Zerkle et al., 2012; Izon et al., 2015; 2017).

Low δ^{13}C$_{org}$ excursions are generally thought to represent extensive assimilation of ^{13}C depleted substrates (i.e., methane) into sedimentary organic matter by methane-oxidising bacteria (methanotrophs), potentially in response to an increase in environmental methane production and availability (O'Leary, 1988; Zerkle et al., 2005). The correlations between S-MIF and δ^{13}C$_{org}$ trends thus suggest altered atmospheric chemistry associated with enhanced methane in the environment. Beyond speculation, the ultimate trigger for Neoarchaean PHE formation and the extent to which these events were driven or influenced by biological processes remains unknown. It has been posited that a methane haze could be generated abiotically via tectonic perturbations (i.e. volcanism or serpentinisation) (Daines and Lenton, 2016). Alternatively, recent work suggests that PHEs occurred as a result of increased methanogenesis that was triggered by enhanced primary productivity and organic carbon export to the sediments (e.g., Izon et al., 2017). Following this scenario, the source of the associated negative δ^{13}C$_{org}$ excursions would have been enhanced methane cycling and incorporation into sediments, either via anaerobic oxidation of methane (AOM) or aerobic methanotrophy.

Low temperature Cu isotope geochemistry is a relatively novel system (see Moynier et al., 2017 for a recent review). Our current understanding of δ^{65}Cu variation indicates limited variability in the δ^{65}Cu of igneous rocks, as well as sediments that have undergone physical, but minimal low temperature chemical processes (i.e., clastic river sediments, lake sediments, ocean sediment, aerosols, and mineral dust), and that these δ^{65}Cu signatures (see section 2 for the definition of δ^{65}Cu) are broadly similar. Of specific interest to this study are natural samples that have experienced a higher degree of

physical, chemical, and biological processing in the environment and which record a larger isotopic fractionation range (Fig. 1a; Moynier et al., 2017).

Copper is a bio-essential trace metal used by all forms of life for a multitude of functions (Madigan et al., 2015) and biological uptake via plants, microbes, and enzymes has been shown to impart a Cu isotope fractionation (Moynier et al., 2017). In particular, Cu is a key element used to regulate the enzymatic activity of certain aerobic methanotrophs. Methanotrophs use methane monooxygenase (MMO) to catalyse the oxidation of methane to methanol. Methane monooxygenase exists in two forms, iron (Fe)-dependent cytoplasmic or soluble methane monooxygenase (sMMO) and Cu-dependent membrane bound or particulate methane monooxygenase (pMMO; e.g., Hakemian et al., 2008; Semrau et al., 2010; 2018). Given that Cu is used by certain aerobic methanotrophs in order to regulate enzyme activity (e.g., Madigan et al., 2015; Semrau et al., 2010), and that biological uptake of Cu by other Cu-using metabolisms imparts a resolvable isotope effect (Naverrete et al., 2011), Cu isotopes could provide a window into ancient methane cycling.

Testing this hypothesis, this chapter explores the potential of Cu isotopes as a proxy for aerobic methanotrophy in the Late Archaean via the generation of a high-resolution $\delta^{65}Cu$ record through the youngest of three identified PHEs from the ~2.6-2.5 Ga Campbellrand-Malmani carbonate platform (Izon et al., 2017). These data, when examined alongside previously published C and S isotope data, establish an important role for aerobic methane oxidation in the incorporation of methane into Late Archaean sediments.
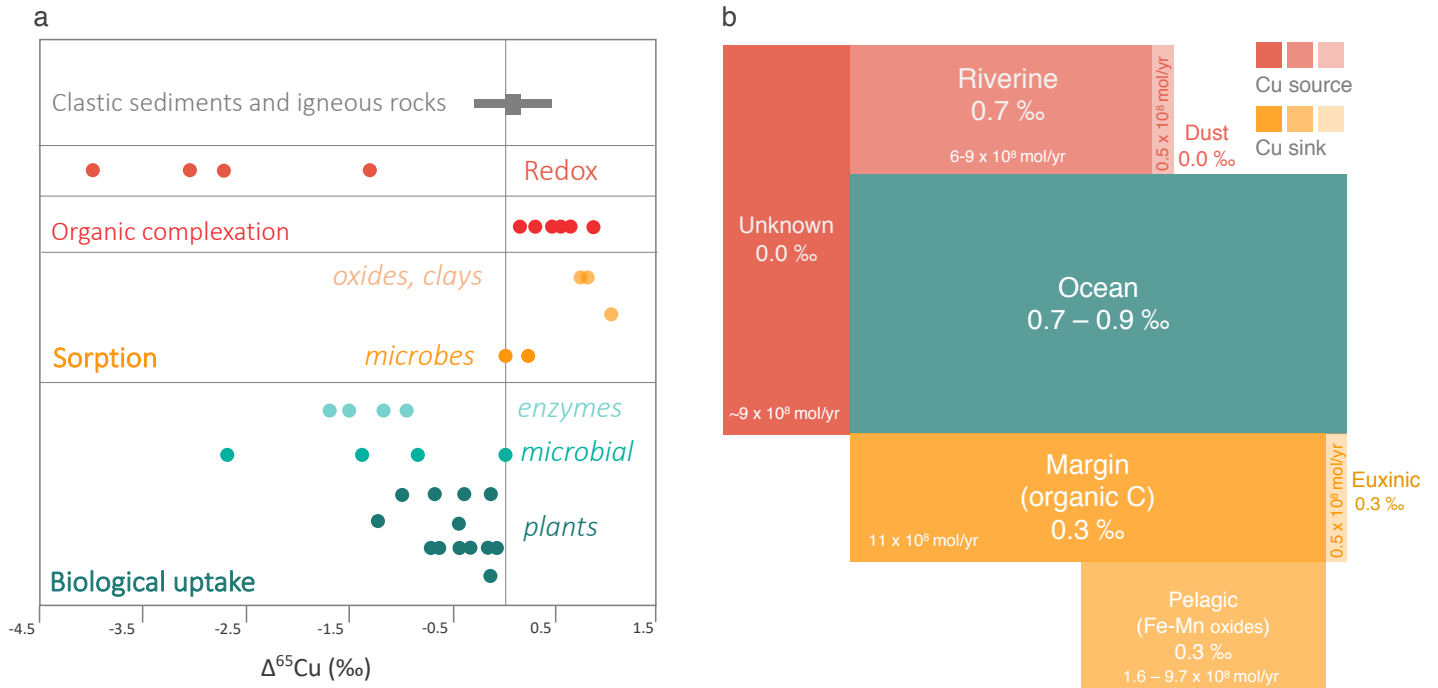
Figure 1 (reproduced from Chapter 1): (a) Copper isotope fractionation induced by low-temperature biogeochemical processes (Moynier et al., 2017), defining Δ as $\Delta_{A\text{-}B} = \delta_A - \delta_B$; redox refers to abiotic redox reactions between aqueous Cu(II) and solid Cu(I) precipitates $\Delta_{\text{reduced-oxidised}}$ (Zhu et al., 2002, Ehrlich et al., 2004; Mathur et al, 2005); biological uptake: $\Delta_{\text{organism-external}}$; microbial sorption: $\Delta_{\text{sorbed-solution}}$; abiotic sorption (oxides, clays): $\Delta_{\text{sorbed-free ion}}$; organic complexation: $\Delta_{\text{complexed-free ion}}$. Data points represent the isotopic composition of the sample relative to 0. (b) Copper isotope oceanic mass-balance (after Little et al., 2017). Boxes are scaled and shaded by magnitude, where their length and colour reflect the flux magnitude (mol/yr). Isotope compositions are expressed as δ values.

54

3.2. Results

Copper isotope and abundance data from core GKF01 are provided in table 1 and presented in Figure 2. In this Figure, the δ^{65}Cu data are plotted against stratigraphic height; also shown are Cu concentrations vs. stratigraphic height. There is no significant correlation between Cu concentrations and δ^{65}Cu ($R^2 = 0.17$), Cu concentrations and S ($R^2 = 0.11$), or δ^{65}Cu and S ($R^2 = 0.002$) (Figure 3). Rare earth element and yttrium values (REY$_{SN}$) were normalized to Post-Archean Australian Shale (PAAS; Taylor and McLennan, 1985). REY$_{SN}$ anomalies (namely Eu$_{SN}$) were calculated using the equations of Lawrence et al. (2006) which are commonly used to assess the preservation and redox history of Archean and Proterozoic carbonates (Tostevin et al., 2016; Bellefroid et al., 2018; Warke et al., 2018; 2019).

A negative δ^{65}Cu excursion exists between 838.6 m – 850.8 m. Here, values deviate from an average pre-excursion background ratio of 0.05 ‰ ± 0.08 ‰ (close to current estimates of BSE of 0.06‰; Moynier et al., 2017) to -0.66 ‰ over approximately 12 m of stratigraphy. Up-section from this interval, the δ^{65}Cu values return to similar background values of 0.05‰ ± 0.08‰ over 4m of stratigraphy and persist for the majority of the measured section (37m). When integrated with previously published S-MIF and δ^{13}C$_{org}$ data (Fig. 2; Izon et al., 2017), there is a clear offset, with the δ^{65}Cu excursion occurring below the S-MIF and δ^{13}C$_{org}$ excursions. This pattern is independent of lithological variations, as the background remains consistent across multiple facies changes. In addition to this, the excursion itself transects a calcareous mudstone and a mudstone, which appears to have little impact on the data.

Depth (m)	Cu (ppm)	$\delta^{65}Cu$	2SD
800.18	1.92	0.15	0.05
802.13	1.38	-0.01	0.08
807.73	2.61	0.12	0.06
817.47	2.49	-0.08	0.07
822.75	2.34	-0.03	0.02
826.28	14.2	0.01	0.06
829.22	20.41	0.06	0.03
830.53	49.8	-0.02	0.04
831.45	30.99	0.08	0.03
832.28	41.8	0.07	0.11
833.08	37.63	-0.01	0.04
833.9	22.7	0.17	0.03
834.49	37.86	0.13	0.02
835.05	41.3	0.01	0.04
835.88	40.91	0.08	0.02
836.45	37.7	0.15	0.15
837.04	37.36	0.07	0.05
837.79	30.7	-0.03	0.04
838.58	6.15	-0.24	0.03
839	1.8	-0.37	0.08
841	4.9	-0.66	0.07
843.5	1.3	-0.33	0.07
846.5	4	-0.12	0.15
850.8	2.8	-0.12	0.03
853.3	7.19	0.19	0.04
863.4	67.03	0.09	0.06
877.6	0.78	0.09	0.06
881	30.54	0.01	0.04

Table 1: Cu isotope and concentration data from this study.
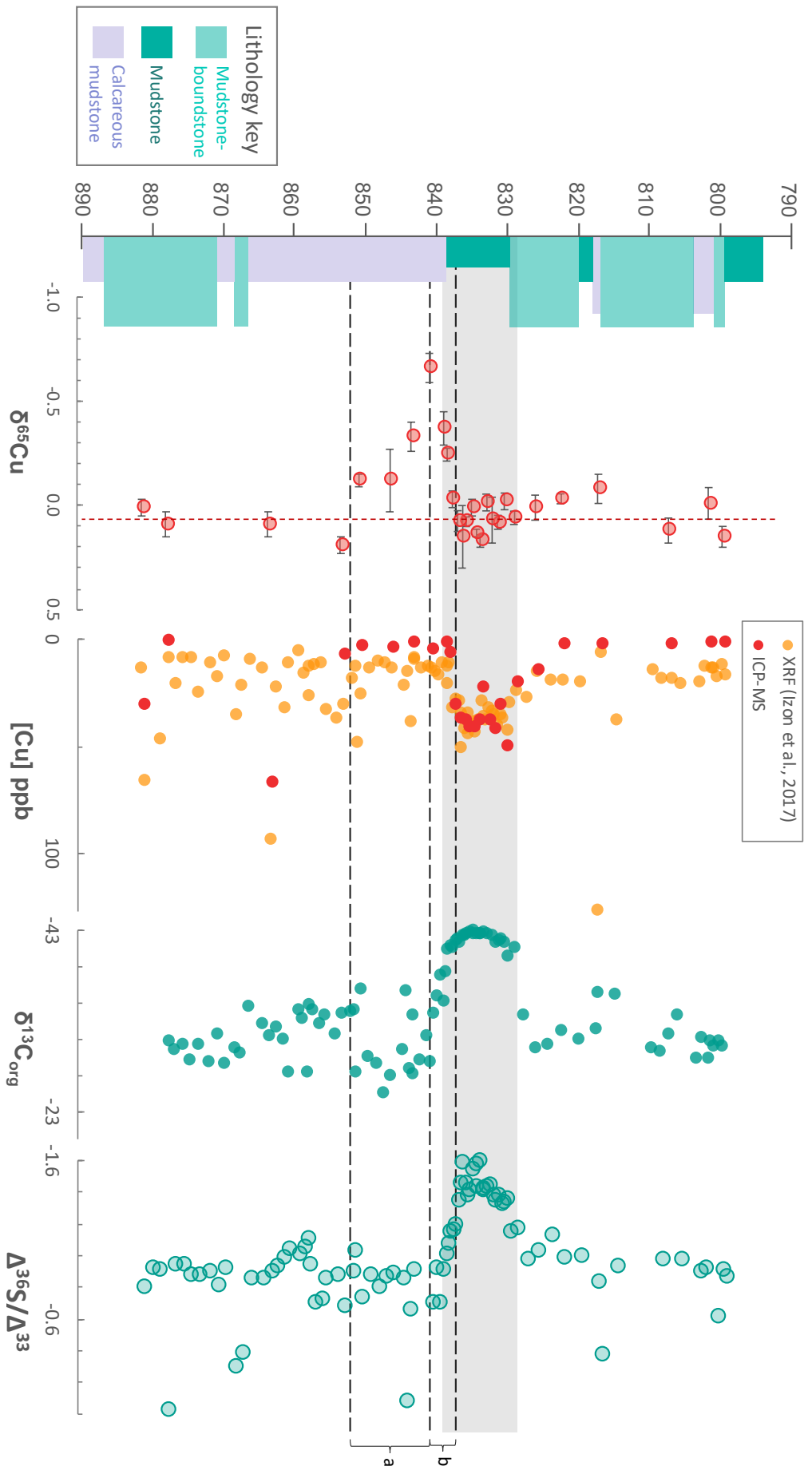
Figure 2: The stratigraphic distribution of the Cu isotope (δ^{65}Cu) and abundance ([Cu]) data from core GKF01. These data are accompanied by carbon and sulphur isotope data from Izon et al. (2017). The solid grey bar highlights the putative PHE interval (Zerkle et al., 2012; Izon et al., 2017). The red vertical dashed line represents the average Cu isotope background (0.06 ‰), while the horizontal dashed grey lines mark the onset (a), nadir (b) and termination (c) of the δ^{65}Cu excursion seen between 838.6- and 850.8-meters core depth. Copper isotope values show an inverse relationship with δ^{13}C$_{org}$ values, with high δ^{13}C$_{org}$ values observed during the onset of the Cu-isotope excursion and low values during the recovery. The stratigraphic column follows Izon et al. (2017) and is simplified from http://general.uj.ac.za/agouron/.

3.3. Discussion

3.3.1 Syn- and post-depositional processes that can affect Cu isotope systematics

3.3.1.1 Diagenesis and metamorphism

The potential for post-depositional alteration to affect $\delta^{65}Cu$ values must first be considered, particularly given the age of these rocks. The Campbellrand Subgroup has undergone sub-greenschist grade regional metamorphism (Button, 1973). The peak metamorphic temperatures recorded by Campbellrand carbonates are only ~250 °C (Eroglu et al., 2017). Nonetheless, lower temperature diagenetic processes can reset or alter carbonate trace metal and isotopic inventories. The carbonate geochemistry of the Campbellrand Subgroup, including core GKF01, has been well studied in relation to primary seawater vs secondary alteration signatures (Schröder et al., 2006; 2009; Fischer et al., 2009; Eroglu et al., 2015; 2017; 2018; Warke et al., 2019). Here, the diagenetic processes (dolomitisation styles, fluid interaction) that may have altered the upper Nauga Formation and factors that may affect Cu systematics are considered.

As outlined above, SEM-EDS analysis of these samples confirms that sulphides constitute the dominant Cu-bearing phase in GKF01. Copper is, however, also noted within the Upper Nauga Formation ferroan dolostones that host Cu-bearing sulphides and hence dolomite could represent an additional pool of Cu in these samples. Synchrotron X-Ray Fluorescence has shown that microbial fabric-retentive ferroan dolomite in GKF01 can contain up to 20 ppm Cu, although generally concentrations in the ferroan dolomite are lower than detection (~1 ppm; Warke et al., 2019). This form of dolomitisation, driven by seawater derived fluids (Warke et al., 2019), is common in the studied interval and is therefore unlikely to account for the higher Cu concentrations measured in this study.
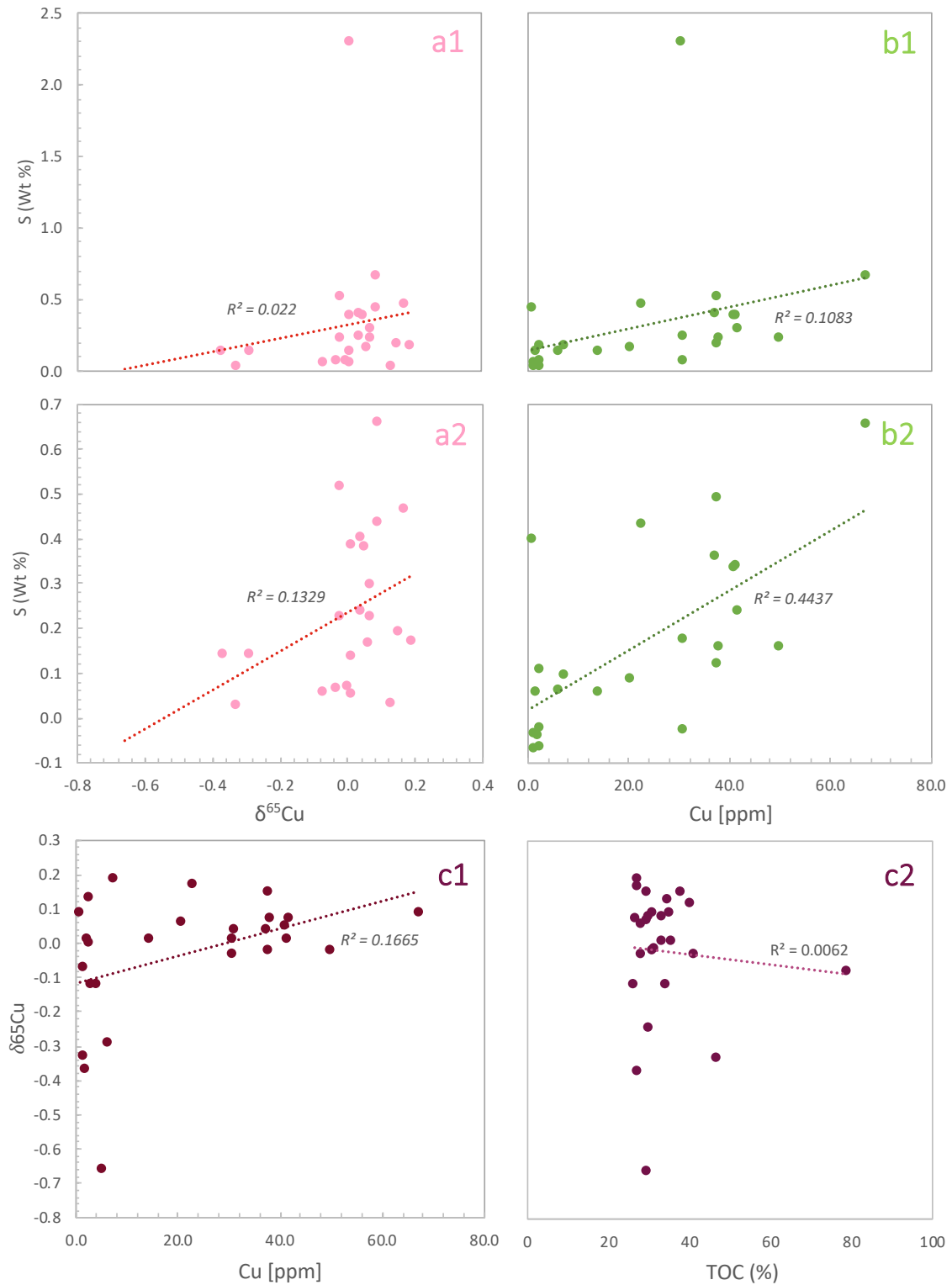
Figure 3: Sulphur (Wt%) plotted against Cu concentrations and δ^{65}Cu concentrations from this study. Figures a1 and a2 show δ^{65}Cu vs S; a1 including an outlier and a2 excluding the outlier. In either case, the value of R^2 remains low. Similarly, figures b1 and b2 show Cu concentrations vs S; b1 including an outlier and b2 excluding the outlier. The R^2 value is not significantly impacted by this outlier in this instance. Figure c1 shows δ^{65}Cu v Cu concentrations and figure c2 shows δ^{65}Cu vs TOC.

Fabric destructive dolomitsation, driven by interaction of precursor carbonate phases with a burial brine, is also known to affect the Campbellrand Subgroup (Sumner, 1996). Dolomite precipitating from such a fluid could enrich Cu host dolostones up to concentrations of 150 - 1500 ppm (Warke et al., 2019). As concentrations above 126 ppm are not observed in this study, and this portion of GKF01 retains discernible microbial fabrics (Schröder et al., 2006; 2009), it is possible to discount this mechanism as exerting a significant control on Cu concentrations in our samples. Further, burial brines and other fluids (discussed below) would significantly alter carbonate isotope ($\delta^{18}O_{carb}$ and $\delta^{13}C_{carb}$) systematics. Significant interaction with post-depositional fluids can be expected to progressively lower $\delta^{18}O_{carb}$ values from Archean seawater values of around -7 to -8 ‰ to values as low as -17 ‰ (Eroglu et al., 2017). In GKF01 both $\delta^{18}O_{carb}$ and $\delta^{13}C_{carb}$ values are consistent with Neoarchean seawater values and show no evidence of disturbance over the interval examined in this study, and over the $\delta^{65}Cu$ excursion interval (Figure 4, Fischer et al., 2009; Eroglu et al., 2017).

Post-depositional hydrothermal fluids with high fluid to rock ratios – capable of corroding Cu-sulphide minerals - can severely disturb carbonate systematics. In addition to causing pronounced and coupled lowering of $\delta^{18}O_{carb}$ and $\delta^{13}C_{carb}$ values, as discussed above, they can strongly alter carbonate-bound, shale-normalised, Rare Earth Element and Yttrium (REY_{SN}) trends. Hydrothermal alteration of this manner leads to characteristic REY_{SN} arrays that are depleted in the heavier lanthanides, lack Y/Ho anomalies, and carry a strong positive Eu anomaly (Tostevin et al., 2016; Warke et al., 2018).
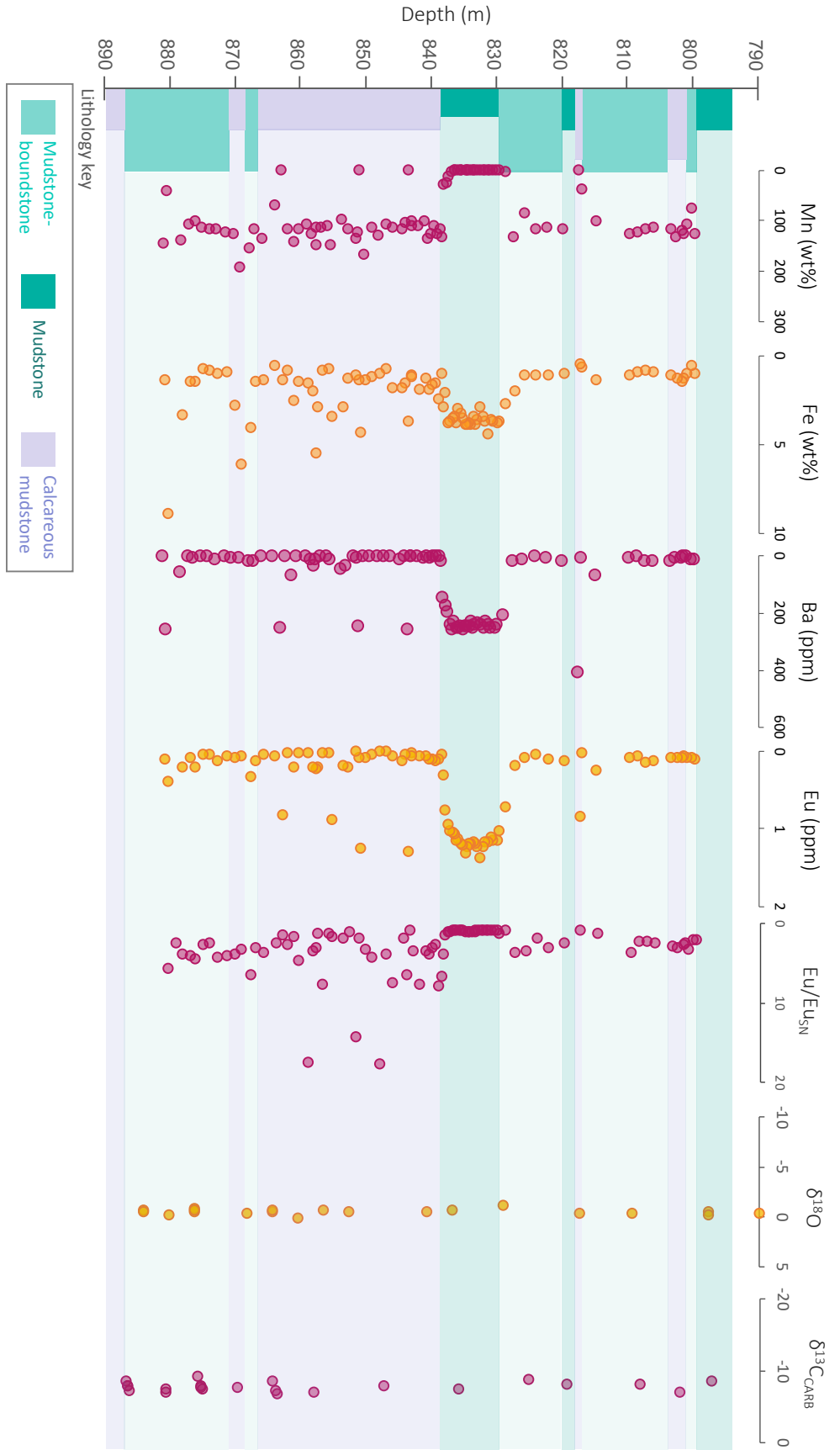
Figure 4: Selected trace element and isotope data plotted against stratigraphy for the section measured in this study. The stratigraphic log has been extrapolated across the plot to highlight the impact of any lithological changes on the respective elemental concentrations. Data for Mn and Fe were obtained from Zerkle et al. (2020); Oxygen- and carbonate carbon isotope data were obtained from Fischer et al. (2009). Europium concentrations represent the sum of ^{151}Eu and ^{153}Eu.

61

Dolomitic facies in the upper Nauga Formation, however, show no evidence of such disturbance and preserve robust seawater REY$_{SN}$ arrays (Eroglu et al., 2017; Warke et al., 2019) albeit with the small, positive, shale-normalised Eu anomaly (Eu$_{SN}$) that is characteristic of Neoarchean seawater which is discussed below. Therefore, there is no evidence - either from considering the sulphides themselves or from considering the susceptible host sediments - to suggest that Cu-sulphides have been significantly altered. Finally, the Transvaal Supergroup was affected by the Kheis orogenic event (c. 1.92 Ga) which promoted epigenetic Zn and Pb mineralisation and pyrrhotitisation of Fe-bearing minerals (De Kock et al., 2009). A previous S-isotope study found no acid volatile sulphur (AVS; Izon et al., 2017). In Precambrian rocks AVS commonly occurs in later diagenetic sulphide phases (e.g., Paiste et al., 2018); the absence of AVS precludes pervasive pyrrhotitisation, demonstrating that the Kheis orogeny had little impact on the sulphide inventory over the examined interval.

3.3.1.2 Possible primary (hydrothermal) controls

Hydrothermal vent materials display a relatively large range of $\delta^{65}Cu$ attributed to multiple mineralisation events or remobilisation of Cu (over 9 ‰; e.g. Larson et al., 2003; Mason et al., 2005). Thus, an unrecognised hydrothermal influence has the potential to obscure, or even overprint, primary sedimentary $\delta^{65}Cu$ values. There is no discernible evidence of enhanced hydrothermal flux in core GKF01, with no significant enrichments in common hydrothermal elements such as Ba, Mn, and Fe (e.g. German and Von Damm, 2003) (Figure 4). Importantly, there is no significant relationship between these hydrothermal proxies and their corresponding $\delta^{65}Cu$ compositions (R^2 values for $\delta^{65}Cu$ vs Mn: 0.16; $\delta^{65}Cu$ vs Fe: 0.05; $\delta^{65}Cu$ vs Ba: 0.18).

During the Neoarchean, primary seawater signals carry a hydrothermal signal inherited from the stronger influence of hydrothermal processes on seawater metal inventories (Beukes and Gutzmer, 2008). Hydrothermal input imparts positive shale-normalised Eu anomalies (Eu$_{SN}$) in Neoarchean platform carbonates and have been previously noted in the Campbellrand Subgroup (Eroglu et al., 2017; Warke et al., 2019) as well as in this study (Figure 4). Fluctuations in the Fe and Mn content of Campellrand carbonates is also

thought to follow the changing hydrothermal influence on seawater at the time of deposition, rather than significant modification during dolomitisation as limestone and dolostone Fe and Mn concentration ranges often overlap (Eroglu et al., 2015; 2017; 2018).

In Figure 5 (panels 1-4), there exists a weak positive relationship between Cu and Eu concentrations (R^2: 0.19; n=91) but no relationship exists between Cu concentration and Eu_{SN} anomalies (R^2: 0.02; n=91). This strongly suggests that the Cu hosted within the Lower Nauga units is not directly controlled by hydrothermal seawater input. Only a weak positive relationship exists between Eu concentration and $\delta^{65}Cu$ values (R^2: 0.15; n=28).
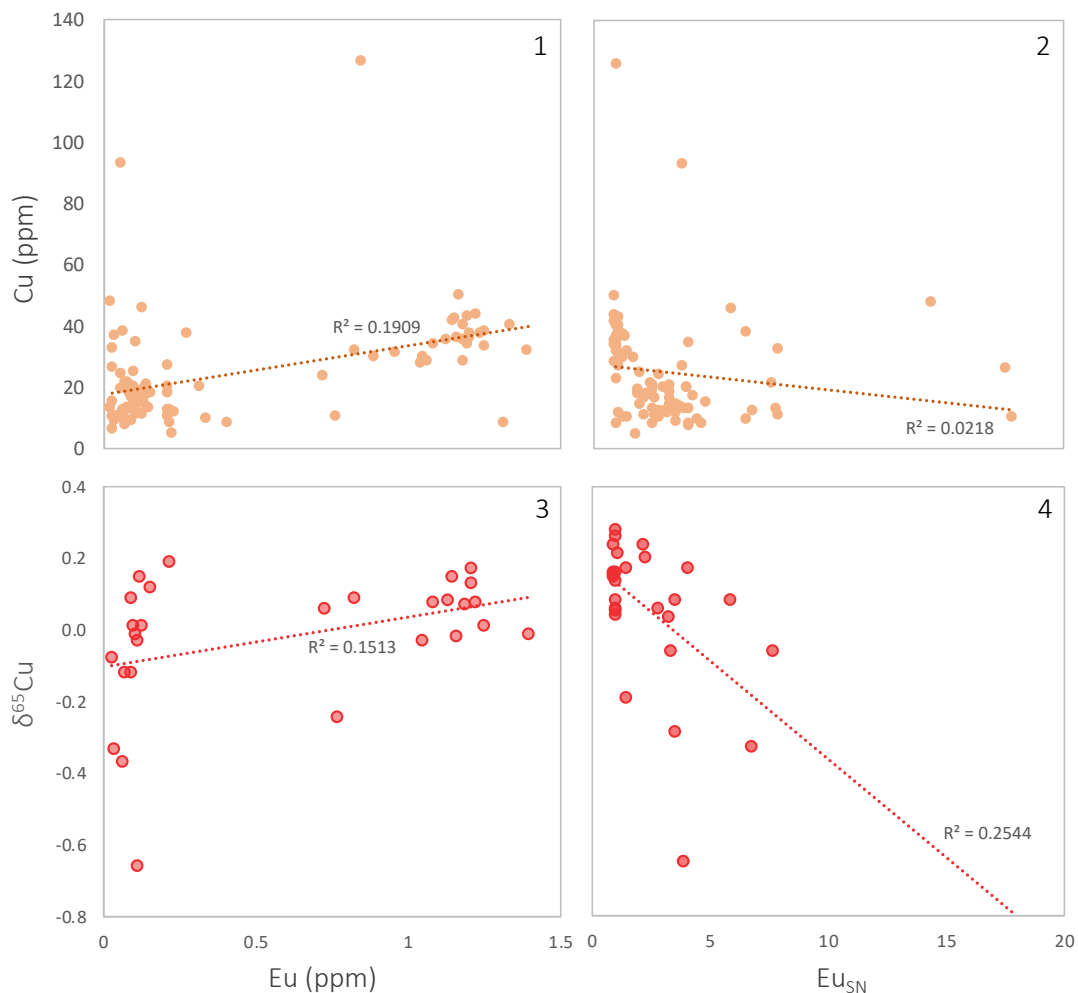
Figure 5: Scatter plots showing (1) a weak positive relationship between Cu and Eu concentrations; (2) no relationship between Eu_{SN} anomalies and Cu concentrations; (3) a weak positive relationship between Eu concentrations and Cu isotope composition; (4) a weak negative relationship between Eu_{SN} anomalies and Cu isotope composition.

The δ^{65}Cu signal of hydrothermal inputs are still unconstrained but hypothesised to be a source of isotopically light Cu relative to seawater (Fig. 1b; Little et al., 2017). Hence, if periods of higher hydrothermal input significantly lowered δ^{65}Cu values, a co-relationship with higher Eu$_{SN}$ anomalies may be evident. There is only a weak negative relationship between these two variables (R^2: 0.25; n=28; Figure 5, panels 1-4). This relationship weakens further when only negative δ^{65}Cu values are considered (R^2: 0.15; n=12). Therefore, while the possibility that increased hydrothermal influence may partly cause a negative δ^{65}Cu excursion cannot be totally precluded, given the size of the dataset and the weakness of the trends observed, it does not appear to be the dominant driver of the observed δ^{65}Cu trends. Therefore, the following discussion considers other, specifically biological, drivers below.

3.3.2. Primary Cu isotope fractionation mechanisms

Copper isotope ratios exhibit a range of 2.5 ‰ in "low temperature" environments; Fig. 1a summarises the measured constraints on known Cu isotope fractionations. The dominant low-temperature processes that account for negative δ^{65}Cu signals in mineral phases and biological products are redox reactions and biological uptake; in the modern oxidative ocean environment there is a significant range in Cu isotope fractionation associated with Cu-sulphides, for example (Mathur et al., 2009). As such, this discussion focuses on these possible mechanisms for producing the negative δ^{65}Cu excursion observed in this study. However, in order to first assess whether the excursion is driven by a change in lithology, a simple mass balance model was constructed using sample Cu/Al ratios to calculate the proportion of sedimentary and biological endmembers. The calculated authigenic Cu component and its isotopic composition is shown below (Figure 6), and demonstrates that the Cu isotope signal is unlikely to be driven by a change in the proportion of detrital and authigenic/bioauthigenic components.
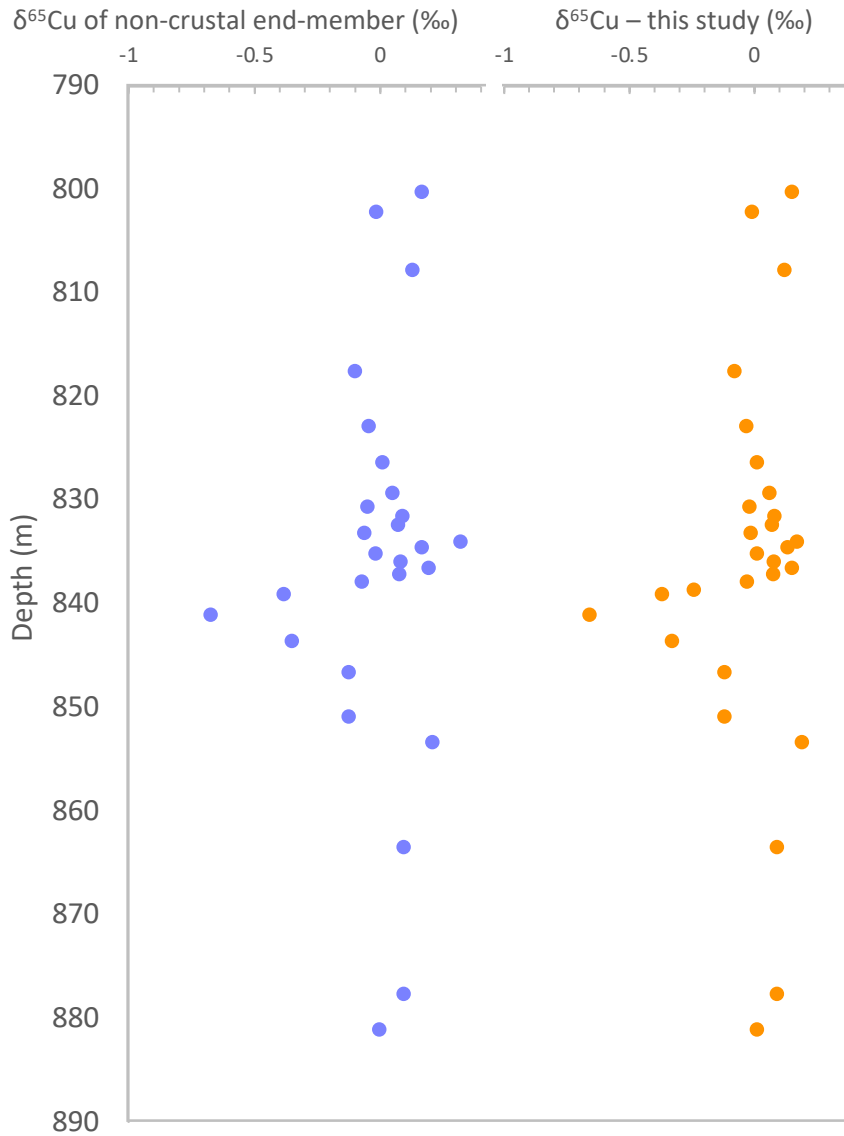
Figure 6: Modelled $\delta^{65}Cu$ (‰) of the non-crustal end-member based on known crustal average Cu/Al ratios for a late Archaean felsic crust (e.g., Tang et al., 2016; Chen et al., 2020) and the estimated $\delta^{65}Cu$ of BSE (e.g., Moynier et al., 2017), calculated by mass balance (blue circles). Copper isotope data from this study (orange circles) is plotted alongside for comparison.

3.3.2.1. Redox

Redox reactions are an important control on the chemical speciation of Cu, which exists as native Cu(0), "reduced" Cu(I) and "oxidised" Cu(II) in Earth materials (Moynier et al., 2017). Importantly, the reduction of aqueous Cu(II) has been demonstrated to produce measurable and relatively large isotopic fractionations. The reduction of Cu(II) to an iodide precipitate (Zhu et al., 2002) and Cu(I)S (covellite; Ehrlich et al., 2004) enriches

65

the reduced phase in ^{63}Cu, with respective fractionation factors of +1.004 ‰ and +3.06 ‰. Additionally, via abiotic oxidative leach experiments, Mathur et al (2005) demonstrated that Cu(I) in chalcocite (Cu_2S) and chalcopyrite ($CuFeS_2$) was 1.3 ‰ and 2.7 ‰ lighter than aqueous Cu(II). Copper sulphides in dolomites further indicate the association between Cu(I) and ^{63}Cu, again implying a negative fractionation during the reduction of aqueous Cu(II) (Asael et al., 2007).

Due to their apparent susceptibility to oxygen availability, Cu isotopes have been investigated as a potential palaeoredox proxy. Chi-Fru et al. (2016) observed a transition from predominantly shale-hosted negative $\delta^{65}Cu$ compositions in Late Archaean shales to more positive ratios in the wake of the GOE. Assuming that banded iron formations (BIFs) preferentially sequester ^{65}Cu, leaving residual seawater (and thus shales) depleted in ^{65}Cu, the authors interpreted the temporal increase in $\delta^{65}Cu$ values to record the waning deposition of BIFs through the Late Archaean-Proterozoic transition. The post-GOE loss of the BIF ^{65}Cu-sink, along with a heightened oxidative weathering flux, increased the ocean inventory of ^{65}Cu, promoting the observed post-GOE shale-hosted ^{65}Cu enrichments. For the Late Archaean, Chi-Fru et al. (2016) present four data points, with $\delta^{65}Cu$ values ranging from ~-0.6‰ to +0.2‰. While these values bracket the GKF01 dataset (Figure 2), $\delta^{65}Cu$ in GKF01 are not consistently depleted as would be predicted by their model, and there is limited evidence of contemporaneous BIF formation in the measured section of GKF01. Moreover, recent Cu isotope analyses of BIFs from the Transvaal Supergroup (Thibon et al., 2019) have determined an average $\delta^{65}Cu$ range of ~0 ‰, suggesting that BIF Cu isotope compositions are not related to oceanic reservoir effects. Instead, BIF $\delta^{65}Cu$ values from the Transvaal reflect variation in Cu provenance (volcanic ash deposits in this instance) and, this considered, the authors posit that Cu has limited use as a redox proxy during BIF formation. It therefore seems unlikely that, in this instance, changes in BIF deposition were responsible for the observed short-term variability seen in GKF01 $\delta^{65}Cu$, and alternative mechanisms should be sought.

3.3.2.2 Biological uptake: Aerobic methanotrophy

While there are currently no direct experimental studies of Cu isotope fractionation during aerobic methanotrophy, there is evidence for a microbially induced fractionation of Cu isotopes during Cu uptake by other types of organisms such as Pseudomonas aeruginosa and yeast (Zhu et al,. 2002), Escherichia coli (Zhu et al., 2002; Navarrete et al., 2011), Bacillus subtilis (Navarrete et al., 2011) and Thiobacillus ferooxidans (e.g. Mathur et al., 2005; Kimball et al., 2009). Both Zhu et al. (2002) and Navarrete et al. (2011) found that live bacterial and yeast cells preferentially incorporate ^{63}Cu, resulting in an isotopic fractionation relative to the starting media of -1.0‰ – -2.3‰. While speculative, these fractionations are hypothesised to involve the reduction of Cu(II) to Cu(I) within the cell membrane. In contrast, studies involving Thiobacillus ferooxidans, an acidophilic autotroph commonly found in acid mine drainage, show a preferential association of ^{65}Cu with T. ferooxidans. This is due to the formation of isotopically heavy Cu nanoparticles around the cell and is thought to develop as a cellular response to high environmental metal concentrations (Mathur et al., 2005; Kimball et al. 2009). Thus, to recapitulate: cellular uptake of Cu likely involves a redox state change and leads to preferential incorporation of light Cu, and sorption of Cu to cells leads to the preferential incorporation of heavy Cu.

This study speculates that, given the importance of Cu to pMMO, it is likely that biological Cu uptake by organisms utilising this enzymatic pathway would result in similar fractionation of Cu isotopes to that observed in the studies of Zhu et al. (2002) and Navarrete et al. (2011). It has been previously demonstrated that Ni, an element of enzymatic importance in methanogenesis, is similarly fractionated during uptake by methanogens (Cameron et al., 2009) and uptake of Mo during N_2 fixation by cyanobacteria has been shown to induce a large fractionation in Mo isotopes (Zerkle et al., 2010). While Cu is used by a wide variety of enzymes and proteins in the modern environment, many of these are involved in oxidase reactions that likely evolved after the GOE (Zerkle et al., 2005). As most of these enzymes and proteins relate to more widespread metabolic functions rather than specific metabolisms (i.e. aerobic methanotrophy), this study also hypothesises that any significant 'generic' uptake of Cu

could be evidenced by a strong correlation between $\delta^{65}Cu$ and TOC, which is not indicated by our data (R^2 of $\delta^{65}Cu$ vs TOC (%) = 0.006; Figure 3).

3.3.3. Cu isotopes in context

In order to consider the roles of redox and biological uptake on the $\delta^{65}Cu$ signal measured in core GKF01, the prevailing Late Archaean conditions must also be considered. Here, the Late Archaean reducing weathering model presented by Hao et al. (2017) is adopted as the background state; there is no evidence of high O_2 levels in this interval of core GKF01 and therefore the possibility of redox processes as drivers of the $\delta^{65}Cu$ excursion can be discounted. Specifically, Fe-speciation data from this section (Izon et al., 2017) suggest an anoxic, ferruginous water column during deposition of the $\delta^{65}Cu$ excursion, with evidence of local water-column oxygenation in the overlying interval. In addition to this, the persistence of S-MIF throughout the entire succession necessitates an oxygen-free atmosphere (Izon et al., 2017). Finally, the absence of a correlation between $\delta^{65}Cu$ and total S (Figure 3) argues that the extent of reduction and sulphidisation associated with MSR was not the dominant control on sedimentary $\delta^{65}Cu$ values. As such, the possibility of an isotopically fractionated Cu input is ruled out as an explanation for the negative excursion presented here. Similarly, while downward diffusion of O_2 into anoxic sediments during a period of transient water column oxidation could mobilise isotopically heavy Cu (either via sulphide oxidation or organic ligands), elemental ratios from the core show no evidence for enhanced weathering or terrestrial influx in association with this part of the section (as discussed in Zerkle et al., 2020). The organic-carbon rich shale directly above the $\delta^{65}Cu$ excursion shows Fe speciation evidence for mild localised oxygen availability in the water column, but this has no bearing on atmospheric oxygen concentrations; the continued presence of S-MIF throughout these strata precludes significant atmospheric oxygenation (Izon et al., 2017), further arguing against oxidative weathering as a driver for the Cu isotope excursion. The presence of oxygen in the water column but not the atmosphere suggests that it is derived through local oxygenic photosynthesis in surface waters (Izon et al., 2017). The oxidation state of the bottom waters currently remains unknow, however organic-rich marine sediments rapidly turn anoxic, suggesting anoxic bottom waters throughout this lithological change.

Given the arguments presented above, the remainder of this discussion is focussed on the two most plausible mechanisms via which marine Cu could be incorporated into shales under reducing conditions (Figure 7). For both mechanisms, we consider the measured Cu to be derived from organic matter that, under microbial sulphate reducing (MSR) conditions, has been either incorporated into pyrite or has formed its own sulphide phases, such as CuS or CuS_2 (e.g., Tribovillard et al., 2006).
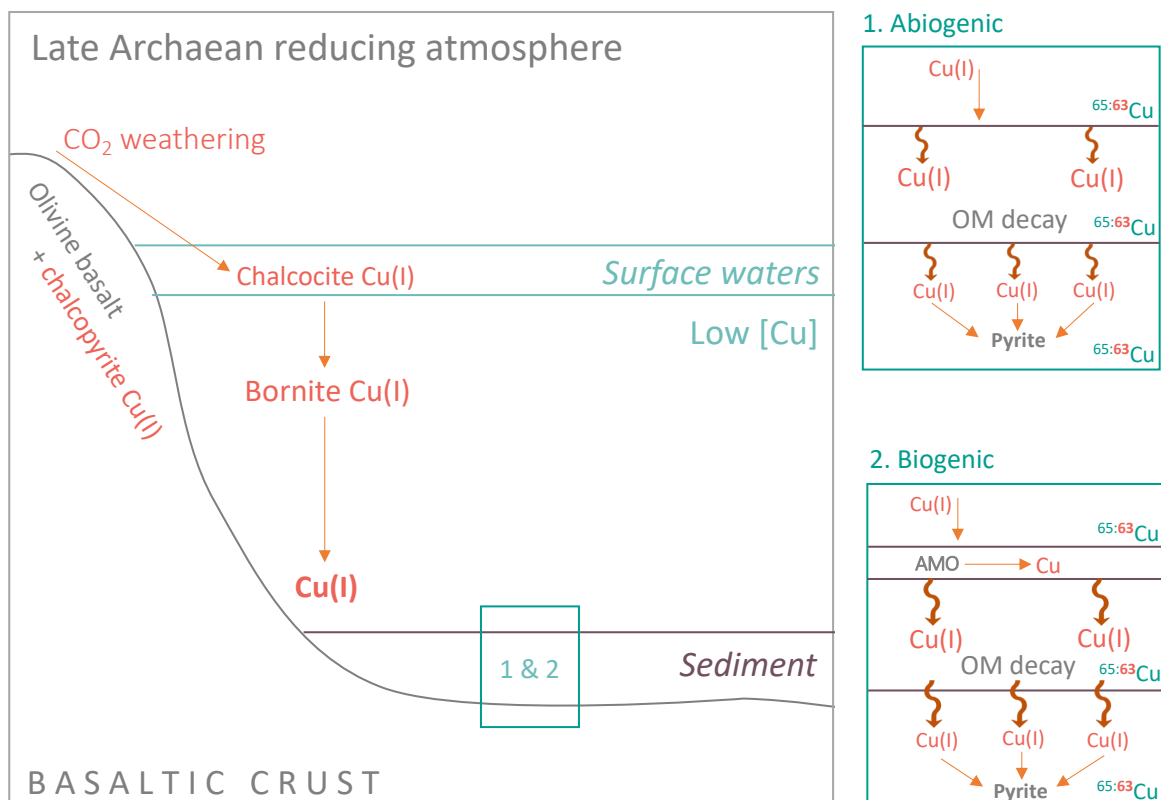
Figure 7: Hypothetical late Archaean weathering regimes showing the potential supply routes (a) and sedimentation pathways of Cu (b). Panel a corresponds to typical Late Archaean reducing conditions as predicted by Hao et al. (2017). The role of biology superimposed on to this weathering regime results in two hypothetical sedimentation pathways (scenarios 1 & 2) that could potentially cause the negative Cu isotope fractionation measured in GKF01

Under reducing atmospheric conditions ($pCO_{2,g}$ = $10^{-1.5}$ bars; $pH_{2,g}$ = $10^{-5.0}$ bars), chalcopyrite ($CuFeS_2$) is weathered from olivine basalt crust, forming chalcocite (Cu_2S) in surface waters, leading to further precipitation of bornite (Cu_5FeS_4) in deeper sections of the water column (Hao et al., 2017). These processes would lead to low overall riverine and oceanic Cu concentrations which are reflected in the low Cu concentrations

measured in core GKF01 (Figure 2). While model predictions indicate that Cu(II) could be present within the chalcopyrite crystal lattice (i.e. Klekovkina et al., 2014), the state of Cu within chalcopyrite is generally believed to be Cu(I) (Goh et al., 2006), which implies that no redox fractionation would occur between weathering and transport to ocean sediments.

In scenario (1) (Fig. 6b.1; Abiogenic), it is assumed that marine Cu would be isotopically light, relative to modern seawater, as it is transferred directly from basalt-hosted sulphide to the oceans without oxidative breakdown. As such, the isotopic composition of marine Cu should be very similar to average basalt Cu isotope composition (as sulphides represent the major Cu host in these rocks; Moynier et al., 2017). This prediction agrees well with the isotopically light $\delta^{65}Cu$ background values of 0.06 ‰ (relative to modern seawater values of 0.5 ‰ – 0.9 ‰; e.g., Little et al., 2017), which are almost identical to estimates for bulk silicate Earth (BSE, 0.08 ‰; Moynier et al., 2017). This is also shown in more modern Devonian black shales which formed in a reducing basin and which possess overlapping $\delta^{65}Cu$ values of 0.04 ± 0.16‰ (Mathur et al., 2012). In this scenario, Cu isotope fractionation occurs due to enhanced assimilation of reduced (and therefore light) Cu into sulphides. Given that there is no observable correlation between $\delta^{65}Cu$ and total S (fig. S2), this scenario is considered to be unlikely.

Under scenario (2) (Fig. 6b.2; Biogenic), Cu(I) is taken up via aerobic methanotrophs, and the negative $\delta^{65}Cu$ excursion largely reflects enhanced uptake of ^{65}Cu-depleted Cu during aerobic methanotrophy. While experimental studies of Cu isotope fractionation during aerobic methanotrophy are lacking, enhanced methanotrophy is supported by the extremely depleted $\delta^{13}C_{org}$ values (< -38‰) in the overlying PHE interval (Fig. 2). Carbon isotope values <-38‰ represent extensive assimilation of organic matter into sediment via methanotrophy (Hayes et al., 1999). The established presence of enhanced methane cycling coupled with an excursion in $\delta^{65}Cu$, a bioessential trace metal for aerobic methanotrophic bacteria, provides evidence for a biological mechanism for the negative $\delta^{65}Cu$ excursion. Therefore, the implications for this interpretation are considered in the

remainder of this discussion, acknowledging the caveat that it is currently not possible to differentiate between specific methanotrophic pathways.

3.3.4. A biological origin for the Cu isotope excursion

3.3.4.1 Anaerobic oxidation of methane

Given the low availability of oxygen in the Late Archaean, the negative $\delta^{13}C_{org}$ excursion within the PHE has previously been attributed to incorporation of methane into sediments via anaerobic oxidation of methane (AOM) coupled to microbial sulphate reduction (MSR; Izon et al., 2017). The metabolic pathway utilised by anaerobic methanotrophs is generally considered to be a reversal of the methanogenesis metabolic pathway and therefore reliant on Ni (e.g., Hallam et al., 2004). Thus, while AOM could have been the dominant metabolism accounting for enhanced incorporation of methane into sediments during the PHE, it fails to account for the $\delta^{65}Cu$ excursion. Nevertheless, AOM remains a significant metabolism throughout the late Archaean and must be considered in any discussion surrounding methane cycling.

If AOM was the dominant form of methanotrophy operating throughout the PHE section analysed in this study, the preceding negative $\delta^{65}Cu$ excursion could represent a pulse of aerobic methanotrophy occurring before or in the early stages of the purported PHE. This pulse could have been triggered by a perturbation in nutrient availability driven by hydrothermal input, which we preclude as the dominant cause for the $\delta^{65}Cu$ excursion but acknowledge as potentially occurring at this time (section 4.1.2). Any Cu provided by hydrothermal input could have been rapidly consumed by aerobic methanotrophs, allowing Ni-dependent AOM to become the dominant form of methanotrophy for the remainder of the PHE. As AOM is most commonly coupled to sulphate reduction (e.g., Moran et al., 2007), and accounting for the low sulphate conditions that persisted throughout the Late Archaean (Izon et al., 2017), it is likely that AOM would also have been supressed, allowing methane to accumulate in the atmosphere and leading to haze formation. While possible, this case is considered

unlikely; there is no significant evidence for an increased flux in Cu before the PHE and therefore alternative interpretations are considered.

3.3.4.2 Aerobic methane oxidation

Alternatively, aerobic methane oxidation could have remained the dominant pathway for methanotrophy throughout the duration of the PHE. This is supported by Fe-speciation data from Izon et al (2017) which suggest an oxic environment of deposition during the PHE. However, given that previously published Fe-speciation data (Izon et al., 2017) suggest anoxic conditions before the PHE, there are three significant points to consider for this interpretation, specifically: the bioavailability of Cu in a reducing environment, the impact of oxygen limitation on aerobic metabolisms in a reducing environment, and the stratigraphic occurrence of the δ^{65}Cu excursion before the onset of the $\delta^{13}C_{org}$ excursion.

Methanotrophs have a specific Cu uptake system, whereby an extracellular Cu-complexing agent (a chalkophore) is excreted by the methanotroph in order to extract Cu from the surrounding environment (Yoon et al., 2010; Semrau et al., 2010). For example, methanobactin (MB), which was first identified in pMMO-expressing bacteria (Kim et al., 2004), binds either Cu(I) without an oxidation state change, or Cu(II), which is subsequently reduced to Cu(I) (Choi et al., 2006). In the reduced Late Archaean environment modelled by Hao et al (2017), most, if not all Cu, was bound as Cu(I) sulphides. This would have decreased Cu bioavailability, creating a challenging environment from which microbes could extract Cu. It has been suggested that, in similar modern environments, some methanotrophs are capable of expressing specific chalkophores to extract Cu from mineral-bound Cu complexes, giving them a competitive advantage over cells that do not (Semrau et al., 2010). Chalkophore production appears to be widespread in both gammaproteobacteria methanotrophs and alphaproteobacteria methanotrophs (Choi et al., 2008; Semrau et al., 2010). The presence of chalkophores also brings forth another potential Cu isotope fractionation mechanism; the transport of Fe by siderophore-producing bacteria have been shown to fractionate Fe isotopes, with evidence to suggest that the dissolution of Fe in minerals by the siderophore causes this fractionation (Brantley et al., 2001).

Aerobic methanotrophic bacteria use CH_4 as their sole source of carbon and are also obligate aerobes, making them dependent on O_2 and limited by O_2 availability (e.g., Roslev and King, 1994). As above, previously published Fe speciation data for this section indicate anoxic, ferruginous depositional conditions during the Cu isotope excursion, with localized oxygenation during the PHE. However, the extent of this oxygenation was likely limited to the local water column or sediment-water interface, with the persistence of S-MIF throughout this section indicating low atmospheric O_2 (Izon et al., 2017). In addition, even local oxygen availability would have been limited due to the widespread occurrence of Fe(II) and other reduced compounds that would have quickly consumed O_2 in the sediments (Zerkle et al., 2012). It has been shown that some aerobic methanotrophs are able to survive under both carbon and O_2 starved conditions, suggesting that methane oxidation can occur in environments that do not continuously support aerobic methanotrophic growth (Roslev and King, 1994). Further investigation has since demonstrated that methanotrophs which live at the low end of the O_2 gradient in natural environments have established mechanisms for survival in such environments (Knief, 2015). For example, experiments have demonstrated that under low O_2 conditions and under prolonged O_2 starvation, the model gammaproteobacteria methanotroph Methylomicrobium buryatense 5GB1 maintained a metabolic state that combined fermentation and respiration, secreting acetate and formate (Gilman et al., 2017). Given the adaptive abilities of aerobic methanotrophs (both in terms of accessing reduced Cu and surviving under O_2 starved conditions) and in the absence of evidence to the contrary, the possibility of aerobic methanotrophy can be considered as relevant when interpreting geochemical data from sediments of this age, recognising the limitations with respect to the lack of evidence for Cu isotope fractionation by aerobic methanotrophs.

The sequence of changes captured by the examination of multi-proxy geochemical datasets at high resolution further supports this interpretation. Through 863 m – 817 m, $\delta^{65}Cu$ values becomes more negative over approximately 7 m of stratigraphy, reaching a minimum value of -0.66 ‰ at 841 m (Figure 2, dashed line (a)); the most negative $\delta^{65}Cu$ value measured coincides with the onset of the large $\delta^{13}C_{org}$ excursion. From this point

(Fig. 2, dashed line (b)), the $\delta^{65}Cu$ values return to baseline rapidly, over ~4m of stratigraphy, and remain in this state for the majority of the $\delta^{13}C_{org}$ excursion.

Significant changes in $\Delta^{33}S/\Delta^{36}S$ over this same section (Figure 2) have been interpreted to represent changes in global atmospheric chemistry at high atmospheric CH_4 (Izon et al., 2017), whereas low $\delta^{13}C_{org}$ values have been interpreted to reflect local production and consumption of methane. Lower $\delta^{13}C_{org}$ values can therefore imply locally high methane concentrations, as it has been demonstrated that higher volumes of methane lead to much faster aerobic methane oxidation (Sherry et al., 2015). The less depleted background $\delta^{13}C_{org}$ values throughout the majority of this section could thus be representative of lower levels of aerobic methane oxidation and, by extension, lower methane concentrations.

In low methane environments, type I methanotrophs that express pMMO have the competitive advantage over type II methanotrophs, which thrive under high CH_4 low O_2 settings (Hanson and Hanson, 1996). When methane concentrations increase, methanotrophs that express sMMO (soluble methane monooxygenase, containing an Fe metal centre rather than Cu) take over as dominant methane oxidisers (Semrau et al., 2010). If this was similarly the case in the Neoarchaean, the negative $\delta^{65}Cu$ excursion can be interpreted as representing pMMO-expressing methanotrophs thriving in the relatively low methane conditions indicated by the relatively high $\delta^{13}C_{org}$ values. The fast return of the $\delta^{65}Cu$ to background values coincides with the sudden decrease in $\delta^{13}C_{org}$ which, if applicable to this interval, could suggest the takeover of Fe-utilising sMMO-expressing methanotrophs in response to higher methane availability (Figure 8). This ecological change is supported by the fact that we continue to observe extensive assimilation of organic matter into sediment via methanotrophy, yet this is not visible in the $\delta^{65}Cu$ record. Alternatively, the disappearance of the Cu isotope excursion during the PHE could be the result of pMMO-expressing methanotrophs using Cu to completion, such that no isotope effect is expressed. In this instance, the observed C isotope excursion (Figure 2) is the result of Cu-dependent aerobic methanotrophy rather than Fe-dependent aerobic methanotrophy. We acknowledge, however, that these interpretations are contingent on the demonstration that Cu isotopes are fractionated by methanotrophic bacteria and that further work is required in this field.
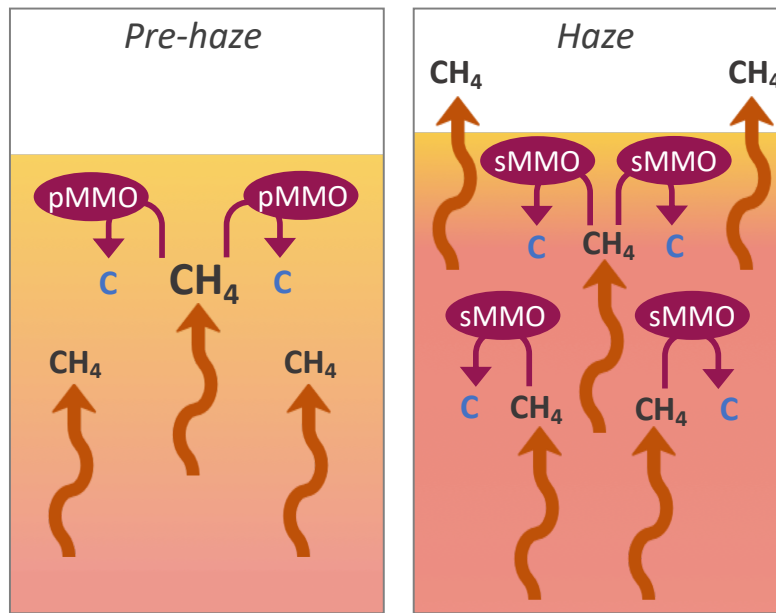
Figure 8: Differential methane monooxygenase (MMO) expression under different methane concentrations. Panel a depicts pre-haze conditions, where at low methane conditions methane is consumed by Cu-dependent pMMO-expressing methanotrophs. As methane concentrations increase, (Panel b) pMMO-expressing methanotrophs are out-competed by Fe-dependent sMMO-expressing methanotrophs.

3.4. Conclusions

Examining a ~2.5 Ga sedimentary succession that is associated with an episode of organic haze formation, this study presents a new high-resolution $\delta^{65}Cu$ record that reveals a pronounced negative $\delta^{65}Cu$ excursion. Precluding post-depositional alteration and abiotic redox reactions, this is interpreted as reflecting aerobic methanotrophy under low methane conditions, however it must be stressed that further work is required in order to draw a firmly definitive conclusion.

While most Cu-dependent metabolisms are assumed to have evolved after the GOE (Zerkle et al., 2005), estimates for the origin of aerobic methanotrophy range between 2.91 – 2.15 Ga. Due to the disappearance of S-MIF at 2.4-2.3 Ga and the subsequent implications for environmental oxygen availability, the younger end of this age range is often favoured (e.g. Battistuzzi et al., 2004). However, given the ever-emerging evidence

for oxygenic photosynthetic life prior to the disappearance of S-MIF (e.g. Crowe et al., 2013; Lyons et al., 2014), along with evidence suggesting the presence of oxygenic oases before the GOE (e.g., Olson et al., 2013; Planavsky et al., 2014; Yang et al., 2019), there is scope for this assumption to be reconsidered. The new δ^{65}Cu data presented in this study may support an earlier emergence of aerobic methanotrophy, arguing for the presence of Cu-dependent aerobic methanotrophy by ~2.5 Ga, approximately 200 Myr before the disappearance of S-MIF (Luo et al., 2016; Fig. 8). This is consistent with models predicting the existence of aerobic ecosystems before the GOE, notably aerobic methanotrophy, which is postulated to have suppressed methane and oxygen fluxes to the atmosphere (i.e., Daines and Lenton, 2016).

Besides demonstrating the potential utility of δ^{65}Cu as an isotopic biomarker of aerobic methanotrophy in Late Archaean rocks, the presence of an established pre-GOE aerobic methane sink has important implications for models resolving the role of methane cycling in modulating climate and atmospheric redox transitions on the early Earth, including the Great Oxidation Event (e.g., Catling et al., 2007; Daines and Lenton, 2016). Moving forward, these data illustrate the importance of continuing to develop δ^{65}Cu as an isotopic biomarker capable of resolving early-Earth's early methane cycle, thus providing important constraints for climate and biogeochemical models alike.
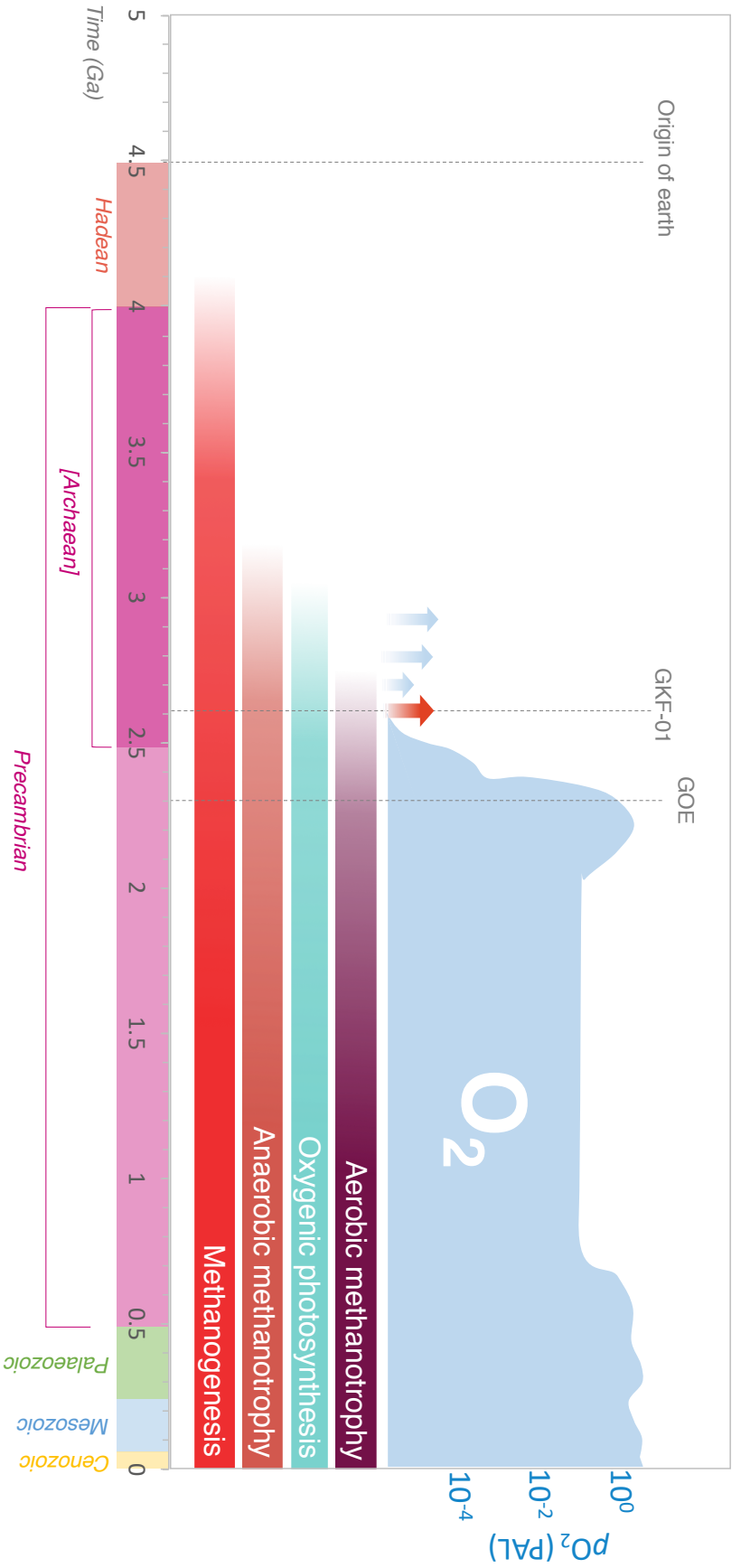
Figure 9: The temporal evolution of key metabolic pathways. Here, the copper isotope evidence for aerobic methanotrophy from Core GKF01 provides a minimum age constraint on the emergence of aerobic methanotrophy. The red arrow indicates PHEs and the blue arrows signify episodic pre-GOE oxygenation events. Alternate constraints on biological innovation follow Battistuzzi et al. (2004), while the evolution of pO_2 and the occurrence of PHEs follows Lyons et al. (2014) and Izon et al. (2017), respectively. The time-scale follows that recommended by the Geological Society of America (Walker et al., 2018).

Chapter 4

A copper isotope profile of a mid-Archaean evaporitic lake system.

4.1. Introduction

The Hamersley Basin of the Western Australian Pilbara Craton represents one of the best-preserved ancient depositional basins on Earth (Trendall et al., 2004). Within this basin the Fortescue Group, which rests unconformably on top of the Pilbara Craton, has been subjected to numerous palaeoenvironmental and geochemical studies due to its age, preservation, and unique stratigraphy. Broadly, the c. 2.75 Ga Fortescue group comprises a series of intercalated sandstone and mafic basalts, shales, and palaeosols which grade up into mafic basalts and stromatolitic carbonates near the top of the unit, cut in the middle by a felsic porphyry deposit (Blake et al., 2004). The top of the section is generally believed to reflect a shallow, closed, and alkaline lacustrine environment, while the base of the section reflects a deeper and more open/ephemeral setting (e.g., Buick et al., 1990; Stüeken et al., 2017).

Numerous studies have provided robust organic carbon isotope ($\delta^{13}C_{org}$) data from the Fortescue group, recording some of the lowest known preserved $\delta^{13}C_{org}$ values in geological history within the Tumbiana Formation (a ~2.7 Ga section of the Fortescue group, exhibiting $\delta^{13}C_{org}$ values of almost -60‰, e.g., Hayes (1994); Eigenbrode and Freeman, 2006). The $\delta^{13}C_{org}$ values of sedimentary organic matter throughout the Archaean are relatively variable but low when compared to Phanerozoic and modern

marine sediments, a trend indicative of ecosystem incorporation of ^{13}C-depleted substrates via the incorporation of photosynthetic biomass by carbon fixation pathways prior to the post-GOE domination of heterotrophic respiration (which imparts a limited C isotope fractionation) (Hayes, 1994). Within the Tumbiana formation, these low $\delta^{13}C_{org}$ values are generally believed to represent assimilation of CH_4 into organic matter via a combination of aerobic methanotrophy (AMO) and anaerobic methanotrophy (AOM), with numerous arguments presented in support of AMO in particular (e.g., Eigenbrode and Freeman, 2006; Thomazo et al., 2009; Yoshiya et al., 2012; Stüeken et al., 2017). These arguments are largely based on the limited evidence for the sulphate and ferrous Fe required for AOM (e.g., Thomazo et al., 2009 Czaja et al., 2010) and the presence of shallow-water stromatolites likely built by oxygenic phototrophs (due to the scarcity of electron donors other than H_2 and O_2) which would have provided the O_2 required for AMO (Buick, 1992). However, in sediments reflecting deeper depositional environments within the Fortescue group, the covariance between low $\delta^{13}C_{org}$ and low $\delta^{56}Fe$ suggests a direct coupling of AOM and Fe-reducing bacteria (Yoshiya et al., 2012). As such, it is possible that the Tumbiana system hosted both AOM and AMO, with the latter metabolism dominating in shallower, mildly oxic environments and the former metabolism dominating in deeper, anoxic environments. This interpretation is supported by the $\delta^{13}C_{kerogen}$ values analysed by Eigenbrode and Freeman (2006), which provide a variable shallow water $\delta^{13}C_{kerogen}$ signal of -57 to -28‰ (implying a mixture of photosynthetic, methanogenic, and methanotrophic biomass) and a more consistently depleted deep-water signal of -40 to -45‰.

Evidence for aerobic metabolisms such as oxygenic phototrophs (Buick, 1992) and aerobic methanotrophs (Eigenbrode and Freeman, 2006) at 2.7 Ga represents a significant upheaval of the biogeochemical cycling of carbon. Prior to this time, Earth's biosphere was presumably dominated by near-surface methanogenesis and environmental anoxia (e.g., Hayes, 1994). The emergence of aerobic metabolisms would suggest that oxygenic photosynthesis was well enough established in localised settings (such as the Tumbiana) that it could support the emergence of oxygen-dependent metabolisms (Buick, 1992). However, the extent to which AMO, as opposed to AOM, is responsible for depleted $\delta^{13}C_{org/kerogen}$, as well as the hypothesised distribution of metabolisms as a function of water

depth and in marine versus terrestrial settings remains unconstrained. Furthermore, arguments for niche biological differentiation in the Archaean terrestrial setting of the Fortescue group have recently emerged, based on the diverse environments exhibited across the basin (Stüeken et al., 2017; Stüeken and Buick, 2017). Both open and closed hydrologic settings, along with felsic and mafic substrates, could have driven biochemical evolution; the open, felsic system envisaged for the other sections of the Fortescue group have been shown to be associated with ecosystems dominated by methanogenesis, while the open and mafic system envisaged for the Mt. Roe formation indicates a system dominated by methanotrophy and sulphate reduction. In contrast, the closed, mafic environment of the Tumbiana and Kylena formations have been suggested to indicate an ecosystem comprising methanotrophy, oxygenic photosynthesis, and minor levels of sulphate reduction (Stüeken et al., 2017).

Early arguments for the prevalence of AOM throughout the entirety of the Archaean eon are based around the evidence for dominantly anoxic oceans, which would have restricted the widespread evolution and diversification of aerobic metabolisms (Hinrichs, 2002). Atmospheric anoxia throughout the Archaean is substantiated by the mass-independent fractionation of sulphur isotopes (S-MIF) measured in sediments older than c. 2.43 Ga (i.e., pre-GOE), the preservation of which is only possible under atmospheric O_2 concentrations less than 10^{-5} present atmospheric levels (Pavlov and Kasting, 2002). Nevertheless, under a reducing atmosphere, ephemeral surface water oxygen oases occurred, potentially providing enough free oxygen for some degree of exploitation by microorganisms (e.g. Yang et al., 2019).

Metals are important micronutrients and can provide additional biomarkers for ancient metabolisms as well as palaeoredox conditions. Previous studies of Mo and Fe isotopes within the Tumbiana Formation in particular have begun to build a picture of metal biogeochemical cycling within this system. Czaja et al. (2010) analysed bulk-rock samples from core SV1 of the Tumbiana Formation and found Fe isotope compositions close to crustal average (~0‰), noting that the predominant Fe bearing phases in the core were phyllosilicates, suggesting minimal Fe redox cycling in the depositional environment. The presence of Fe within the phyllosilicate phase has also been interpreted as indicating

limited Fe bioavailability (Stüeken et al., 2017). In contrast, Yoshiya et al. (2012) present Fe isotope measurements from in-situ pyrites of Fortescue Group which display significant variation (-4.2‰ to +3.0‰), the lowest of which are found within the tuffaceous mudstones of the Mingah Member (Tumbiana Formation) and which occur contemporaneously with extremely low $\delta^{13}C_{org}$ in the parent rocks. This covariance is interpreted as being strongly indicative of AOM coupled to bacterial Fe-reduction (Yoshiya et al., 2012). The latter study further suggests the partitioning of Fe into sulphides during early diagenesis. Lastly, Mo isotope analyses of bulk-rock samples from the Tumbiana Formation yield a large range in Mo isotope values (-0.1‰ to +1.8‰), implying the presence of Mo in aqueous solution within the Tumbiana environment. The source of Mo in this instance is hypothesised to be due to localised oxidative weathering, and the Mo isotope fractionations are thought to be due to partial sequestration into sulphide minerals (Stüeken et al., 2017). The Tumbiana Formation therefore provides a good opportunity to test the utility of Cu isotopes as a biomarker for AMO (i.e., Zavina-James, in review; Chapter 3, this thesis), since the presence of this metabolism has been proposed by previous studies. The Tumbiana Formation also provides a contrasting environment to that of the Upper Nauga Formation studied in Chapter 3, as it has been suggested to represent a hyperalkaline lacustrine environment in which oxygenic photosynthesis could have taken place in the surface waters. Such an environment could therefore presumably support other aerobic metabolisms (Stüeken et al., 2017).

In this study, a high-resolution Cu isotope analysis is applied to core SV1, a ~200m transect of the Tumbiana formation which has been subjected to previous organic carbon isotope analysis (Eigenbrode and Freeman, 2006). These data are examined within the palaeoenvironmental context of the Tumbiana formation, including aqueous speciation models which consider Cu cycling in conventional Archaean marine and lacustrine settings as well as high pH lacustrine settings. The study yields Cu isotope values close to bulk silicate earth (BSE), which likely reflect the mafic provenance of the input to the system and which, when considered alongside the above, provide further evidence that the Tumbiana formation was deposited in a shallow lacustrine environment.

4.2. Materials and methods

4.2.1 Materials: The Tumbiana Formation and Core SV1

The Tumbiana Formation belongs to the Fortescue Group, which makes up the basal unit of the greater Mount Bruce Supergroup (Hamersley Basin). It lies unconformably on top of the granite-greenstone Pilbara Craton and is up to 7km thick in some areas. The Hamersley Basin is one of the best-preserved ancient depositional basins on Earth; U-Pb age data from zircons of the Fortescue Group suggest that the accumulation of basin-fill occurred between 2.78 – 2.63 Ga, with the Tumbiana deposited between 2.73 and 2.72 Ga (Trendall et al., 2014 and references therein). The Tumbiana Formation is commonly less than 200m thick and consists of stromatolitic and clastic carbonate, argellite, sandstone, primary and reworked volcanic tuff, and minor conglomerates. In addition, subaerial basaltic flows make up a minor component of the Tumbiana Formation, occurring as thin (1-3 m thick) flows which are interbedded with volcaniclastic facies (Packer, 1990; Thorne and Trendall, 2001). For this study, samples of the Tumbiana formation were obtained from the diamond drill core CRA Pilbara DDH84SV1 (hereon referred to as core SV1). The location of core SV1, along with a generalised geological map of the Pilbara Craton, is shown in Figure 1.
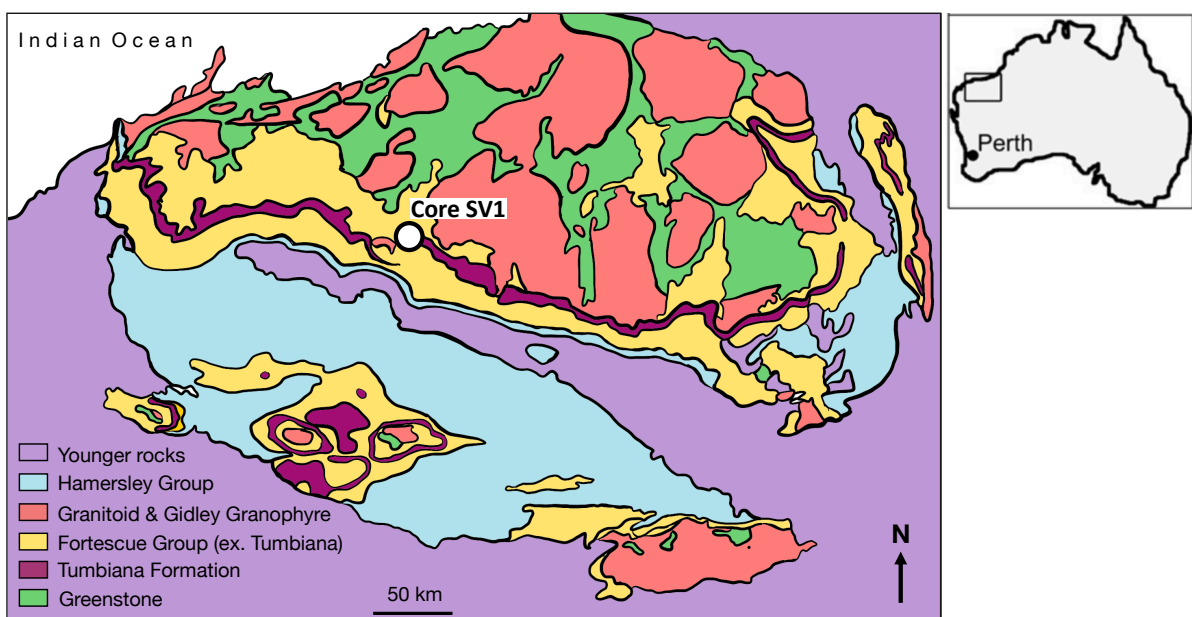
Figure 1: A generalised geological map of the Hamersley Province, Western Australia. The location of Core SV1 is indicated by a white circle. The Tumbiana Formation is shown in dark purple (modified from Blake, 1993 and Thorne and Trendall, 2001).

Core SV1 transects the entirety of a ~150 m thick section of the shallower Tumbiana Formation and comprises two lithofacies. Figure 2 presents a sedimentary log of this core as described by Eigenbrode and Freeman (2006), within the context of the surrounding geology. At the base of the Tumbiana formation is a cross-bedded tuffaceous sandstone, which is believed to represent a high-energy fluvial environment of deposition. Above this, stromatolitic boundstone beds comprising shallowing-upwards cycles of silicified black shale or chert which grade into silicified and sandy-silty mat-bound lime grainstones. These grainstones then grade into silicified, non-dolomitised stromatolite-bound lime grainstones with small stromatolites, fenestrae, mud cracks, and sand. Within the sequence, fine disseminated pyrites are frequently observed within the tuffaceous sandstones and microbial mat laminae (Eigenbrode and Freeman, 2006). The mud cracks exhibited in core SV1, along with the noted presence of halite casts observed in other sections of the Tumbiana Formation, indicate a shallow-water depositional environment which may have experienced periods of (localised) hypersalinity (Buick, 1992). For a detailed discussion of the depositional environment, please refer to section 4.4.2 of this chapter.

The SV1 samples analysed in this study were supplied from previous sampling of the core by Eigenbrode and Freeman (2006). Samples were processed and crushed under trace metal clean conditions (as described by Eigenbrode and Freeman, 2006). Depth intervals for which corresponding $\delta^{13}C_{kerogen}$ measurements already exist (i.e., those presented in Eigenbrode and Freeman, 2006) were selected where possible for consistency across studies.
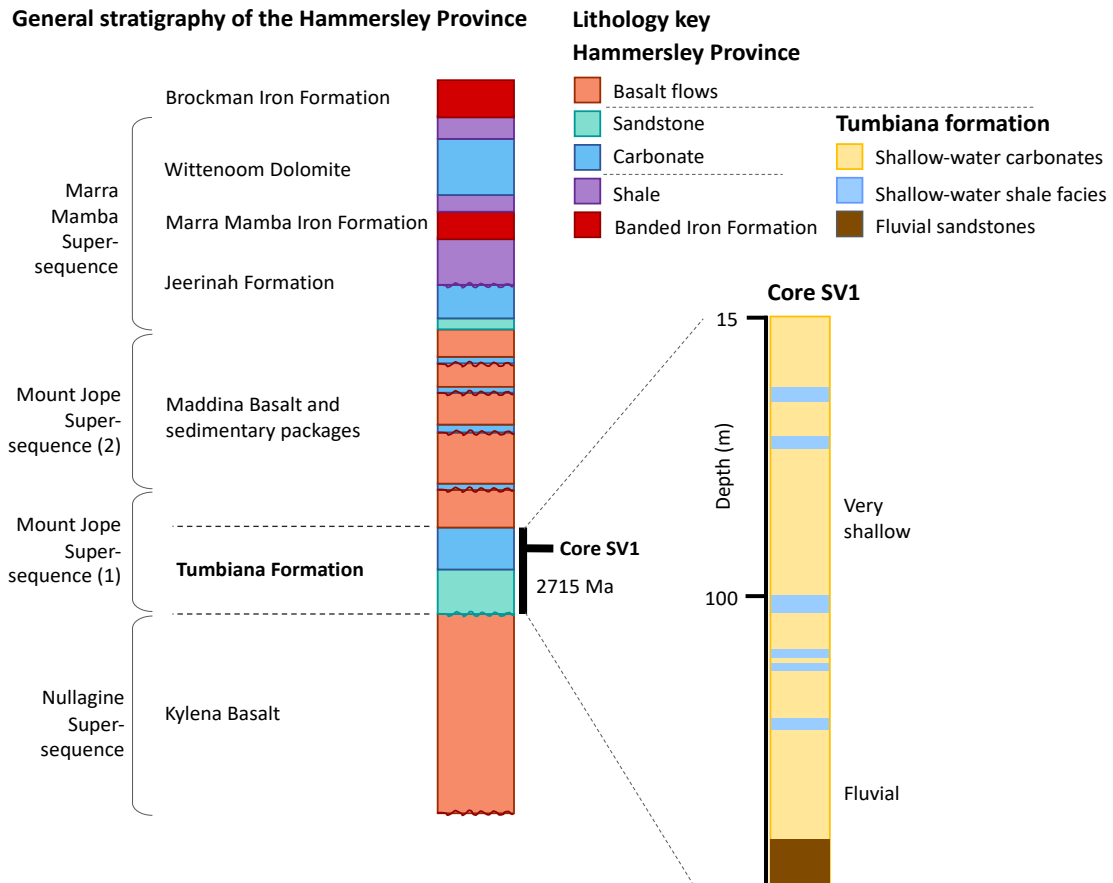
Figure 2: A simplified stratigraphic section of the Hamersley Province geology and Core SV1 (i.e., the Tumbiana Formation). Adapted from Eigenbrode and Freeman (2006).

4.2.2. Methods

Sample powders were weighed and digested following the methods described in Chapter 2 of this thesis. Copper concentration and isotope analyses were performed as described in Chapter 2. The TOC and S data presented in this chapter are from Eigenbrode and Freeman (2006).

4.2.2.1. Copper speciation models

In order to provide a full picture of copper cycling in the Tumbiana section, Cu speciation and mineral saturation as a function of pH was modelled for modern seawater, anoxic Archaean seawater (pe = -5), mildly oxic Archaean seawater (pe = 0), an alkaline lake with a fully oxidised water column (Walker Lake, USA), and a stratified alkaline lake (Mono Lake, USA). For the latter system, the model was run twice to account for conditions

above and below the chemocline. Rationale for selecting Walker Lake and Mono Lake, along with descriptions of these lakes, can be found in section 4.3.3 of this chapter. All models were made using the USGS programme PHREEQC Version 3 using the minteq.v4 database. Eh (or pe) values of 0 and -5 were chosen because 0 approximately coincides with the point at which organic matter is no longer oxidatively respired (i.e., the 'organic matter fence' in the terminology of Krumbein & Garrels, 1952), while -5 is below the redox state required for sulphate reduction to sulphide (the 'sulphate-sulphide fence'), as was likely to have been the case in an anoxic Archaean ocean. The variation in pH was implemented by running each solution multiple times whilst manually changing the pH input values. The model inputs are listed in table 1. These models only consider the small inorganic pool of Cu within the respective systems (i.e., the pool of Cu not sorbed to minerals surfaces or bound to organic ligands, e.g., Little et al., 2017).

Element	Modern seawater (mol/kg)	Archaean seawater (mol/kg)	Walker Lake (mol/kg)	Mono Lake (a) (mol/kg)	Mono Lake (b) (mol/kg)
Ca^{2+}	1.07×10^{-2}	1.07×10^{-2}	2.35×10^{-4}	1.79×10^{-4}	1.43×10^{-4}
Cl^{-}	5.91×10^{-1}	5.91×10^{-1}	5.94×10^{-2}	2.73×10^{-1}	3.02×10^{-1}
Cu^{+}	7.26×10^{-9}	7.26×10^{-9}	1.01×10^{-8}	1.35×10^{-7}	1.03×10^{-7}
Fe^{2+}	1×10^{-9}	1×10^{-4}	7.21×10^{-8}	1.05×10^{-5}	4.85×10^{-6}
K^{+}	1.05×10^{-2}	1.05×10^{-2}	3.92×10^{-3}	4.18×10^{-2}	4.58×10^{-2}
Mg^{2+}	5.66×10^{-2}	5.66×10^{-2}	5.04×10^{-3}	1.62×10^{-3}	1.74×10^{-3}
Mn^{2+}	1×10^{-9}	1.1×10^{-9}	9.14×10^{-8}	9.48×10^{7}	1.07×10^{-6}
Na^{+}	5.06×10^{-1}	5.06×10^{-1}	1.36×10^{-1}	1.39	1.51
SO_4^{2-}	3.10×10^{-6}	2×10^{-2}	6.59×10^{-2}	1.13×10^{-1}	1.21×10^{-1}
pe		-0.5, 0			0
Alkalinity	2.1	2.1	44.8	632.5	691

Table 1: Speciation and saturation model input values. Modern seawater and Archaean seawater composition data are from Stüeken, 2020. Walker Lake and Mono Lake composition data are from Domagalski, 1994. Alkalinity for both lakes is assumed to be carbonate alkalinity. All units are in mol except for alkalinity, which is in milliequivalents/litre.

4.3. Results

4.3.1. Trace metal data

Table 1 provides results for the trace metal data analysed in this study. Correlation coefficients (R) were calculated for all elemental pairings which are presented as R^2 values in table 2. There are notable correlations between V and Co ($R^2 = 0.69$), V and Cr ($R^2 = 0.52$), Ni and V ($R^2 = 0.61$), and Ni and Cr ($R^2 = 0.72$), concurrent with a mafic/ultramafic sediment source (e.g., Otamendi et al., 2016). Figure 3 shows Cu abundances from this study plotted against TOC, total S, and $\delta^{13}C_{kerogen}$ for the same samples analysed by Eigenbrode and Freeman (2006). Furthermore, a weak correlation between Cu and TOC ($R^2 = 0.30$) can be observed. By comparison, there is no relationship between Cu and total S ($R^2 = 0.02$), or Cu and $\delta^{13}C_{kerogen}$ in these samples ($R^2 = 0.00$).

	V	Cr	Mn	Fe	Co	Ni	Cu	Zn	As	Ag
V	1.00									
Cr	0.52	1.00								
Mn	0.22	0.20	1.00							
Fe	0.31	0.36	0.01	1.00						
Co	0.69	0.35	0.18	0.15	1.00					
Ni	0.61	0.72	0.20	0.26	0.50	1.00				
Cu	0.22	0.32	0.02	0.18	0.08	0.47	1.00			
Zn	0.02	0.00	0.02	0.00	0.03	0.00	0.08	1.00		
As	0.01	0.00	0.01	0.02	0.01	0.07	0.00	0.00	1.00	
Ag	0.02	0.11	0.13	0.03	0.04	0.12	0.07	0.04	0.25	1.00

Table 2: Correlation coefficients (expressed as R^2 values) for the trace metals analysed in this study.
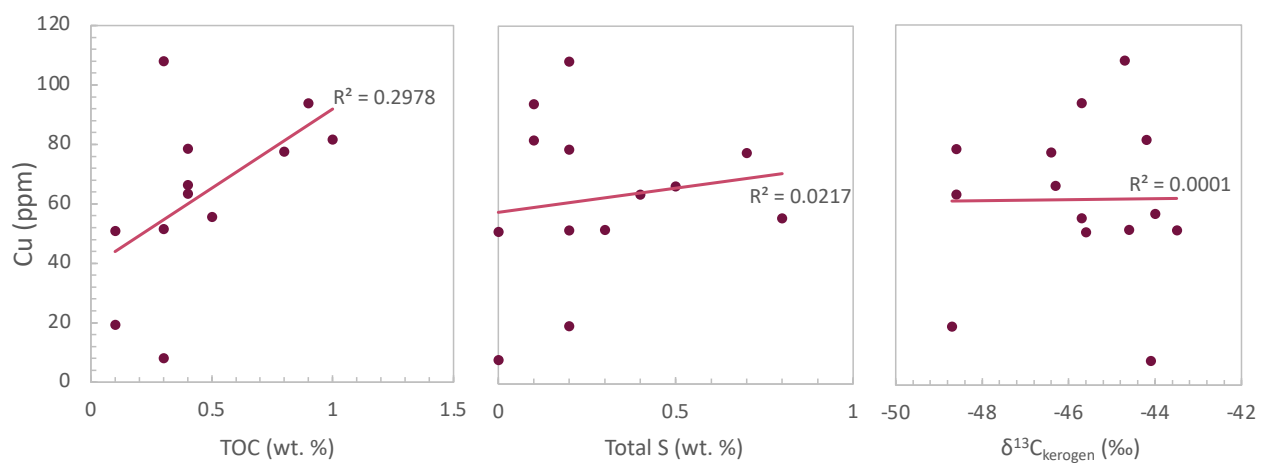
Figure 3: Cross-plots for Cu abundance data generated in this study measured against TOC, total S, and $\delta^{13}C_{kerogen}$ data for the same samples from Eigenbrode and Freeman (2006).

Depth (m)	δ^{65}Cu (‰)	2SD (‰)	V [ppm]	Cr [ppm]	Mn [ppm]	Fe [ppm]	Co [ppm]	Ni [ppm]	Cu [ppm]	Zn [ppm]	As [ppm]	Ag [ppm]
28.1	0.05	0.03	85.59	86.24	987.66	56563	20.54	46.75	51.10	109.74	6.50	0.15
47.9	0.04	0.06	198.47	129.95	1166.68	63789	38.77	77.39	95.95	44.75	7.76	0.11
51.6	0.04	0.02	99.85	80.53	901.32	39469	31.05	47.28	19.53	13.06	8.34	0.04
64.7	0.07	0.03	214.08	170.44	565.29	90680	44.81	88.12	76.42	73.32	2.13	0.14
70.9	0.02	0.03	135.35	108.15	250.00	47999	21.38	36.73	8.19	50.94	2.54	0.06
73.4	0.05	0.04	165.31	186.34	1107.87	122179	39.27	74.54	57.12	99.74	4.38	0.22
78.9	-0.01	0.05	153.71	75.57	1026.99	88671	23.67	61.10	68.90	57.03	8.09	0.02
81.3	0.08	0.01	169.95	200.05	462.38	70933	31.79	92.01	81.79	126.32	12.41	0.06
98.2	0.06	0.04	88.03	113.18	616.00	81295	18.19	50.64	63.63	42.82	6.79	0.08
100.1	0.11	0.06	83.15	74.04	4009.17	75387	15.90	40.17	51.65	33.60	5.78	-0.03
103.3	0.05	0.03	185.51	225.19	746.56	108829	29.05	91.84	94.00	62.11	8.72	0.16
105.4	0.03	0.08	77.85	103.99	2638.78	47447	16.03	44.89	51.85	30.00	4.12	0.05
110.4	0.06	0.05	145.28	164.39	690.74	74303	28.37	100.14	77.65	76.02	14.13	0.15
116.7	0.1	0.02	93.85	103.37	1085.53	51531	21.34	63.05	55.75	59.98	22.97	0.36
117	0.05	0.02	70.91	76.82	1502.58	59197	13.11	36.80	66.46	279.03	6.64	0.12
126.4	0.06	0.04	131.46	138.81	841.75	56758	36.86	76.14	78.71	91.73	4.66	0.12
140.6	0.06	0.1	131.58	163.72	538.37	68964	21.97	71.58	108.22	123.56	3.03	0.17

Table 1: Copper isotope and trace metal data analysed in this study.

88

4.3.2. Copper isotope data

Copper isotope analyses of the SV1 core (Figure 5; table 3) reveal a limited range in Cu isotope composition across the core, with an average (0.05 ± 0.05 ‰; 2SD) that is within error of bulk silicate earth (BSE) values (i.e., + 0.06 ± 0.18 ‰ (2SD); Moynier et al., 2017) and the average of the 'background' values for core GKF01 (0.05 ‰ ± 0.08 ‰, Zavina-James et al., *in review*; Chapter 3, this thesis). Referring to Figure 4, there is no correlation between δ^{65}Cu and TOC (R^2 = 0.05), or $\delta^{13}C_{kerogen}$ (R^2 = 0.03), and only a very weak correlation between δ^{65}Cu values and total S concentrations (R^2 = 0.13).
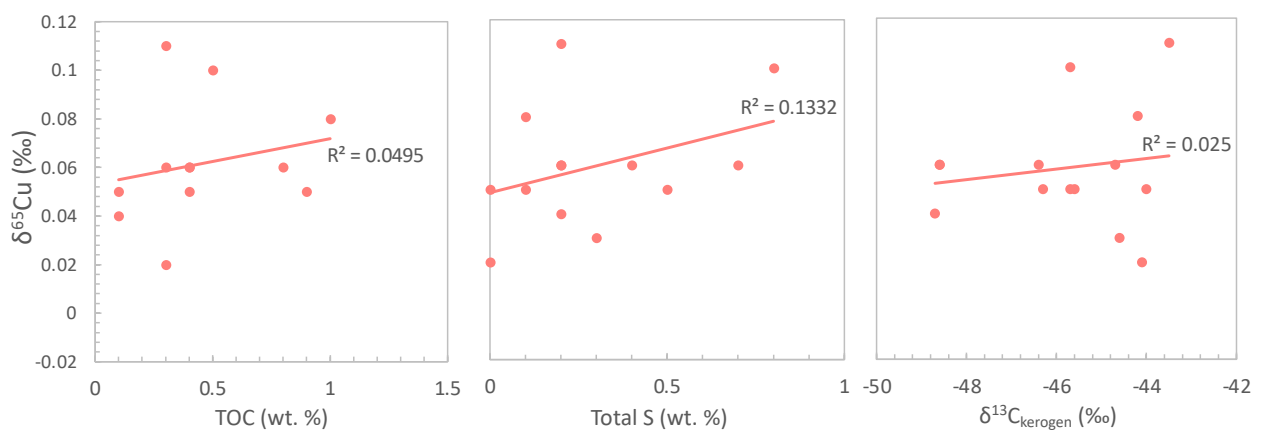
Figure 4: Cross-plots for Cu isotope data generated in this study measured against TOC, total S, and $\delta^{13}C_{kerogen}$ data for the same samples from Eigenbrode and Freeman (2006).
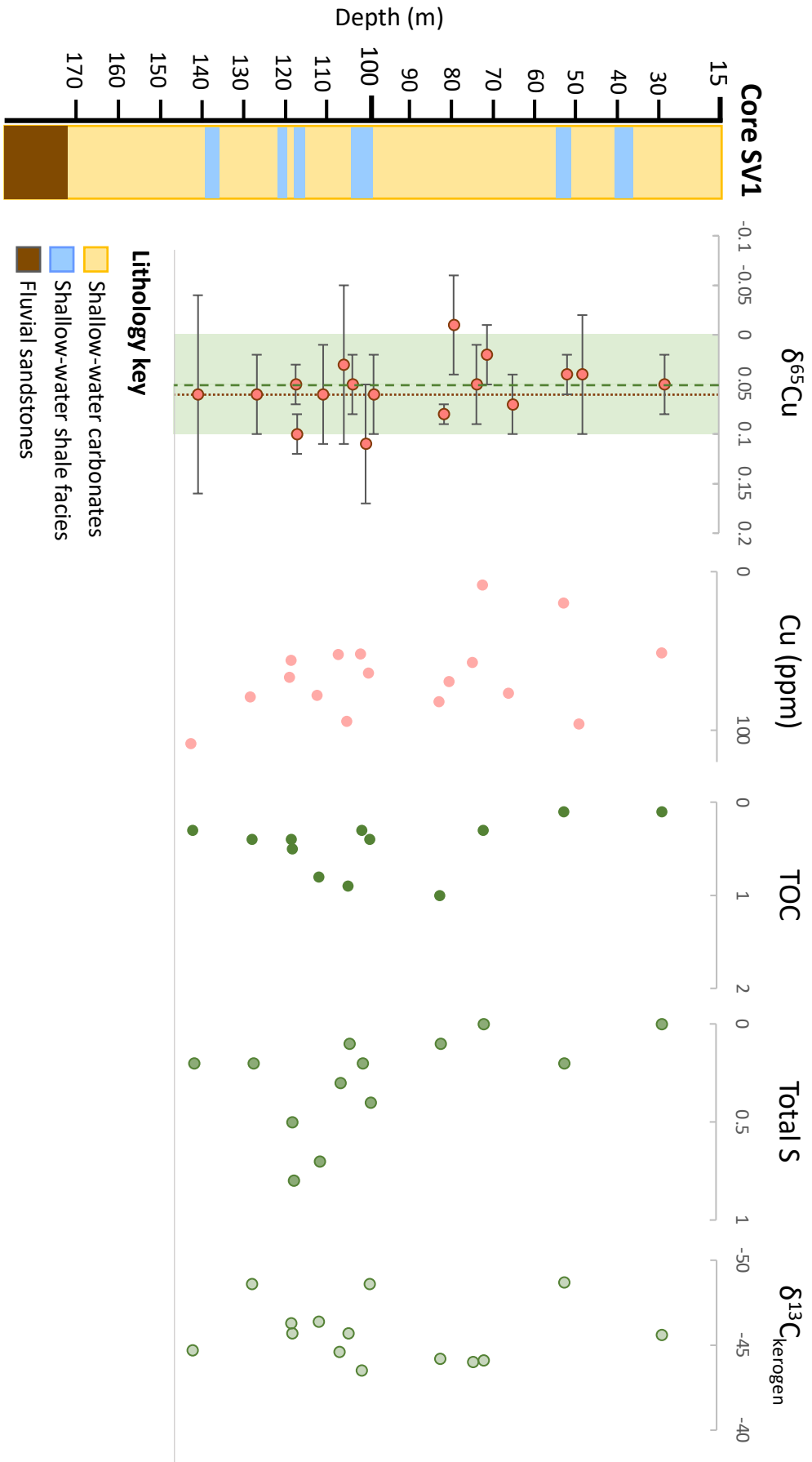
Figure 5: Copper isotope (δ^{65}Cu) and abundance data (this study) along with TOC, total S, and δ^{13}C$_{kerogen}$ plotted against core SV1 stratigraphy and depth. Error bars on δ^{65}Cu represent two standard deviations based on three Cu isotope measurements. The green dashed line reflects the average Cu isotope value for core SV1, and the orange dotted line marks modern BSE values.

90

4.3.3. Copper speciation models

The Cu speciation and mineral saturation models are shown in Figures 6a and 6b (modern seawater), 6c and 6d (anoxic Archaean seawater, pe = -5), 6e and 6f (mildly oxic Archaean seawater, pe = 0), 6g and 6h (an alkaline lake with a fully oxidised water column - Walker Lake) 6i and 6j (the surface of a stratified alkaline lake - Mono Lake) and 6k and 6l (below the chemocline of a stratified alkaline lake - Mono Lake). Not all species are plotted in Figures 6a-6j and, as such, the species do not necessarily sum to 100%. This is especially the case at extreme pH values because species that make up a negligible proportion of total Cu at neutral pH are not shown.

Figure 6a shows that in modern seawater (pH ~8.1), Cu is present mainly as complexes with carbonate ions ($CuCO_3$ and $Cu(CO_3)_2^{2-}$) and as Cu hydroxides complexes ($CuOH^+$, $Cu(OH)_2$, and $Cu(OH_3^-)$), consistent with Alberede (2004), and that modern seawater is almost saturated with respect to Cu-Fe oxide ($CuFeO_2$). In the anoxic Archaean system (pe = -5; Figures 6c and 6d) and at the proposed Archaean seawater pH of 6.5 (e.g., Halevy and Bachan, 2017), the two dominant Cu species are $Cu(S_4)_2^{3-}$ and Cu chloride complexes ($CuCl^+$, $CuCl_2$, $CuCl_4^{2-}$). In this system, Archaean seawater is oversaturated with respect to CuS and almost saturated with respect to Cu metal (i.e., pure, elemental Cu). However, when the oxidising potential (pe) of the Archaean model system is raised to 0 (slightly oxic; Figures 6e and 6f), the oxidation of S results in Cu chloride complexes becoming the dominant species, followed by Cu^{2+}, and the water is saturated in $CuFeO_2$.

Figures 6a – 6l: Speciation and saturation models for: modern seawater (6a and 6b), reducing Archaean seawater (6c and 6d), mildy oxic Archaean seawater (6e and 6f), Walker Lake (6g and 6h), Mono lake (above chemocline; 6i and 6j), and Mono Lake (below chemocline; 6k and 6l).

Mono Lake (surface)
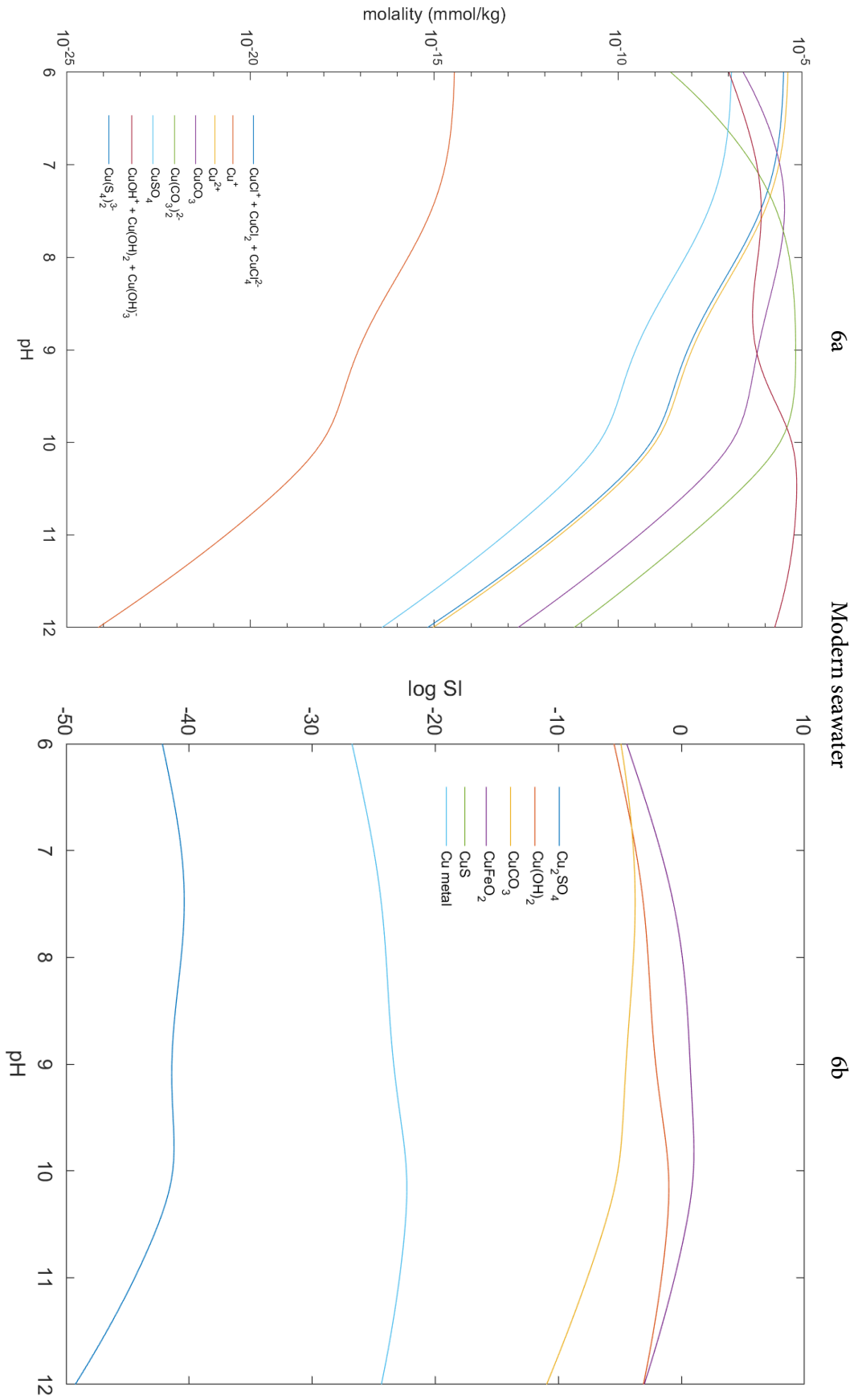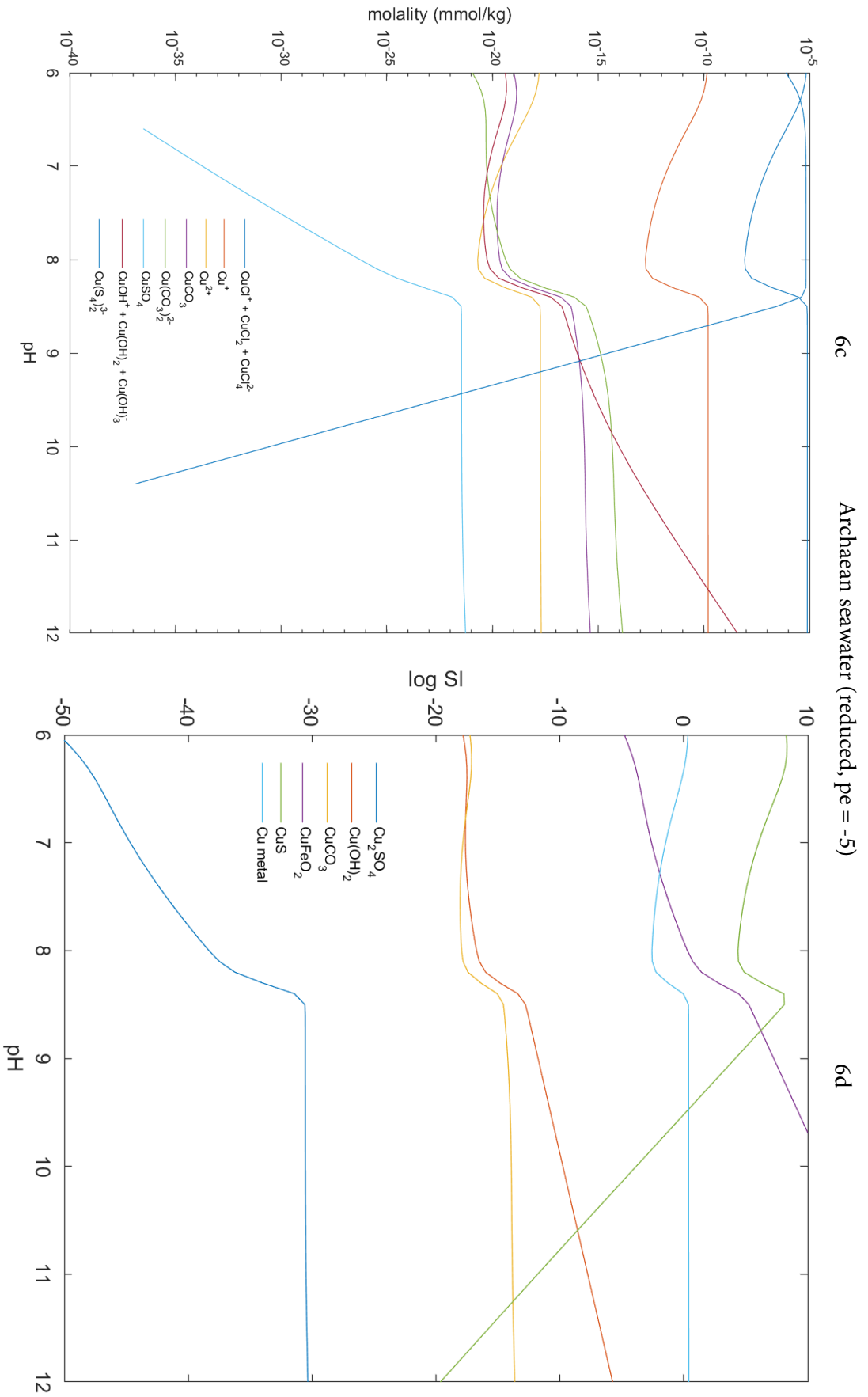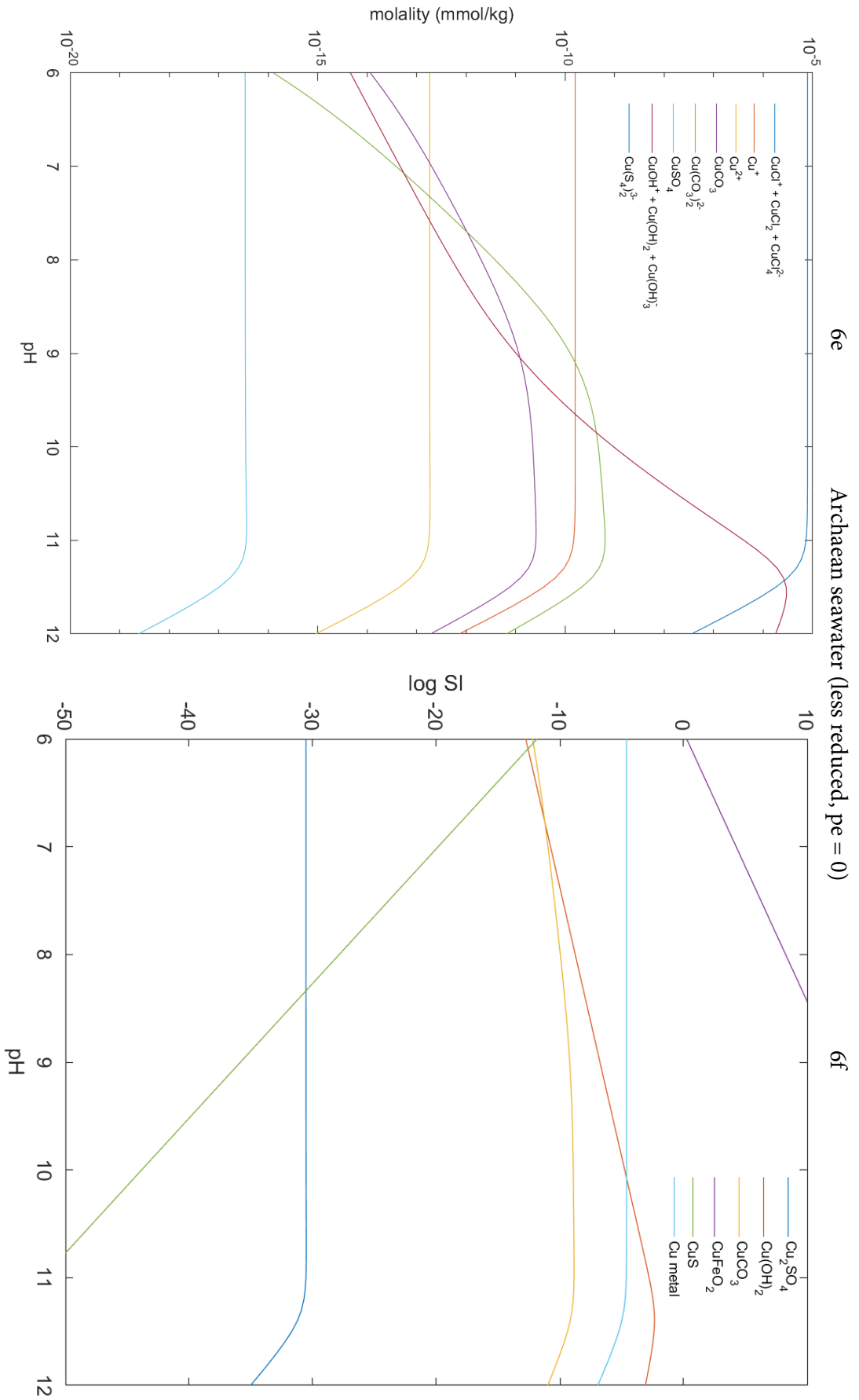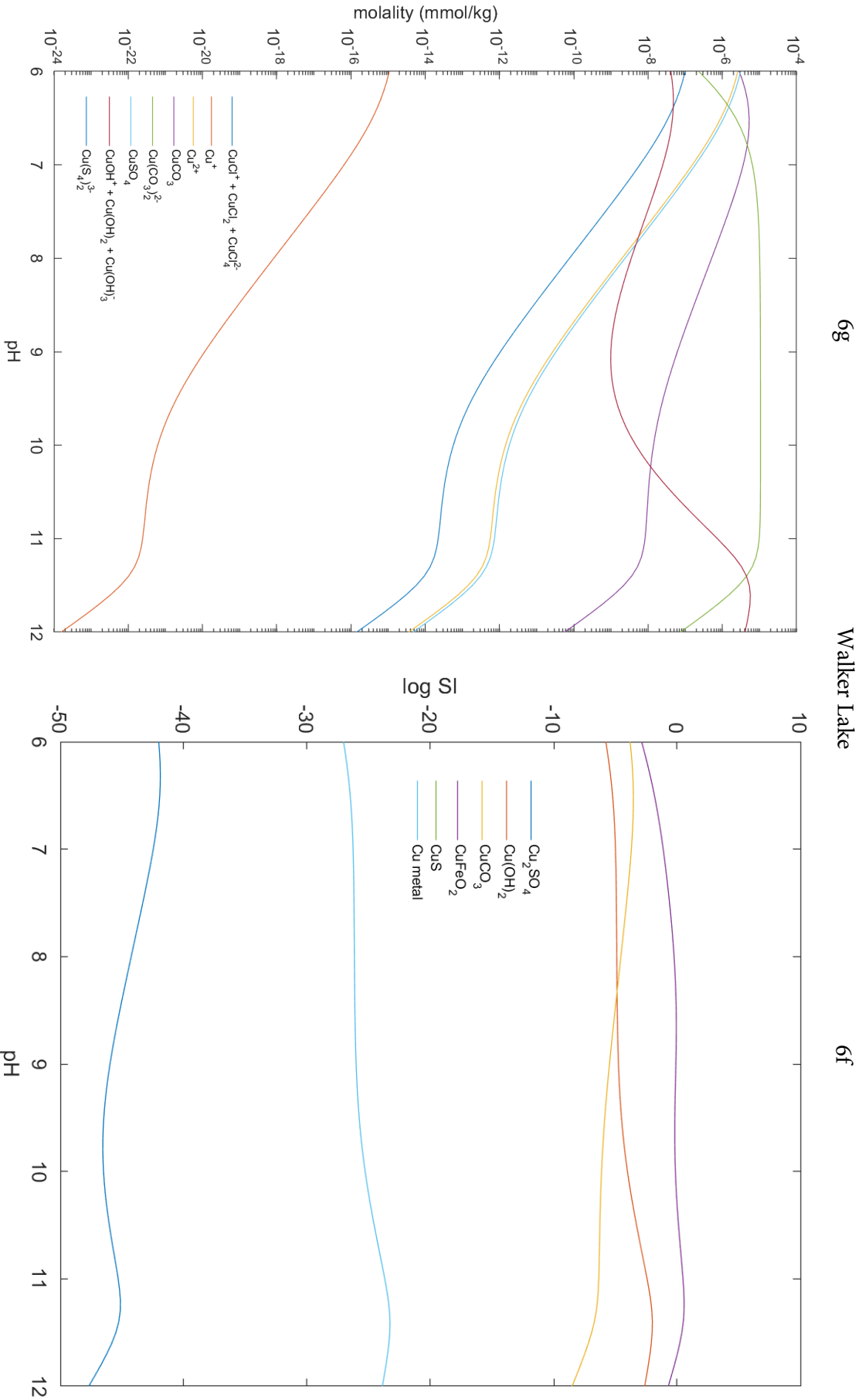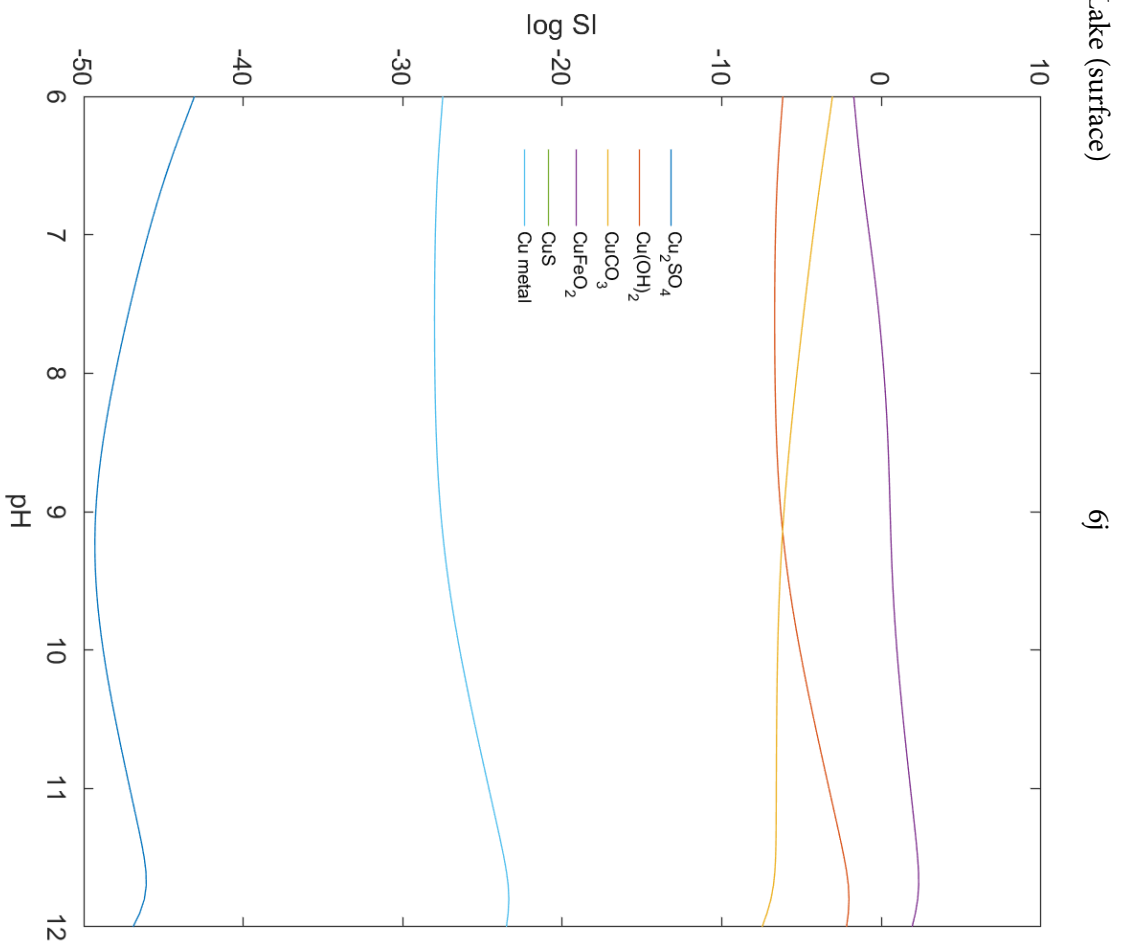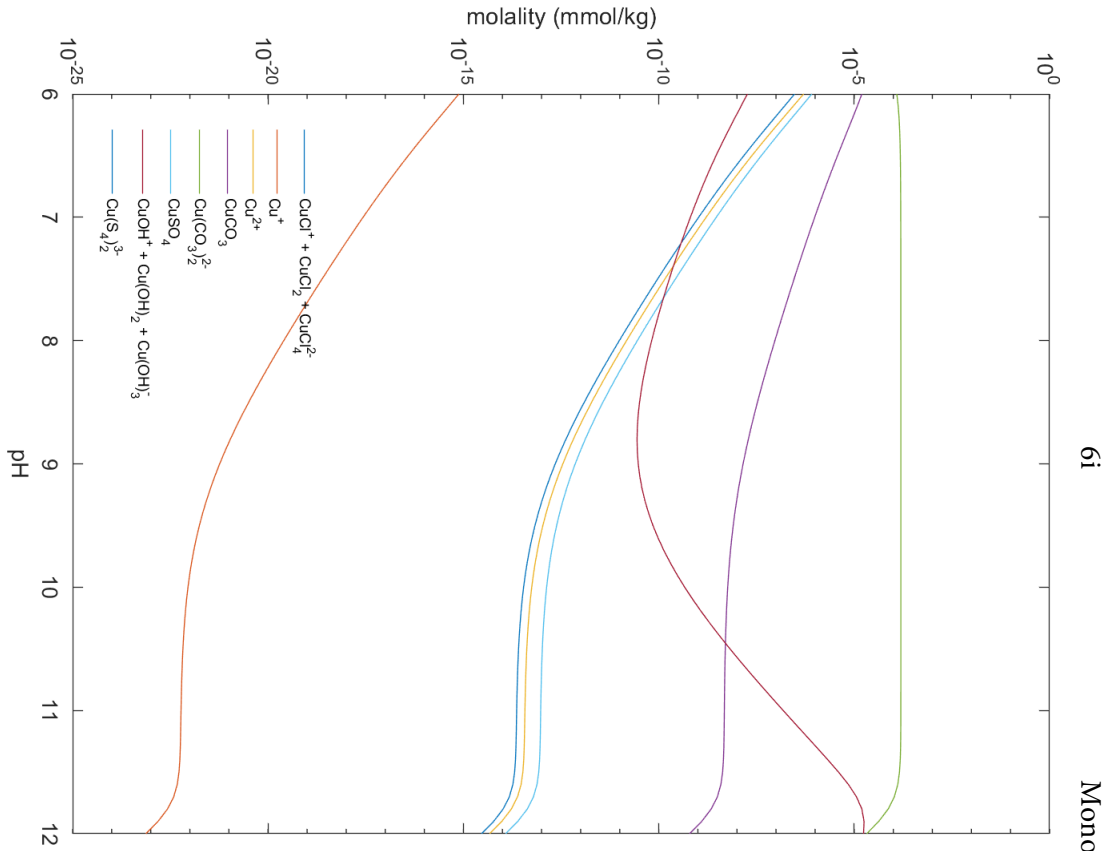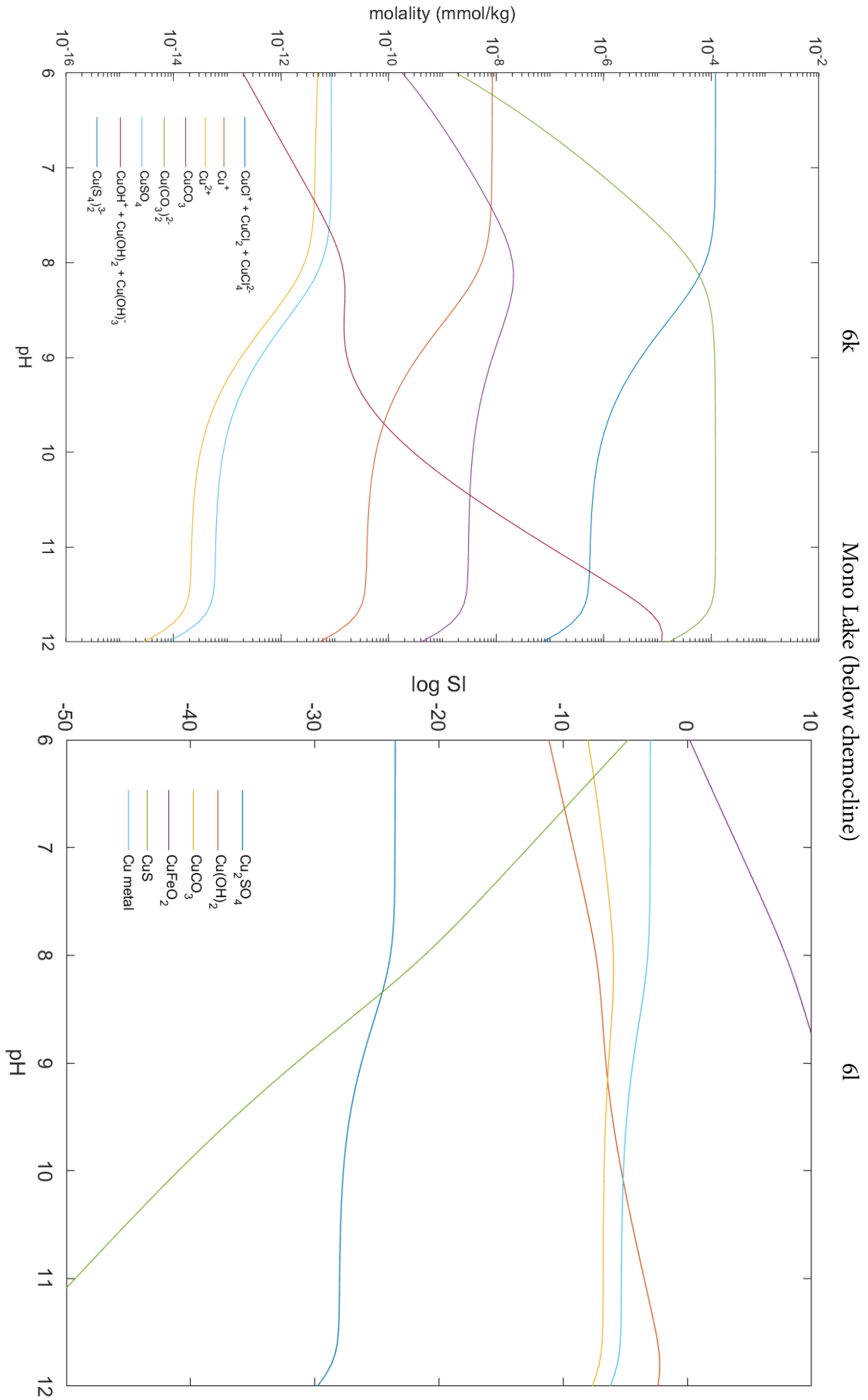
4.4. Discussion

This section details the processes which can impact Cu isotope compositions in sedimentary rocks, examining both pre- and post-depositional processes. Acknowledging that the samples analysed in this study were measured as 'bulk' sediment, it is likely that the Cu isotope composition of core SV1, as presented here, reflects a detrital origin. However, given the unique nature of the depositional environment, the age of the rocks, and the recent evidence for aerobic methanotrophy occurring in the Tumbiana (e.g., Stueken et al., 2017), other possible explanations are also explored.

4.4.1. Post-depositional alteration

Considering the age of the rocks analysed in this study, the effects of post-depositional alteration processes must be factored into any interpretations of geochemical data. The Tumbiana formation experienced estimated maximum temperatures of *c.* 300°C (e.g. Thomazo et al., 2009), although elsewhere within the Hamersley province these temperatures have been estimated to have reached between 100°C and 200°C (Yoshiya et al., 2012). These low temperatures have been used to provide robust arguments against significant resetting of organic C isotopes (e.g. Eigenbrode and Freeman (2006); Thomazo et al. (2009); Yoshiya et al. (2012); Stüeken et al. (2017)). As reported by Eigenbrode and Freeman (2006), while organic C isotope values of between -30‰ and -20‰ were previously considered to represent an alteration trend, the sediments of the Hamersley province with C isotope values of around -30‰ have a small (0.2%) TOC range, which is inconsistent with thermal alteration patterns. In addition, Yoshiya et al. (2012) analysed samples from both altered and un-altered samples to evaluate the influence of secondary alteration processes on organic C isotopes, finding that the alteration exhibited by these samples had a negligible impact on organic C isotope composition. Czaja et al. (2010) found no evidence for large-scale S redistribution, either via post-depositional fluid flow (ruled out by carbonate-derived $\delta^{18}O$ values reflective of those of unaltered Neoarchaean Carbonates) or secondary pyritization. The distribution of fine-grained disseminated pyrite observed by Thomazo et al. (2009) and Eigenbrode and Freeman (2006) has also been interpreted to indicate sedimentary-derived pyrite rather than formation via thermochemical S reduction (the latter of which accompanies hydrothermal alterative

processes). This is supported by the detailed analysis of 210 in-situ pyrite grains from the wider Fortescue Group, which strongly suggest primary pyrite formation via bacterial Fe reduction coupled to AOM (Yoshiya et al., 2012). Finally, within core SV1, the preservation of primary S-MIF signals within sulphide phases further demonstrates the limited impact of metamorphism and/or hydrothermal alteration on the preservation of these phases (Izon et al., 2015).

No apparent overprinting by redox or hydrothermal activity is evidenced by the trace metals for which enrichment factors (EF) were calculated either. Briefly, EFs represent the extent to which metals are enriched (or reduced) relative, in this case, to Archaean crustal values (e.g., Iqbal and Shah, 2015). Here, EFs were calculated using Fe concentrations as a reference metal for the following relationship: $EF = (C_x/C_{ref})_{sample}/(C_x/C_{ref})_{crust}$, where C_x is the average concentration of the metal of interest and C_{ref} refers to the mean concentration of reference element for normalisation. Conservative elements such as Fe, Al, Cr, Li, Mn, Sc, and Ti are often used for normalisation as their flux from crust rock sources is considered to be unform over long periods of time (Sutherland, 2005). In this instance, Fe was used as a conservative element rather than Cr or Mn because it is present in the highest abundance. Enrichment factors > 2 for V (EF = 0.56), Ni (EF = 0.54), and Cr (EF = 0.61) are consistent with those observed by Stüeken et al. (2017) and are reflective of a mafic Archaean crust and mafic sediment provenance (Rudnick and Gao, 2014; Taylor and McLennan, 1995). Additionally, low EFs for Cu (0.87) and Zn (1.07) argue against inputs from syn- or post-depositional hydrothermal fluids. Finally, Stüeken et al (2017) also note the absence of marked depletions in first row transition metals, arguing against metasomatic alternation, which is similarly observed in other geographic regions of the Fortescue group.

4.4.2 The palaeoenvironment of the Tumbiana Formation

While early work on the Tumbiana Formation argued for a supra- to intertidal shallow marine environment of deposition (e.g., Trendall and Blockley, 1970; Trendall, 1983; Morris and Horwitz, 1983; Packer, 1990; Thorne and Trendall, 2001), numerous studies have since suggested that the Tumbiana Formation actually represents an ancient series

of intermontane or ephemeral lacustrine environments (Buick, 1990; Buick, 1992). The evidence for large scale cross-stratification, limited lateral facies, and wave ripple crests throughout the succession has been used to support the interpretation of the Tumbiana Formation as representing the transgression of river/channel sediment deposits to coastal, shallow, and deep marine palaeoenvironment units (Thorne and Trendall, 2001). Typical marine sedimentary structures such as herringbone cross-stratification, desiccation cracks, beach rosettes, gypsum pseudomorphs, and climbing ripples are also detailed by Packer (1990), however no other studies have been able to confirm the presence of herringbone cross-stratification and the remaining aforementioned sedimentary structures are not unique to marine environments (Coffey, 2011). Buick (1990) noted symmetrical wave ripples (characteristic of a standing water body) and a lack of unidirectional current structures, along with scarce evidence for dolomitisation of carbonate sediments (indicative of low Mg/Ca burial brines) as evidence for a lacustrine environment of deposition. Further evidence for inhibited sulphate precipitation during evaporite paragenesis of carbonate and halite constrains this further to a possible ephemeral saline lake (Buick, 1992). Further studies have since supported this interpretation: Awramik and Buchheim (2009) suggest that the covariance of symmetrical ripples, desiccation cracks, abrupt lithological and facies changes, rare earth element (REE), and $^{87}Sr/^{86}Sr$ signatures that are distinct from contemporaneous marine signatures are lacustrine in origin. Similar REE patterns in the Tumbiana Formation are also noted by Coffey (2011), who proposes that the Tumbiana Formation carbonates formed in gently sloping alkaline ponds, lakes, or embayments reaching depths of ~30m.

Irrespective of whether the Tumbiana Formation reflects a shallow marine or ephemeral/shallow lacustrine environment, the dominant source of sediment input to the aqueous system likely possessed a significant control on elemental biogeochemical cycling. The system received frequent input of fine basaltic volcanic ash, evidenced by layers of fine and medium-grained basaltic tuff within stromatolite layers, draped over symmetrical wave ripples, and filling desiccation cracks (Stüeken et al., 2014). Evidence of frequent volcanism is concurrent with the hypothesis that the Tumbiana system formed in half-grabens which themselves formed via rifting of the Pilbara craton (i.e. Blake and Barley, 1992). It has thus been posited that the continued input of mafic

volcanic material into a restricted lacustrine basin would have greatly raised the pH of the water column and, indeed, modern alkaline lakes are largely associated with volcanism; the East African Rift Valley, Turkey, and the Western USA all possess examples of this (Stüeken et al., 2014). The combination of glassy basaltic tuff, carbonate, cyanobacteria (e.g., Buick, 1992), and evaporation (e.g., Buick, 1990; Awramik and Buchheim, 2009) within Tumbiana sediments suggest that the Tumbiana lakes were alkaline, with pH values exceeding 9 (Stüeken et al., 2014). This is further supported by the presence of heavy nitrogen (N) isotope ratios coupled with low N concentrations, which are believed to reflect the volatisation of NH_3 at high pH, a process which occurs in modern alkaline lakes (Stüeken et al., 2014). Finally, Fe speciation data shows that ferrous Fe was insoluble and that sulphide concentrations were low, which is also consistent with an elevated pH relative to marine systems (Stüeken et al., 2017). In modern alkaline lakes associated with volcanism, such as the lakes of the East African` Rift Valley, alkalinity develops due to the hydrolysis of volcanic rocks (mainly glasses and lavas), which generates high concentrations of Na^+, SiO_2^-, and total dissolved inorganic carbonate (DIC). Such lakes are characterised by their extremely high rates of primary productivity, attributed to the dense populations of cyanobacteria which dominate surface waters, and are thought to be more productive than freshwater lakes (e.g. Pecorianio et al., 2015).

Thus, the Tumbiana Formation represents a shallow water setting, with arguments for both marine and lacustrine depositional environments. Major inputs to the system came from volcanic ash rainout (e.g. Stüeken et al., 2014) and fresh riverine sediment (e.g. Arndt, 2011), which could have raised the pH of the water column. The depositional basin was likely restricted, and it is presumed that, while the marine basin would have been connected to a larger reservoir (Trendall and Blockley (1970), the lacustrine system was likely a closed, stagnant, evaporitic lake (Stüeken et al., 2017). As described in section 2.1 of this chapter, stromatolite structures are common throughout the Tumbiana Formation, the presence of which has been suggested to indicate that cyanobacteria were abundant primary producers within the lake. The limited (but present) sulphide levels observed by Stüeken et al. (2017) and Thomazo et al. (2009) suggest that H_2O was the most prevalent electron donor with the system (Stüeken et al., 2017). The presence of any sulphide (or Fe^{2+}) could support anoxygenic phototrophy, however $\delta^{56}Fe$ values measured

in the Tumbiana Formation reflect crustal average ($\delta^{56}Fe$ = ~0‰, where $\delta^{56}Fe$ = $^{56}Fe/^{54}Fe$ ratio expressed as parts per 1000 deviations relative to the standard IRMM-014) and Fe itself is bound to phyllosilicates, which indicates minimal Fe redox cycling (Czaja et al., 2010). As Fe-minerals such as carbonates, oxides, and sulphides are scarce within the Tumbiana Formation, it is also possible that the reduced solubility of Fe under alkaline conditions led to the retention of Fe in clays and zeolite minerals during volcanic ash alteration (Stüeken et al., 2017).

Regardless, organic input from neither cyanobacteria nor anoxygenic photoautotrophs can account for the extremely low $\delta^{13}C_{org}$ signatures within core SV1. Values of $\delta^{13}C_{org}$ isotopically heavier than -35‰ are generally indicative of the Calvin-Benson-Bassham cycle, a pathway used by many organisms including cyanobacteria (e.g., Zerkle et al., 2005). In the case of the Tumbiana Formation, $\delta^{13}C_{org}$ values ranging from -57‰ to -28‰ (-49‰ to -42‰ in core SV1) are interpreted as representing a combination of aerobic methanotrophy, which uses O_2 as an oxidant, and AOM, which most commonly uses SO_4^{2-} (although Fe oxides and nitrates have been known to be used by certain anaerobic methane oxidising archaea (ANME)) as an oxidant (Ettwig et al., 2016). It has also been observed that aerobic methanotrophy is favoured in systems sustained by mafic volcanism (e.g. Eigenbrode and Freeman, 2006; Czaja et al., 2010; Stüeken et al., 2017). The presence of ephemeral O_2 oases in water bodies prior to the GOE has been implied (i.e., Yang et al., 2019) and numerous studies of the Tumbiana Formation have proposed O_2 availability in shallow/surface waters (e.g. Czaja et al., 2010; Yoshiya et al., 2012; Stüeken et al., 2015; Stüeken et al., 2017) based, as previously noted, on the abundant stromatolites and limited evidence for Fe and S cycling in the shallow-water sections.

4.4.3 Depositional environment of the Tumbiana Formation in core SV1

Ratios of V/Cr and Ni/Co have previously been used as geochemical indices for the interpretation of bottom-water redox chemistry (i.e., Jones and Manning, 1993). Figure 7 shows these ratios as a function of depth for core SV1. The ratio of V/Cr has been proposed to reflect palaeo-oxygenation where post-depositional alteration can be ruled out: V/Cr ratios > 2 suggest anoxic depositional conditions with high aqueous H_2S

concentrations overlying sediment, while V/Cr ratios < 2 imply more oxidising conditions with H$_2$S only present within the sediment (Ernst, 1970). Vanadium is usually concentrated in sediment deposited under reducing conditions and may be bound to organic matter, while Cr usually exists within detrital clastic fractions of sediments and can substitute for Al within clays (Jones and Manning, 1993). Within core SV1, V/Cr ratios range between 0.75 – 2.03 (with an average of 1.06), arguing for an oxic to sub-oxic depositional environment for the Tumbiana formation. The ratio of Ni/Co has also been used to infer redox state, where high values are thought to reflect reducing conditions. Notably, diagenetic pyrites exhibit Ni/Co ratios > 1 (Jones and Manning, 1993). All Ni/Co ratios calculated for core SV1 are greater than 1, which could imply the presence of reducing conditions within the sediment. It should be noted, however, that while such ratios may provide some information regarding environmental redox conditions, Cr and Co are influenced by the abundance and type of detrital material, which can limit their use as reliable redox proxies (Tribovillard et al., 2006).
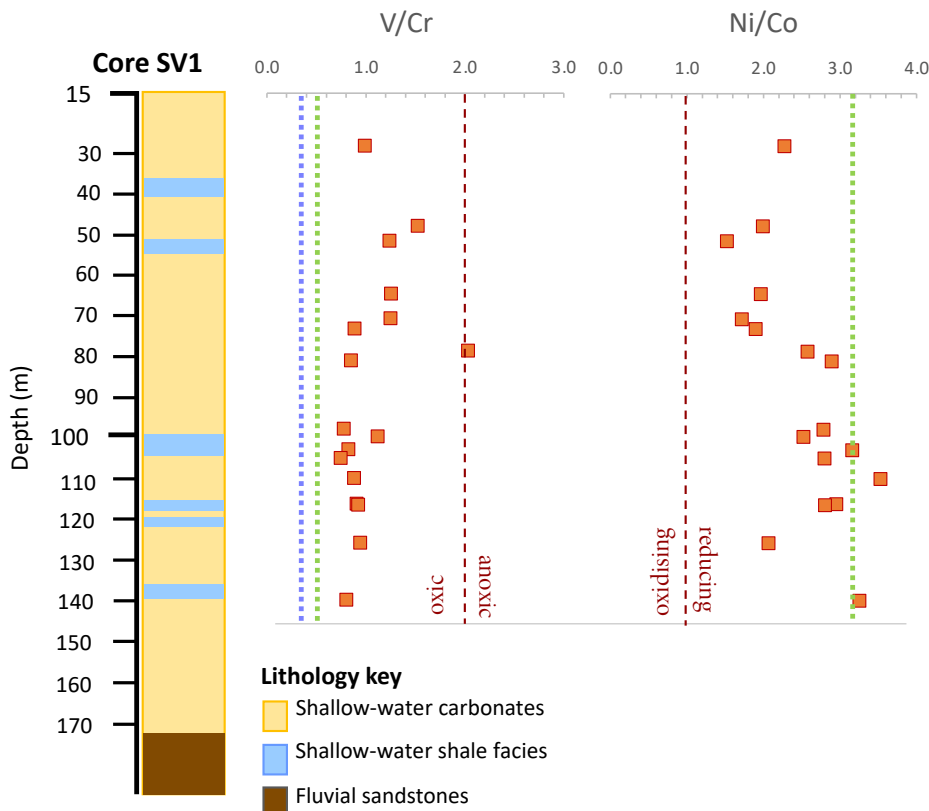
Figure 7: Core SV1 V/Cr and Ni/Co ratios. These ratios are proposed as reflecting redox conditions at the water-sediment interface (V/Cr) and sediment (Ni/Co) (e.g., Jones and Manning, 1993). Green dashed lines reflect average Archaean basalt V/Cr and Ni/Co ratios (Condie, 1992) and the blue dashed line reflects the average Kylena basalt V/Cr ratio; Ni/Co ratios are estimated at 7.40 (Stueken et al., 2017).

Here, common indicators of detrital materials (i.e., Ti and Al) were not analysed, and thus the Cr and Co data cannot be normalised to account for this. Nevertheless, these trace metal ratios provide some bearing on the depositional environment and are broadly concurrent with previous studies suggesting that the Tumbiana system may have been mildly oxic (e.g. Czaja et al., 2010; Yoshiya et al., 2012; Stüeken et al., 2015; Stüeken et al., 2017; see sections 4.2.1 and 4.4.2 of this chapter), with some oxygen present at the sediment-surface interface but none below, and that the dominant sedimentary inputs were derived from mafic/ultramafic volcanic activity. Aside from the correlations and ratios discussed, trace metal abundances within core SV1 are fairly stable, implying that no significant environmental or sediment source changes occurred throughout the deposition of this section of the Tumbiana formation. Copper abundances show an average of 65.1 ppm (range: 8.2 – 108.2 ppm) and do not significantly fluctuate down-core, consistent with those reported by Stüeken et al. (2017), which average at 63.5 ppm, and higher than the Cu abundances in core GKF01 (chapter 3, this thesis) which average at 20.7 ppm.

4.4.4. Copper cycling in the Tumbiana

Given the strong lines of evidence which support a shallow lacustrine system (Buick, 1990; 1992; Awramik and Buchheim, 2009; Coffey, 2011; Stüeken et al., 2014; Stüeken et al., 2017), Cu cycling within the Tumbiana under lacustrine conditions will be considered in the interpretation of the Cu isotope data generated in this study. For the purposes of discussion, the model systems will compare the behaviour of Cu under:

(i)   approximate **Archaean lacustrine** conditions (which are here based on Achaean seawater chemistry and pH (~6.5; Halevy and Bachan, 2017)).

(ii)   **high pH Archaean lacustrine** conditions (~9; Stüeken et al., 2017), which are based on the chemistry of two modern alkaline lakes (Walker Lake and Mono Lake).

It should also be noted that all constraints on the modern Cu cycle are based on the marine system and that, as far as I am aware, no studies of Cu cycling in modern or ancient lacustrine systems have been undertaken. Therefore, as a starting point for

discussion, it is thus assumed that all processes occurring in the marine system are also occurring in the lacustrine system.

4.4.4.1. Modern marine copper cycling

The Cu isotope composition of modern marine sediments is homogenous at ~+0.3‰ and isotopically light relative to seawater values, which range between +0.6 and +0.9‰ (Little et al., 2017); Figure 8 (reproduced from Chapter 1) shows the Cu isotope mass-balance in the modern ocean. These isotopically light Cu output fluxes are thought to be controlled by equilibrium isotope fractionation between (1) isotopically heavy Cu complexed to organic ligands and the isotopically light reactive Cu^{2+} species which is scavenged by particulates and delivered to the sediment or (2) the same ligand bound pool of Cu and isotopically light Cu sorbed to particulates, which deliver Cu to the sediment. In modern euxinic environments where nearly all Cu is removed from the water column (such as the Black Sea and at the sediment-water interface of sub-oxic to oxic continental margin sediments), the sediments still exhibit light (+0.3‰) Cu isotope compositions. This is believed to reflect the 'shuttling' of bioauthigenic Cu (i.e., light Cu) to restricted deeper basins, where it is then removed via sulphide precipitation (a process which favours the uptake of ^{63}Cu) (e.g. Little et al., 2017).

The mass-imbalance between the ocean and the sinks of Cu imply an unknown but isotopically light (relative to both the ocean and the sinks) source of Cu (~0‰) which is hypothesised to be hydrothermal input (e.g. Little et al., 2014) or possibly partial dissolution of continental sediments (e.g. Vance et al., 2008; Little et al., 2017; 2018). Given the lack of evidence for hydrothermal input within the Tumbiana formation (i.e., trace metal data from this study, Stüeken et al., 2017), this will not be considered in the discussion. Partial dissolution of continental sediments cannot be discounted, however, and will be considered within this interpretation.
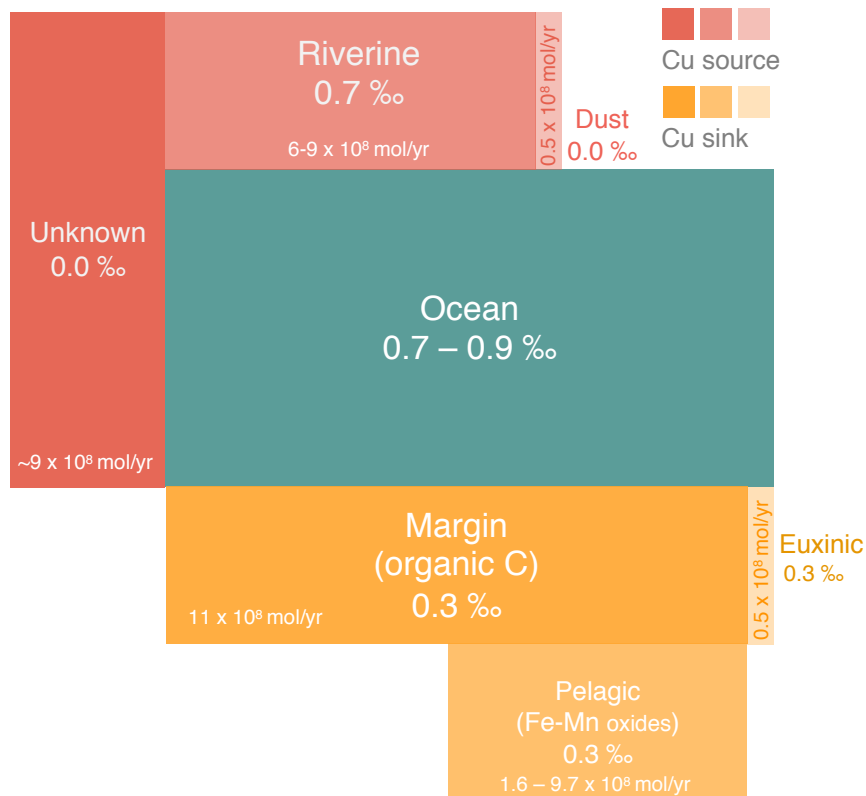
Figure 8: Copper isotope oceanic mass-balance (after Little et al., 2017). Boxes are shaded and scaled by magnitude, where their lengths and colour reflect their flux magnitude (mol/yr). Red boxes are sources, orange boxes are sinks.

4.4.4.2 Archaean lacustrine Cu cycling

Currently, there are no full constraints on the processes controlling Cu cycling in the Archaean and, as such, estimations of the Cu isotopic composition of Archean seawater are lacking. Analysis of the Cu isotopic composition of marine black shales across the GOE exhibit a shift from broadly negative δ^{65}Cu values to consistently positive δ^{65}Cu values, with a pre-GOE average δ^{65}Cu signal of ~ -0.3‰ and a post-GOE average δ^{65}Cu signal of ~+0.2‰, similar to that of modern sediments (Chi-Fru et al., 2016). This shift has been interpreted by the authors to represent waning BIF formation (ferric oxyhydroxides are associated with heavy Cu removal) and an increase in the delivery of oxidised Cu from continental sulphides (supplying heavy Cu). By implication, Archaean BIFs are thus expected to be isotopically heavy in Cu relative to Archaean sediments. However, a comprehensive analysis of Neoarchean BIFs (the Joffre iron formation from the Hamersley Supergroup and the Kuruman, Griquatown and Hotazel iron formations from the Transvaal Supergroup) has since shown that the average δ^{65}Cu signal for BIFs is

very close to 0‰ (the average $\delta^{65}Cu$ value for the Western Australia BIF is slightly negative at -0.24±0.22‰ but within analytical error). These data suggest a Cu source controlled largely by the input of volcanic ash in all four systems and show no evidence for Cu isotope fractionation during the deposition of Fe or Mn oxyhydroxides and, instead, likely reflect the isotopic composition of the Cu source (Thibon et al., 2019). Notably the $\delta^{65}Cu$ values obtained from the Transvaal BIFs by Thibon et al. (2019) are similar to the background $\delta^{65}Cu$ values measured in core GKF01 (0.05‰; Chapter 3, this thesis), which are identical to the $\delta^{65}Cu$ signal measured in this study and close to estimates for BSE (0.06‰).

Based on model (i), that the Tumbiana Formation reflects an Archaean lacustrine conditions, a schematic model of Cu cycling in such an environment is presented below (Figure 9). The system transects a depth of ~30m (i.e., the hypothesised depth of the Tumbiana Formation depositional environment; Coffey (2011)). The dominant inputs of Cu are riverine transport of weathered basaltic minerals and volcanic ash rainout, which are here assumed to carry BSE Cu isotope signatures as (a) the anoxic atmosphere would inhibit oxidative weathering, and (b) the V/Co, C/Cr, Ni/V, and Ni/Cr relationships from these analyses along with Al/Cu and Ti/Cu ratios from other studies (Czaja et al., 2010; Thomazo et al., 2009; Stüeken et al., 2017) further corroborate a volcanic/terrigenous sediment source to the system. Hence, the possibility of an isotopically fractionated Cu input is hereon ruled out and it is assumed that all Cu delivered to the system would arrive in its reduced form, either as chalcocite (Hao et al., 2017) or bound to volcanic ash deposits (with the latter pathway likely represented the dominant source of Cu to the system; Stüeken et al., 2017).
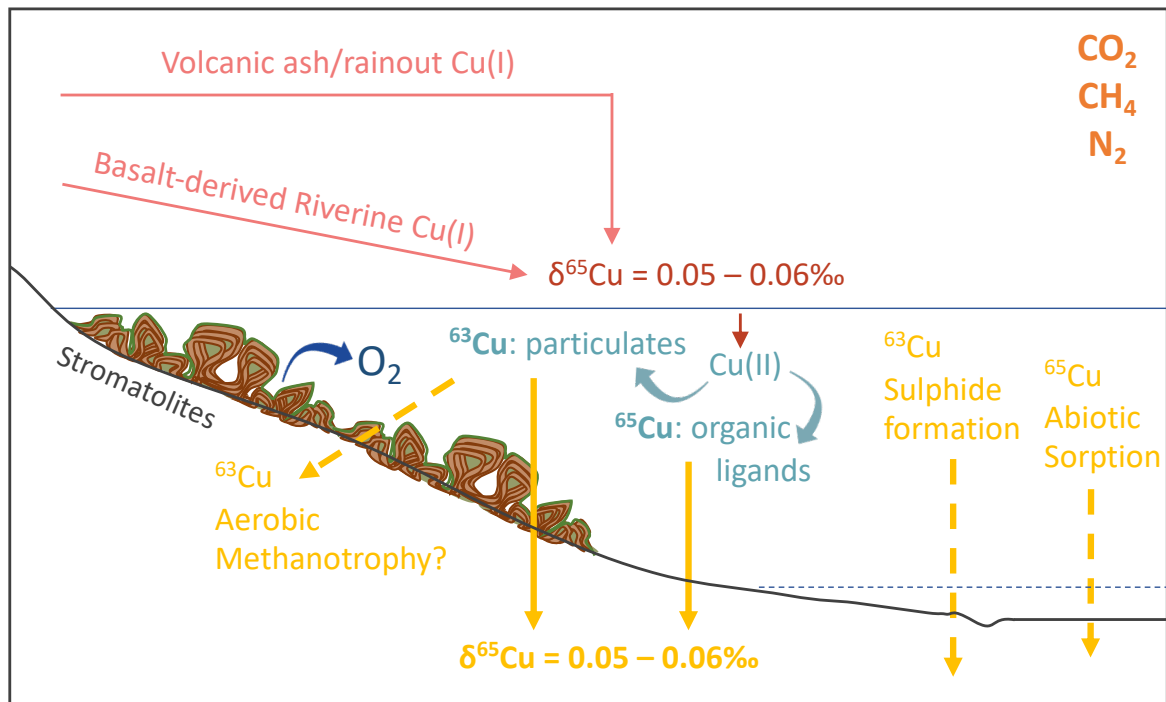
Figure 9: A schematic model representing the Cu cycling in the Tumbiana palaeoenvironment (under Archaean lacustrine conditions), where red text and arrows show Cu inputs, blue arrows and text show Cu in the water column, and yellow text and lines show possible Cu outputs (dotted lines), as well as the known isotopic output (solid lines).

Given the evidence for a mildly oxygenated water column (i.e., the abundant stromatolites coupled with evidence for low sulphate and Fe redox cycling (section 4.2, this chapter; Czaja et al., 2010; Yoshiya et al., 2012; Stüeken et al., 2015; Stüeken et al., 2017), as well as the V/Cr ratios derived from this study (Figure 6)), the schematic model includes an assumed oxygenated surface layer, which would lead to the oxidation of the mineral-bound, reduced Cu(I), releasing Cu^{2+} into solution. In contrast to the ~2.5 Ga system presented in Chapter 3, which presents a completely anoxic system in which surface water Cu concentrations were low, surface water Cu concentrations in the Tumbiana were likely to have been relatively high (Hao et al., 2017). Referring to speciation models 6e and 6f, at pH ~6.5 the dominant dissolved Cu species are likely to be Cu-chlorides and Cu^{2+}, and the water column is projected to be over-saturated with respect to $CuFeO_2$, as is the case for modern seawater.

In such a system, the primary fractionation mechanisms for Cu isotopes are therefore hypothesised to have been similar to the modern ocean processes: ^{65}Cu preferentially

being attached to organic ligands and ^{63}Cu either preferentially sorbing to or being scavenged by particulates and being delivered to the sediment. Scavenging of Cu by particulate organic matter is also believed to play a considerable role in the delivery of Cu to the sediment (i.e., Little et al., 2017). In the modern marine setting, phytoplankton produce ligands which regulate free Cu^{2+} concentrations; up to 99.9% of marine Cu is organically complexed (Bruland et al., 2014). Models of Archaean seawater suggest low abundance of organic ligands (see Stüeken, 2020), indicating (by implication) a limited influence of ligands on Cu isotope fractionation in a marine setting. However modern, closed, evaporitic lacustrine systems have higher dissolved organic content (DOC), and it is therefore possible that organic ligands could have played a larger role in similar ancient environments. Modern marine outputs of Cu also include Fe-Mn crusts and organic-rich sediments, both of which exhibit a homogenous Cu isotope composition of +0.3‰; Any Cu isotope fractionations associated with these outputs are thought to be the result of sulphide formation, i.e., the preferential incorporation of ^{63}Cu into FeS_2 during the reduction of Fe in the sediment (e.g., Little et al., 2014; 2017).

4.4.4.3 Archaean high pH lacustrine Cu cycling

When interacting with water, Cu forms free metal cations, variable soluble complexes, and insoluble particles or precipitates. The distribution of these Cu species in natural aqueous environments is controlled by the major dissolved ion content, alkalinity, and redox chemistry of the water. Figure 10 shows a simple Eh/pH diagram of the Cu-O-H system (Brookins, 1988). At low pH, Cu is soluble and exists dominantly as Cu^{2+}. Increasing pH promotes the formation of Cu_2O (cuprite), CuO (tenorite) and CuO_2^{2-}. (Brookins, 1988). At intermediate pH levels in natural environments (~6.5 – 12) Cu most frequently precipitates out of solution as Cu-hydroxide ($Cu(OH)_2$) and Cu carbonate ($CuCO_3$). Copper will also form complexes with common anions such as SO_4^{2-}, OH^-, PO_3^{4-}, HCO_3^-, NO_3^-, and CO_2^{3-} (e.g. Cuppett et al., 2006), but is almost always predominantly complexed to organic molecules when these are present (e.g. Moynier et al., 2017). For example, in a modern high-elevation alkaline lake (pH *c.* 8; Pacheta Lake, Arizona) Cu is chiefly found to be complexed to insoluble organic ligands, with around 17% of total Cu contained within amorphous insoluble Fe-Mn hydroxides and 5% of Cu bound to sulphide phases (Williamson and Parnell, 1994). Thus, similar to in marine systems, the

109

above inorganic species are only relevant with respect to the small, inorganic (and presumably bioavailable) pool of Cu^{2+} (Little et al., 2014b). All alkaline lakes are characterised by pH values greater than 9, a chemical composition in which Na^+ is the main cation, and by the presence of high HCO_3^- and CO_3^{2-} contents. In some instances, the main anionic species may be Cl^- or SO_4^{2-}, although the latter is rare (Percoraino et al., 2015).
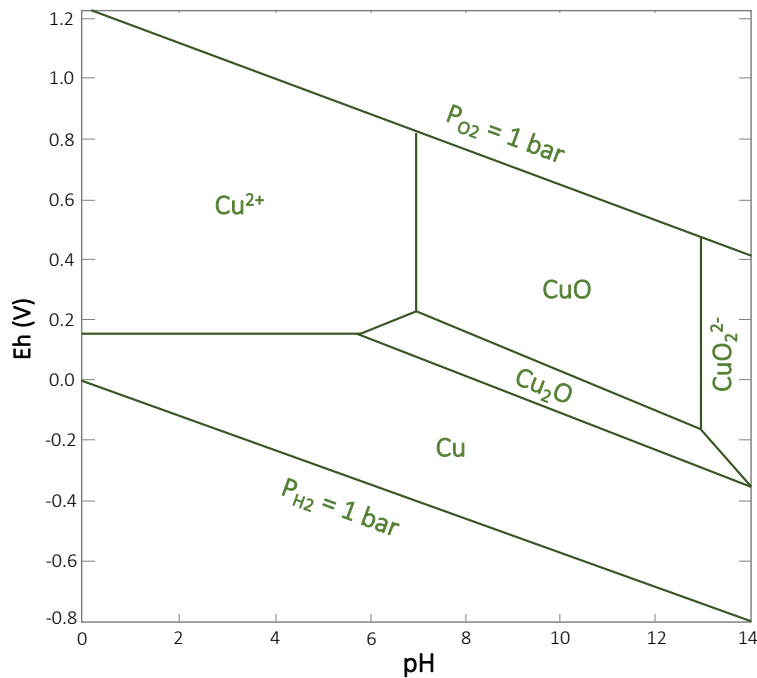
Figure 10: Eh/pH diagram of the Cu-O-H system at 25°C (redrawn from Brookins, 1988).

Other modern alkaline lakes (Mono Lake – California, Walker Lake – Nevada, Great Salt Lake – Utah) paint a complicated picture of Cu distribution, in which local physiochemical conditions and bottom brine compositions play a large role in the chemistry of Cu and other trace metals. Within the water column, the oxygen concentration, pH, sulphate concentration, and location of the chemocline all significantly impact trace metal geochemistry. Further to this, the location of organic matter degradation (along with the oxidants involved) and the location of the reductive dissolution of metal oxides exert further control on the behaviour and distribution of trace metals during early diagenesis (Domagalski et al., 1990). For the purposes of this study, Walker Lake and Mono Lake are used as two possible models for Cu behaviour in a hypothetical alkaline Tumbiana Lake. Both models assume predominant input from

riverine Cu transport, noting that in the Tumbiana system Cu was also supplied via volcanic ash rainout. Both input mechanisms supply the system with reduced Cu(I).

Walker Lake – an unstratified, closed basin alkaline lake - has a pH of 9.2 and a depth of ~33m. The combination of oxygenated water and high pH leads to low trace metal concentrations throughout the water column; fine particulate oxides and organic matter scavenge the majority. Near the sediment-water interface, metals are tightly bound to oxides. Below the sediment-water interface, the reductive dissolution of Fe and Mn oxides and the subsequent release of trace metals occurs. The low sulphide concentrations which persist throughout the lake result in a higher proportion of Cu-organic ligand complexation relative to sulphide precipitation and early diagenetic pyrite formation. Within Walker Lake sediments, organic ligands (humic complexes) represent the dominant sink of Cu (Domagalski et al., 1990).

Mono Lake has a chemically stratified water column, a pH of 9.65, and a depth which ranges from 30-33m with a chemocline present at 15-18m. As with Walker Lake, the high pH and oxygen concentration leads to low trace metal abundances, however sulphate concentrations increase below the chemocline, and are four times higher at the sediment-water interface. Concentrations of Cu are greatest near the chemocline and bottom waters, where Fe and Mn oxides begin to dissolve and FeS precipitation occurs. These processes increase within the upper layers of sediment, where Cu is mobilised and released via reductive dissolution of Fe-Mn oxides and organic matter. Once mobilised, as with Walker Lake, Cu is taken up via sulphide formation or by complexation to organic ligands. However, while the low sulphate concentrations promote extensive Cu-ligand complexation in Walker Lake, the high sulphate concentrations with Mono Lake lead to higher levels of Cu-sulphide formation (Domagalski et al., 1990). Figure 11 presents a schematic diagram illustrating these processes with hypothesised Cu isotope partitioning added. The speciation relates to the small, free pool of Cu which is not bound to ligands or sorbed to Fe and Mn oxides and is discussed below.

Speciation models and mineral saturation calculations 6g and 6h (Walker Lake) predict Cu speciation and mineral saturation over a range of pH values for the small, free Cu^{2+} on

pool a Walker Lake-like system. Like modern seawater, at pH 9.2, the dominant species is Cu carbonate, which remains fairly stable across pH ranges because of the very high alkalinity of these lake systems. However, while modern seawater Cu carbonate speciation is evenly split between $Cu(CO_3)_2^{2-}$ and $CuCO_3$, $Cu(CO_3)_2^{2-}$ predominates in Walker lake. Copper hydroxide complexes, Cu^{2+}, Cu sulphate, and Cu chloride concentrations decrease with increasing pH. At pH 9.2, the lake water is almost saturated with respect to $CuFeO_2$.

Mono Lake has been modelled twice to account for conditions above and below the chemocline. Models 6i and 6j, which show Cu speciation and mineral saturation above the chemocline, are similar to those of Walker Lake, where $Cu(CO_3)_2^{2-}$ is the dominant species, although at lower concentrations (10^{-4} mmol/kg, whereas Walker Lake has $>10^{-5}$ mmol/kg), and at pH 9.65 the lake water is saturated with respect to $CuFeO_2$. Below the chemocline (i.e., models 5k and 5l), at pH above ~8, Cu speciation remains similar, although below pH ~8, Cu chlorides are the foremost Cu species. Unlike Walker Lake, mineral saturation state changes; the water is highly oversaturated with respect to $CuFeO_2$, although Cu metal, Cu hydroxide, and Cu carbonate are all present in relatively high quantities.
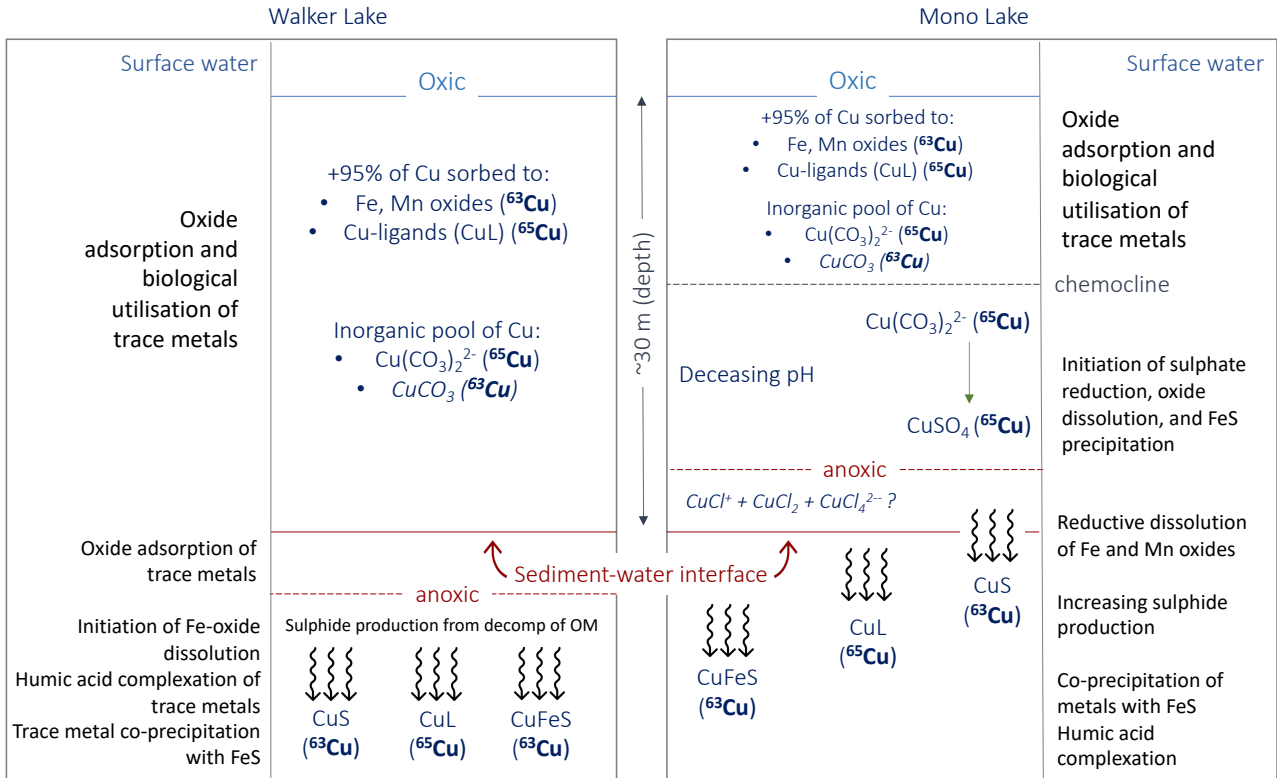
Figure 11: The hypothesised cycling of Cu and Cu isotopes in Walker Lake and Mono Lake, based on data from Domagalski et al (1994) and the speciation models presented in this thesis.

It has been demonstrated that Cu associated with the $Cu(CO_3)_2^{2-}$ and $CuSO_4$ complexes is isotopically heavier than the free Cu^{2+} ion (+0.6‰), while the Cu in precipitated carbonates (either in $CuCO_3$ or in solid solutions within carbonates of other elements) are predicted to be isotopically light with respect to dissolved Cu (by around -0.62‰) (Figure 12, redrawn from Fujii et al., 2013). At pH 8.22 and in the absence of carbonates, $Cu(OH)_2$ is isotopically heavier than bulk seawater, however in a system with carbonate, this isotopic fractionation is minimal at +0.02‰ (Fujii et al., 2013)
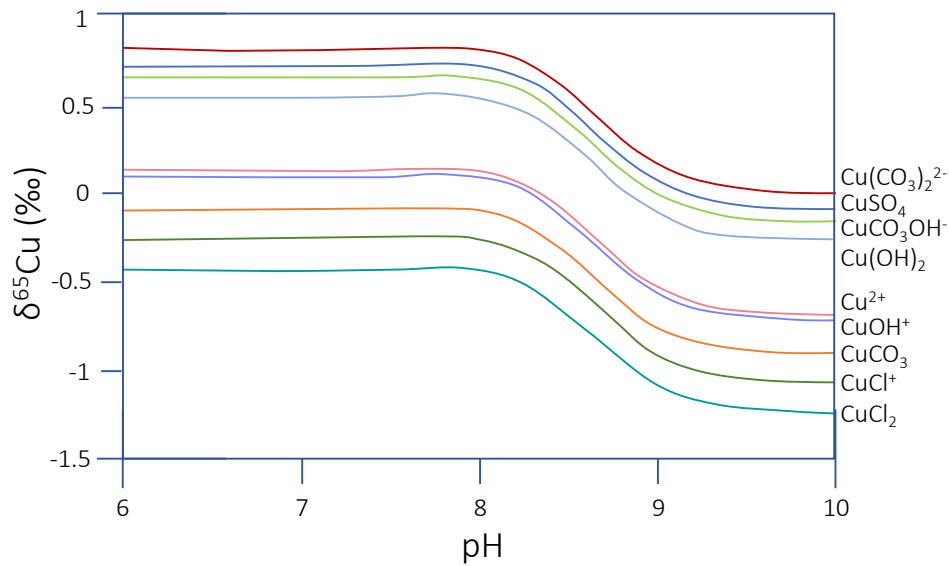
Figure 12: Copper isotopic variations as a function of pH for aqueous Cu(II) species (modified from Fujii et al., 2013).

These speciation models show that, even at the boundary of oxidising and reducing conditions (i.e., below the chemocline of Mono Lake) the dominant Cu species remains $Cu(CO_3)_2^{2-}$, unless the pH is below 8. At pH 9, this species has an isotopic composition close to bulk solution as it is by far the most abundant species (Figure 12), indicating that the remaining inorganic pool of Cu is not being isotopically fractionated by this. However, despite the high alkalinity of the system, the only mineral which is oversaturated in all these systems is $CuFeO_2$, for which no information on Cu isotope fractionation exists. The broader implication of this is that, in these systems, the dissolved Cu pool is either: i) not a source of tangible Cu isotope fractionation and that Cu-ligand complexation and Cu scavenging by Fe and Mn oxides remains the dominant control on aqueous Cu isotope fractionation, or ii) if there are no constrainable biological processes fractionating $\delta^{65}Cu$ and thus inorganic precipitation is more important, either $CuFeO_2$ precipitation does not preferentially incorporate one Cu isotope over the other or all aqueous species are homogenised within the sediment. Iron minerals such as carbonates, oxides, and sulphides are scarce within the Tumbiana formation (e.g., Stüeken et al., 2017), suggesting the re-partitioning of Fe into sulphides within the sediment, as observed within both the Wilson and Mono lake models.

4.4.5 Possible Cu isotope fractionation mechanisms

From this point forwards, two possible environments of deposition for the Tumbiana formation are considered, in order to explore how knowledge of this ancient system would affect the interpretation of the Cu isotope data presented here.

1) Alkaline lake. Based on the trace metal data for this section which indicates oxygen at the sediment-water interface, the Wilson Lake model is used going forward as the probable analogue for a lacustrine high-pH Tumbiana Formation (speciation models 6g and 6h; Figure 11).

2) 'Conventional' Archaean lacustrine setting (modelled on Archaean seawater). Here, Cu speciation is considered within the context of speciation models 6e and 6f (mildly oxidising).

Comparing these two possibilities, the principal differences which may impact Cu cycling are Cu speciation where, under conventional Archaean settings, Cu-chloride species dominate the water column, and the water is oversaturated with respect to $CuFeO_2$. In contrast, high pH conditions lead to a water column dominated by $Cu(CO_3)_2^{2-}$ and $CuCO_3$ and a water column mildly saturated in $CuFeO_2$. In both systems, the majority of Cu in solution would still likely be sorbed to- or scavenged- by Fe-Mn oxide particulates (preferentially taking up ^{63}Cu) or complexed to organic ligands, which take up ^{65}Cu.

These prevailing environmental conditions can, in turn, lend themselves to three leading hypotheses which may account for the $\delta^{65}Cu$ signal recorded in the Tumbiana formation. Explored in detail below, these are: (1) the dominant processes which were cycling Cu in this system did not produce appreciable Cu isotope effects; (2) any processes occurring which did fractionate Cu isotopes have since become obscured by sediment homogenisation; (3) the dominant processes that were cycling Cu in this system were fractionating Cu isotopes but proceeded to completion. The latter hypothesis could imply two further possibilities: (2a) that the Tumbiana therefore represents a closed/restricted basin with relatively low levels of Cu, or (2b) that there were high rates of Cu cycling (potentially driven by AMO) in an open and/or non-Cu-limited environment (i.e., Cu is

115

taken up by, but not an integral part of, some process). These hypotheses are considered below within the context of both Archaean lacustrine and Archaean high-pH lacustrine conditions described above.

1) Dominant processes cycling Cu in this system did not produce appreciable Cu isotope effects

The simplest explanation of the BSE-like $\delta^{65}Cu$ values preserved throughout core SV1 is that no processes were significantly fractionating Cu isotopes within this marine/lacustrine system, and that the sedimentary $\delta^{65}Cu$ is thus chiefly governed by the $\delta^{65}Cu$ signature of the inputs. In core GKF01 (Zavina-James et al., *in review*; Chapter 3, this thesis) sedimentary $\delta^{65}Cu$ values deviate from a BSE background state to ~-0.6‰. Ruling out potential other fractionation mechanisms, this signal is attributed to uptake by aerobic methanotrophic bacteria – an interpretation which suggests that no other processes besides aerobic methanotrophy result in a Cu isotope fractionation in the Cu delivered to the sediment. By extension, it is possible that similar processes were governing Cu cycling in both the Tumbiana Formation and the Upper Nauga Formation, with the former system lacking uptake by aerobic methanotrophs. As such, if this hypothesis is correct, it could directly imply that aerobic methanotrophy was not occurring in the Tumbiana Formation at 2.7 Ga. However, unlike the Upper Nauga Formation, the Tumbiana Formation depositional environment was likely mildly oxic, which precludes the occurrence of potential redox-related Cu isotope fractionations in the water column. Therefore, the respective systems cannot simply be transposed onto one another and treated in a similar fashion, and the implications of a less reduced water column are explored below.

If this hypothesis – a lack of Cu isotope fractionation in this system – is correct, it has the interesting implication that several other processes which are known to fractionate Cu isotopes in modern environments can be ruled out, or other constraints can be placed on Cu cycling within this system. These processes are now dealt with in turn.

Cu sorption to particulates/mineral surfaces. Based on this hypothesis, the Cu isotope data presented here could negate any significant sorption or scavenging of Cu in the Tumbiana environment. Major Cu precipitates in the modern ocean are chalcocite and ferrite-Cu (e.g. Stüeken et al., 2017), both of which are associated with an enrichment in ^{63}Cu (e.g. Moynier et al., 2017); scavenging and sorption of Cu by Fe-Mn oxides and scavenging of Cu by particulate organic matter constitute a significant mechanism by which Cu is transported to the sediment. Thus, it is anticipated that if these processes were governing Cu isotope behaviour, the isotopic record would also be enriched in ^{63}Cu. Given that this is not the case, within the framework of this hypothesis, the environment of deposition must have been such that Cu delivery and removal was such that sorption can be ruled out. This would be the case if, for example, some other process such as ligand formation dominated.

Biological Cu cycling that does not impart an isotopic fractionation. It has also been recently demonstrated that photosynthesising cyanobacteria, for which Cu is a key micronutrient, are not associated with any net Cu isotope fractionation in seawater (Yang et al., 2020). If all other Cu cycling processes can be effectively ruled out, then these data could be explained by cyanobacterial Cu cycling. There is a weak correlation between Cu and TOC in core SV1 (R^2 = 0.3; Figure 3) which is not reflected in the relationship between δ^{65}Cu (R^2 = 0.05; Figure 4), indicating a moderate association between Cu and TOC that is not reflected in the isotope record. These relationships could therefore indicate Cu uptake by photosynthesising cyanobacteria if these organisms were indeed present in the Tumbiana Formation.

The incorporation of Cu into sulphide minerals. Copper sulphide formation has been shown to fractionate Cu isotopes, preferentially incorporating ^{63}Cu (Asael et al., 2006), however the lack of a notable correlation between SV1 δ^{65}Cu values and S concentrations (Figure 4) argues against an association between Cu and sulphides in this instance. Under both conventional Archaean pH lacustrine conditions and high pH lacustrine conditions, this, along with the BSE composition of the Cu preserved in this part of the Tumbiana formation, implies a minimal role of sulphide formation in Cu (isotope) cycling.

117

Cu isotope fractionation between dissolved Cu species. The modelled Cu speciation for oxic conventional Archaean conditions (i.e., pe = 0, pH = 6.5) shows that Cu-chlorides are the dominant aqueous Cu species. It is not currently known whether CuCl formation fractionates Cu isotopes, which means it is not possible to assess the degree to which this aspect of Cu speciation could result in an isotopic fractionation, or otherwise. If the speciation models are indeed applicable to the Tumbiana environment, then the lack of Cu isotope fractionation compared to BSE could imply that the formation of CuCl complexes in solution are not associated with an isotopic fractionation. Modelling or experimentally determining whether or not CuCl complexes are associated with an isotopic fractionation is clearly a priority for future research given than these dominate Cu speciation in many environments.

Delafossite precipitation. Within an alkaline setting, the mineral saturation calculations predict that this system is oversaturated with respect to delafossite ($CuFeO_2$), such that this may be the dominant inorganic means by which Cu is removed. It is currently not known whether the formation of this mineral is associated with a Cu isotope fractionation; the Cu isotope data generated in this study could be explained by the precipitation of $CuFeO_2$ within the water column if such a process does not lead to Cu isotope fractionation from BSE values. However, this relatively rare mineral has not been described in relation to any modern or ancient alkaline lake setting. One possibility is that reduction of $CuFeO_2$ occurs in the sediment such that it is not preserved, but a more likely explanation is perhaps that the PHREEQC speciation models do not consider Cu incorporation into other mineral phases. For example, a high degree of Cu incorporation into Fe precipitates could result in this being the dominant inorganic sink of Cu. Given that these are associated with a Cu isotope fractionation, this hypothesis would seem unlikely.

To summarise, in either an alkaline or Archaean seawater pH setting, the most likely implication of this hypothesis is that, in the absence of a Cu isotope excursion associated with aerobic methanotrophy, anaerobic methanotrophy remained the dominant CH_4-assimilation pathway within the system at this time. This can be drawn from the fact that the other processes discussed (Cu chloride and delafossite precipitation) are currently

under constrained or, in the case of Cu-sulphide precipitation, are unlikely to have been occurring within a suboxic water column. However, aerobic methanotrophy is not solely dependent on Cu, and in the Upper Nauga Formation it is hypothesised that increased CH_4 concentrations lead to Fe-dependent aerobic methane cycling; the Fe-containing sMMO enzyme is expressed at high CH_4 conditions (e.g., Semrau et al., 2011; Zavina-James et al., *in review;* Chapter 3, this thesis). The $\delta^{65}Cu$ excursion in core GKF01 occurs at a point where $\delta^{13}C_{org}$ values are (relatively) heavy (~-33‰) and it is hypothesised that CH_4 production is not at its 'peak' at this point. In contrast, $\delta^{13}C_{ker}$ values throughout core SV1 maintain extremely light values of ~-45‰, which could imply that higher levels of CH_4 production and consumption are consistently occurring in the Tumbiana Formation than in the Upper Nauga Formation. As such, while the BSE signatures of the $\delta^{65}Cu$ record of SV1 could imply no biological Cu cycling, and therefore no aerobic methanotrophy, it is also possible that consistently higher levels of CH_4 lead to an environment where Fe-dependent sMMO-expressing aerobic methanotrophs dominate.

2) *Copper isotope fractionations were obscured by homogenisation within the sediment*

The Tumbiana samples analysed in this study were homogenous bulk-rock powders and therefore all Cu isotope measurements reflect the bulk isotopic composition of the sediment. As the Cu isotope data from core SV1 do not deviate from BSE, it is possible that if all Cu isotopes were being fractionated by the processes discussed above, any individual processes may not be discerned by bulk measurement. In this scenario, even if processes such as ligand formation, scavenging, and biological uptake were fractionating Cu isotopes, the overall homogenised sediment signal would reflect the input signal (i.e., BSE). There are two distinct ways in which this could occur. The first is the homogenisation of several processes that fractionate dissolved Cu, and the second is that a fractionation of dissolved Cu is occurring and preserved in a sedimentary phase, however the signal measured here is that of the bulk sediment, which has a signature controlled by volcanic detrital input. Such effects are also more likely in a shallow, closed basin with minimal lateral transport, further supporting the hypothesis that the Tumbiana Formation reflects a shallow lacustrine basin.

If the system was characterised by processes that impart a Cu isotope fractionation, but these are obscured in the sediment by recombination of different phases, then this information could be used to place additional constraints on the nature of the system. Lacustrine deposits of an Eocene lake (Eastern Utah and Western Colorado) show that in a closed shallow basin, lateral transport of organic materials is generally fairly uniform. As water depth and basin size increases, the lateral transport of organic matter from marginal shelves towards the central basin increases (Johnson et al., 2018). Therefore, in a smaller, shallow, closed environment (such as that envisaged for the Tumbiana) organic matter would not necessarily be laterally transported, i.e., ligands could preferentially form with the heavy Cu isotope but ultimately end up in the sediment with ^{63}Cu derived from processes acting in the opposite direction. However, if the Tumbiana was a larger and more complex lacustrine system with a deeper central basin (or, indeed, a marine basin), it is anticipated that organic matter (and with it, the ^{65}Cu fraction) could be removed to sections of the lake not recorded by core SV1. Shuttling of organic material with a heavy Cu isotopic composition to a deeper part of the basin would of course mean that recombination of different Cu bearing phases in the sediment is no longer possible, which would rule out this hypothesis. Therefore, if the reason for the BSE Cu isotope values of this section is because of the mixing of different organic and inorganic components in the sediment, it provides further evidence for a closed, lacustrine environment of deposition for the Tumbiana Formation.

3) *Any processes that are significantly fractionating Cu isotopes are proceeding to completion in this system*

The final possibility which could conceivably account for the BSE-like Cu isotope signal in SV1 is that any process(es) that are fractionating Cu isotopes are using all available Cu, such that no fractionation effect is observed. Complete utilization of Cu implies either (a) low Cu availability in a closed basin/restricted environment, or (b) high rates of Cu cycling in an open environment. Copper concentrations within the sediment are relatively high compared to those of core GKF01 (Chapter 3, this thesis), which likely reflects Cu input via frequent volcanic ash rainout, but which may also indicate minimal lateral transport of Cu-bearing phases and/or dissolved Cu (either via ligands or

circulation). Any inorganic Cu cycling pathway is unlikely to proceed to completion, because the solution will become undersaturated with respect to any mineral incorporating Cu before Cu is used up. The only active biological process which could be using Cu to completion is cellular uptake.

The prolific levels of aerobic methanotrophy, which are hypothesised based on the extremely depleted $\delta^{13}C_{org}$ and $\delta^{13}C_{kerogen}$ values (e.g., Eigenbrode and Freeman, 2006; Thomazo et al., 2009; Czaja et al., 2010; Stüeken et al. 2017), could have used all available Cu to completion. Modern alkaline lakes sustained by mafic inputs are characterised by extremely high rates of cyanobacterial primary productivity (Pecorianio et al., 2015). The Tumbiana Formation depositional environment could have hosted similarly prolific productivity, evidenced by stromatolites (e.g., Stüeken et al., 2017). While aerobic methanotrophy can be sustained in anaerobic conditions, it is most efficient in oxygenated environments and Cu-dependent metabolisms are most abundant in high-O_2, low CH_4 settings (Semrau et al., 2011). Therefore, while under hypothetical Archaean marine environments, the predominantly reducing environment was not conducive to excessive aerobic methanotrophy (e.g., Zavina-James et al., *in review*; Chapter 3, this thesis), a system with localised oxygen production such as the Tumbiana could create an environment advantageous to such a metabolism. Based on experiments by Navarrete et al. (2011), which measured Cu isotope fractionation during Cu uptake by a variety of microbes (both pure strains and consortia), a Rayleigh model is presented in Figure 13. This model demonstrates that in order to produce a BSE-like Cu isotope record in the sediments, aerobic methanotrophs would hypothetically need to have consumed +90% of all available Cu, which is possible in a system with low Cu concentrations and where these organisms may be Cu-limited.
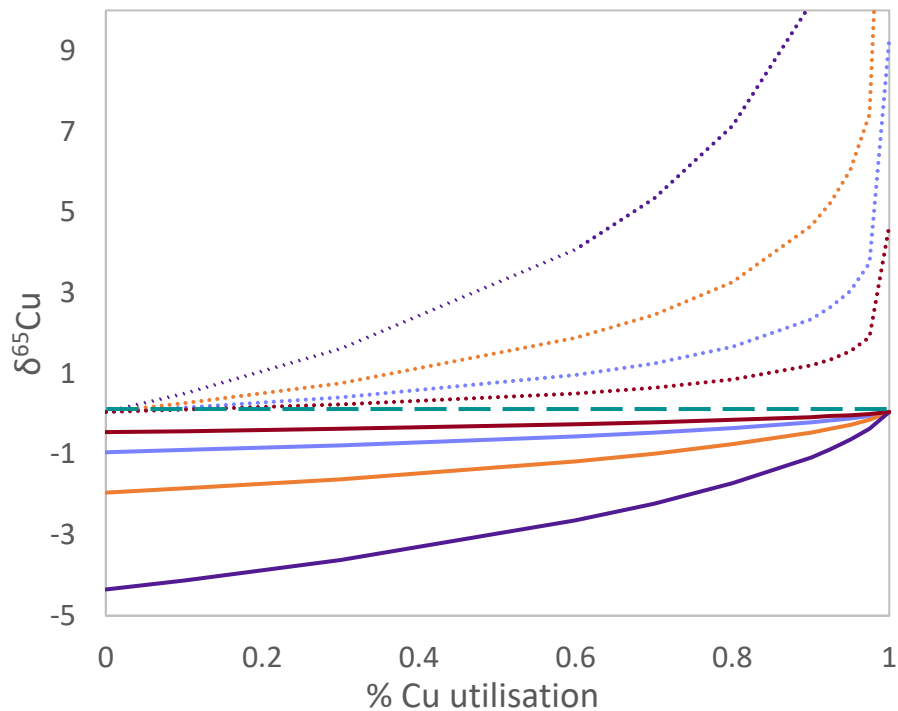
Figure 13: A closed-system Rayleigh distillation model calculated for epsilon values -0.5 (dark red lines), -1 (light purple lines), -2 (orange lines), and -4.4 (dark purple lines) (after Navarrete et al., 2011). Dotted lines reflect substrate and solid lines reflect product, the latter of which is reflected in the sediment. The dashed teal line reflects BSE (after Mariotti, 1980).

4.5 Conclusion

In this chapter, a high-resolution analysis of Cu isotopes within a 2.7 Ga drill core from the Tumbiana Formation, Western Australia was undertaken. This section was chiefly selected due to the ample evidence for aerobic methanotrophy previously generated from contemporaneous samples (Eigenbrode and Freeman, 2005) and by numerous independent studies (e.g., Czaja et al., 2010; Stüeken et al., 2017). Copper isotope analyses revealed a consistent BSE signal throughout the core.

Considering the above, along with existing arguments for a lacustrine environment (e.g., Buick, 1990; Buick, 1992; Coffey et al, 2013), the lack of variability within the Cu isotope data point to a closed basin, especially within the context of hypotheses (1) (i.e., no processes are fractionating Cu) which further implies a shallow, closed, evaporating basin

in which limited circulation and distal processes (such as extensive sulphide formation within deeper, pelagic sections) are not occurring, and (2): that all Cu is being used to completion in a system with low levels of Cu cycling in a closed basin. If Cu-ligands are significant in this system and lateral transport of these ligands is occurring, the residual pool would be isotopically light. Unless this was equally offset by adsorption/scavenging of Cu, it is possible aerobic methanotrophy was not occurring within the Tumbiana system, as this would presumably further isotopically deplete the dissolved pool of Cu. As the Cu isotope record provides no evidence for this, and based on the consideration above, the most likely explanations for the BSE Cu isotope record measured in core SV1 if the water column was alkaline are:

(1) No processes within the system are fractionating Cu isotopes. This is more likely in a marine/open basin environment, where circulation more readily transports any Cu-bearing fractions to other parts of the system. This interpretation further implies that either (a) anaerobic methane oxidation remained the dominant C-assimilation pathway within the Tumbiana, and that aerobic methanotrophy may not have been occurring at all, or (b) that higher levels of CH_4 production was sustained within the system, giving Fe-dependent, sMMO-expressing aerobic methanotrophs a competitive advantage.

(2) All Cu-bearing phases, species, precipitates, and ligands are homogenised within the sediment. Referring back to Figure 11, it is shown that in both Wilson Lake and Mono Lake, once Cu is mobilised within the sediment it partitions Cu-sulphides, Cu-Fe-Sulphides, and Cu-ligands. Without separating these phases and analysing them independently, it is not possible to distinguish if any of these processes exert a dominant control on Cu isotope fractionation during early-stage diagenesis. In any case, this hypothesis is also more indicative of a closed basin with minimal lateral transport of material within the water column.

(3) Over 90% of Cu is utilised by a Cu-dependent process, such that no isotopic fractionation of Cu is observable. Accounting for the evidence for biological

productivity within this system and assuming that (if alkaline) Archaean lakes were as highly productive as modern alkaline lakes, extensive assimilation of Cu by Cu-dependent aerobic methanotrophs in not entirely impossible. Alternatively, yet in a similar vein, any processes taking Cu are doing so indiscriminately, such as photosynthesising cyanobacteria. Directly, the implication of this hypothesis is that the Cu isotope signal reported here either reflects low levels of Cu cycling in a closed basin, or high levels of Cu cycling in an open basin.

Finally, acknowledging that none of these hypotheses can be completely ruled out with the data presented here - including that the Tumbiana formation represents a shallow lacustrine system – these isotope data could simply reflect a system in which no processes fractionate Cu, and that the dominant C-assimilation pathway is anaerobic methane oxidation.

In order to further constrain these hypotheses, future Cu isotope work on core SV1 and the wider Tumbiana Formation could focus on different fractions of the sediment, such as the organic fraction, the sulphide fraction, and the carbonate fraction. Alternatively, analysing other well-preserved cores from the Hamersley province which reflect different depositional environments could further constrain the biogeochemical cycling of Cu within a potential non-marine ancient system. Finally, Cu/Al and Cu/Ti ratios could provide useful tools in establishing whether the majority of Cu is detrital in origin, and that the isotope composition presented here merely reflects the isotopic composition of the Cu source.

Chapter 5

Development of Ni isotope analyses for ancient carbonate-rich shales: Lessons and ways forward.

5.1 Introduction

Nickel is a bioessential trace metal utilised by methanogens in the production of methane (e.g. Silva and Williams, 2009). Broadly, the process by which CO_2 is reduced to CH_4 (methanogenesis) is as follows: $CO_2 \rightarrow R\text{-}CH\text{=}O \rightarrow CH_2 \rightarrow CH_3 \rightarrow CH_4$, where a series of enzymes strip oxygen atoms from carbon and add hydrogen. Importantly, the final reaction (methyl to methane) is performed by methyl-coenzyme M reductase (MCR) and catalysed by the Ni-dependant cofactor F430 (Madigan and Martinko, 2015). Nickel-cofactor F430 is exclusively found in methanogenic Archaea and anaerobic methanotrophic archaea, the latter of which are proposed to employ reverse-methanogenesis in order to metabolise CH_4 (Thauer, 1998; Krüger et al., 2003). Notably, recent work on mass-dependent Ni stable isotopes (i.e., Cameron et al., 2009) has revealed clear potential for this isotope system to be developed as a biomarker for methanogenic activity in the geological record.

Methanogenic archaea were prominent in the Archaean biosphere, exploiting extreme environments and thriving under the anaerobic conditions of the early atmosphere (e.g. Nisbett et al., 2011). The impact that these microorganisms had on atmospheric evolution throughout the late Archaean in particular has drawn fresh attention, as recent studies have suggested that Earth's atmosphere experienced a series of haze events, during which

time it was dominated by a methane-rich hydrocarbon haze similar to that of Saturn's moon, Titan (Zerkle et al., 2012; Izon et al., 2015; Izon et al., 2017). Applying the Ni isotope system to sedimentary sequences that record these periodic haze events (PHEs) could provide valuable clues as to the provenance of these methane fluxes. Based on existing evidence that Ni isotopes are fractionated by methanogenic activity, where the biomass assimilate the lighter isotope (^{60}Ni) (i.e., Cameron et al., 2009), it is anticipated that a light Ni isotope signal would occur contemporaneously alongside the C-S anomaly identified by Izon et al. (2017).

Nickel isotope analyses are complex and prone to issues during both the sample preparation and spectroscopy stages. The results of this study are severely impacted by issues likely stemming from column oversaturation during the sample preparation stage; much of the discussion section of this chapter focuses on analysing the technical issues associated with attempting to obtain Ni isotope ratios in ancient sedimentary materials.

5.1.1 Terrestrial Ni isotope cycle

In the modern marine system, Ni behaves as a nutrient (Sclater et al., 1976; Bruland, 1980); depleted in the photic zone (likely as a result of biological uptake) and relatively enriched at depth. Despite this, the isotopic composition of seawater remains homogenous (δ^{60}Ni = 1.44 ± 0.15 ‰; Cameron and Vance, 2014; where δ^{60}Ni is defined as the permil (‰) deviation in ^{60}Ni/^{58}Ni relative to the NIST SRM 986 Ni isotope standard), suggesting that the drawdown of Ni from the surface ocean does not discriminate between the isotopes (Cameron and Vance, 2014). In contrast, weathering, transport-to and removal-from the ocean has been demonstrated to have a significant impact on Ni isotope fractionation. The average riverine Ni isotope composition is +0.8 ‰ which, while considerably lighter than the ocean, remains heavier than Bulk Silicate Earth (BSE) (Cameron and Vance, 2014). The Ni isotope composition of BSE is calculated to be 0.11 ± 0.01 ‰ (Elliott et al., 2017; Klaver et al., 2020), a value based on measurements from various studies. In addition to BSE, Wu et al (2019) measured granite, sediment, diamictite, and loess in order to constrain the Ni isotope composition of the Upper Continental Crust (UCC) at 0.11 +- 0.14 ‰, which is in excellent agreement with BSE.

The homogeneity of Ni isotope composition across the materials representing BSE and UCC indicate that there are no evident fractionations occurring during high-temperature lithogenic processes. Figure 1 provides a schematic overview of modern marine Ni cycling.

The disparity between riverine and BSE composition implies that the weathering of silicate rocks leads to the significant fractionation of Ni isotopes, where the weathered product is isotopically heavier than the residue. This is corroborated by the Ni isotopic composition of weathering residues such as soils, dunite residues, and laterites, which are isotopically light (bedrock samples: +0.06 ± 0.20 ‰; laterites: -0.21 ‰) (Spivak-Birndorf et al., 2018). However, while Ni isotopes are sensitive to weathering, they are not redox sensitive (e.g. Porter et al., 2014), however there is evidence suggesting that sorption of Ni to Fe oxyhydroxides drives a fractionation where the oxidation of Fe^{2+} released from bedrock and precipitation leads to the retention of a light pool of Ni in solid weathering products (Gueguen et al., 2020, 2021; Little et al., 2020). This enriches the dissolved phase in the heavy isotope (Wasylenki et al., 2015).
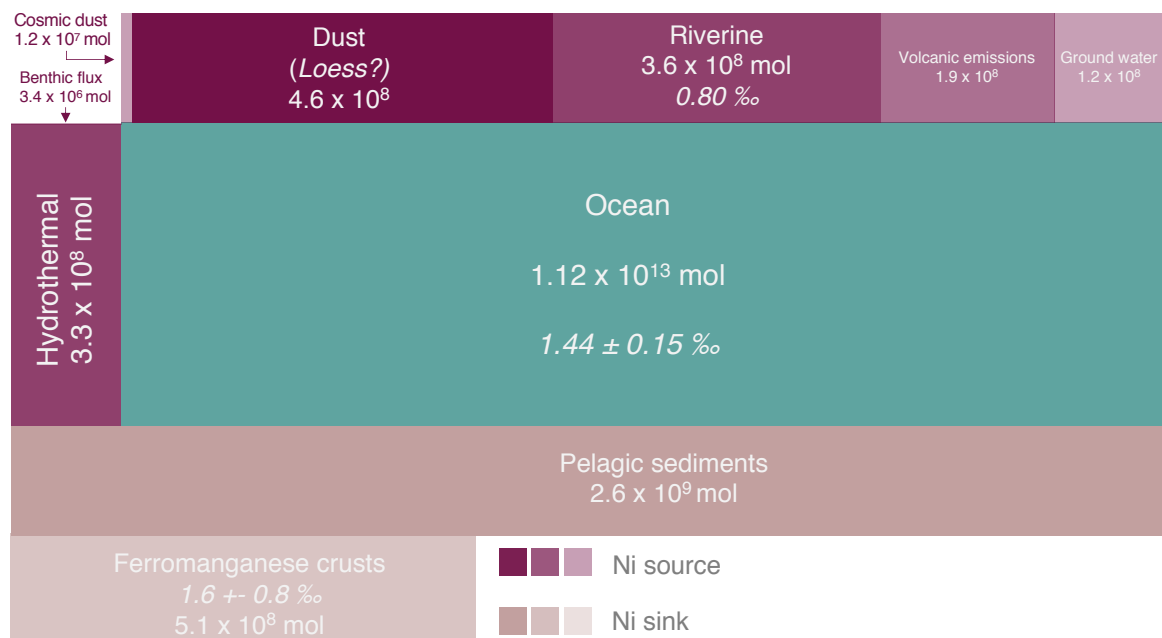
Figure 1: Nickel isotope oceanic mass balance (expressed as $\delta^{60}Ni$, ‰) based on current data. Boxes are scales and shaded by relative magnitude, where their length and shade reflect the flux magnitude (mol/yr). Isotope values where known are italicised. Deep purple boxes represent Ni sources, while beige boxes represent Ni sinks (riverine values and oceanic Ni isotope values from Cameron et al., 2014; oceanic molar concentration and all data for ferromanganese crusts from Gall et al., 2013).

A major oceanic sink of Ni is ferromanganese crusts (Peacock and Sherman, 2007). Gall et al (2013) demonstrate that Ni isotope values of these crusts vary between 0.9 ‰ - 2.5 ‰ and are broadly reflective of seawater composition (Cameron and Vance, 2014) yet covering a much larger range. Thus, the incorporation of Ni during the formation of ferromanganese crusts is thought not to significantly fractionate Ni isotopes although, as demonstrated by Wasylenki et al. (2015), sorption of Ni onto ferromanganese crusts or (speculatively) banded iron formations (BIFs) may have constituted a larger sink of Ni previously in Earth's history.

As such, modern (and ancient) Ni oceanic mass balance is still yet to be fully understood; there is a clear and significant imbalance between oceanic inputs and outputs (e.g. Elliott and Steele., 2017). It has been postulated that marine Ni cycling in the Archaean decreased, possibly due to weathering of continental crust with a decreased Ni content, where marine Ni abundances dropped from an estimated >300 to <50 ppm (i.e. Keller and Schoene, 2012). It is believed that this drop in Ni availability suppressed methanogenesis, contributing to the facilitation of the build-up of O_2 which ultimately led to the GOE (e.g. Konhauser et al., 2009; 2015). However, analyses of Ni isotope compositions in Precambrian glacial diamictites indicate that the onset of oxidative sulphide weathering continued the delivery of Ni to the oceans, sustaining methanogenesis at this time (Wang et al., 2019).

Here, in order to understand the role of biogenic methane in PHE formation, the Ni mass-dependent isotopic system is applied to late Archaean carbonate-rich shales and develop a method for further analyses of samples of this nature. Nickel isotopes are here hypothesised to have strong potential as proxies for methanogenesis and, by implication, perturbations in methane cycling throughout geological history. Methanogenesis is an ancient metabolism which represents some of the most primitive forms of life on Earth and which has played a crucial role in earth's environmental history. Continuing the development of methods with which mass-dependent Ni isotope compositions can be accurately determined in ancient shales and carbonates will greatly impact our understanding of the biological controls on Earth's atmospheric evolution.

5.2. Materials and methods

A description of the samples used in this study can be found in Chapter 2 of this thesis.

5.2.1 Nickel isotope analysis

5.2.1.1. Sample digestions

Sample digestions were undertaken at the University of St Andrews under trace metal clean laboratory conditions (class 100 hoods). High-precision mass-dependent analysis by double spike requires ~1.5 - 2 µg of Ni. Nickel concentrations were initially determined using ICP-MS after fusion dissolution and the amount of each rock powder required for double spike analyses was calculated. These masses ranged from 50 – 570 mg. Each rock powder was weighed into a pre-cleaned Savillex PTFE 15 mL vial, after which 0.5-1 mL of concentrated distilled $HNO_3$was added, followed directly by 2-4 mL of concentrated, Romil super-pure HF. The beakers were tightly sealed and placed on a hot plate overnight at 140°C to digest. Once dissolution of the silicate was completed the beakers were opened and evaporated to dryness at 120°C. Three more stages using aqua regia, HCl, and HNO_3 were performed to ensure completed digestion of fluorides. Final residues were taken up in 2 mL (4 mL for samples above 100 mg) concentrated HNO_3.

5.2.1.2 Nickel concentration measurements

Prior to double-spiking, Ni concentrations were measured again in the SESAME Laboratory at Indiana University Bloomington on an Agilent 7700 quadrupole ICP-MS. The instrument was calibrated with several dilutions of multi-element ICP standards and analytical errors are estimated at ± 5%, based on repeated measurements of selected samples over multiple analytical sessions. Sample Ni concentrations measured via ICP-MS were systematically lower than those measured via fusion-enhanced ICP-MS, and these lower values were selected for calculating sample-spike volumes. However, Figure 2 shows Ni concentrations measured at St Andrews via fusion ICP-MS plotted against the

Ni concentrations measured at IU Bloomington, demonstrating a strong relationship (R^2=0.99) between both measurements. Nevertheless, for consistency, all Ni concentrations referred to henceforth will be based on IU Bloomington measurements.
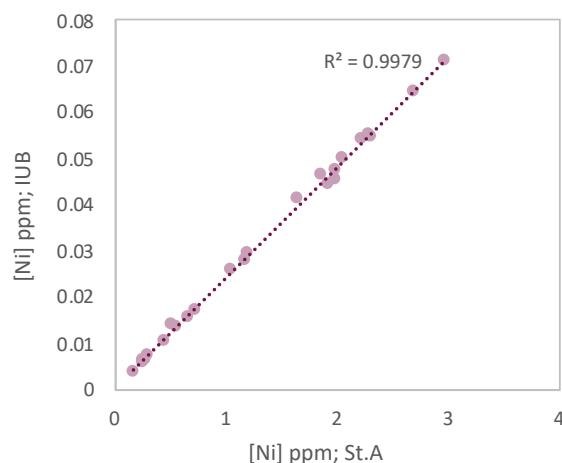
Figure 2: Ni concentrations analysed at IU Bloomington (IUB) and St Andrews (St.A)

5.2.1.3 Column chemistry

Column chemistry and isotope analyses were conducted at Indiana University, Bloomington. A double-spike strategy for mass bias correction was employed, assuming samples were all related by mass-dependent isotope fractionation with exponential law behaviour. Sample solutions containing approximately 1 µg of Ni were spiked with a ^{61}Ni - ^{62}Ni double spike (approximately 41% ^{61}Ni and 54% ^{62}Ni) in order to obtain a spike-sample ratio of 64:36, which minimises double-spike method uncertainties according to Rudge et al. (2009). To ensure that the sample and spike were fully equilibrated, samples beakers were sealed and refluxed at 60 °C for 30 minutes immediately and allowed to completely cool prior to column chemistry.

Purification of Ni from matrix elements was undertaken via a three-stage cation exchange chromatography procedure. A detailed description of the protocols used can be found in tables 1a to 1c. All separation procedures were performed with 2 mL of pre-cleaned Bio-Rad 200-400 mesh AG 50W-X8 resin loaded onto Bio-Rad polyprep columns. The first column uses a HCl:acetone mixtures to separate Ni from major matrix elements and follows methods described by Strelow et al. (1971) and Tang and Dauphus, (2012). The

sample was dissolved in 0.2 mL of 10M HCl and then diluted with 0.8 mL of acetone and then loaded onto the column and washed with two 1 mL aliquots of 2M HCl:acetone mixture. Manganese, Fe, and Cr were then eluted in 5 mL of the acid-acetone mixture. Following this, Ni was eluted in 1 mL and 3 mL aliquots of 6 M HCl. The sample was the left to evaporate to a small volume (<100 µl). For column two, which serves to separate nickel from Mg, Ca, Al, and Ti, the sample was dissolved in 1 mL of mixed acid containing 15% 10M HCl and 85% concentrated acetic acid (hereafter 1.5M HCl:85 % acetic) following the work of Korkisch and Ahluwalia (1967). Nickel was immediately eluted in 15 mL of the 1.5M HCl : acetic mixed acid, which was added in two 1mL aliquots, one 3mL aliquot, and two 5mL aliquots to ensure all material was washed into the column and to ensure consistent flow through the column. The sample was left to evaporate to a small volume (<100 µl) overnight. Finally, for column three, the sample was dissolved in 1 mL of 0.9 M HNO_3 and loaded onto the column. Sodium and potassium were eluted in 16 mL of 0.9 M HNO_3, followed by nickel in 4 mL of 6 M HCl.

Step	Action	Purpose
0	Sample dissolved in 1ml 20% 10M HCl + 80% Acetone	
1	Column washed in MQ 3 times	Wash
2	2ml AG50W-X8 cation resin loaded	Load resin
3	4ml 6M HCl added	Wash
4	Full tank MQ	Wash
5	4ml 20% 10M HCl + 80% Acetone added	Condition
6	Load 1ml sample	Load sample
7	1ml 20% 10M HCl + 80% Acetone	Elute Mn, Fe
8	1ml 20% 10M HCl + 80% Acetone	
9	5ml 20% 10M HCl + 80% Acetone	
10	1ml 6M HCl	Collect Ni
11	3ml 6M HCl	

Table 1a: Nickel column chemistry protocol for column 1, which separates Ni from Mn and Fe.

Step	Action	Purpose
0	Sample dissolved in 1ml 15% 10M HCl + 85% Acetic acid	
1	Column washed in MQ 3 times	Wash
2	2ml AG50W-X8 cation resin loaded	Load resin
3	4ml 6M HCl added	Wash
4	Full tank MQ	Wash
5	4ml 15% 10M HCl + 85% Acetic acid added	Condition
6	Load 1ml sample	Load sample
7	1ml 15% 10M HCl +85% Acetic acid	
8	1ml 15% 10M HCl +85% Acetic acid	
9	3ml 15% 10M HCl +85% Acetic acid	Collect Ni
10	5ml 15% 10M HCl +85% Acetic acid	
11	5ml 15% 10M HCl +85% Acetic acid	

Table 1b: Nickel column chemistry protocol for column 2, which separates Ni from Mg, Ca, Al, and Ti

Step	Action	Purpose
0	Sample dissolved in 1mL 0.9 M HNO_3	
1	Column washed in MQ 3 times	Wash
2	1.8ml AG50W-X8 cation resin loaded	Load resin
3	4ml 6M HCl added	Wash
4	Full tank MQ	Wash
5	4 mL 0.9 M HNO_3 added	Condition
6	Load 1ml sample	Load sample
7	1 mL 0.9 M HNO_3	
8	3 mL 0.9 M HNO_3	
9	5 mL 0.9 M HNO_3	Elute Na, K
10	5 mL 0.9 M HNO_3	
11	2 mL 0.9 M HNO_3	
12	4 mL 6 M HCl	Collect Ni

Table 1c: Nickel column chemistry protocol for column 3, which separates Ni from Na and K.

After initial column chemistry, a selection of samples (including both carbonate-rich shales and shales) were analysed via ICP-MS to assess whether concentrations of impurities (primarily Fe, Al, Na, K, Ca, and Mg) were low enough so as not to interfere with Ni measurements. Magnesium in particular is difficult to separate from Ni (e.g. Strelow et al., 1971) (see table 2). All three column chemistry procedures were then repeated to further purify Ni from these elements before isotope measurements. Five United States Geological Survey (USGS) standards were processed for column chemistry alongside samples (table 3).

Sample ID	Mg (ppm)			Al (ppm)			Ca (ppm)			K (ppm)			Fe (ppm)		
	pre	post	% removed	pre	post	% removed	pre	post	% removed	pre	post	% removed	pre	post	% removed
1B	18082	139	99	102	0.25	100	299963	1930	94	53	-0.90	102	412	0.02	100
1K	502	0.00	100	3092	0.01	100	24	-0.21	101	1495	-1.05	100	668	0.01	100
2G	5389	1.74	100	8417	0.76	100	8169	2.39	100	4334	6.19	100	2257	0.03	100
2J	17885	82	100	113	0.34	100	29892	3132	90	38	1.11	97	806	1.41	100
2K	17842	0.07	100	133	0.47	100	29067	0.35	100	37	-1.80	105	731	0.02	100
3C	18426	81	100	46	0.30	99	30737	6381	79	39	-0.71	102	361	0.11	100
3E	16862	310	98	1223	0.25	100	285507	3341	88	704	0.39	100	588	0.14	100
3I	18306	289	98	965	0.24	100	282262	1.44	100	724	10.48	100	710	0.14	100

Table 2: Pre- and post-column measurements of selected elements which are known to interfere with Ni separations. Measurements were made from a selection of samples which represented the various rock matrices within core GKF01.

5.2.1.4 Nickel isotope measurements

Nickel isotopic ratios were measured using a Nu Plasma II multicollector inductively coupled plasma mass spectrometer at Indiana University Bloomington with an Aridus II desolvating nebuliser. The Ni concentration was ~250 ppb. The four Ni isotopes (^{58}Ni, ^{60}Ni, ^{61}Ni, and ^{62}Ni) used for the double spike inversion were measured simultaneous on Faraday cups, with ^{60}Ni in the axial cup. ^{57}Fe was also measured and used to correct for interference of ^{58}Fe on ^{58}Ni, although this correction was generally small, with the highest voltage measured on ^{57}Fe being 0.01 V compared to an average voltage of 3.3 V on ^{58}Ni. Additionally, the background of ^{60}Ni was <1 mV, which is negligible relative to sample signals of ~3-4 V. Each analysis consisted of 25 10-second integrations with a 2-second magnet settling time. Blank subtraction was performed using periodic measurement of signals from distilled 0.32 M HNO_3. Instrumental mass bias was corrected using both sample-standard bracketing (Ni-spiked SRM 986) and the double spike. The Ni isotopic data represent the average of 4-5 sample-standard brackets. Reported uncertainties are either 2 standard deviations (2SD) for the 4-5 replicate measurements or the long-term 2SD for primary and secondary standards (± 0.06 ‰), whichever is larger.

Sample name	Sample type	Reference	δ^{60}Ni	2SD	n
SDO-1	Shale	This study	0.23	0.07	4
		Wu et al., 2019	0.61	0.06	3
		Gueguen et al., 2013	0.59	0.03	5
Nod-A	Manganese nodule	This study	1.34	0.04	4
		Wu et al., 2019	1.02	0.05	6
		Gueguen et al., 2013	1.03	0.06	6
		Gueguen et al., 2018	1.04	0.05	3
		Ratié et al., 2016	1.06	0.09	-
		Gueguen et al., 2016	1.06	0.04	-
WSJ-274	Internal standard	This study	0.78	0.05	4
		previous measurements*	0.70	0.08	-

Table 3: Geological and internal Ni isotope standard data. Previous measurements of sample WSJ-274 were made by Shuijiong Wang at IU Bloomington.

The Ni isotope results are reported in the conventional δ notation in per mille (‰) relative to National Institute of Standards and Technology standard reference material (SRM) 986:

$$\delta^{60}\text{Ni} = \left[\frac{\left({}^{60}Ni \middle/ {}_{58}Ni \right)_{sample}}{\left({}^{60}Ni \middle/ {}_{58}Ni \right)_{SRM986}} - 1 \right] x\ 1000$$

5.3 Results

Nickel isotope and concentration data from core GKF01 are presented in table 4 and Figure 3. In this Figure, Ni isotope data are plotted alongside stratigraphy and Ni abundance. Due to the low concentrations of Ni present in the samples selected for this study, isotope measurements could only be obtained from 24 of the 40 original samples (60%) (see table 4 for Ni concentrations of analysed samples). There is no significant correlation between measured Ni isotope values and Ni concentrations ($R^2 = 0.19$; Figure 4a). In order to provide context, the Ni isotope data have also been plotted alongside $\delta^{13}C_{org}$ data and S-MIF data presented as the slope between $\Delta^{33}S$ vs. $\Delta^{36}S$ ($\Delta^{33}S/ \Delta^{36}S$) from Izon et al. (2017). There is a demonstrable relationship between Ni concentrations and the haze interval (c. 830 – 840 m), however this is not observed in the Ni isotope data. These data show a 1.34‰ range in isotope composition, with average value of 0.39‰. There is a discernible cluster of highly repeatable measurements between approximately 830 – 843 m depth, which appear to deviate slightly relative to the other measurements. These data also correspond to the samples with the highest Ni concentration. Considering the data without these high concentration samples, there is a background δ^{60}Ni value of 0.5‰, while the cluster average is 0.3‰.
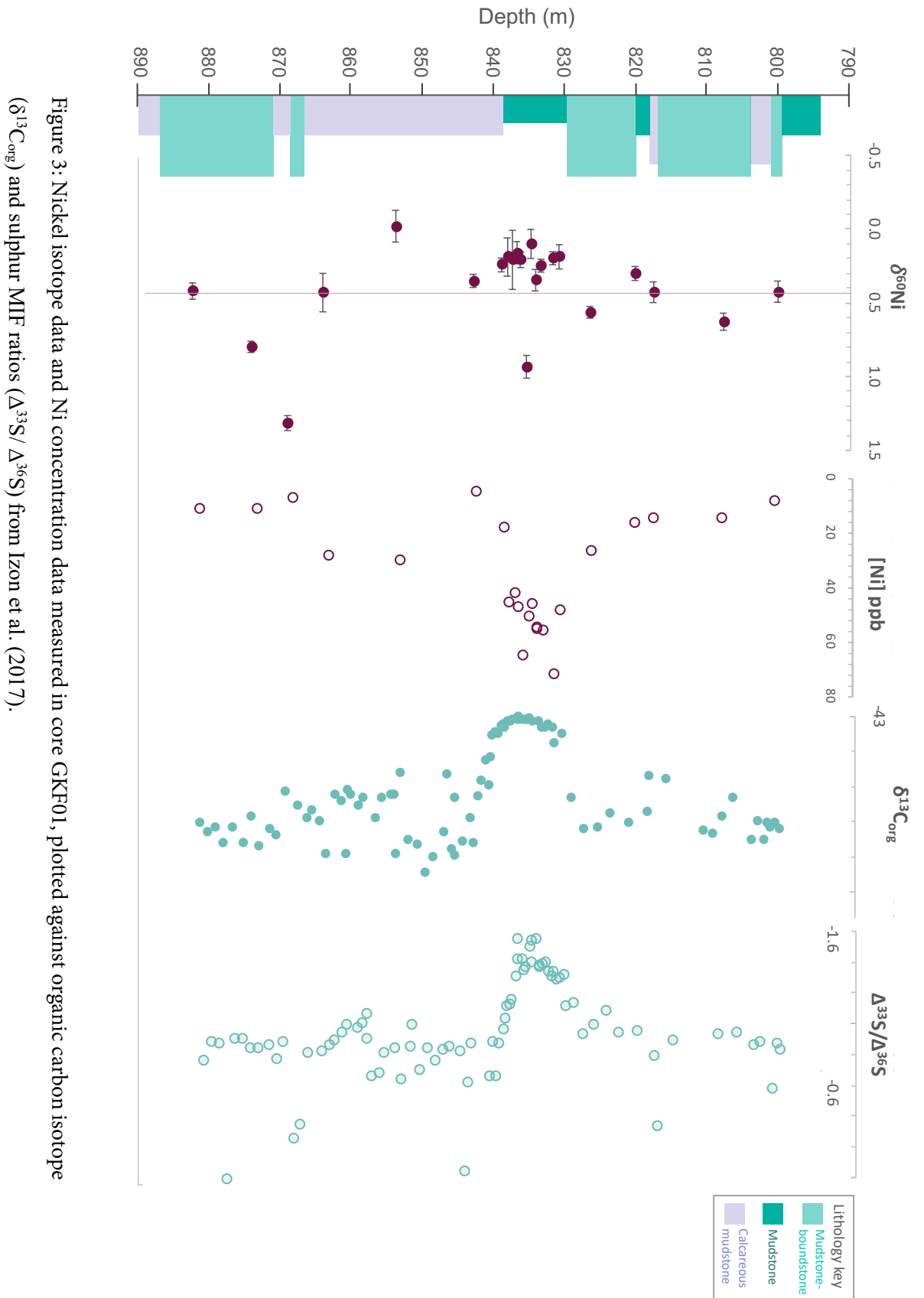
Figure 3: Nickel isotope data and Ni concentration data measured in core GKF01, plotted against organic carbon isotope ($\delta^{13}C_{org}$) and sulphur MIF ratios ($\Delta^{33}S$ / $\Delta^{36}S$) from Izon et al. (2017).

However, table 3, which presents standard data for this study alongside previously published values, show that the standards measured in this study are not in agreement with these previously published values, causing significant question marks over the accuracy of these data. While an in-house standard solution (WSJ-274) which was processed via column chemistry alongside the rest of the samples does not appear to deviate to the same extent, this alone cannot alleviate concerns over accuracy.

Depth (m)	Ni (ppb)	$\delta^{60}Ni$ (‰)	2SD (‰)
800.18	7.44	0.42	0.07
807.73	14.04	0.63	0.06
817.47	13.86	0.43	0.07
820	15.85	0.30	0.05
826.28	25.98	0.56	0.04
830.53	47.46	0.19	0.08
831.45	71.4	0.20	0.04
833.08	55.42	0.25	0.04
833.9	54.19	0.35	0.07
833.9	54.71	0.30	0.07
834.49	45.43	0.10	0.10
835.05	50.24	0.93	0.08
835.88	64.5	0.21	0.05
836.45	46.66	0.16	0.08
837.04	41.3	0.21	0.20
837.79	44.6	0.19	0.13
838.58	17.22	0.24	0.05
842.5	4.04	0.35	0.04
853.3	29.53	-0.02	0.11
863.4	27.83	0.43	0.13
868.3	6.66	1.31	0.05
873.4	10.31	0.80	0.04
881.5	10.73	0.42	0.06
881.5	6.02	0.46	0.07

Table 4: Nickel concentration and isotope data for individual samples by depth analysed in this study.

5.4. Discussion

5.4.1. Nickel column chemistry

While issues arising from mass spectrometry cannot be entirely ruled out, given that the internal standard (WSJ-274) is consistent with previous analyses, it is likely that any issues with the data collected for this study arose during the Ni separation procedures.

Nickel can be separated from elements such as Zn, Co, Cu (II), Mn (II), Fe (II), U (VI) and other such elements that freely form chloro-complex ions by using a HCl – acetone mixture on a cation resin such as AG 50-W X4 (Victor., 1985). Further separation of Ni can prove to be challenging, particularly when purifying Ni from other common matrix elements that are prevalent in silicate rocks (such as K, Be, Mn, Ca, and Al). This is because of their similar partition coefficients onto the resin, i.e., the ability of the chromatographic system to chemically distinguish between sample components. This is compounded in studies of samples such as this because Ni usually exists in a significantly lower abundance than these matrix elements, although this is not the case for some samples (such as Fe meteorites) (e.g., Gall et al., 2012). Broadly, this issue has been solved by Wahlgren et al. (1970), who employed acetone and dimethylglyoxime (DMG) to successfully separate >95% of nickel from silicon-iron samples. The separation of Mg from Ni is particularly challenging, especially when the Mg:Ni ratio is high. Successful Ni analyses require a high degree of separation from Mg due to: (1) the potential for argide formation during mass spectrometry (an argide interference produced on ^{24}Mg can interfere with low abundance ^{64}Ni) and (2) their similar chemical behaviours, which can lead matrix effects on each other in the plasma, leading to non-exponential (and thus non-correctable) instrumental mass fractionations. Given this, a C_{matrix}/C_{Ni} of <0.5 is required. (e.g., Spivak-Birndorf et al., 2018).

Numerous separation protocols have therefore been developed in attempts to circumvent these issues. A vast majority of these methods utilise DMG as an Ni complexing agent, but those that do not often require multiple passes over a series of days (i.e., Tang and

Dauphus, 2012) or specialist equipment (e.g. Ireland et al., 2013). Below, I will review the current reagents and methods used for Ni separation from various matrices.

5.4.1.1 Dimethylglyoxime

Dimethylglyoxime (DMG) is a chemical compound that can be used to identify and measure Ni. When DMG comes into contact with Ni, it forms a red complex called nickel-bis(dimethylglyoximate), or $Ni(dmgH_2)$ (Tchugaeff, 1905). Given the strong complexing nature of DMG (e.g., Godycki et al., 1953) it has consistently been employed to aid the separation of Ni from matrix elements. Numerous published methods utilise DMG, with protocols varying depending on the specifics of the study. Broadly, there are two methods of use: (1) Liquid-liquid extraction, which uses two immiscible liquids which are combined and separated. For example, Quitte and Oberli (2006) used a combination of HCl, NH_4OH, and DMG in ethanol to chelate Ni from the sample matrix, before adding chloroform to extract the organic Ni-containing phase. Method (2), which involves column chromatography in addition to DMG, can be further broken down into two approaches. The first approach utilises an Ni-specific resin (e.g., Eichrom Ni resin), where the DMG is contained inside pores of a polymethacrylate resin. When the Ni-containing sample is loaded, a Ni-DMG precipitate occurs on the resin, where it is held and readily separated from the aqueous sample (e.g., Cameron et al., 2009). Approach 2 involves passing an acid-DMG mixture through a cation resin column such that the Ni is held, while other elements are instantly eluted. The Ni can then be eluted in acetone, as DMG is highly soluble in acetone and forms an acetone-soluble complex with Ni (Victor, 1986; Steele et al., 2011).

Variants of method (2) employing Ni-specific resin, initially designed and utilised by Quitte and Oberli (2006), have been successfully utilised in the separation of Ni from biological samples, meteorites, basalts, and continental sediments (Cameron et al., 2009); silicates and a variety of reference materials (basalt, dolerite, peridotite, manganese nodules, coal, shales, and granite) (Gueguen et al., 2013); ocean and river samples (Cameron and Vance, 2014); organic rich sediments and shales (Porter et al., 2014; Pašava et al., 2018; Ciscato et al., 2018), and carbonates (Castillo-Alvarez et al., 2020). The second

approach of this method has many variants, however in essence, the separation of Ni from silicates via ion exchange chromatography typically requires three steps. The DMG is used in the second step of the process and involves the use of acids (commonly HCl and citric acid) being added to the sample. After the addition of acids, the sample is brought up to a neutral pH with ammonia. Dimethylgyloxime in an organic medium (e.g., ethanol (Quitte and Oberli, 2006), or acetone (Steele et al., 2011; Regelous et al., 2008; Victor, 1989) is then added to chelate the Ni. In order to extract the Ni, chloroform can be used (Quitte and Oberli, 2006), however alternatives to chloroform include other strong oxidisers such as hydrogen peroxide (Gall et al., 2012), or HNO_3 (Steele et al., 2011). This technique has been successfully employed in the analysis of Ni isotopes in meteorites (Steele et al., 2011; 2012), ferromanganese crusts (Gall et al., 2012), and most recently in granite, sediment, diamictite, and loess samples (Wu et al., 2019).

The use of DMG in the separation of Ni presents challenges, however. The DMG-acetone method is dependent on Ni concentrations and column volume, and thus may require high volumes of DMG to completely separate Ni from Mg, Na, and Ca. Large quantities of DMG can cause problems because the $Ni(DMG)_2$ must be entirely broken down in order to recover all of the Ni (Gall et al., 2012). The DMG-ethanol method, which uses chloroform to break down $Ni(DMG)_2$, additionally results in some Ni loss, as chloroform is highly miscible with the aqueous phase (Quittes and Oberli., 2006). For mass-dependent Ni isotope studies, methods involving the use of Ni-specific resin are favoured as the method may result in poor quantitative yields via Ni volatilisation with chloroform (>70%; Quitte and Oberli., 2006), and therefore may not be suitable for the study of some mass-dependent fractionation effects where Ni concentrations are small. Ion exchange procedures involving Ni-specific resin, on the other hand, allow for quantitative extraction of Ni. The use of Ni-specific resin does, however, also present its own set of issues. It also uses large amounts of DMG (although it is bound to the resin bed). The Ni eluted in this process is a DMG-resin polymer mixture, which can be challenging to decompose. Furthermore, in order for the chemistry to work, samples must be adjusted to pH 8-9 before being loaded onto the resin, which results in lost analyte. The ultimate success of the Ni extraction is therefore dependent on sample pH (Gall et al., 2012).

In summary, it is considered that in order to measure mass-dependent Ni isotopes, one must employ a technique which results in the highest Ni yield, often involving Ni-specific resin, as the low Ni yields gained in liquid-liquid separation methods can cause mass-dependent fractionations during the procedure. However, in lieu of this, some other techniques for Ni separation have been proposed. Tang and Dauphus (2012) employ a multiple-pass method to purify Ni from Fe meteorites. The three-step process separates Ni in a HCl-acetone mixture on Biorad AG 50 X12 200-400 mesh resin (i.e. non-Ni specific). Nickel is extracted by eluting 150 mL of the HCl-acetone mixture (based on Strelow et al., 1971) five times to ensure complete separation of Mg from Ni. The problem with this method is that it takes a very long time (each elution takes ~14 hours) and, in addition to this, the HCl-acetone mixture becomes unstable as acetone evaporates, and so fresh batches of the mixture acid need to be mixed every hour. This presents a time-consuming process, which limits the number of samples that one can process in a given time. For precise Ni-Mg separation (a critical step) Ireland et al. (2013) present the Teflon High Performance Liquid Chromatography (T-HPLC) method, which works in a single pass and also employs a HCl - acetone mixture. The method is fully automated, and takes place on an 80 cm long column at 65°C. For most rock matrices, one pass through the T-HPLC system is adequate for the full separation of Ni from Mg. The limitation of this technique, however, is that it is time consuming (10 hours per sample) and requires a specific method-set up with specialised equipment, making it less accessible than other methods.

Finally, Wu et al (2019) have propose a novel method to separate Ni from a variety of geological matrices. The purification scheme utilises DMG and acetone as organic reagents over a four-step procedure involving five chromatographic columns that sequentially purify Ni. This method shows promise for further measurements of mass-dependent stable nickel isotopes without necessitating Ni-specific resin. The methods developed by Wasylenki et al. (2015) were employed and adapted (based on Wang et al., 2019) in this study, and use neither DMG based liquid-liquid extraction nor Ni-specific resin. A detailed description of the column chemistry protocol is described above (tables 1a to 1c) in the methods section of this chapter, however, in brief, the method used HCl-acetone and HCl-acetic acid on AG50W-X8 cation exchange resin (based on the method

proposed by Korkisch and Ahluwalia, 1967). This method has been successfully employed in the measurement of Ni isotopes in synthesised ferrihydrites, and when applied to laterites (Spivak-Birndorf et al., 2018), this method resulted in sharp Ni-Mg separations; basalt standard BHVO-1 began with a Mg/Ni ratio of 346 but, after purification, had a ratio of 0.3. This method was then further adapted by Wang et al. (2019) and this adaptation was applied to this study – the difference being an extra step using HNO_3.

In the case of this study, it can be demonstrated that the column chemistry applied was successful in removing the bulk of the matrix elements (in most cases, almost 100%). Table 2 in section 5.2.1.3 of this chapter provides pre- and post-column measurements of selected major matrix elements and demonstrates the presence of matrix elements after column-chemistry. Separation factors calculated from these measurements are shown in table 5. The separation factors are varied, and relatively low for Ca, Al, and Mg in the case of samples 2J, 3C, and 3E, however broadly reflect successful separation of these matrix elements from the sample. However, the low Ni concentrations present in all samples required large volumes of sample, leading to higher amounts of matrix elements being loaded onto the columns. The column chemistry method employed for these analyses did not use DMG, and thus many of these matrix elements are retained on the column, leading to potential column oversaturation by matrix elements and possible fractionation of Ni isotopes via Ni loss on the column.

Sample ID	Mg	Al	Ca	K	Fe
1B	286	877	34	-	45793
1K	-	64871	-	-	31751
2G	3289	11778	3635	744	89969
2J	109	167	5	17	285
2K	987714	1017	297572	-	126232
3C	149	101	3	-	2062
3E	7	667	1	242	560
3I	131	8469	40772	143	10159

Table 5: Separation factors for Mg, Al, Ca, K, and Fe calculated from the values presented in table 2 (section 5.2.3.3). Blanks represent samples for which post-column concentration measurements equalled 0 or were below detection limit.

5.4.1.2 Column saturation

A significant concern with column chemistry is the oversaturation of the resin within the column. Ion exchange resins comprise cross-linked polystyrene chains with functional groups attached, which act as ion-exchange sites. The number of active sites within the resin are finite, and successful elution chromatography is dependent on there being enough ion exchange sites available to accommodate and exchange the sample ions. The number of active sites can be calculated for a given sample, and it is recommended that the capacity of the resin is not exceeded. In general, a resin at <10% capacity is considered to yield optimum separation (Schonbachler and Fehr, 2014). Table 6 provides a summary of column saturation calculations for the analyses presented in this chapter. Saturation is shown as % of resin capacity, which is measured in milliequivalents per millilitre (mEq/mL), where milliequivalents represent the amount of substance needed to combine with 1 mol of hydrogen ions per millilitre of hydrated resin (e.g., Korkisch, 1989). Column saturation was calculated by first converting major charged element concentrations per sample into milliequivalents (millimoles*1), adding these together, dividing them by volume of sample taken for double spiking (and thus the volume of sample taken for column chemistry), and then converting this value to a percentage of the total resin capacity for the protocol used (1.5 mEq/mL; where 2m: of resin was added to each column and thus total capacity was 3.4 mEq/mL. Only elements which 'stick' to the resin under the column conditions count towards the capacity taken up, and thus Fe and Mn are excluded here (Shonbachler and Fehr, 2014). The table demonstrates that only two samples (1F and 1G, however 1G was not analysed) did not saturate the column. The impact of an oversaturated column on the separation of elements in summarised in a schematic diagram (Figure 5). As there are a finite number of active sites per gram of resin, ddding a sample which contains, for example, 1.7 mEq of charge to a column containing 1.7 mEq of active sites (i.e., 100% capacity) will lead to full occupation of these sites by the sample. The most significant implication of this is that, due to the isotopic fractionation of Ni associated with partitioning onto the resin, the eluant which is then washed off will be isotopically fractionated relative to the bulk sample, and the remaining fraction is lost during the first matrix elution. The degree of isotopic fractionation is

dependent on the degree to which the column was saturated, and so varies across samples and cannot be corrected for.

As previously stated, it is exceptionally difficult to separate Ni from Mg due to their similar partition coefficients. If the column does become oversaturated, some amount of Ni will not be retained on the resin and lost as it is eluted with the matrix elements. This results in Ni loss during the procedure, likely accompanying a fractionation, although the extent to which the latter has affected the samples measured in this study is difficult to quantify.

The results of column saturation calculations for individual samples can be seen in Appendix C (Figures 1A – 4D). It should be noted that approximately half of these samples underwent column chemistry but were not analysed for Ni isotopes, as the method employed could not separate Ni from Mg to a sharp enough degree. Asterisks next to sample IDs in table 6 indicate samples from which an Ni isotope measurement was made. Given the extent to which these samples saturated the columns, it is unlikely that many of the final Ni isotope measurements provide an accurate Ni isotope ratio. Figure 4 plots the weight of sample processed prior to column chemistry (in mg, calculated for ~1.5-2 μg total Ni), and the amount of Ni present in the samples prior to double spiking (in μg) against measured Ni isotope ratios. The lack of a distinct relationship suggests that the isotopic analyses have not been impacted by this step of the procedure. In order to progress the original aims of this study, an alternative column chemistry protocol, better geared towards carbonate element separation, must be sought.

Sample ID	Depth	Weight (mg)	μg Ni/sample	[Ni] ppm	Saturation (mEq)	% of resin capacity (1.7 mEq/ml)
1A *	800.18	570.00	8.90	0.30	2.84	83.50
1B	802.13	570.00	4.15	0.16	2.92	86.00
1C *	807.73	570.00	8.28	0.52	2.67	78.62
1D *	817.47	570.00	10.69	0.55	1.40	41.06
1E	822.75	50.00	3.20	0.12	0.48	14.12
1F *	826.28	570.00	9.15	1.04	0.22	6.47
1G	829.22	50.00	4.94	0.63	0.32	9.41
1H *	830.53	50.00	7.18	1.98	0.84	24.71
1I *	831.45	50.00	8.09	2.96	0.62	18.24

1J	832.28	50.00	8.11	2.39	0.70	20.71
1K *	833.08	50.00	6.06	2.29	0.74	21.71
1L *	833.90	50.00	8.58	2.21	0.75	22.06
1LR *	833.90	50.00	9.58	2.31	0.73	21.47
2A *	834.49	50.00	6.50	1.98	0.88	25.88
2B *	835.05	50.00	7.20	2.05	0.82	24.12
2C *	835.88	50.00	9.57	2.68	0.67	19.71
2D *	836.45	50.00	6.46	1.85	0.93	27.35
2E *	837.04	50.00	6.17	1.64	1.05	30.88
2F *	837.79	50.00	5.29	1.93	9.82	288.82
2G *	838.58	50.00	2.32	0.72	1.67	49.03
2H	839.00	570.00	4.12	0.32	2.69	78.97
2I	840.00	570.00	2.41	0.21	2.65	77.97
2J	841.00	570.00	2.70	0.14	2.90	85.24
2K *	842.50	570.00	2.67	0.16	2.86	84.24
2L	843.50	570.00	3.50	0.12	2.98	87.53
2LR	843.50	570.00	3.50	0.13	2.97	87.41
3A	844.50	570.00	4.00	0.20	2.93	86.18
3B	846.50	570.00	3.47	0.20	2.91	85.59
3C	848.50	570.00	2.01	0.12	2.98	87.59
3D	850.80	570.00	10.00	0.14	3.00	88.26
3E *	853.30	570.00	7.34	1.18	2.31	68.00
3F	857.40	570.00	2.17	0.14	0.52	15.32
3G	859.50	570.00	3.77	0.10	0.51	15.00
3H *	863.40	50.00	4.58	1.16	1.74	51.18
3I *	868.30	50.00	2.34	0.28	2.91	85.56
3J	873.40	570.00	8.42	0.74	2.62	76.91
3K *	877.60	570.00	4.20	0.25	2.89	85.09
3L *	881.00	570.00	5.10	0.45	2.23	65.47
3LR *	881.00	570.00	5.10	0.25	2.32	68.12
4A	817.87	50.00	6.67	2.38	0.73	21.47
4D *	820.25	570.00	10.75	0.66	5.29	155.68

Table 6: Milliequivalents (mEq) loaded on to resin per sample. These calculations are based on 1 mL of sample loaded on to 2 mL of Bio-Rad 200-400 mesh AG 50W-X8 resin (capacity: 1.7 mEq/ml) (as per this study). Nickel ([Ni ppb]) refers to the Ni concentration of the sample. Asterisks mark samples from which an Ni isotope measurement was made. For a full break down of individual element saturations per sample, please see tables A1 – D4 (Appendix C). The initial amount of sample weighed, along with the amount of Ni per sample prior to double spiking (ug Ni) is also indicated.
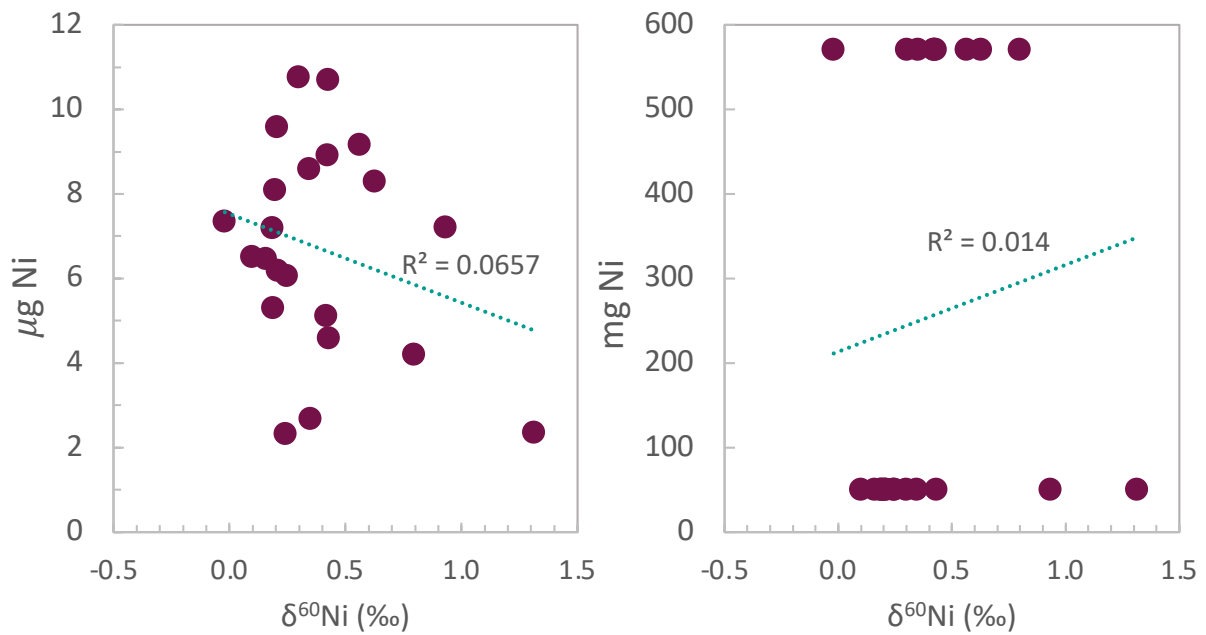
Figure 4: The relationships between μg Ni and δ^{60}Ni, and mg Ni and δ^{60}Ni (see table 6 for values) indicating no distinct relationships between initial volume of sample measured (mg, for 1.5-2 μg Ni), the concentration of Ni prior to double spiking (μg Ni), and the Ni isotope ratios analysed in this study.
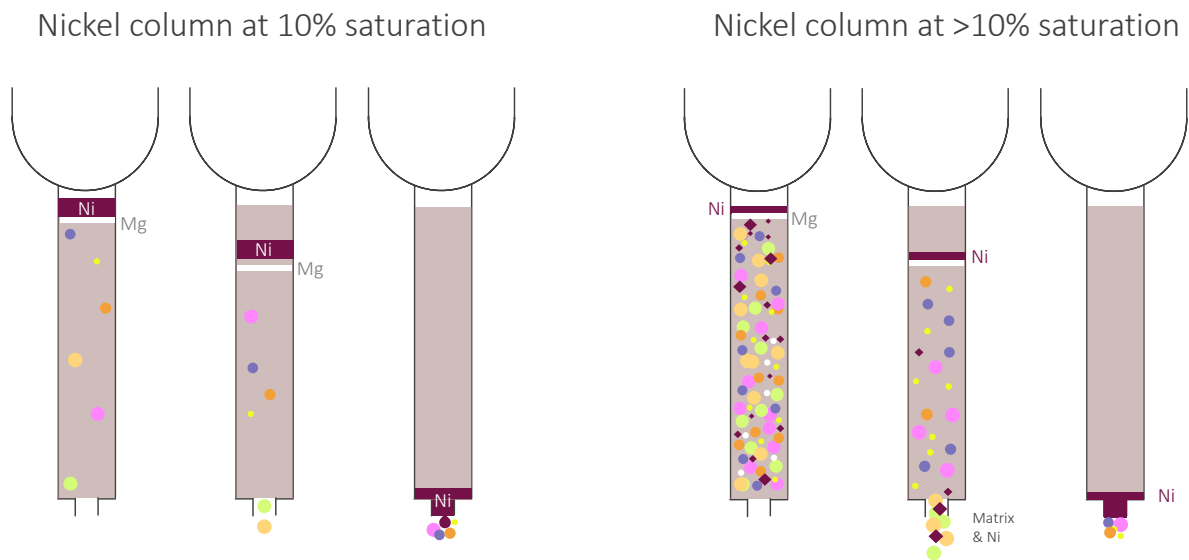
Figure 5: Column oversaturation schematic based on the initial HCl-acetone column used for the analyses presented in this chapter. On the left: a Ni column at <10% saturation, where elements are distributed widely throughout the column. On the right: a Ni column at >10% saturation, where elements are packed together. Nickel is represented as a purple band and as additional purple diamonds in the right panel. Magnesium is represented as a white band, and other matrix elements are shaded by their flame test colour and scaled by their relative atomic masses.

5.4.2 Ways forward

Previous geochemical analyses of this interval of GKF01 have shown a major shift in the dynamics of Earth's atmosphere at ~2.5 Ga (Zerkle et al., 2012; Izon et al., 2015; Izon et al., 2017). Carbon-sulphur anomalies demonstrate perturbations in CH_4 flux to the atmosphere, and this has already been further investigated via Cu isotopes (see Chapter 3, this thesis), revealing a Cu-isotope excursion which precludes the C-S anomaly and has been interpreted as representing aerobic methanotrophy. Methanogenic archaea have been shown to fractionate Ni by up to 1‰ (Cameron et al., 2009), and so have the potential to provide a robust proxy for biological methanogenesis over geological time. As such, and in the suite of rocks analysed in this chapter in particular, Ni isotopes provide a unique and potentially valuable tool for understanding the role of methanogenic archaea in the late Archaean C-S anomalies.

5.4.2.1 Nickel isotopes in GKF01

Figure 6 presents the Ni isotope data analysed in this study, where data points are shaded by column saturation (as calculated above). From this Figure, it is possible to identify one sample which did not oversaturate the resin. This sample provides an Ni isotope value of 0.5‰. Below this, there are a cluster of highly repeatable measurements which only slightly oversaturated the column (10% - 25%) saturation. While 25% saturation may result in some Ni loss, the repeatability of measurements within this interval at up to 25% saturation indicate that this degree of oversaturation may not have severely impacted the data. Considering the data within this interval (i.e., between c. 827 – 839 m depth) with column saturation $\leq$ 25%, $\delta^{60}Ni$ has an average signal of 0.28‰. On the other hand, the entire dataset has a range of 1.34‰ with average of 0.39‰. It is worth noting that the data points spanning 827 – 839 m are all shales with comparatively higher TOC values (~ 2 Wt. % compared to a 'background' of ~0.28 Wt. %), contained a higher proportion of [Ni], and which also were less prone to over-saturating the columns in general, likely due to higher initial Ni/Mg ratios. Nickel concentrations between 827 – 839 m depth correlate strongly to TOC and $\delta^{13}C_{org}$ (Figure 7) which is also consistent with black shale trends; trace metal drawdown is associated with shale deposition (e.g., Ganai et al., 2018). These

trends are not apparent when Ni isotopes are considered alongside these parameters, however (Figure 6).
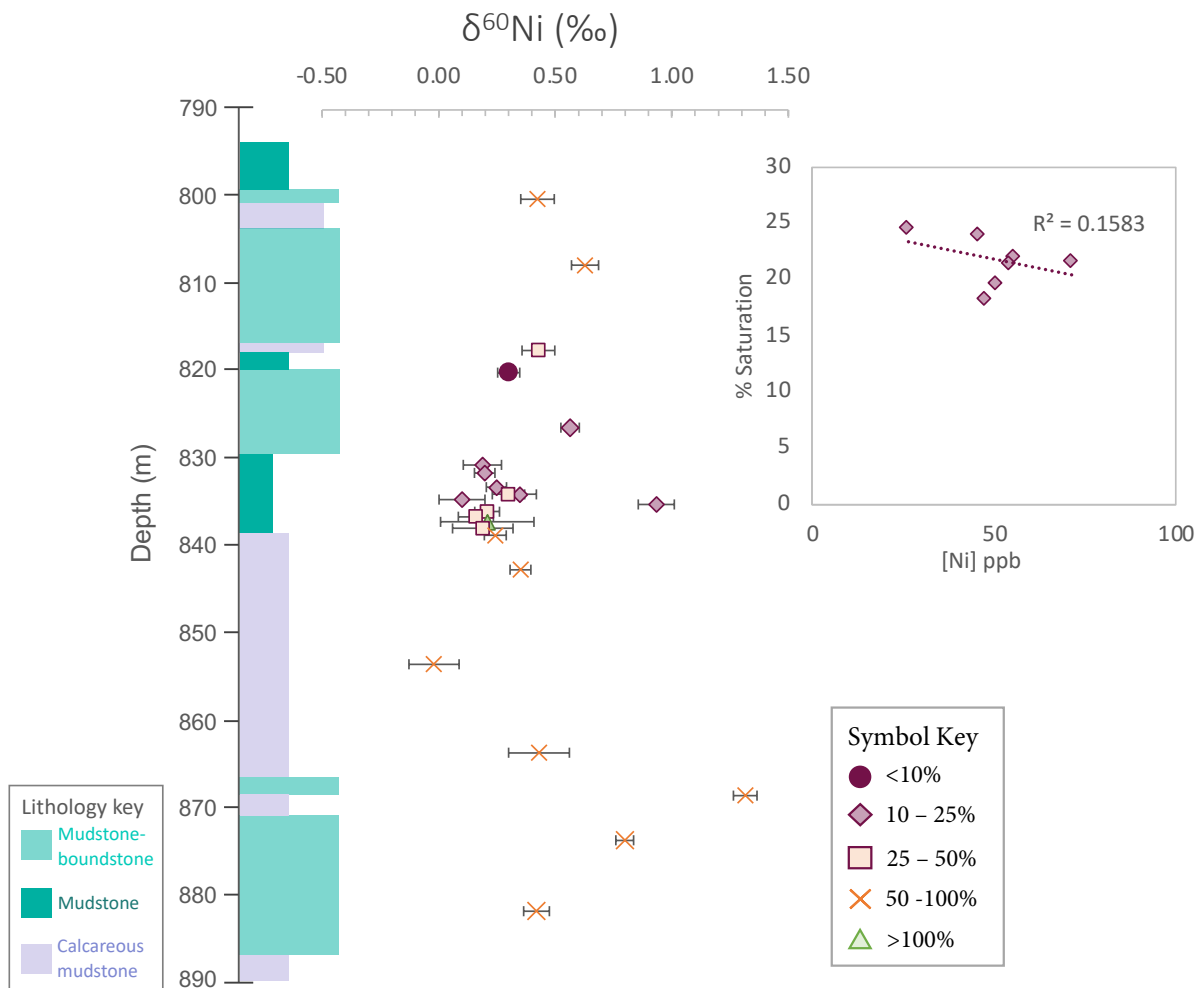
Figure 6: Nickel isotope data shown by column saturation percentage. Column saturation is indicated by symbol shape and colour; the dark purple circle indicates the sample which did not over-saturate the column (i.e., <10% saturation); light purple diamonds indicate samples which moderately saturated the column (10-25%); orange squares indicate samples which oversaturated the columns by 25-50%; orange crosses indicate samples which oversaturate the columns by 50-100%; the green triangle represents the sample which oversaturated the column by over 100%. Error bars are 2SD. The inset graph plots % saturation against Ni concentration for samples which saturated the column by between 10-25%.
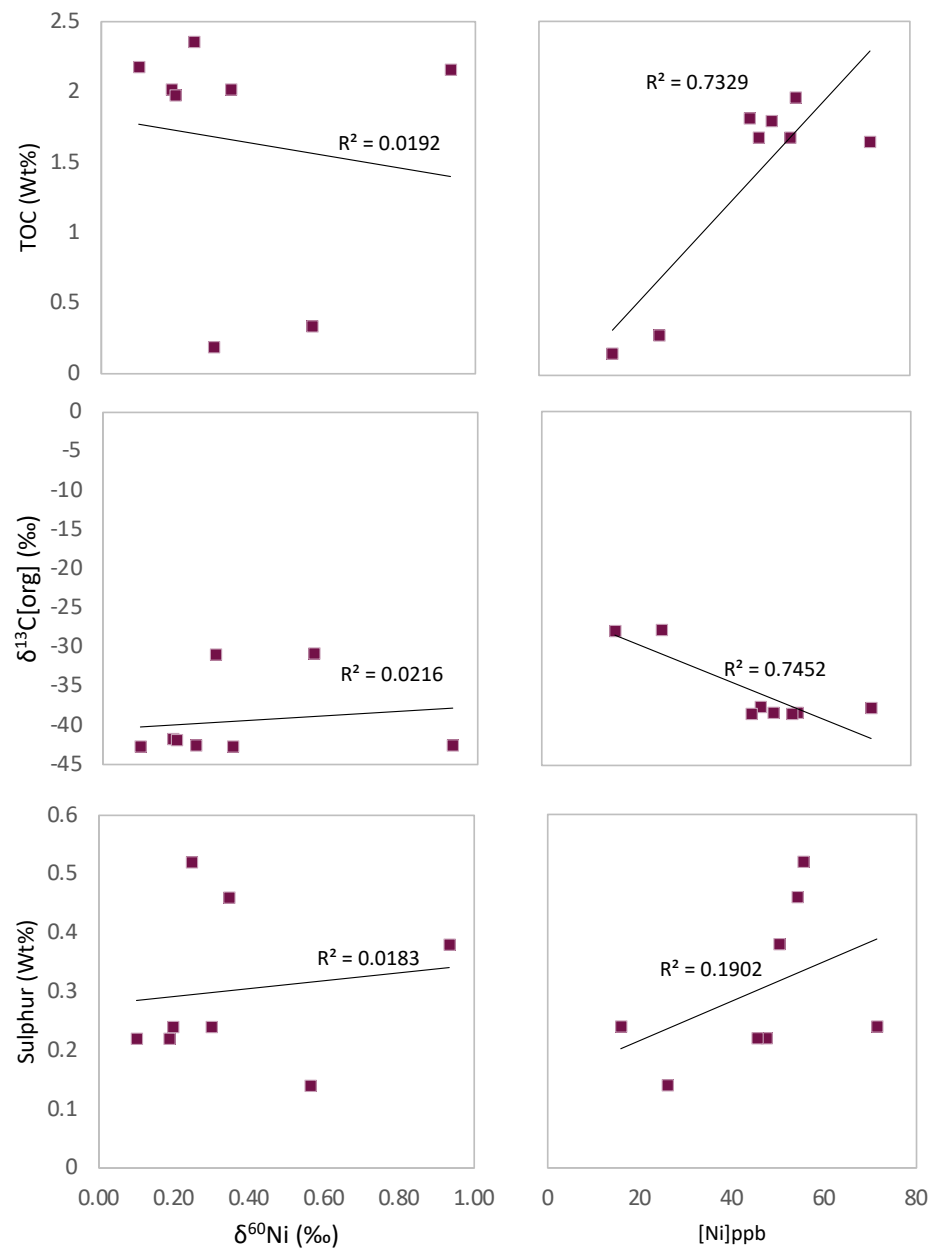
Figure 7: Nickel isotope and abundance data plotted against S, $\delta^{13}C_{org,}$ and TOC (from Izon et al., 2017) for samples which saturated the columns by under 25%. Strong relationships are apparent between Ni concentrations and $\delta^{13}C_{org}$ and TOC, however such trends are conveyed by the isotope data.

Figure 8 plots the average (dark purple circle) and range (dark purple line) of Ni isotope values from this study (specifically the interval between 827 – 839 m; 0.28‰ range). These data are plotted alongside the averages and ranges of other comparative geological materials, including two black shale studies, and the average composition of continental

sediments, basalts, and meteorites as calculated by Cameron et al. (2009). Based on these values, our Ni isotope data fall broadly within the range of two previous black shale studies (Porter et al., 2014; Pašava et al., 2019) and are consistent with the aforementioned abiotic and terrestrial values from Cameron et al. (2009). They also reflect modern black sea euxinic sediment (Vance et al., 2016).
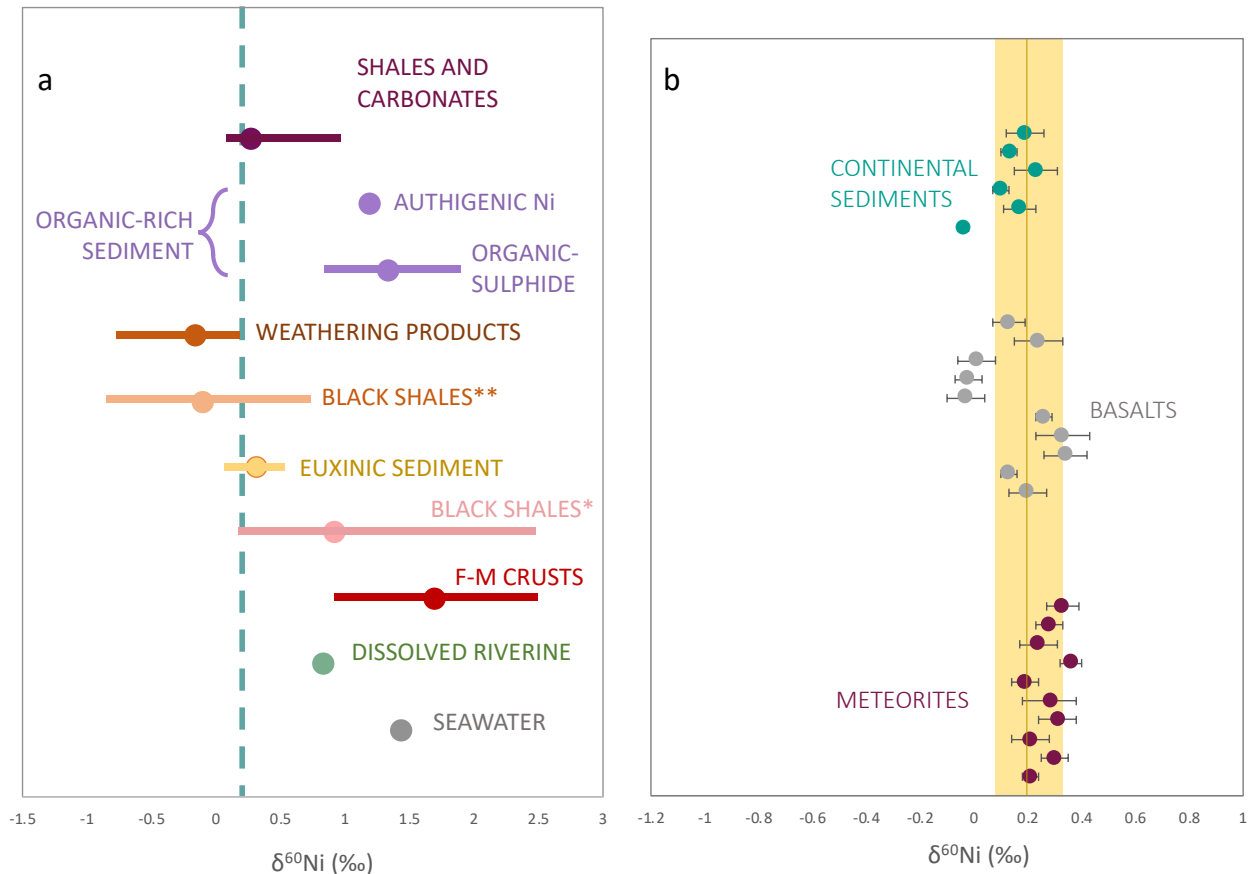
Figure 8: Nickel isotope distributions across a range of geological materials. Panel A plots the data from this study (shales and carbonates; dark purple circle and line) alongside two fractions of modern organic rich sediment (the organic-sulphide fraction and authigenic Ni fraction; Ciscato et al., 2018), weathering products (ultramafic rocks, ores, and soil: Ratie et al., 2015; Spivak Birndorf et al., 2018), black shales** (Palaeoproterozoic, Neoproterozoic, Early Cambrian, and Devonian from Finland, Czechia, China, and Canada respectively; Pašava et al., 2019), Black Sea Euxinic Sediment (Vance et al., 2016), black shales* (Devonian, United Kingdom; Porter et al., 2014), Ferromanganese crusts (Gall et al., 2013), dissolved riverine Ni (Cameron and Vance, 2018), and seawater Ni (Cameron and Vance, 2014). Circles represent average values, and lines represent the ranges. The dashed blue line at 0.2‰ represents the average values for continental sediments, basalts, and meteorites measured by Cameron et al. (2009), which are expanded upon in panel B.

Three key studies of Ni isotope behaviour in modern and ancient organic marine sediments broadly point to three possible controls on Ni isotopes in the marine system:

the weathering environment and source of dissolved Ni (i.e. Porter et al., 2014), sulphidisation of organic matter and the removal of Ni into sulphides (i.e. Pašava et al., 2019), and the degree of uptake in the photic zone (i.e. Ciscato et al., 2018). The Devonian shales analysed by Porter et al. (2014) yielded Ni isotope values ranging between 0.2‰ to 2.5‰, with predominantly higher δ^{60}Ni values than those of abiotic and terrestrial samples as well as modern-day seawater and dissolved riverine Ni. While the Ni isotope values reported in this study are, on average, heavier than those of GKF01, they do reflect the values observed in ferromanganese (F-M) crusts (0.9‰ to 2.5‰). The authors interpret this similarity between shales and F-M crusts covariance as an indicator that the processes governing the Ni isotope values of F-M crusts are likely similar to those governing Ni isotope distribution in the shales; factors ubiquitous to the marine environment play a large role in the Ni isotopic fractionations of these samples. Like our study, Porter et al. (2014) do not observe any correlation between δ^{60}Ni and TOC or [Ni] concentrations, and thus interpret the heavy Ni isotope composition as controlled by the local weathering environment and the dominant sources of dissolved Ni to the ocean. Therefore, our isotope data could be reflective of the local weathering environment at the time of deposition.

Alternatively, the other study involving black shales presents a dataset with significantly more scatter, possibly owing, in part, to the breadth of samples measured. The δ^{60}Ni values in these shales range from -0.84‰ to +0.62‰ (median -0.10‰) (Pašava et al., 2019) which, in contrast to the values reported by Porter et al. (2014), are lighter than abiotic and terrestrial samples, seawater, riverine Ni, and F-M crusts. These authors note that the range in δ^{60}Ni measured in their shales is close to that of the weathering products of mafic and ultramafic rocks (e.g., Ratié et al., 2015; Spivak-Birndorf et al., 2018). Based on this similarity, and considering the assumed low contribution of direct biological Ni uptake along with the dominant residence of Ni within Fe/Ni sulphides, Pašava et al. (2019) interpret the light Ni isotope values in these shales to reflect sulphidisation of organic matter and the removal of Ni into sulphides. Sulphidisation processes have also been suggested to account for the Ni isotope values in modern euxinic sediments (Vance et al., 2016).

Further δ^{60}Ni analyses of modern organic-rich sediments in upwelling zones reveal that the organic - pyrite fractions (isolated from a combination of organic- and carbonate-rich sediments) maintain a Ni isotope signal that is close to that of modern seawater (Ciscato et al., 2018). The observed relationship between Ni concentrations, TOC, and δ^{60}Ni in the sediments analysed by Ciscato et al. (2018) implies that the δ^{60}Ni signal reflects biological Ni uptake in the photic zone, and that this signal survives transport to the sediment

Again, acknowledging the caveats above, I will spend the remainder of this discussion considering potential interpretations of this dataset within the capacity of Figure 2a and the aforementioned shale study interpretations. The average δ^{60}Ni value of the central cluster of our dataset (0.28‰) is consistent with the isotopically heavier weathering products analysed by Ratié et al. (2015) and Spivak-Birndorf et al. (2018), as well as with the lighter black shales analysed by Porter et al. (2014) and, to an extent, the isotopically heavier black shales analysed by Pašava et al. (2018) (plotted in Figure 7). The data presented in this study are also consistent with δ^{60}Ni values measured in Black Sea euxinic sediments, which the authors suggest are also controlled by sulphidisation processes (Vance et al., 2016).

Within core GKF01, SEM-EDX analyses indicate that any discernible Ni is present within the sulphide fraction of the samples, and it has been previously suggested (see Chapter 3) that these sulphides formed during the primary diagenesis of organic matter via microbial sulphate reduction (MSR). If searching for biosignatures reflective of such a process within the Ni isotope system, we would anticipate any evidence for methanogenic fractionation of Ni isotopes to manifest as a negative Ni isotope excursion to lighter isotope compositions. While it still cannot be yet ruled out, as all interpretations of the Ni isotopes measured in this study must be treated with caution, the above studies suggest that these data could be more representative of sulphidisation processes occurring within the sediment, and therefore potentially reflect the localised removal of Ni into sulphides. However, due to the limited nature of this dataset, there is no 'background' signal from which to evaluate this interval against. As within this thesis it has been previously suggested that biotic signals are preserved within the sulphide phases, it cannot completely be ruled out that the role of biology in recorded the signal presented here. It

would therefore be prudent to briefly assess these data within the context of previously generated unequivocal evidence for CH_4 cycling throughout core GKF01. Notably, given that methanogens are known to fractionate Ni isotopes, the potential lack of signal within this interval is remarkable.

Chapter 3 has demonstrated that diagenesis is unlikely to have contributed to any significant overprinting of Cu isotopic signatures in these samples, and this argument can be extended to Ni; it has been demonstrated that Cu and Ni behave similarly during early-stage diagenesis (e.g., Audry et al., 2006). As such, a primary cause must be sought. While the Archaean 'Nickel famine' (a hypothesis which proposed that Ni cycling in the Archaean rapidly decreased and led to the widespread suppression of methanogenic metabolisms (i.e., Konhauser et al., 2009) has been largely discounted, Ni was by no means abundant in the late Archaean marine system. In a recent Ni isotope study of Mesoarchaean and Palaeoproterozoic glacial deposits, which were previously considered for use as Universal Continental Crust (UCC) proxies, Wang et al. (2019) demonstrated that an increase in oxidative weathering of crustal sulphides released a small but sustained pool of Ni to rivers and oceans. To that end, it is possible that Ni sustained methanogenic activity throughout the Archaean, however the low availability of Ni – especially during a period of enhanced methanogenic activity – led to a period of non-selective Ni uptake by these organisms. Complete uptake of Ni would lead to a system where Ni input = Ni output, resulting in no discernible Ni isotope fractionations in any bulk-rock analyses.

5.5 Conclusion

This study aimed to produce a high-resolution Ni isotope record of core GKF01 in order to explore the role of methane cycling during a known PHE (e.g., Izon et al., 2017), and to test the hypothesis that Ni isotopes can be applied as biomarkers in geological materials. The samples selected for analysis represented a suite of mudstones, mudstone-boundstones, and carbonate-rich calcareous mudstones deposited in an oxygen-free shallow marine environment at c. 2.5 Ga. Due to the high ratio of matrix elements to Ni reflected in the calcareous mudstones and mudstone-boundstones and the impact on this

on the Ni separation procedures carried out, accurate Ni isotope data could not be acquired for the full suite of samples. The eight samples (spanning 827 – 839 m) which did not oversaturate the columns, and which mainly belong to the organic-rich mudstone layer and the overlying mudstone-boundstone unit, may be able to provide a loose indication of what to expect if further Ni analyses were undertaken of this core. Based on comparisons to previous Ni isotope datasets from similar materials, the eight data points seem to reflect sulphidisation processes, which is consistent with the observation that Ni is contained with the sulphide phase of the samples. As such, the Ni isotope signal could reflect surface-water biological uptake or, alternatively, the source of the Ni. Any future studies directed at further exploring these pilot data must consider the development of analytical methods tailored to these samples.

In order to effectively separate Ni from matrix elements in this suite of samples, the nuances between lithologies must be taken into consideration. While these differences did not pose as issue for Cu measurements (see chapters 3 and 4), it is clear that they had a significant impact on Ni in this instance. Given the differences in carbonate and shale matrices, along with the low Ni concentrations, it is unlikely that one single approach will be successful; the shale samples and carbonate-rich samples require different methods. It is also probable that, while methods which do not use DMG may be successful with certain samples, it is not the case for these in particular. The samples from core GKF01 will ultimately require some form of DMG in order to ensure the highest degree of separation between Ni and matric elements.

For the samples containing a carbonate-rich matric (approximately 50% of this sample set), it would be prudent to employ a method specifically designed for the separation of Ni from carbonate. Castillo-Alvarez et al. (2020) successfully measured mass-dependent Ni stable isotopes in carbonate via a five-step purification method utilising an Ni-specific resin. This method, accompanied by the method used by Porter et al. (2014) to separate Ni from organic-rich shale matrices, could provide a straight-forward protocol for future attempts to measure Ni isotopes in core GKF01. However, while employing methods specifically designed for the sample lithology is an appropriate starting point, this alone will likely not circumvent the issue of column saturation. Alongside the use of DMG/a

Ni-specific resin, larger columns, a higher volume of resin, and a smaller aliquot of sample in the initial load will also increase the chances of successful separation; as such, an experimental, trial-and-error approach will be required to ensure success.

Ultimately, the data generated in this study provide an interesting starting point for further analyses of Ni isotopes in these samples, along with similarly well-preserved lithological units. Applying more robust column chemistry methods to the high-carbonate samples would likely result in the production of more reliable data to further explore the hypotheses outlined earlier in this chapter.

Chapter 6

Conclusions and future work

6.1 Revisiting the aims and objectives

The aim of this thesis was to explore the use of the Cu and Ni isotope systems as biomarkers for biological CH_4 cycling in the mid- to late-Archaean. This overall aim was broken down into five research questions presented in Chapter 1 (see table 1, reproduced from Chapter 1). Each research chapter (chapters 3, 4, and 5) has dealt with at least one research question, applying the isotope geochemical techniques for the respective metal isotope systems to Archaean sedimentary rock sequences. This chapter summarises the results presented in this thesis, and the overall conclusions and wider implications are discussed, along with the possible future directions of this work.

	Research Question	Chapter
1	How can isotopic analysis of Cu and Ni contribute to our understanding of historic methane cycling behaviour in ancient lakes and oceans?	3, 4, 5
2	To what extent can Cu isotopes provide constraints on aerobic methane oxidation in deep time?	3, 4
3	In what way was methane oxidation a contributing factor to the extremely depleted $\delta^{13}C_{org}$ measured in core GKF01?	3, 5
4	Is there evidence of this in older rocks from Western Australia which possess similar $\delta^{13}C_{org}$ signatures to those in GKF01 in a contrasting environment?	4
5	To what extent can Ni isotopes provide constraints on methanogenesis in deep time?	5

Table 1: Research questions addressed in this thesis.

6.2   Answering the research questions

Q.1: How can isotopic analysis of Cu and Ni advance understanding of historic methane cycling behaviour in lakes and oceans? (Chapters 3, 4, and 5)

The respective isotope systems of Cu and Ni have the potential to provide further valuable constraints on two of the key metabolisms which underpin biological CH_4 cycling. Certainly, when examined alongside pre-existing geochemical indicators of biological CH_4 cycling (chiefly C isotopes), both Cu and Ni can provide valuable insights into the ecology of the system.

Chapters 3 and 4 explore the application of Cu isotopes to exceptionally-well preserved sedimentary cores from the Kapvaal and Pilbara cratons respectively. Core GKF01 (Kapvaal craton) represents a suite of *c.* 2.5 Ga sedimentary rocks and has previously been subjected to sulphur (both mass dependent and mass independent) and carbon isotope study, revealing compelling evidence (C-S anomalies) for a series of periodic haze events (PHEs), during which Earth's atmosphere was dominated by a CH_4-rich hydrocarbon haze (e.g., Zerkle et al., 2012; Izon et al., 2017). Of note, the extensively depleted $\delta^{13}C_{org}$ analysed by Izon et al. (2017) in the 100m high resolution section of core GKF01 also analysed in this thesis is strongly suggestive of extensive assimilation of organic matter into sediment which, coupled with the evidence for a CH_4-rich atmosphere, is hypothesised to have occurred via methanotrophy. Previous analyses of core SV1, a *c.* 2.7 Ga sedimentary sequence from the Pilbara craton (Western Australia), have yielded some of the lowest $\delta^{13}C_{org}$ values in the geological record (-48‰) which are also believed to reflect methanotrophy (e.g., Eigenbrode and Freeman, 2006).

Methanotrophy, the biological process by which microbes metabolise CH_4, occurs via two pathways. The first, anaerobic oxidation of methane (AOM), is carried out by a syntrophic consortium of sulphate-reducing bacteria (SRB) and methanotrophic archaea (ANME) in anaerobic environments. Metabolically, AOM is hypothesised to occur via a

reversal of the Ni-dependent methanogenesis pathway (e.g., Hallam et al., 2004). This pathway has been suggested as the methanotrophic pathway responsible for the strongly depleted $\delta^{13}C_{org}$ found in late Archaean rocks, largely due to the fact that it is an anaerobic metabolism and that it likely evolved soon after biotic methanogenesis and prior to any O_2-based metabolisms (Sauterey et al., 2020). However, the dependence of ANME on forming consortia with SRB means that this metabolism is, to a degree, sulphate dependent. Geochemical data from GKF01 and SV1 cores, as well as other well-preserved sections, indicate low-sulphate conditions persisted throughout the mid- to late-Archaean (Crowe et al., 2014), possibly limiting the degree to which SRB-linked AOM could have occurred.

Methane can also be metabolised via aerobic methane oxidation, which is carried out by two classes (α and γ) of Proteobacteria. Aerobic methanotrophs metabolise CH_4 with the help of the methane monooxygenase (MMO) enzyme, either in Cu-dependent particulate (pMMO) or the Fe-dependent soluble (sMMO) form. Type I methanotrophs (pMMO-expressing γ-Proteobacteria) possess a competitive advantage over type II (sMMO-expressing α-Proteobacteria) in low CH_4 environments, however, increases in CH_4 concentrations cause this relationship to switch (Hanson and Hanson, 1996). Relating this to metal usage, one would expect a higher degree of Cu usage in low CH_4 conditions, reflecting the expression of pMMO within the microbial communities. Therefore, in order for Cu isotopes to reflect aerobic methanotrophy in any given section, the prevailing environmental conditions would need to reflect a relatively low CH_4 environment. Previous isotope studies have demonstrated that Cu isotopes are fractionated by microbes such as Escherichia coli (e.g., Navarrete et al., 2011), however this is yet to be demonstrated in aerobic methanotrophs. Nevertheless, this thesis hypothesises that aerobic methanotrophs do fractionate Cu isotopes and the remaining discussion works under the assumption that this could be the case.

Q.2: To what extent can Cu isotopes provide constraints on aerobic methane oxidation in deep time? (Chapters 3 & 4)

In core GKF01 (analysed in high resolution in Chapter 3) a Cu isotope excursion occurs at the base of the C-S anomaly, between 838.6 – 850.8 m. In this 12m section, $\delta^{65}Cu$ values deviate from a background of 0.05‰ (close to BSE estimates) to -0.66‰. Precluding diagenetic, mineralogical, and redox Cu isotope fractionation effects, this signal is interpreted to represent an increase in aerobic methanotrophy under low CH_4 conditions (the latter of which is reflected in the contemporaneous $\delta^{13}C_{org}$ and S-MIF data; Izon et al. (2017)). The sharp recovery of the $\delta^{65}Cu$ excursion is thus further interpreted as representing a relatively sharp switch to Fe-dependent sMMO-based aerobic methanotrophy due to the rapid increase in CH_4; O_2-starved conditions would suppress high levels of aerobic methanotrophy, leading to a system where CH_4 production > CH_4 consumption. Precluding diagenesis, Chapter 3 thus provides strong evidence to suggest that Cu isotopes are a valid proxy for aerobic methanotrophy, and in this instance has provided appreciable constraints on aerobic methanotrophy in deep time.

In core SV1 (analysed in Chapter 4), the $\delta^{65}Cu$ record is stable throughout the 100m section, with absolute values similar to bulk silicate Earth. This likely reflects the $\delta^{65}Cu$ value of the Cu inputs to system. While this may imply a lack of Cu uptake by aerobic methanotrophy, the presence of aerobic methanotrophy cannot be entirely discounted. Instead, the lack of variation within the $\delta^{65}Cu$ record could be explained by Fe-dependent sMMO-expressing aerobic methanotrophs, which are believed to possess a competitive advantage in environments with high levels of CH_4 (e.g., Semrau et al., 2011). Alternatively, Cu could be being used to completion by pMMO-expressing aerobic methanotrophy, as high biological productivity levels are known to have been sustained within the Tumbiana system (e.g., Stueken et al., 2017).

In Chapter 4, Cu isotopes may not provide direct constraints on deep time aerobic methanotrophy and instead reflect overprinting by volcanic detrital input (or sedimentary phase homogenisation). However, the lack of variation in this high-resolution $\delta^{65}Cu$ record could highlight the ecological significance of the pMMO-sMMO

switch in aerobic methane cycling. Certainly, these data highlight the importance of the prevailing depositional environmental conditions in understanding ancient Cu cycling. Ultimately, these Cu isotope investigations demonstrate clear potential for Cu isotopes to provide constraints on deep-time aerobic methanotrophy.

Q3: In what way was aerobic methane oxidation a contributing factor in the extremely depleted $\delta^{13}C_{org}$ measured in core GKF01 (Chapters 3 & 5) and Q4: is there evidence of this in older rocks from Western Australia, which possess similar $\delta^{13}C_{org}$ signatures to those in GKF01 in a contrasting environment? (Chapter 4)

As discussed above, aerobic methanotrophy has previously been suggested as the metabolism responsible for the depleted $\delta^{13}C_{org}$ records observed throughout Archaean drill cores, however $\delta^{13}C_{org}$ records alone are not enough to differentiate between methanotrophic pathways. Copper isotopes have the potential to reflect certain aerobic methanotrophy pathways, and it has already been demonstrated that Ni isotopes are fractionated by methanogenic archaea (Cameron et al., 2009). It is also possible that anaerobic methanotrophy. which is hypothesised to involve a reversal of the methanogenesis pathway, could also fractionate Ni isotopes, however given the lack of evidence for this, the primary application of Ni isotopes to core GKF01 was to investigate methanogenic activity.

while it can be said with some confidence that aerobic methanotrophy occurred at the base of the PHE, it cannot be established from this research whether aerobic methane oxidation directly contributed to the depleted $\delta^{13}C_{org}$ previously recorded in this core. Chapter 3 does not directly answer Q.3, as the Cu-dependent pMMO enzyme is predominantly expressed in low CH_4 conditions and is therefore presumably absent during the PHE interval. However, if aerobic methanotrophy was occurring at the base, and accounting for the low sulphate conditions, it is likely that some form of aerobic methanotrophy continued throughout the section. Based on what is known about ecology of methanotrophic bacteria, it is possible that the methanotrophy occurring throughout the PHE was carried out by Fe-dependent s-MMO expressing methanotrophs, and

therefore α-proteobacteria are responsible for the depleted $\delta^{13}C_{org}$. Further to this, the Ni isotope record presented in Chapter 5 may suggest that Ni isotopes were either not fractionated by biology during this interval or Ni was used to completion. The former interpretation would further support the predominance of an aerobic methanotrophic metabolism, while the latter could indicate extensive assimilation of Ni by both methanogenic archaea and anaerobic methanotrophic bacteria, such that all Ni is used to completion.

The Cu isotope data presented in Chapters 3 and 4 demonstrate that the ability of Cu isotopes to record aerobic methane oxidation depends strongly on the depositional environment. Based on these findings, it is likely better to focus future Cu isotope analyses of a similar nature on shallow marine environments.

Q5: To what extent can Ni isotopes be utilised as a proxy for methanogenesis in deep time? (Chapter 5)

As it has already been demonstrated that Ni isotopes are fractionated by methanogenic Archaea (i.e., Cameron et al., 2009), the application of the system to ancient sedimentary rocks is a natural next step. However, the nature of biological Ni utilisation (namely the use of Ni by methanogens and anaerobic methanotrophs) has the potential to complicate the interpretation of Ni isotope signals in geological materials. The data presented in Chapter 5 could be indicative of a system in which the high levels of methanogenesis lead to complete consumption of Ni, yet the presence of AMO could also contribute to this. Understanding the nuances between these two metabolisms may require larger scale Ni isotope analyses across a wide range of depositional environments and time periods (e.g., across GOE). The processes by which Ni is incorporated into sulphides may also require further attention, as the initial data collected in Chapter 5 are also consistent with the Ni isotope values of euxinic sediments (which are hypothesised to be controlled by sulphidisation processes).

Table 2 summarises the metabolisms investigated in this thesis along with their metal centres, estimated divergence times, and metabolic pathways. Below, the environmental conditions and ages of the geological cores analysed are shown. The Cu isotope values are also provided.

Metabolism	Kingdom/class	Metal centre(s)	Electron acceptor	Estimated divergence	Metabolic pathway
Anaerobic methanotrophy	Archaea	Ni (cofactor F_{430})	SO_4^{2-} NO_3^- Fe(III)	~3.6 Ga (based on Euryarchaeota divergence from Archaea)	MCR
Aerobic methanotrophy	Alpha (α)-Proteobacteria	Fe (sMMO)	O_2	2.7 - 2.5 Ga	Serine
	Gamma (γ)-Proteobacteria	Cu (pMM)			RuMP

Core	Environment	Metals present		Age (Ga)	$\delta^{65}Cu$ (‰)
GKF01	Shallow marine	Cu, Ni, Fe (trace)	CH_4, CO_2	2.5	+0.05 to -0.66
SV1	Shallow (high pH?) lacustrine	Cu, Ni, Fe	O_2, CH_4, CO_2	2.7	+0.05

Table 2: Summary table of the metabolisms and environments studied in this thesis. Age constraints for divergence times come from Battistuzzi et al. (2004) and Moore et al. (2017).

6.3 Future work

The work in this thesis addresses several outstanding questions pertaining to late Archaean CH_4 cycling by exploring the use of novel metal isotope systems as geochemical proxies. The use of these novel techniques applied to unique and exceptionally well-preserved geological materials has created a solid base from which to expand and capitalise on this information. This thesis has provided compelling evidence for the

presence of aerobic methanotrophy preceding a PHE, which can, by extension, demonstrate a biological impact on earth's atmosphere prior to the GOE. Furthermore, this thesis provides the first high resolution Cu and Ni isotope records across two ancient and well-preserved sedimentary drill cores. The data generated through these analyses provide a clear basis from which to conduct further analyses.

Based on the data presented here, several potential research directions can be identified. Initially, these are:

1) Exploring whether aerobic methanotrophic bacteria fractionate Cu isotopes. Such experiments should consider the use of both natural populations of aerobic methanotrophs, alongside pure cultures. Initial experiments could involve establishing the Cu, O_2, and CH_4 limitations of these organisms, so as to ensure both a) the expression of pMMO, and b) that the ratio of biomass:Cu is high enough that any Cu uptake is discernible. Most growth medias provide a surplus of trace metal nutrients, and so care should be taken to create an effective media for effective isotopic analyses.

2) Undertake Cu isotope analyses in high resolution across another PHE within the Upper Nauga Formation, in order to investigate whether Cu isotopes exhibit similar behaviour during other periods of enhanced CH_4 cycling. If a similar Cu isotope excursion is measured at the base of an early PHE, it could provide evidence of ecological patterns; Cu isotopes could effectively 'predict' or mark the beginnings of enhanced CH_4 cycling across other cores.

3) Verifying the GKF01 Ni isotope data presented in Chapter 5 by repeating Ni isotope analyses via a DMG-based separation method. While there is reasonable evidence to suggest that the data are reflective of the true Ni isotopic composition of these sediments, expanding the analyses to the entire core will provide conclusive data with which to proceed.

4) In a similar vein to point (2), undertaking Ni isotope analyses of core SV1, to test both the applicability of Ni isotopes as biomarkers in ancient sedimentary rocks, but also to investigate the behaviour of Ni isotopes in a productive lacustrine system with higher O_2 availability.

5) Targeting specific fractions of the core SV1 sediments. Core SV1 does not exhibit the same perturbations as core GKF01 with regards to C-S data, and an excursion in either Cu or Ni is not anticipated. As such, if future Cu isotope analyses of the organic fraction or of the sulphide phases within core SV1 provided Cu isotope values which consistently deviate from BSE-type values, these data could rule out complete consumption.

6) Undertaking further geochemical and biological investigations of anaerobic methane oxidation, in order to first ascertain whether this metabolism is truly Ni-dependent and, if so, to explore whether Ni isotopes are also fractionated by this metabolic process.

APPENDIX A

SEM spectra:
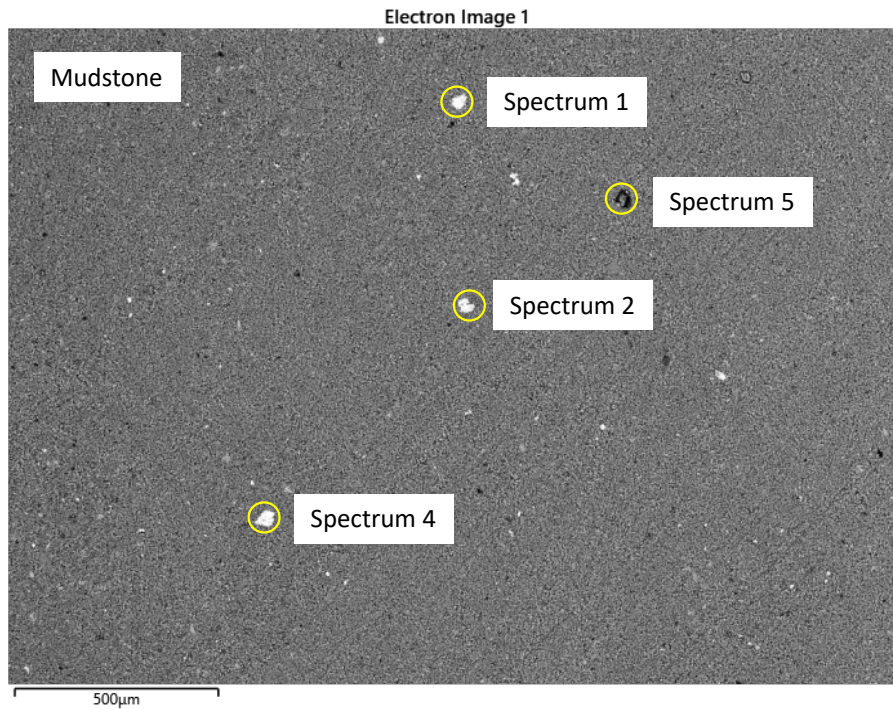
Figure 1a: SEM image of a mudstone sample from core GKF01 (834.93 - 834.95 depth)
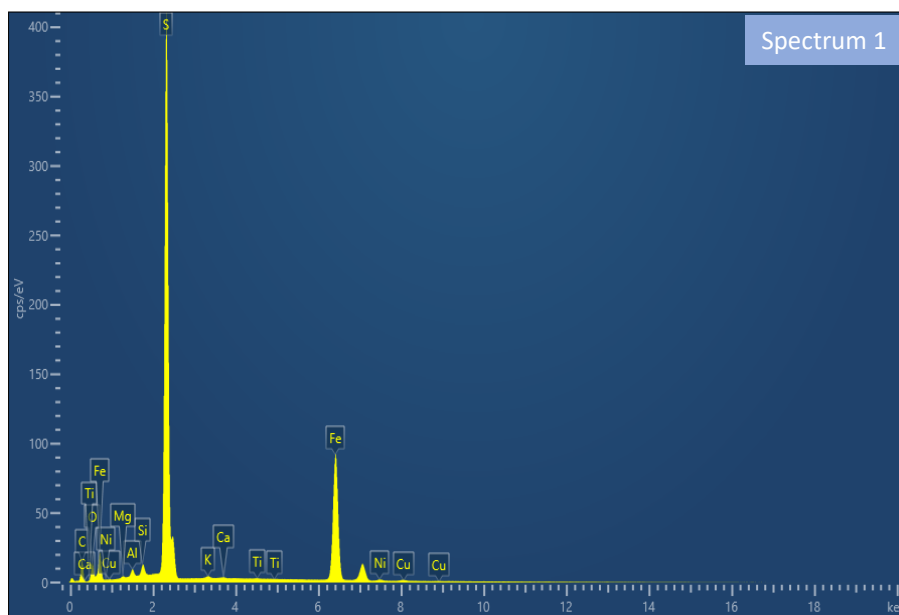
Figure 1b: Spectrum 1 at full scale (sulphide).
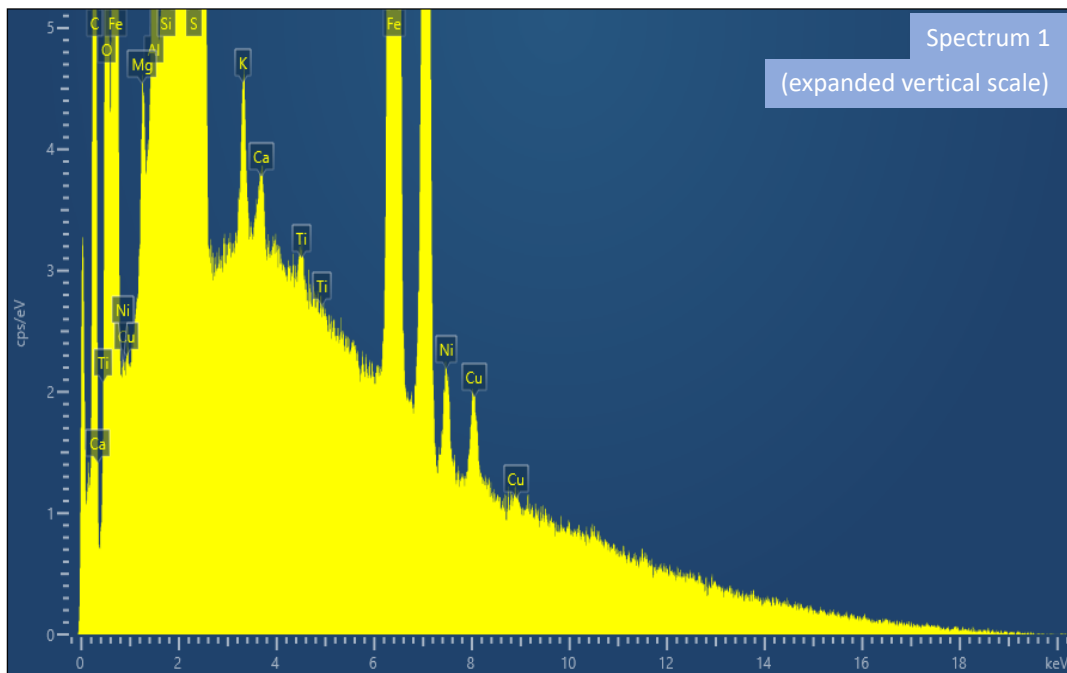
Figure 1c: Spectrum 1 with an expanded vertical scale, showing Ni and Cu peaks (sulphide).
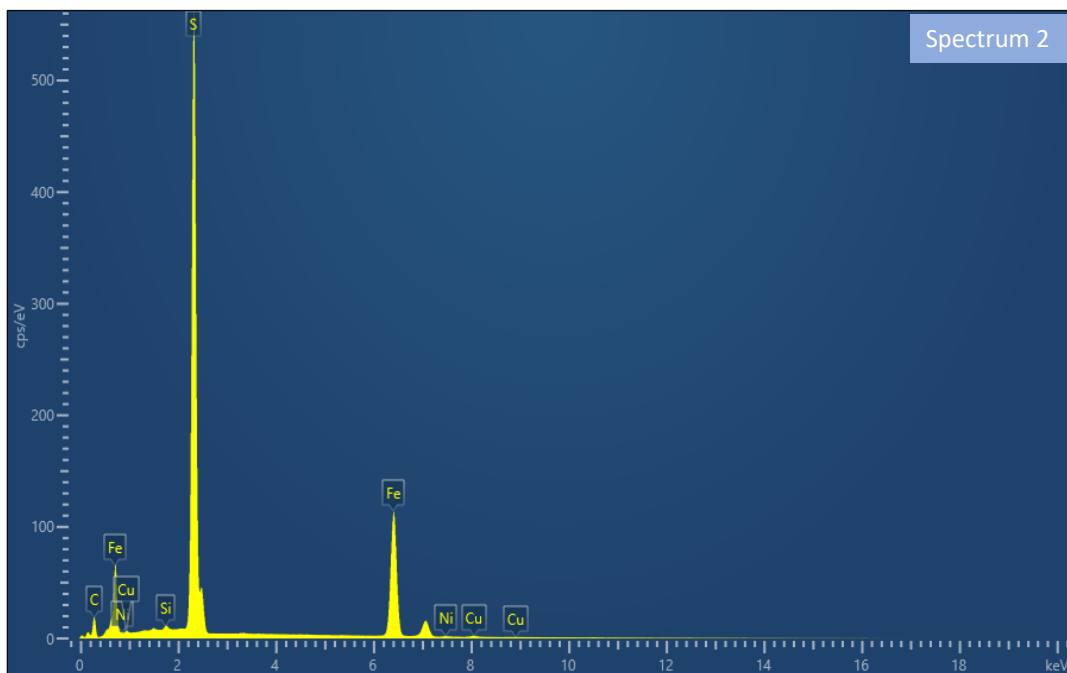
Figure 1d: Spectrum 2 at full scale (sulphide).
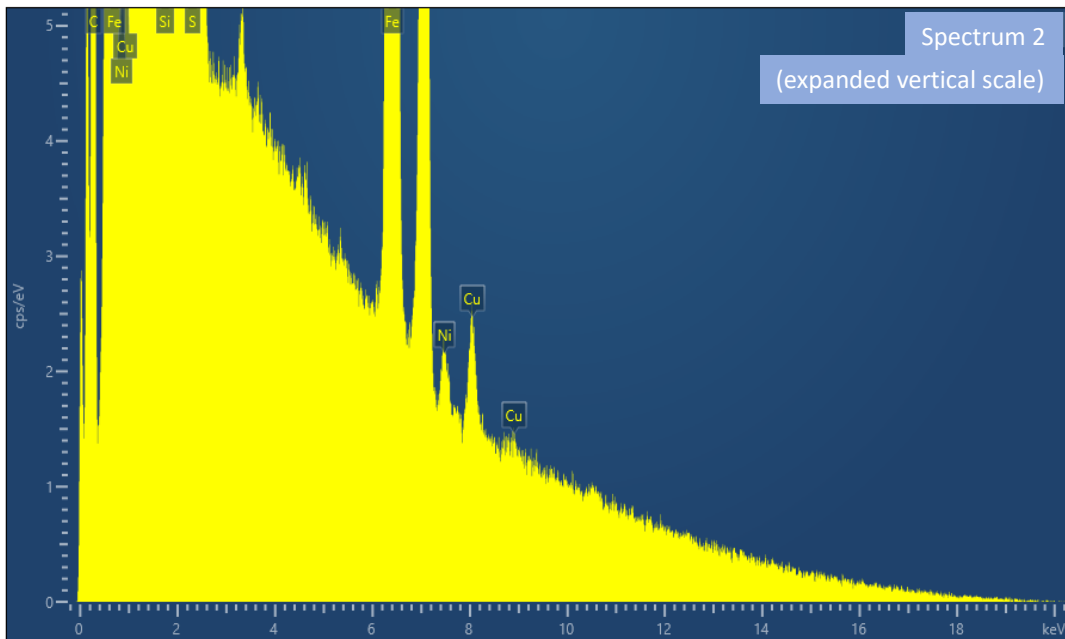
Figure 1e: Spectrum 2 with an expanded vertical scale to highlight Cu and Ni peaks (sulphide).
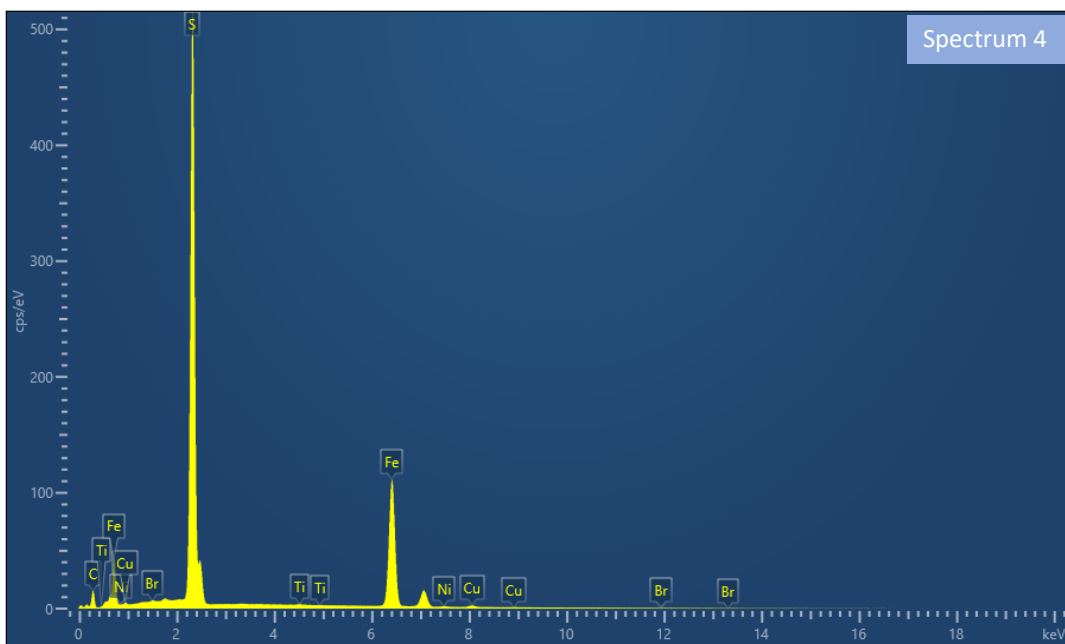
Figure 1f: Spectrum 4 at full scale (sulphide).
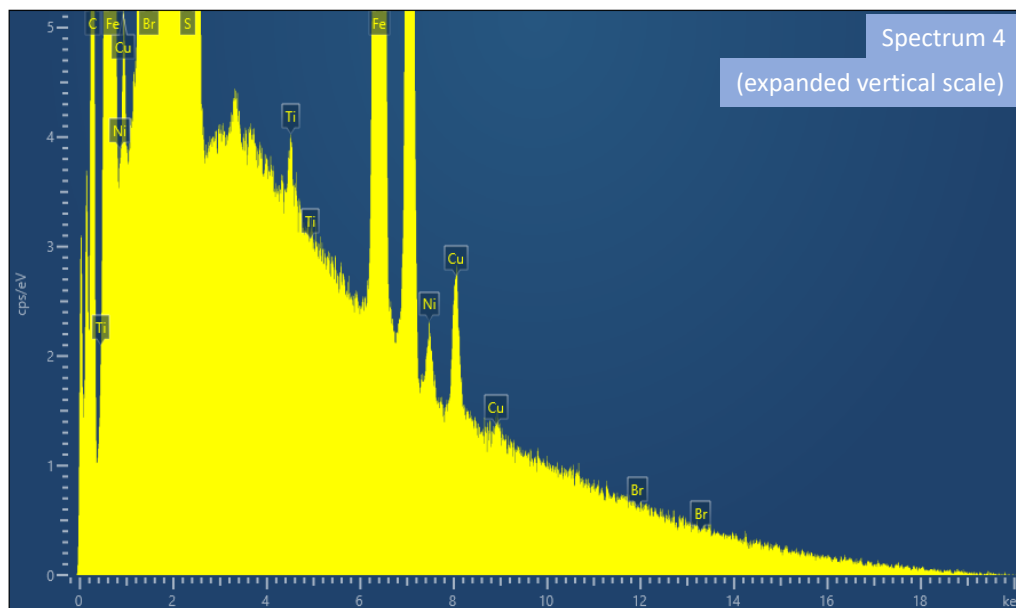
Figure 1g: Spectrum 4 with an expanded vertical scale (sulphide).
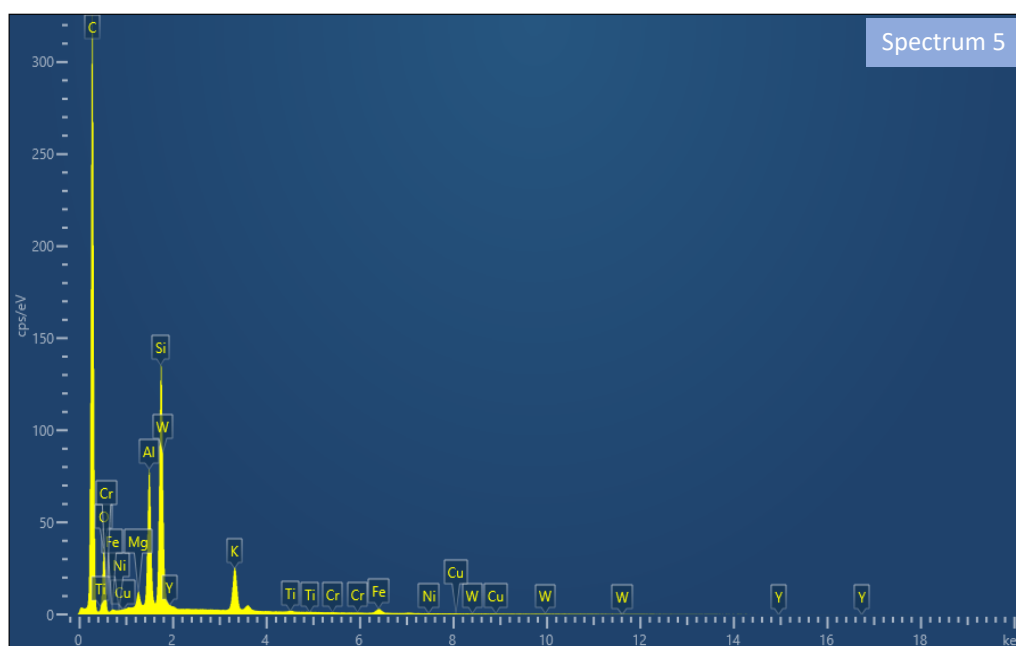
Figure 1h: Spectrum 5 (organic-rich matrix/pore space)
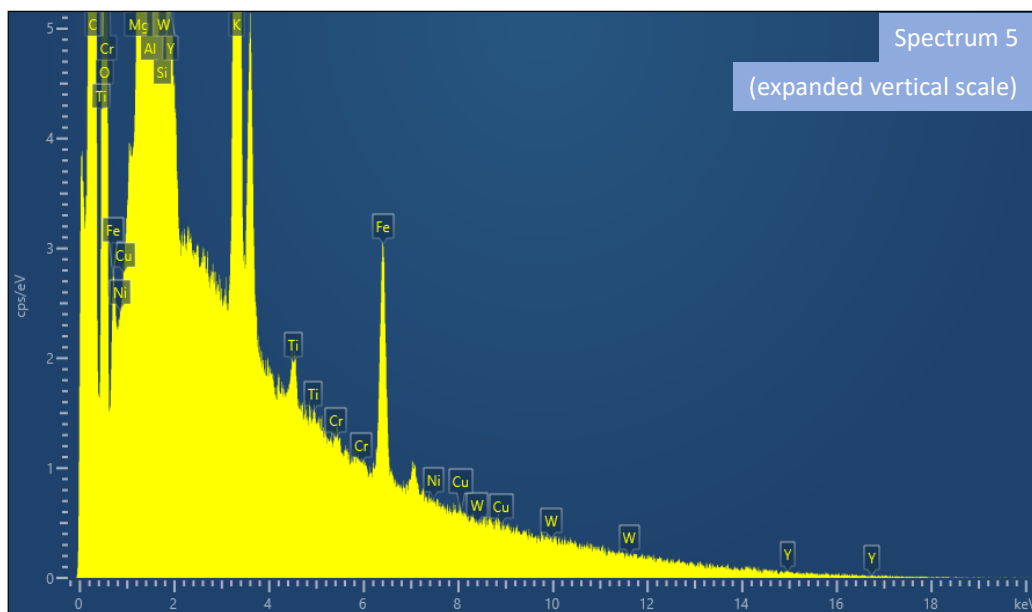
Figure 1i: Spectrum 5 with expanded vertical scale showing low Cu and Ni (organic-rich matrix/pore space).
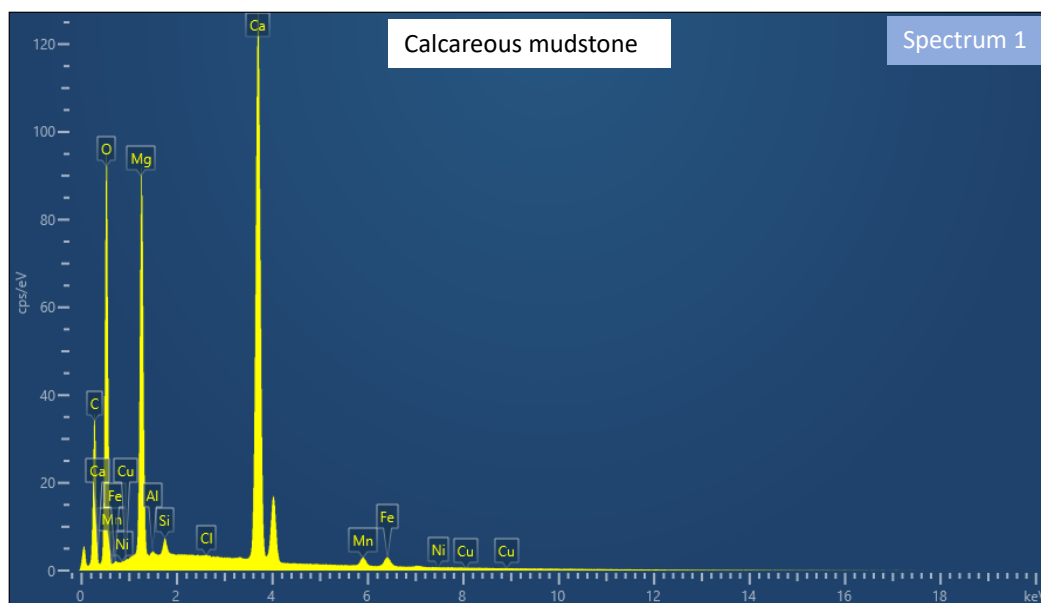
Figure 2a: Spectrum 1, averaging a whole area of sample (depth 846m; calcareous mudstone).
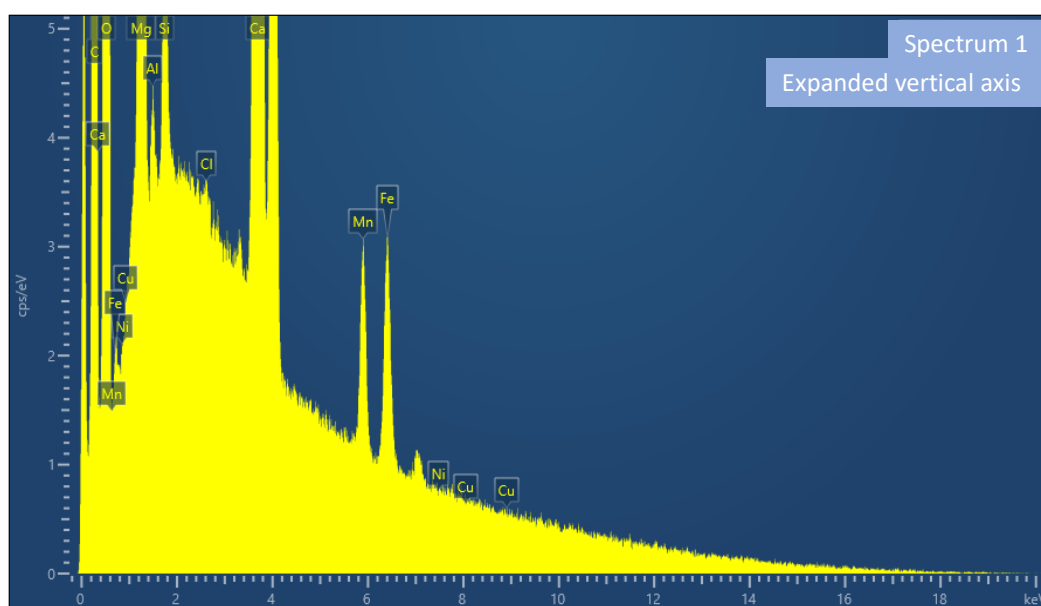
Figure 2b: Spectrum 1, averaging a whole area of sample with expanded vertical axis (depth 846m; calcareous mudstone).
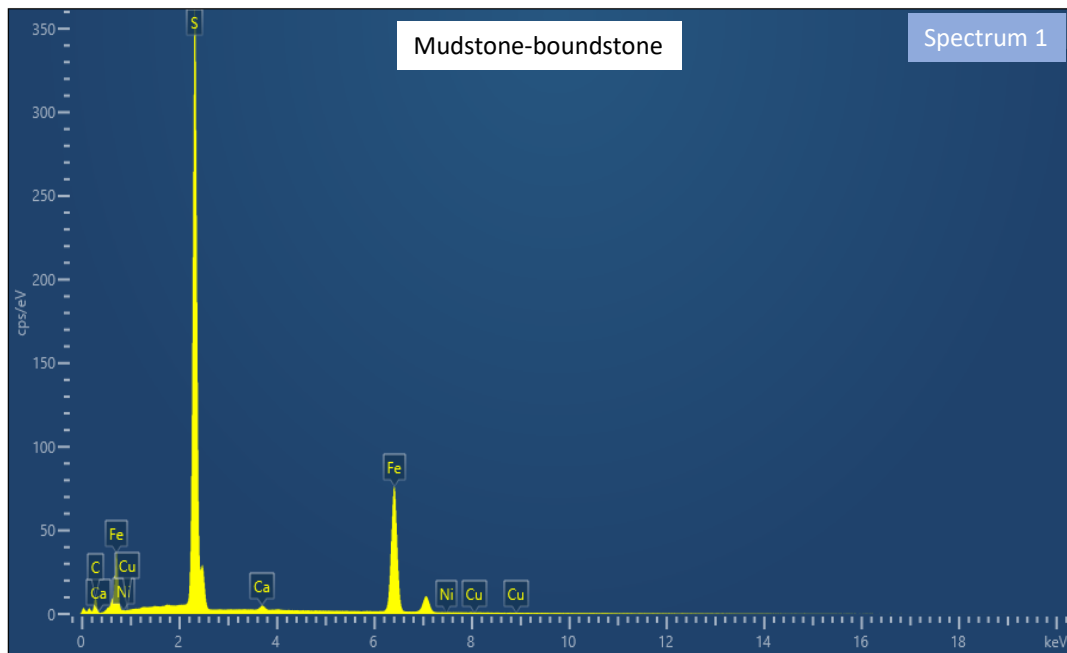
Figure 3a: Spectrum 1, pyrite (depth 826m; mudstone/boundstone).
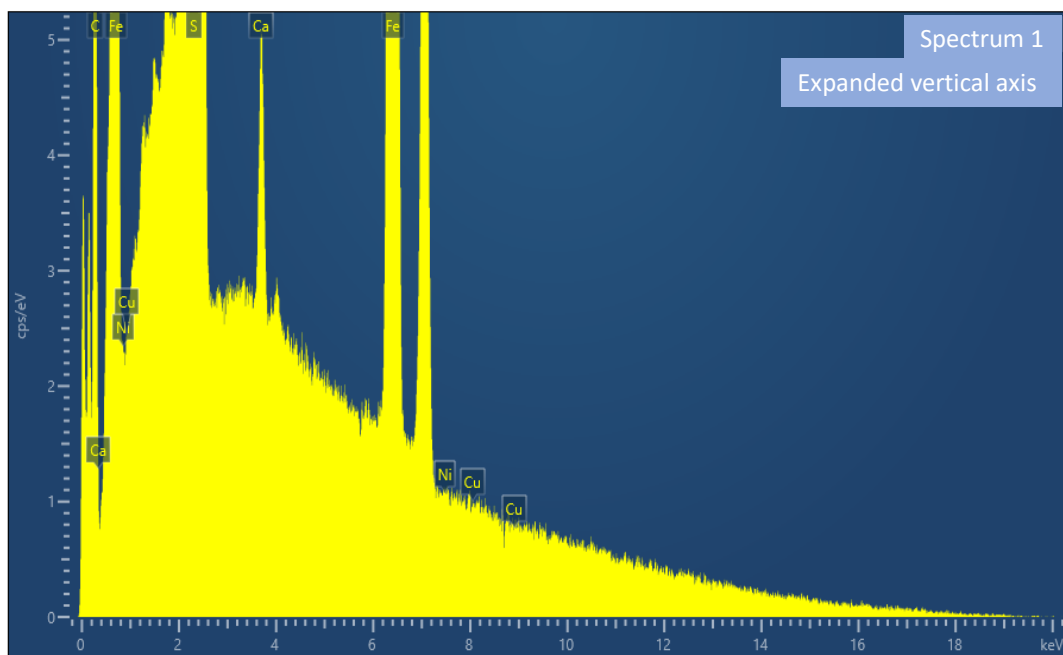
Figure 3b: Spectrum 1, pyrite, expanded vertical axis (depth 826m; mudstone/boundstone).
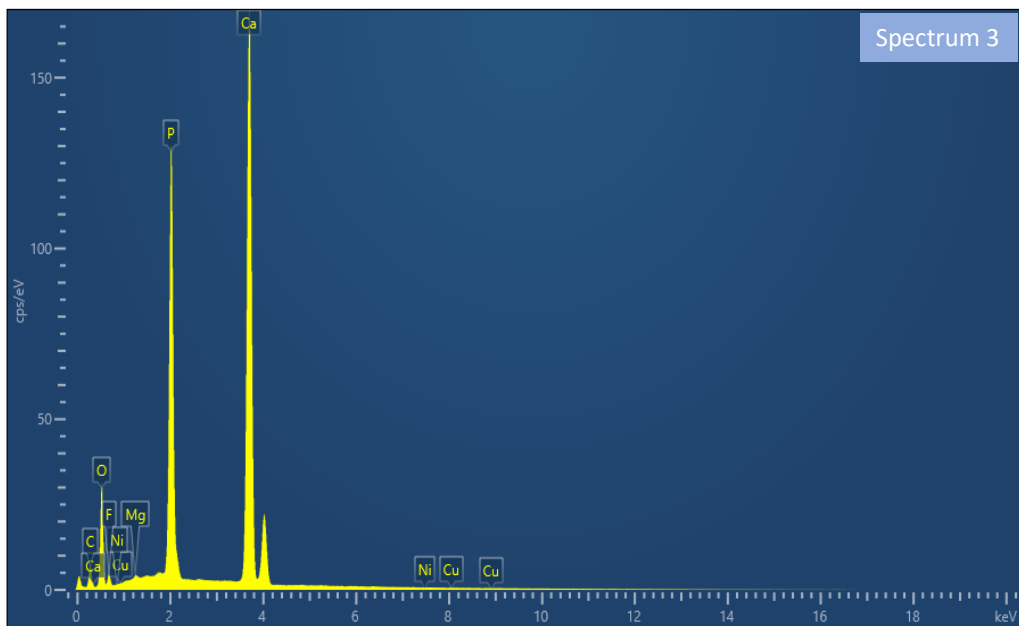
Figure 3c: Spectrum 3, matrix (depth 826m; mudstone/boundstone).
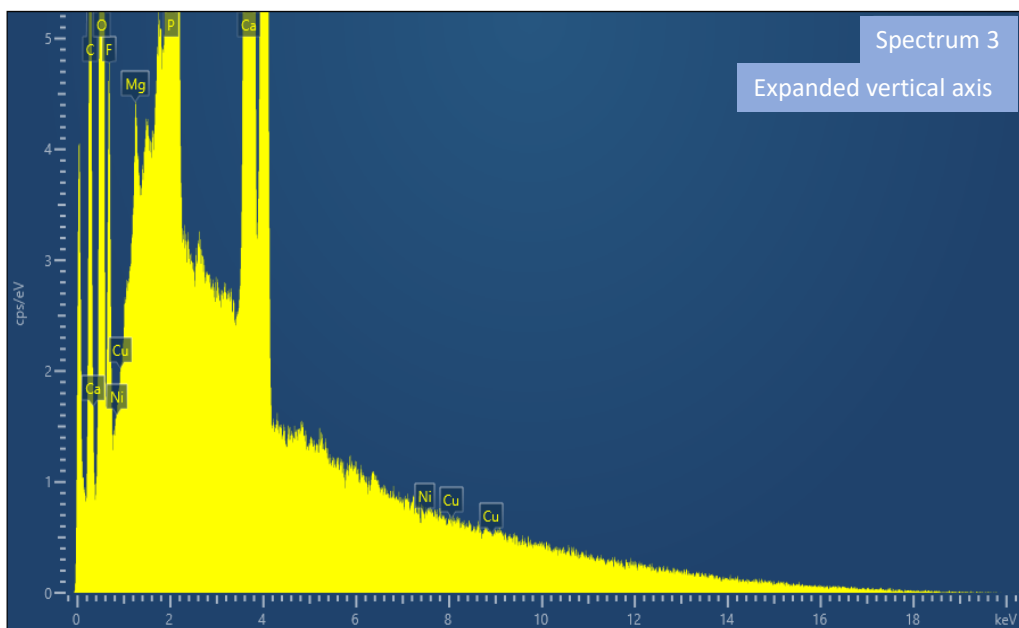
Figure 3d: Spectrum 3, matrix (depth 826m; mudstone/boundstone).

APPENDIX B

Major element data for core GKF01 determined by C-Ray Fluorescence (XRF).

Depth	Na Wt. %	Mg Wt. %	Al Wt. %	Si Wt. %	P Wt. %	S Wt. %	K Wt. %	Ca Wt. %	Ti Wt. %	Mn Wt. %	Fe Wt. %	CARB % carb
800.18	0.29	12.30	0.27	1.39	0.00	0.05	0.14	21.08	0.01	0.69	0.14	96.58
800.70	0.40	12.54	0.28	2.45	BDL	0.02	0.09	20.25	0.01	0.63	0.13	95.07
801.32	0.33	13.08	0.07	0.18	BDL	BDL	0.03	21.21	0.00	0.63	0.19	99.32
801.79	0.41	12.60	0.05	0.16	BDL	BDL	0.03	21.56	0.00	0.66	0.22	99.53
802.13	0.41	12.69	0.07	0.38	BDL	0.06	0.04	21.03	0.00	0.62	0.29	99.04
802.97	0.38	12.36	0.13	0.54	BDL	0.00	0.03	21.74	0.01	0.72	0.24	98.34
803.85	0.52	12.74	0.64	2.32	BDL	0.03	0.15	19.69	0.03	0.64	0.22	93.06
806.41	0.66	12.07	0.32	3.47	BDL	0.06	0.18	19.70	0.02	0.62	0.11	93.07
807.73	0.56	12.36	0.35	2.37	BDL	0.03	0.18	20.18	0.01	0.61	0.09	94.96
808.95	0.50	12.83	0.09	1.23	BDL	0.00	0.04	20.75	0.00	0.63	0.09	97.58
810.18	0.56	12.89	0.16	1.14	BDL	0.01	0.07	20.55	0.01	0.63	0.16	97.51
815.21	0.53	11.47	1.29	5.59	BDL	0.14	0.78	18.21	0.09	0.59	0.29	84.31
817.47	0.36	6.50	0.27	31.70	BDL	0.18	0.03	10.11	0.00	0.30	0.23	47.98
817.87	0.21	2.18	9.84	36.64	0.24	0.43	7.71	1.01	1.02	0.02	0.38	5.75
820.25	0.58	12.42	0.30	1.78	BDL	0.07	0.19	20.47	0.01	0.65	0.16	95.31
822.75	0.86	11.77	0.25	4.54	BDL	0.07	0.13	19.33	0.01	0.65	0.20	91.41
824.50	0.59	13.12	0.08	0.34	BDL	BDL	0.04	21.03	0.00	0.64	0.19	99.18
826.28	0.60	12.59	0.36	0.91	BDL	0.14	0.22	20.79	0.02	0.76	0.36	96.54
827.87	0.58	12.10	0.42	2.64	BDL	0.03	0.22	20.18	0.02	0.70	0.47	93.91
829.22	0.08	2.12	9.45	36.59	0.02	0.16	4.88	1.52	0.32	0.06	2.00	8.74
830.20	0.13	2.49	10.97	35.35	0.03	0.17	5.46	0.33	0.30	0.03	2.53	3.37
830.53	0.14	2.30	11.79	32.49	0.03	0.22	5.68	0.06	0.32	0.02	2.46	3.50
831.14	0.57	2.17	12.42	33.36	0.03	0.23	6.03	0.07	0.29	0.02	2.59	3.92
831.45	0.14	2.14	12.32	34.26	0.02	0.24	5.94	0.07	0.30	0.02	2.59	2.94
831.90	0.15	2.03	12.18	33.88	0.04	0.07	5.72	0.08	0.31	0.02	3.14	3.81
832.28	0.11	2.08	12.56	33.67	0.03	0.30	6.03	0.06	0.33	0.02	2.66	2.27
832.65	0.10	2.02	12.89	33.55	0.02	0.19	6.14	0.06	0.34	0.02	2.44	4.82
833.08	0.05	2.01	12.37	33.59	0.04	0.52	5.98	0.10	0.31	0.02	2.67	0.00
833.58	0.11	2.05	12.61	33.69	0.01	0.35	6.02	0.05	0.33	0.02	2.60	3.35
833.90	0.12	2.14	12.25	33.80	0.03	0.46	5.85	0.06	0.31	0.02	2.71	4.50
834.05	0.13	2.27	12.05	34.15	0.03	0.30	5.87	0.07	0.29	0.02	2.64	4.42
834.49	0.08	2.38	12.25	33.70	0.02	0.22	5.96	0.06	0.30	0.02	2.75	4.59
834.93	0.16	2.09	11.92	34.13	0.03	0.42	5.78	0.07	0.31	0.02	2.72	4.06

835.05	0.09	2.26	11.91	34.31	0.03	0.38	5.83	0.06	0.31	0.02	2.68	3.77
835.34	0.06	1.90	10.21	29.33	0.02	0.24	4.95	0.05	0.29	0.02	2.25	3.09
835.88	0.09	2.05	11.97	34.64	0.02	0.38	5.88	0.07	0.32	0.02	2.52	2.88
836.06	0.13	2.12	11.74	35.33	0.02	0.17	5.88	0.06	0.30	0.02	2.36	3.43
836.45	0.14	2.04	11.83	35.38	0.02	0.19	5.85	0.05	0.31	0.02	2.26	2.89
836.90	0.17	3.41	7.45	36.47	0.04	0.07	3.71	4.60	0.20	0.22	2.53	4.10
837.04	0.13	2.16	11.02	36.21	0.03	0.40	5.54	0.05	0.30	0.02	2.33	3.41
837.30	0.09	2.20	10.42	35.91	0.03	0.40	5.20	0.88	0.26	0.04	2.38	4.93
837.79	0.13	2.79	8.29	35.70	0.04	0.06	4.43	2.82	0.21	0.14	2.46	11.47
838.08	0.19	2.02	10.34	33.71	0.04	0.05	5.18	0.11	0.29	0.02	2.62	18.67
838.58	0.22	3.78	5.91	33.23	0.02	0.14	3.04	5.73	0.17	0.28	1.58	25.21
838.78	0.23	12.10	0.40	1.83	BDL	0.12	0.13	20.56	0.02	0.79	0.89	94.23
839.00	0.20	11.97	0.05	3.28	BDL	0.14	0.03	20.23	BDL	0.75	0.97	94.48
839.50	0.30	12.41	0.07	1.86	BDL	0.03	0.03	20.65	BDL	0.69	0.71	96.72
840.00	0.25	11.64	0.24	6.58	BDL	BDL	0.07	19.03	0.01	0.62	0.50	32.69
840.50	0.27	11.74	0.21	5.32	BDL	BDL	0.05	19.49	0.01	0.62	0.47	90.87
841.00	0.32	12.55	0.08	1.30	BDL	BDL	0.03	20.98	0.00	0.66	0.57	97.65
841.50	0.28	12.24	0.18	3.27	BDL	0.04	0.04	20.30	0.00	0.67	0.36	94.13
842.50	0.38	12.52	0.09	2.26	BDL	0.01	0.03	20.40	BDL	0.61	0.51	96.11
843.50	0.26	12.80	0.06	1.21	BDL	BDL	0.03	21.11	BDL	0.62	0.35	98.56
843.50	0.39	12.97	0.17	0.40	BDL	0.02	0.03	20.88	0.01	0.63	0.43	99.00
844.00	0.40	12.90	0.04	0.58	BDL	BDL	0.03	21.13	BDL	0.58	0.38	98.94
844.50	0.26	12.95	0.05	0.59	BDL	BDL	0.03	21.16	BDL	0.58	0.39	91.98
845.00	0.04	12.49	0.67	3.35	BDL	0.08	0.14	19.38	0.03	0.60	0.63	98.14
846.50	0.09	12.80	0.12	1.01	BDL	BDL	0.03	21.22	BDL	0.61	0.50	92.95
847.50	0.00	12.06	0.04	4.58	BDL	BDL	0.03	20.25	BDL	0.53	0.22	99.27
848.50	0.06	12.93	0.03	0.47	BDL	BDL	0.03	21.57	BDL	0.61	0.25	98.91
849.70	0.05	12.86	0.11	0.46	BDL	0.00	0.03	21.73	0.01	0.63	0.26	99.69
850.80	0.05	13.03	0.06	0.16	BDL	BDL	0.03	21.71	BDL	0.63	0.26	83.02
851.70	0.06	10.37	1.06	8.21	BDL	0.20	0.66	17.97	0.05	0.81	0.81	98.66
852.10	0.14	12.87	0.04	0.90	BDL	BDL	0.03	21.43	BDL	0.64	0.28	91.07
853.30	0.14	11.83	0.86	3.53	BDL	0.06	0.49	20.00	0.04	0.60	0.41	81.40
854.20	0.19	11.31	1.11	7.56	BDL	0.17	0.38	17.65	0.04	0.59	1.00	94.08
855.80	0.01	12.21	0.61	1.45	0.23	0.28	0.10	20.74	0.03	0.75	1.34	96.84
856.40	0.15	12.64	0.06	2.01	BDL	0.01	0.03	21.05	BDL	0.66	0.26	99.16
857.40	0.20	12.95	0.04	0.48	BDL	BDL	0.03	21.43	BDL	0.65	0.29	95.08
858.00	0.17	12.23	0.38	1.12	BDL	0.41	0.05	20.78	0.01	0.86	1.35	77.47
858.20	0.13	10.48	0.93	9.15	BDL	1.07	0.22	16.57	0.03	0.65	2.07	89.58
858.80	0.20	11.49	0.28	5.35	BDL	0.33	0.11	19.32	0.01	0.71	0.83	97.06
859.50	0.19	12.61	0.04	1.83	BDL	0.01	0.03	20.76	BDL	0.68	0.49	99.13
860.90	0.16	12.67	0.05	0.40	BDL	0.00	0.03	21.49	BDL	0.74	0.60	83.95
861.90	0.16	10.73	1.52	6.30	BDL	0.19	1.14	18.13	0.04	0.76	0.94	99.36
862.60	0.19	12.91	0.05	0.30	BDL	BDL	0.03	21.56	BDL	0.73	0.26	5.35

863.40	0.10	1.77	9.29	36.12	0.10	0.03	8.81	0.97	1.34	0.03	1.11	51.38
864.50	0.25	11.15	0.57	14.93	BDL	0.66	0.21	19.36	0.03	0.82	1.55	98.32
866.30	0.17	4.90	0.17	21.76	BDL	0.03	0.03	7.69	0.00	0.31	0.15	92.95
867.50	0.30	12.87	0.07	0.85	BDL	0.11	0.03	22.09	BDL	0.89	0.47	91.22
868.30	0.44	12.85	0.68	2.64	BDL	0.16	0.51	19.83	0.04	0.62	0.50	95.56
869.80	0.19	10.86	0.15	2.52	BDL	0.10	0.05	20.48	0.00	1.12	2.73	97.12
870.80	0.24	10.20	0.19	8.86	BDL	0.50	0.03	15.29	0.01	0.45	0.52	99.35
871.90	0.37	13.06	0.07	0.32	BDL	BDL	0.03	21.22	BDL	0.73	0.25	96.08
873.40	0.41	12.39	0.24	1.37	BDL	0.12	0.13	20.95	0.02	0.72	0.39	98.85
874.50	0.52	12.71	0.07	0.55	BDL	0.00	0.03	21.84	BDL	0.75	0.30	97.18
875.60	0.48	12.65	0.10	1.49	BDL	0.05	0.03	20.88	0.00	0.71	0.20	96.06
876.70	0.32	12.51	0.20	1.82	BDL	0.02	0.05	20.58	0.01	0.71	0.30	98.52
877.60	0.40	12.77	0.08	0.73	BDL	0.01	0.03	21.16	0.00	0.69	0.33	90.14
878.80	0.34	9.54	0.79	11.40	BDL	0.44	0.36	13.98	0.03	0.49	0.67	94.07
879.80	0.60	12.07	0.12	3.36	BDL	0.04	0.05	20.18	0.01	0.78	0.28	41.83
881.00	0.46	6.38	5.38	17.84	0.03	2.29	4.35	8.64	0.75	0.32	4.40	-

APPENDIX C

Tables 1A – 4D: Column saturation calculations for individual samples processed for column chemistry in this study. Green tabs indicate samples from which an isotope measurement was obtained; red tabs indicate that no measurement could be made. 'X.XXX' mL refers to the volume of sample taken for double spiking prior to column chemistry.

1A	3.931	mL
Element	mEq	
Ni	3.8E-05	
Mg	5.353	
Al	0.159	
Ca	5.561	
Ti	0.003	
Na	0.066	
K	0.019	
Ni (spike)	7.5E-06	
TOTAL	11.160	
ON COLUMN	2.839	

1B	6.034	mL
Element	mEq	
Ni	0.000	
Mg	8.689	
Al	0.066	
Ca	8.731	
Ti	0.001	
Na	0.149	
K	0.008	
Ni (spike)	0.000	
TOTAL	17.643	
ON COLUMN	2.924	

1C	2.734	mL
Element	mEq	
Ni	0.000	
Mg	3.589	
Al	0.066	
Ca	3.551	
Ti	0.002	
Na	0.086	
K	0.016	
Ni (spike)	0.000	
TOTAL	7.310	
ON COLUMN	2.673	

1D	2.101	mL
Element	mEq	
Ni	0.000	
Mg	1.444	
Al	0.081	
Ca	1.362	
Ti	0.000	
Na	0.042	
K	0.002	
Ni (spike)	0.000	
TOTAL	2.933	
ON COLUMN	1.396	

1E	4.88	mL
Element	mEq	
Ni	0.00	
Mg	1.14	
Al	0.03	
Ca	1.14	
Ti	0.00	
Na	0.04	
K	0.00	
Ni (spike)	0.00	
TOTAL	2.36	
ON COLUMN	0.48	

1F	1.23	mL
Element	mEq	
Ni	0.00	
Mg	0.13	
Al	0.01	
Ca	0.13	
Ti	0.00	
Na	0.00	
K	0.00	
Ni (spike)	0.00	
TOTAL	0.27	
ON COLUMN	0.22	

1G	1.834	mL
Element	mEq	
Ni	0.000	
Mg	0.071	
Al	0.427	
Ca	0.031	
Ti	0.005	
Na	0.001	
K	0.051	
Ni (spike)	0.000	
TOTAL	0.587	
ON COLUMN	0.320	

1H	0.742	mL
Element	mEq	
Ni	0.000	
Mg	0.025	
Al	0.173	
Ca	0.000	
Ti	0.002	
Na	0.001	
K	0.017	
Ni (spike)	0.000	
TOTAL	0.218	
ON COLUMN	0.841	

1I	0.62	mL
Element	mEq	
Ni	0.00	
Mg	0.02	
Al	0.13	
Ca	0.00	
Ti	0.00	
Na	0.00	
K	0.02	
Ni (spike)	0.00	
TOTAL	0.16	
ON COLUMN	0.62	

1J	0.634	mL
Element	mEq	
Ni	0.000	
Mg	0.018	
Al	0.148	
Ca	0.000	
Ti	0.001	
Na	0.001	
K	0.016	
Ni (spike)	0.000	
TOTAL	0.185	
ON COLUMN	0.704	

1K	0.660	mL
Element	mEq	
Ni	0.000	
Mg	0.018	
Al	0.154	
Ca	0.001	
Ti	0.001	
Na	0.000	
K	0.017	
Ni (spike)	0.000	
TOTAL	0.192	
ON COLUMN	0.738	

1L	0.664	mL
Element	mEq	
Ni	0.000	
Mg	0.020	
Al	0.155	
Ca	0.000	
Ti	0.001	
Na	0.001	
K	0.017	
Ni (spike)	0.000	
TOTAL	0.194	
ON COLUMN	0.752	

1LR	0.645	mL
Element	mEq	
Ni	0.000	
Mg	0.019	
Al	0.150	
Ca	0.000	
Ti	0.001	
Na	0.001	
K	0.016	
Ni (spike)	0.000	
TOTAL	0.188	
ON COLUMN	0.728	

2A	0.748	mL
Element	mEq	
Ni	3.62E-05	
Mg	0.026	
Al	0.182	
Ca	3.92E-04	
Ti	0.002	
Na	4.59E-04	
K	0.020	
Ni (spike)	7.23E-06	
TOTAL	0.232	
ON COLUMN	0.888	

2B	0.715	mL
Element	mEq	
Ni	3.46E-05	
Mg	0.023	
Al	0.164	
Ca	3.76E-04	
Ti	0.002	
Na	5.00E-04	
K	0.018	
Ni (spike)	7.52E-06	
TOTAL	0.207	
ON COLUMN	0.823	

2C	0.610	mL
Element	mEq	
Ni	3.63E-05	
Mg	0.017	
Al	0.132	
Ca	3.27E-04	
Ti	0.001	
Na	3.82E-04	
K	0.015	
Ni (spike)	7.22E-06	
TOTAL	0.166	
ON COLUMN	0.666	

2D	0.773	mL
Element	mEq	
Ni	3.45E-05	
Mg	0.023	
Al	0.180	
Ca	3.59E-04	
Ti	0.002	
Na	0.001	
K	0.021	
Ni (spike)	7.65E-06	
TOTAL	0.227	
ON COLUMN	0.929	

2E	0.828	mL
Element	mEq	
Ni	3.45E-05	
Mg	0.027	
Al	0.189	
Ca	3.97E-04	
Ti	0.002	
Na	0.001	
K	0.022	
Ni (spike)	7.21E-06	
TOTAL	0.241	
ON COLUMN	1.049	

2F	0.734	mL
Element	mEq	
Ni	3.42E-05	
Mg	0.342	
Al	1.372	
Ca	0.210	
Ti	0.013	
Na	0.008	
K	0.169	
Ni (spike)	7.22E-06	
TOTAL	2.113	
ON COLUMN	9.815	

2G	1.608	mL
Element	mEq	
Ni	3.44E-05	
Mg	0.618	
Al	1.305	
Ca	0.568	
Ti	0.015	
Na	0.019	
K	0.155	
Ni (spike)	7.27E-06	
TOTAL	2.680	
ON COLUMN	1.667	

2H	3.402	mL
Element	mEq	
Ni	3.43E-05	
Mg	4.479	
Al	0.025	
Ca	4.589	
Ti	0.00	
Na	0.040	
K	0.003	
Ni (spike)	7.20E-06	
TOTAL	9.135	
ON COLUMN	2.685	

2I	4.956	mL
Element	mEq	
Ni	3.41E-05	
Mg	6.464	
Al	0.177	
Ca	6.410	
Ti	0.002	
Na	0.074	
K	0.011	
Ni (spike)	7.50E-06	
TOTAL	13.139	
ON COLUMN	2.651	

2J	6.499	mL
Element	mEq	
Ni	3.07E-05	
Mg	9.248	
Al	0.079	
Ca	9.373	
Ti	0.001	
Na	0.126	
K	0.006	
Ni (spike)	7.32E-06	
TOTAL	18.833	
ON COLUMN	2.898	

2K	6.516	mL
Element	mEq	
Ni	3.49E-05	
Mg	9.262	
Al	0.093	
Ca	9.151	
Ti	0.00	
Na	0.148	
K	0.006	
Ni (spike)	7.05E-06	
TOTAL	18.660	
ON COLUMN	2.864	

2L	6.524	mL
Element	mEq	
Ni	2.60E-05	
Mg	9.655	
Al	0.175	
Ca	9.427	
Ti	0.003	
Na	0.152	
K	0.006	
Ni (spike)	5.94E-06	
TOTAL	19.419	
ON COLUMN	2.976	

2LR	6.562	mL
Element	mEq	
Ni	2.83E-05	
Mg	9.699	
Al	0.175	
Ca	9.469	
Ti	0.003	
Na	0.153	
K	0.006	
Ni (spike)	6.25E-06	
TOTAL	19.506	
ON COLUMN	2.972	

3A	5.489	mL
Element	Meq	
Ni	3.61E-05	
Mg	8.015	
Al	0.040	
Ca	7.940	
Ti	0.00	
Na	0.083	
K	0.005	
Ni (spike)	7.25E-06	
TOTAL	16.082	
ON COLUMN	2.930	

3B	5.89	mL
Element	Meq	
Ni	3.79E-05	
Mg	8.46	
Al	0.11	
Ca	8.50	
Ti	0.00	
Na	0.03	
K	0.01	
Ni (spike)	8.56E-06	
TOTAL	17.11	
ON COLUMN	2.91	

3C	6.308	mL
Element	Meq	
Ni	2.57E-05	
Mg	9.307	
Al	0.032	
Ca	9.415	
Ti	0.00	
Na	0.025	
K	0.006	
Ni (spike)	5.78E-06	
TOTAL	18.784	
ON COLUMN	2.978	

3D	6.374	mL
Element	Meq	
Ni	2.85E-05	
Mg	9.475	
Al	0.058	
Ca	9.569	
Ti	0.00	
Na	0.020	
K	0.006	
Ni (spike)	5.94E-06	
TOTAL	19.127	
ON COLUMN	3.001	

3E	1.117	mL
Element	Meq	
Ni	3.50E-05	
Mg	1.204	
Al	0.118	
Ca	1.234	
Ti	0.002	
Na	0.008	
K	0.016	
Ni (spike)	8.48E-06	
TOTAL	2.582	
ON COLUMN	2.312	

3F	6.586	mL
Element	Meq	
Ni	2.94E-05	
Mg	1.701	
Al	0.007	
Ca	1.708	
Ti	0.00	
Na	0.014	
K	0.001	
Ni (spike)	0.001	
TOTAL	3.432	
ON COLUMN	0.521	

3G	6.313	mL
Element	Meq	
Ni	2.13E-05	
Mg	1.601	
Al	0.007	
Ca	1.599	
Ti	0.00	
Na	0.013	
K	0.001	
Ni (spike)		
TOTAL	3.221	
ON COLUMN	0.510	

3H	1.11	mL
Element	Meq	
Ni	3.54E-05	
Mg	0.19	
Al	1.32	
Ca	0.06	
Ti	0.07	
Na	0.01	
K	0.29	
Ni (spike)	7.29E-06	
TOTAL	1.93	
ON COLUMN	1.74	

3I	3.877	mL
Element	Meq	
Ni	3.45E-05	
Mg	5.529	
Al	0.394	
Ca	5.177	
Ti	0.010	
Na	0.100	
K	0.068	
Ni (spike)	7.02E-06	
TOTAL	11.277	
ON COLUMN	2.909	

3J	1.573	mL
Element	Meq	
Ni	3.42E-05	
Mg	1.985	
Al	0.052	
Ca	2.035	
Ti	0.002	
Na	0.034	
K	0.007	
Ni (spike)	7.07E-06	
TOTAL	4.115	
ON COLUMN	2.615	

3K	4.447	mL
Element	Meq	
Ni	3.65E-05	
Mg	6.333	
Al	0.057	
Ca	6.366	
Ti	0.001	
Na	0.104	
K	0.004	
Ni (spike)	7.40E-06	
TOTAL	12.865	
ON COLUMN	2.893	

3L	3.284	mL
Element	Meq	
Ni	4.55E-05	
Mg	2.235	
Al	2.547	
Ca	1.835	
Ti	0.133	
Na	0.085	
K	0.473	
Ni (spike)	1.01E-05	
TOTAL	7.310	
ON COLUMN	2.226	

3LR	4.798	mL
Element	Meq	
Ni	3.81E-05	
Mg	3.398	
Al	3.873	
Ca	2.790	
Ti	0.203	
Na	0.130	
K	0.720	
Ni (spike)	8.74E-06	
TOTAL	11.113	
ON COLUMN	2.316	

4A	0.64	mL
Element	Meq	
Ni	3.46E-05	
Mg	0.02	
Al	0.12	
Ca	0.01	
Ti	4.56E-03	
Na	9.57E-04	
K	0.02	
Ni (spike)	7.25E-06	
TOTAL	0.17	
ON COLUMN	0.73	

4D	1.748	mL
Element	Meq	
Ni	3.44E-05	
Mg	4.487	
Al	0.149	
Ca	4.483	
Ti	0.002	
Na	0.111	
K	0.021	
Ni (spike)	8.56E-06	
TOTAL	9.253	
ON COLUMN	5.293	

References

Albarede, F., 2004. The Stable Isotope Geochemistry of Copper and Zinc. Reviews in Mineralogy and Geochemistry, 55(1), pp.409-427.

Albarede, F., 2013. Geochemistry. Cambridge: Cambridge University Press.

Anbar, A., Duan, Y., Lyons, T., Arnold, G., Kendall, B., Creaser, R., Kaufman, A., Gordon, G., Scott, C., Garvin, J. and Buick, R., 2007. A Whiff of Oxygen Before the Great Oxidation Event?. Science, 317(5846), pp.1903-1906.

Arndt, N., 2011. Tumbiana Formation (Pilbara, Western Australia). Encyclopedia of Astrobiology, pp.1714-1714.

Asael, D., Matthews, A., Bar-Matthews, M. and Halicz, L., 2007. Copper isotope fractionation in sedimentary copper mineralization (Timna Valley, Israel). Chemical Geology, 243(3-4), pp.238-254.

Audry, S., Blanc, G., Schäfer, J., Chaillou, G. and Robert, S., 2006. Early diagenesis of trace metals (Cd, Cu, Co, Ni, U, Mo, and V) in the freshwater reaches of a macrotidal estuary. Geochimica et Cosmochimica Acta, 70(9), pp.2264-2282.

Awramik, S. and Buchheim, H., 2009. A giant, Late Archean lake system: The Meentheena Member (Tumbiana Formation; Fortescue Group), Western Australia. Precambrian Research, 174(3-4), pp.215-240.

Balistrieri, L., Borrok, D., Wanty, R. and Ridley, W., 2008. Fractionation of Cu and Zn isotopes during adsorption onto amorphous Fe(III) oxyhydroxide: Experimental mixing of acid rock drainage and ambient river water. Geochimica et Cosmochimica Acta, 72(2), pp.311-328.

Battistuzzi, F., Feijao, A. and Hedges, S., 2004. BMC Evolutionary Biology, 4(1), p.44.

Bellefroid, E., Hood, A., Hoffman, P., Thomas, M., Reinhard, C. and Planavsky, N., 2018. Constraints on Paleoproterozoic atmospheric oxygen levels. Proceedings of the National Academy of Sciences, 115(32), pp.8104-8109.

Beukes, N. and Gutzmer, J., 2008. Origin and Paleoenvironmental Significance of Major Iron Formations at the Archean-Paleoproterozoic Boundary. Banded Iron Formation-Related High-Grade Iron Ore,.

Beukes, N., 1987. Facies relations, depositional environments and diagenesis in a major early Proterozoic stromatolitic carbonate platform to basinal sequence, Campbellrand Subgroup, Transvaal Supergroup, Southern Africa. Sedimentary Geology, 54(1-2), pp.1-46.

Bigalke, M., Weyer, S. and Wilcke, W., 2010. Copper Isotope Fractionation during Complexation with Insolubilized Humic Acid. Environmental Science & Technology, 44(14), pp.5496-5502.

Bigalke, M., Weyer, S., Kobza, J. and Wilcke, W., 2010. Stable Cu and Zn isotope ratios as tracers of sources and transport of Cu and Zn in contaminated soil. Geochimica et Cosmochimica Acta, 74(23), pp.6801-6813.

Blake, T., 1993. Late Archaean crustal extension, sedimentary basin formation, flood basalt volcanism and continental rifting: the Nullagine and Mount Jope Supersequences, Western Australia. Precambrian Research, 60(1-4), pp.185-241.

Blake, T., Buick, R., Brown, S. and Barley, M., 2004. Geochronology of a Late Archaean flood basalt province in the Pilbara Craton, Australia: constraints on basin evolution, volcanic and sedimentary accumulation, and continental drift rates. Precambrian Research, 133(3-4), pp.143-173.

Blankenship, R., 2010. Early Evolution of Photosynthesis. Plant Physiology, 154(2), pp.434-438.

Blaut, M., 1994. Metabolism of methanogens. Antonie van Leeuwenhoek, 66(1-3), pp.187-208.

Borja, R. and Rincón, B., 2017. Biogas Production ☆. Reference Module in Life Sciences,.

Borrok, D., Nimick, D., Wanty, R. and Ridley, W., 2008. Isotopic variations of dissolved copper and zinc in stream waters affected by historical mining. Geochimica et Cosmochimica Acta, 72(2), pp.329-344.

Brantley, S., Liermann, L. and Bullen, T., 2001. Fractionation of Fe isotopes by soil microbes and organic acids. Geology, 29(6), p.535.

Brookins, D., 1988. Copper. Eh-pH Diagrams for Geochemistry, pp.60-63.

Bruland, K., 1980. Oceanographic distributions of cadmium, zinc, nickel, and copper in the North Pacific. Earth and Planetary Science Letters, 47(2), pp.176-198.

Bruland, K., Middag, R. and Lohan, M., 2014. Controls of Trace Metals in Seawater. Treatise on Geochemistry, pp.19-51.

Buick, R. and Dunlop, J., 1990. Evaporitic sediments of Early Archaean age from the Warrawoona Group, North Pole, Western Australia. Sedimentology, 37(2), pp.247-277.

Buick, R., 1990. Microfossil Recognition in Archean Rocks: An Appraisal of Spheroids and Filaments from a 3500 M.Y. Old Chert-Barite Unit at North Pole, Western Australia. PALAIOS, 5(5), p.441.

Buick, R., 1992. The antiquity of oxygenic photosynthesis: evidence from stromatolites in sulphate-deficient Archaean lakes. Science, 255(5040), pp.74-77.

Button, A., 1973. A regional study of the stratigraphy and development of the Transvaal Basin in the eastern and northeastern Transvaal.. PhD Thesis. University of Witwatersrand, South Africa.

Cameron, V. and Vance, D., 2014. Heavy nickel isotope compositions in rivers and the oceans. Geochimica et Cosmochimica Acta, 128, pp.195-211.

Cameron, V., Vance, D., Archer, C. and House, C., 2009. A biomarker based on the stable isotopes of nickel. Proceedings of the National Academy of Sciences, 106(27), pp.10944-10948.

Canfield DE, Rosing MT, Bjerrum C. Early anaerobic metabolisms. Philos Trans R Soc Lond B Biol Sci. 2006 Oct 29;361(1474):1819-34; discussion 1835-6. doi: 10.1098/rstb.2006.1906. PMID: 17008221; PMCID: PMC1664682.

Canfield, D., 2005. THE EARLY HISTORY OF ATMOSPHERIC OXYGEN: Homage to Robert M. Garrels. Annual Review of Earth and Planetary Sciences, 33(1), pp.1-36.

Castillo Alvarez, C., Quitté, G., Schott, J. and Oelkers, E., 2020. Experimental determination of Ni isotope fractionation during Ni adsorption from an aqueous fluid onto calcite surfaces. Geochimica et Cosmochimica Acta, 273, pp.26-36.

Catling, D., Claire, M. and Zahnle, K., 2007. Anaerobic methanotrophy and the rise of atmospheric oxygen. Philosophical Transactions of the Royal Society A: Mathematical, Physical and Engineering Sciences, 365(1856), pp.1867-1888.

Chao, T. and Sanzolone, R., 1992. Decomposition techniques. Journal of Geochemical Exploration, 44(1-3), pp.65-106.

Chen, K., Rudnick, R., Wang, Z., Tang, M., Gaschnig, R., Zou, Z., He, T., Hu, Z. and Liu, Y., 2020. How mafic was the Archean upper continental crust? Insights from Cu and Ag in ancient glacial diamictites. Geochimica et Cosmochimica Acta, 278, pp.16-29.

Chi Fru, E., Rodríguez, N., Partin, C., Lalonde, S., Andersson, P., Weiss, D., El Albani, A., Rodushkin, I. and Konhauser, K., 2016. Cu isotopes in marine black shales record the Great Oxidation Event. Proceedings of the National Academy of Sciences, 113(18), pp.4941-4946.

Chi-Fru, E., 2014. Evaluating Aerobic Microbial Methane Cycling under Archaean-Proterozoic Environmental Conditions. [Blog] European Commission | CORDIS EU research results, Available at: <https://cordis.europa.eu/project/id/276475/reporting> [Accessed 23 January 2021].

Chistoserdova, L., Vorholt, J. and Lidstrom, M., 2005. Genome Biology, 6(2), p.208.

Choi, D., Do, Y., Zea, C., McEllistrem, M., Lee, S., Semrau, J., Pohl, N., Kisting, C., Scardino, L. and Hartsel, S., 2006. Spectral and thermodynamic properties of Ag(I), Au(III), Cd(II), Co(II), Fe(III), Hg(II), Mn(II), Ni(II), Pb(II), U(IV), and Zn(II) binding by methanobactin from Methylosinus trichosporium OB3b. Journal of Inorganic Biochemistry, 100(12), pp.2150-2161.

Ciscato, E., Bontognali, T. and Vance, D., 2018. Nickel and its isotopes in organic-rich sediments: implications for oceanic budgets and a potential record of ancient seawater. Earth and Planetary Science Letters, 494, pp.239-250.

Claire, M., Kasting, J., Domagal-Goldman, S., Stüeken, E., Buick, R. and Meadows, V., 2014. Modeling the signature of sulfur mass-independent fractionation produced in the Archean atmosphere. Geochimica et Cosmochimica Acta, 141, pp.365-380.

Coffey, J., 2011. A Palaeoenvironmental Study of the 2.7 Ga Tumbiana Formation, Fortescue Basin, Western Australia. PhD. University of New South Wales, Sydney.

Coffey, J., Flannery, D., Walter, M. and George, S., 2013. Sedimentology, stratigraphy and geochemistry of a stromatolite biofacies in the 2.72Ga Tumbiana Formation, Fortescue Group, Western Australia. Precambrian Research, 236, pp.282-296.

Condie, K.C. (1993) Chemical Composition and Evolution of the Upper Continental Crust; Contrasting Results from Surface Samples and Shales. Chemical Geology, 104, 1-37. https://doi.org/10.1016/0009-2541(93)90140-E

Crowe, S., Døssing, L., Beukes, N., Bau, M., Kruger, S., Frei, R. and Canfield, D., 2013. Atmospheric oxygenation three billion years ago. Nature, 501(7468), pp.535-538.

Cui, M., Ma, A., Qi, H., Zhuang, X. and Zhuang, G., 2014. Anaerobic oxidation of methane: an "active" microbial process. MicrobiologyOpen, 4(1), pp.1-11.

Cuppett, J., 2006. Evaluation of Copper Speciation and Water Quality Factors That Affect Aqueous Copper Tasting Response. Chemical Senses, 31(7), pp.689-697.

Czaja, A., Johnson, C., Beard, B., Eigenbrode, J., Freeman, K. and Yamaguchi, K., 2010. Iron and carbon isotope evidence for ecosystem and environmental diversity in the ~2.7 to 2.5Ga Hamersley Province, Western Australia. Earth and Planetary Science Letters, 292(1-2), pp.170-180.

Daines, S. and Lenton, T., 2016. The effect of widespread early aerobic marine ecosystems on methane cycling and the Great Oxidation. Earth and Planetary Science Letters, 434, pp.42-51.

Dauphas, N., Pourmand, A. and Teng, F., 2009. Routine isotopic analysis of iron by HR-MC-ICPMS: How precise and how accurate?. Chemical Geology, 267(3-4), pp.175-184.

de Kock, M., Evans, D. and Beukes, N., 2009. Validating the existence of Vaalbara in the Neoarchean. Precambrian Research, 174(1-2), pp.145-154.

de Kock, M., Evans, D., Kirschvink, J., Beukes, N., Rose, E. and Hilburn, I., 2009. Paleomagnetism of a Neoarchean-Paleoproterozoic carbonate ramp and carbonate platform succession (Transvaal Supergroup) from surface outcrop and drill core, Griqualand West region, South Africa. Precambrian Research, 169(1-4), pp.80-99.

Dodd, M., Papineau, D., Grenne, T., Slack, J., Rittner, M., Pirajno, F., O'Neil, J. and Little, C., 2017. Evidence for early life in Earth's oldest hydrothermal vent precipitates. Nature, 543(7643), pp.60-64.

Domagalski, J., Eugster, H. and Jones, B., 1990. Trace metal geochemistry of Walker, Mono, and Great Salt Lakes. Fluid-Mineral Interactions: A Tribute to H.P. Eugster, 2.

Ehrlich, S., Butler, I., Halicz, L., Rickard, D., Oldroyd, A. and Matthews, A., 2004. Experimental study of the copper isotope fractionation between aqueous Cu(II) and covellite, CuS. Chemical Geology, 209(3-4), pp.259-269.

Eigenbrode, J. and Freeman, K., 2006. Late Archean rise of aerobic microbial ecosystems. Proceedings of the National Academy of Sciences, 103(43), pp.15759-15764.

Elliott, T. and Steele, R., 2017. The Isotope Geochemistry of Ni. Reviews in Mineralogy and Geochemistry, 82(1), pp.511-542.

Endo, Y., Danielache, S. and Ueno, Y., 2019. Total Pressure Dependence of Sulfur Mass-Independent Fractionation by SO$_2$ Photolysis. Geophysical Research Letters, 46(1), pp.483-491.

Endo, Y., Ueno, Y., Aoyama, S. and Danielache, S., 2016. Sulfur isotope fractionation by broadband UV radiation to optically thin SO$_2$ under reducing atmosphere. Earth and Planetary Science Letters, 453, pp.9-22.

Eriksson, P., Bumby, A., Brümer, J. and van der Neut, M., 2006. Precambrian fluvial deposits: Enigmatic palaeohydrological data from the c. 2–1.9 Ga Waterberg Group, South Africa. Sedimentary Geology, 190(1-4), pp.25-46.

Ernst, W., 1970. Geochemical Facies Analysis Volume 11. Amsterdam: Elsevier Science.

Eroglu, S., Schoenberg, R., Pascarelli, S., Beukes, N., Kleinhanns, I. and Swanner, E., 2018. Open ocean vs. continentally-derived iron cycles along the Neoarchean Campbellrand-Malmani Carbonate platform, South Africa. American Journal of Science, 318(4), pp.367-408.

Eroglu, S., Shoenberg, R., Wille, M., Beukes, N. and Taubald, H., 2015. Geochemical stratigraphy, sedimentology, and Mo isotope systematics of the ca. 2.58-2.50 Ga-old Transvaal Supergroup carbonate platform, South Africa. Precambrian Research, (266), pp.27-46.

Eroglu, S., van Zuilen, M., Taubald, H., Drost, K., Wille, M., Swanner, E., Beukes, N. and Schoenberg, R., 2017. Depth-dependent δ13C trends in platform and slope settings of the Campbellrand-Malmani carbonate platform and possible implications for Early Earth oxygenation. Precambrian Research, 302, pp.122-139.

Ettre, L., 1993. Appendix 12a. Nomenclature | Chromatography (IUPAC Recommendations 1993). Encyclopedia of Separation Science, pp.4712-4753.

Ettwig, K., Zhu, B., Speth, D., Keltjens, J., Jetten, M. and Kartal, B., 2016. Archaea catalyze iron-dependent anaerobic oxidation of methane. Proceedings of the National Academy of Sciences, 113(45), pp.12792-12796.

Evans, D., Wade, B., Henehan, M., Erez, J. and Müller, W., 2016. Revisiting carbonate chemistry controls on planktic foraminifera Mg / Ca: implications for sea surface temperature and hydrology shifts over the Paleocene–Eocene Thermal Maximum and Eocene–Oligocene transition. Climate of the Past, 12(4), pp.819-835.

Farquhar, J. and Wing, B., 2003. Multiple sulfur isotopes and the evolution of the atmosphere. Earth and Planetary Science Letters, 213(1-2), pp.1-13.

Farquhar, J., Bao, H. and Thiemens, M., 2000. Atmospheric Influence of Earth's Earliest Sulfur Cycle. Science, 289(5480), pp.756-758.

Farquhar, J., Wu, N., Canfield, D. and Oduro, H., 2010. Connections between Sulfur Cycle Evolution, Sulfur Isotopes, Sediments, and Base Metal Sulfide Deposits. Economic Geology, 105(3), pp.509-533.

Farquhar, J., Zerkle, A. and Bekker, A., 2010. Geological constraints on the origin of oxygenic photosynthesis. Photosynthesis Research, 107(1), pp.11-36.

Fischer, W., Schroeder, S., Lacassie, J., Beukes, N., Goldberg, T., Strauss, H., Horstmann, U., Schrag, D. and Knoll, A., 2009. Isotopic constraints on the Late Archean carbon cycle from the Transvaal Supergroup along the western margin of the Kaapvaal Craton, South Africa. Precambrian Research, 169(1-4), pp.15-27.

Flannery, D., Allwood, A., Summons, R., Williford, K., Abbey, W., Matys, E., Ferralis, N., Spatially-resolved isotopic study of carbon trapped in ∼3.43 Ga Strelley Pool Formation stromatolites, Geochimica et Cosmochimica Acta, Volume 223, 2018, Pages 21-35, ISSN 0016-7037, https://doi.org/10.1016/j.gca.2017.11.028.

Freeman, K., Hayes, J., Trendel, J. and Albrecht, P., 1990. Evidence from carbon isotope measurements for diverse origins of sedimentary hydrocarbons. Nature, 343(6255), pp.254-256.

Fujii, T., Moynier, F., Abe, M., Nemoto, K. and Albarède, F., 2013. Copper isotope fractionation between aqueous compounds relevant to low temperature geochemistry and biology. Geochimica et Cosmochimica Acta, 110, pp.29-44.

Gall, L., Williams, H., Siebert, C. and Halliday, A., 2012. Determination of mass-dependent variations in nickel isotope compositions using double spiking and MC-ICPMS. J. Anal. At. Spectrom., 27(1), pp.137-145.

Gall, L., Williams, H., Siebert, C., Halliday, A., Herrington, R. and Hein, J., 2013. Nickel isotopic compositions of ferromanganese crusts and the constancy of deep ocean inputs and continental weathering effects over the Cenozoic. Earth and Planetary Science Letters, 375, pp.148-155.

Ganai, J., Rashid, S. and Romshoo, S., 2018. Evaluation of terrigenous input, diagenetic alteration and depositional conditions of Lower Carboniferous carbonates of Tethys Himalaya, India. Solid Earth Sciences, 3(2), pp.33-49.

Garvin, J., Buick, R., Anbar, A., Arnold, G. and Kaufman, A., 2009. Isotopic Evidence for an Aerobic Nitrogen Cycle in the Latest Archean. Science, 323(5917), pp.1045-1048.

German, C. and Von Damm, K., 2004. Hydrothermal Processes. In: H. Holland, K. Turekian and H. Elderfield, ed., Treatise on geochemistry, Vol. 6. The oceans and marine geochemistry. Oxford, UK: Elsevier-Pergamon, pp.181-222.

Gilman, A., Fu, Y., Hendershott, M., Chu, F., Puri, A., Smith, A., Pesesky, M., Lieberman, R., Beck, D. and Lidstrom, M., 2017. Oxygen-limited metabolism in the methanotroph Methylomicrobium buryatense 5GB1C. PeerJ, 5, p.e3945.

Goh, S., Buckley, A., Lamb, R., Rosenberg, R. and Moran, D., 2006. The oxidation states of copper and iron in mineral sulfides, and the oxides formed on initial exposure of chalcopyrite and bornite to air. Geochimica et Cosmochimica Acta, 70(9), pp.2210-2228.

Grassineau, N., Nisbet, E., Fowler, C., Bickle, M., Lowry, D., Chapman, H., Mattey, D., Abell, P., Yong, J. and Martin, A., 2002. Stable isotopes in the Archaean Belingwe belt, Zimbabwe: evidence for a diverse microbial mat ecology. Geological Society, London, Special Publications, 199(1), pp.309-328.

Gueguen, B., Rouxel, O., Ponzevera, E., Bekker, A. and Fouquet, Y., 2013. Nickel Isotope Variations in Terrestrial Silicate Rocks and Geological Reference Materials Measured by MC-ICP-MS. Geostandards and Geoanalytical Research, 37(3), pp.297-317.

Gueguen, B., Rouxel, O., The Nickel isotope composition of the authigenic sink and the diagenetic flux in modern oceans, Chemical Geology, Volume 563, 2021, 120050, ISSN 0009-2541, https://doi.org/10.1016/j.chemgeo.2020.120050.

Hakemian, A., Kondapalli, K., Telser, J., Hoffman, B., Stemmler, T. and Rosenzweig, A., 2008. The Metal Centers of Particulate Methane Monooxygenase fromMethylosinus trichosporiumOB3b†‡. Biochemistry, 47(26), pp.6793-6801.

Halevy, I. and Bachan, A., 2017. The geologic history of seawater pH. Science, 355(6329), pp.1069-1071.

Hallam, S., Putnam, N., Preston, C., Detter, J., Rokhsar, D., Richardson, P. and DeLong, E., 2004. Reverse Methanogenesis: Testing the Hypothesis with Environmental Genomics. Science, 305(5689), pp.1457-1462.

Hanson, R. and Hanson, T., 1996. Methanotrophic bacteria. Microbiological reviews, 60(2), pp.439-471.

Hao, J., Sverjensky, D. and Hazen, R., 2017. A model for late Archean chemical weathering and world average river water. Earth and Planetary Science Letters, 457, pp.191-203.

Hao, J., Sverjensky, D. and Hazen, R., 2017. Mobility of nutrients and trace metals during weathering in the late Archean. Earth and Planetary Science Letters, 471, pp.148-159.

Harman, C., Pavlov, A., Babikov, D. and Kasting, J., 2018. Chain formation as a mechanism for mass-independent fractionation of sulfur isotopes in the Archean atmosphere. Earth and Planetary Science Letters, 496, pp.238-247.

Hayes, J., 1993. Factors controlling 13C contents of sedimentary organic compounds: Principles and evidence. Marine Geology, 113(1-2), pp.111-125.

Hinrichs, K. and Boetius, A., 2002. The Anaerobic Oxidation of Methane: New Insights in Microbial Ecology and Biogeochemistry. Ocean Margin Systems, pp.457-477.

Hoehler, T., Alperin, M., Albert, D. and Martens, C., 1994. Field and laboratory studies of methane oxidation in an anoxic marine sediment: Evidence for a methanogen-sulfate reducer consortium. Global Biogeochemical Cycles, 8(4), pp.451-463.

Hou, Q., Zhou, L., Gao, S., Zhang, T., Feng, L. and Yang, L., 2016. Use of Ga for mass bias correction for the accurate determination of copper isotope ratio in the NIST SRM 3114 Cu standard and geological samples by MC-ICPMS. J. Anal. At. Spectrom., 31(1), pp.280-287.

Huang, J., Huang, F., Wang, Z., Zhang, X. and Yu, H., 2017. Copper isotope fractionation during partial melting and melt percolation in the upper mantle: Evidence from massif peridotites in Ivrea-Verbano Zone, Italian Alps. Geochimica et Cosmochimica Acta, 211, pp.48-63.

Iqbal, J. and Shah, M., 2015. Study of Selected Metals Distribution, Source Apportionment, and Risk Assessment in Suburban Soil, Pakistan. Journal of Chemistry, 2015, pp.1-8.

Ireland, T., Tissot, F., Yokochi, R. and Dauphas, N., 2013. Teflon-HPLC: A novel chromatographic system for application to isotope geochemistry and other industries. Chemical Geology, 357, pp.203-214.

Izon, G., Zerkle, A., Williford, K., Farquhar, J., Poulton, S. and Claire, M., 2017. Biological regulation of atmospheric chemistry en route to planetary oxygenation. Proceedings of the National Academy of Sciences, 114(13), pp.E2571-E2579.

Izon, G., Zerkle, A., Zhelezinskaia, I., Farquhar, J., Newton, R., Poulton, S., Eigenbrode, J. and Claire, M., 2015. Multiple oscillations in Neoarchaean atmospheric chemistry. Earth and Planetary Science Letters, 431, pp.264-273.

Johnson, R., Birdwell, J. and Mercier, T., 2018. Controls on organic matter distributions in Eocene Lake Uinta, Utah and Colorado. The Mountain Geologist, 55(4), pp.177-216.

Jones, B. and Manning, D., 1994. Comparison of geochemical indices used for the interpretation of palaeoredox conditions in ancient mudstones. Chemical Geology, 111(1-4), pp.111-129.

Kasting, J. and Siefert, J., 2002. Life and the Evolution of Earth's Atmosphere. Science, 296(5570), pp.1066-1068.

Kasting, J., 1993. Earth's early atmosphere. Science, 259(5097), pp.920-926.

Kasting, J., 2001. EARTH HISTORY: The Rise of Atmospheric Oxygen. Science, 293(5531), pp.819-820.

Keller, C. and Schoene, B., 2012. Statistical geochemistry reveals disruption in secular lithospheric evolution about 2.5 Gyr ago. Nature, 485(7399), pp.490-493.

Kenney, J. and Keeping, E., 1951. Mathematics of Statistics. 2nd ed. Van Nostrand.

Kharecha, P., Kasting, J. and Siefert, J., 2005. A coupled atmosphere-ecosystem model of the early Archean Earth. Geobiology, 3(2), pp.53-76.

Kim, H., Graham, D., DiSpirito, A., Alterman, M., Galeva, N., Larive, C., Asunskis, D. and Sherwood, P., 2004. Methanobactin, a Copper-Acquisition Compound from Methane-Oxidizing Bacteria. Science, 305(5690), pp.1612-1615.

Kimball, B., Mathur, R., Dohnalkova, A., Wall, A., Runkel, R. and Brantley, S., 2009. Copper isotope fractionation in acid mine drainage. Geochimica et Cosmochimica Acta, 73(5), pp.1247-1263.

Klaver, M., Ionov, D., Takazawa, E. and Elliott, T., 2020. The non-chondritic Ni isotope composition of Earth's mantle. Geochimica et Cosmochimica Acta, 268, pp.405-421.

Kleine, T., Münker, C., Mezger, K. and Palme, H., 2002. Rapid accretion and early core formation on asteroids and the terrestrial planets from Hf–W chronometry. Nature, 418(6901), pp.952-955.

Klekovkina, V., Gainov, R., Vagizov, F., Dooglav, A., Golovanevskiy, V. and Pen'kov, I., 2014. Oxidation and magnetic states of chalcopyrite CuFeS2: A first principles calculation. Optics and Spectroscopy, 116(6), pp.885-888.

Knief, C., 2015. Diversity and Habitat Preferences of Cultivated and Uncultivated Aerobic Methanotrophic Bacteria Evaluated Based on pmoA as Molecular Marker. Frontiers in Microbiology, 6.

Konhauser, K., Pecoits, E., Lalonde, S., Papineau, D., Nisbet, E., Barley, M., Arndt, N., Zahnle, K. and Kamber, B., 2009. Oceanic nickel depletion and a methanogen famine before the Great Oxidation Event. Nature, 458(7239), pp.750-753.

Konhauser, K., Robbins, L., Pecoits, E., Peacock, C., Kappler, A. and Lalonde, S., 2015. The Archean Nickel Famine Revisited. Astrobiology, 15(10), pp.804-815.

Korkisch, J. and Ahluwalia, S., 1967. Cation-exchange behaviour of several elements in hydrochloric acid—organic solvent media. Talanta, 14(2), pp.155-170.

Korkisch, J., 1989. Handbook of ion exchange resins: their application to inorganic analytical chemistry : Volume 1. Boca Raton, FL: CRC Press.

Köster, H., 1979. Die Analyse von Kationen nach der Abtrennung durch Ionenaustauscher. Die chemische Silikatanalyse, pp.106-166.

Kraus, K. and Moore, G., 1953. Anion Exchange Studies. VI.1,2 The Divalent Transition Elements Manganese to Zinc in Hydrochloric Acid. Journal of the American Chemical Society, 75(6), pp.1460-1462.

Krüger, M., Meyerdierks, A., Glöckner, F., Amann, R., Widdel, F., Kube, M., Reinhardt, R., Kahnt, J., Böcher, R., Thauer, R. and Shima, S., 2003. A conspicuous nickel protein in microbial mats that oxidize methane anaerobically. Nature, 426(6968), pp.878-881.

Krumbein, W. and Garrels, R., 1952. Origin and Classification of Chemical Sediments in Terms of pH and Oxidation-Reduction Potentials. The Journal of Geology, 60(1), pp.1-33.

Kurzweil, F., Claire, M., Thomazo, C., Peters, M., Hannington, M. and Strauss, H., 2013. Atmospheric sulfur rearrangement 2.7 billion years ago: Evidence for oxygenic photosynthesis. Earth and Planetary Science Letters, 366, pp.17-26.

Larson, P., Maher, K., Ramos, F., Chang, Z., Gaspar, M. and Meinert, L., 2003. Copper isotope ratios in magmatic and hydrothermal ore-forming environments. Chemical Geology, 201(3-4), pp.337-350.

Little, S.H., Archer, C., McManus, J., Najorka, J., Wegorzewski., A.V, Vance., D, Towards balancing the oceanic Ni budget, Earth and Planetary Science Letters, Volume 547, 2020, 116461, ISSN 0012-821X, https://doi.org/10.1016/j.epsl.2020.116461.

Little, S., Archer, C., Milne, A., Schlosser, C., Achterberg, E., Lohan, M. and Vance, D., 2018. Paired dissolved and particulate phase Cu isotope distributions in the South Atlantic. Chemical Geology, 502, pp.29-43.

Little, S., Munson, S., Prytulak, J., Coles, B., Hammond, S. and Widdowson, M., 2019. Cu and Zn isotope fractionation during extreme chemical weathering. Geochimica et Cosmochimica Acta, 263, pp.85-107.

Little, S., Vance, D., McManus, J., Severmann, S. and Lyons, T., 2017. Copper isotope signatures in modern marine sediments. Geochimica et Cosmochimica Acta, 212, pp.253-273.

Little, S., Vance, D., Walker-Brown, C. and Landing, W., 2014. The oceanic mass balance of copper and zinc isotopes, investigated by analysis of their inputs, and outputs to ferromanganese oxide sediments. Geochimica et Cosmochimica Acta, 125, pp.673-693.

Liu, S., Li, D., Li, S., Teng, F., Ke, S., He, Y. and Lu, Y., 2014. High-precision copper and iron isotope analysis of igneous rock standards by MC-ICP-MS. J. Anal. At. Spectrom., 29(1), pp.122-133.

Liu, S., Teng, F., Li, S., Wei, G., Ma, J. and Li, D., 2014. Copper and iron isotope fractionation during weathering and pedogenesis: Insights from saprolite profiles. Geochimica et Cosmochimica Acta, 146, pp.59-75.

Lubnina, N. and Slabunov, A., 2011. Reconstruction of the Kenorland supercontinent in the Neoarchean based on paleomagnetic and geological data. Moscow University Geology Bulletin, 66(4), pp.242-249.

Lubnina, N. and Slabunov, A., 2017. The Karelian Craton in the Structure of the Kenorland Supercontinent in the Neoarchean: New Paleomagnetic and Isotope Geochronology Data on Granulites of the Onega Complex. Moscow University Geology Bulletin, 72(6), pp.377-390.

Luo, G., Ono, S., Beukes, N., Wang, D., Xie, S. and Summons, R., 2016. Rapid oxygenation of Earth's atmosphere 2.33 billion years ago. Science Advances, 2(5), p.e1600134.

Lyons, T., Reinhard, C. and Planavsky, N., 2014. The rise of oxygen in Earth's early ocean and atmosphere. Nature, 506(7488), pp.307-315.

Lyu, Z., Shao, N., Akinyemi, T. and Whitman, W., 2018. Methanogenesis. Current Biology, 28(13), pp.R727-R732.

Madigan, M. and Martinko, J., 2015. Brock Biology of microorganisms. Boston: Pearson.

Maréchal, C., Télouk, P. and Albarède, F., 1999. Precise analysis of copper and zinc isotopic compositions by plasma-source mass spectrometry. Chemical Geology, 156(1-4), pp.251-273.

Margulis, L. and Lovelock, J., 1974. Biological modulation of the Earth's atmosphere. Icarus, 21(4), pp.471-489.

Mariotti, A., Germon, J., Hubert, P., Kaiser, P., Letolle, R., Tardieux, A. and Tardieux, P., 1981. Experimental determination of nitrogen kinetic isotope fractionation: some principles; illustration for the denitrification and nitrification processes. Plant and Soil, 62(3), pp.413-430.

Mathur, R., Jin, L., Prush, V., Paul, J., Ebersole, C., Fornadel, A., Williams, J. and Brantley, S., 2012. Cu isotopes and concentrations during weathering of black shale of the Marcellus Formation, Huntingdon County, Pennsylvania (USA). Chemical Geology, 304-305, pp.175-184.

Mathur, R., Ruiz, J., Titley, S., Liermann, L., Buss, H. and Brantley, S., 2005. Cu isotopic fractionation in the supergene environment with and without bacteria. Geochimica et Cosmochimica Acta, 69(22), pp.5233-5246.

Mathur, R., Titley, S., Barra, F., Brantley, S., Wilson, M., Phillips, A., Munizaga, F., Maksaev, V., Vervoort, J. and Hart, G., 2009. Exploration potential of Cu isotope fractionation in porphyry copper deposits. Journal of Geochemical Exploration, 102(1), pp.1-6.

Moeller, K., Schoenberg, R., Pedersen, R., Weiss, D. and Dong, S., 2012. Calibration of the New Certified Reference Materials ERM-AE633 and ERM-AE647 for Copper and IRMM-3702 for Zinc Isotope Amount Ratio Determinations. Geostandards and Geoanalytical Research, 36(2), pp.177-199.

Moore, E., Jelen, B., Giovannelli, D., Raanan, H. and Falkowski, P., 2017. Metal availability and the expanding network of microbial metabolisms in the Archaean eon. Nature Geoscience, 10(9), pp.629-636.

Morris, R. and Horwitz, R., 1983. The origin of the iron-formation-rich Hamersley Group of Western Australia — deposition on a platform. Precambrian Research, 21(3-4), pp.273-297.

Moynier, F., Vance, D., Fujii, T. and Savage, P., 2017. The Isotope Geochemistry of Zinc and Copper. Reviews in Mineralogy and Geochemistry, 82(1), pp.543-600.

Navarrete, J., Borrok, D., Viveros, M. and Ellzey, J., 2011. Copper isotope fractionation during surface adsorption and intracellular incorporation by bacteria. Geochimica et Cosmochimica Acta, 75(3), pp.784-799.

Nisbet, E. and Fowler, C., 2011. The evolution of the atmosphere in the Archaean and early Proterozoic. Chinese Science Bulletin, 56(1), pp.4-13.

O'Hara, M., Kellogg, C., Parker, C., Morrison, S., Corbey, J. and Grate, J., 2017. Decomposition of diverse solid inorganic matrices with molten ammonium bifluoride salt for constituent elemental analysis. Chemical Geology, 466, pp.341-351.

O'Leary, M., 1988. Carbon Isotopes in Photosynthesis. BioScience, 38(5), pp.328-336.

Olson, S., Kump, L. and Kasting, J., 2013. Quantifying the areal extent and dissolved oxygen concentrations of Archean oxygen oases. Chemical Geology, 362, pp.35-43.

Orphan, V., House, C., Hinrichs, K., McKeegan, K. and DeLong, E., 2002. Multiple archaeal groups mediate methane oxidation in anoxic cold seep sediments. Proceedings of the National Academy of Sciences, 99(11), pp.7663-7668.

Otamendi, J., Tiepolo, M., Walker, B., Cristofolini, E. and Tibaldi, A., 2016. Trace elements in minerals from mafic and ultramafic cumulates of the central Sierra de Valle Fértil, Famatinian arc, Argentina. Lithos, 240-243, pp.355-370.

Packer, B., 1990. Sedimentology, paleontology, and stable-isotope geochemistry of selected formations in the 2.7-billion-year-old Fortescue Group, Western Australia. PhD. University of California, Los Angeles.

Paiste, K., Lepland, A., Zerkle, A., Kirsimäe, K., Izon, G., Patel, N., McLean, F., Kreitsmann, T., Mänd, K., Bui, T., Romashkin, A., Rychanchik, D. and Prave, A., 2018. Multiple sulphur isotope records tracking basinal and global processes in the 1.98 Ga Zaonega Formation, NW Russia. Chemical Geology, 499, pp.151-164.

Pašava, J., Chrastný, V., Loukola-Ruskeeniemi, K. and Šebek, O., 2018. Nickel isotopic variation in black shales from Bohemia, China, Canada, and Finland: a reconnaissance study. Mineralium Deposita, 54(5), pp.719-742.

Pavlov, A. and Kasting, J., 2002. Mass-Independent Fractionation of Sulfur Isotopes in Archean Sediments: Strong Evidence for an Anoxic Archean Atmosphere. Astrobiology, 2(1), pp.27-41.

Peacock, C. and Sherman, D., 2007. Sorption of Ni by birnessite: Equilibrium controls on Ni in seawater. Chemical Geology, 238(1-2), pp.94-106.

Pecoraino, G., D'Alessandro, W. and Inguaggiato, S., 2015. The Other Side of the Coin: Geochemistry of Alkaline Lakes in Volcanic Areas. Advances in Volcanology, pp.219-237.

Planavsky, N., Asael, D., Hofmann, A., Reinhard, C., Lalonde, S., Knudsen, A., Wang, X., Ossa Ossa, F., Pecoits, E., Smith, A., Beukes, N., Bekker, A., Johnson, T., Konhauser, K., Lyons, T. and Rouxel, O., 2014. Evidence for oxygenic photosynthesis half a billion years before the Great Oxidation Event. Nature Geoscience, 7(4), pp.283-286.

Planavsky, N., Partin, C. and Bekker, A., 2011. Carbon Isotopes as a Geochemical Tracer. Encyclopedia of Astrobiology, pp.241-245.

Planavsky, N., Reinhard, C., Wang, X., Thomson, D., McGoldrick, P., Rainbird, R., Johnson, T., Fischer, W. and Lyons, T., 2014. Low Mid-Proterozoic atmospheric oxygen levels and the delayed rise of animals. Science, 346(6209), pp.635-638.

Pokrovsky, O., Viers, J., Emnova, E., Kompantseva, E. and Freydier, R., 2008. Copper isotope fractionation during its interaction with soil and aquatic microorganisms and metal oxy(hydr)oxides: Possible structural control. Geochimica et Cosmochimica Acta, 72(7), pp.1742-1757.

Porter, S., Selby, D. and Cameron, V., 2014. Characterising the nickel isotopic composition of organic-rich marine sediments. Chemical Geology, 387, pp.12-21.

Quitt?, G. and Oberli, F., 2006. Quantitative extraction and high precision isotope measurements of nickel by MC-ICPMS. Journal of Analytical Atomic Spectrometry, 21(11), p.1249.

Ratié, G., Quantin, C., Jouvin, D., Calmels, D., Ettler, V., Sivry, Y., Vieira, L., Ponzevera, E. and Garnier, J., 2016. Nickel isotope fractionation during laterite Ni ore smelting and refining: Implications for tracing the sources of Ni in smelter-affected soils. Applied Geochemistry, 64, pp.136-145.

Reeburgh, W., 2007. Oceanic Methane Biogeochemistry. Chemical Reviews, 107(2), pp.486-513.

Regelous, M., Elliott, T. and Coath, C., 2008. Nickel isotope heterogeneity in the early Solar System. Earth and Planetary Science Letters, 272(1-2), pp.330-338.

Roslev, P. and King, G., 1994. Survival and Recovery of Methanotrophic Bacteria Starved under Oxic and Anoxic Conditions †. Applied and Environmental Microbiology, 60(7), pp.2602-2608.

Rudge, J., Reynolds, B. and Bourdon, B., 2009. The double spike toolbox. Chemical Geology, 265(3-4), pp.420-431.

Rudnick, R. and Gao, S., 2003. Composition of the Continental Crust. Treatise on Geochemistry, pp.1-64.

Sauterey, B., Charnay, B., Affholder, A., Mazevet, S. and Ferrière, R., 2020. Co-evolution of primitive methane-cycling ecosystems and early Earth's atmosphere and climate. Nature Communications, 11(1).

Scheller, S., Goenrich, M., Boecher, R., Thauer, R. and Jaun, B., 2010. The key nickel enzyme of methanogenesis catalyses the anaerobic oxidation of methane. Nature, 465(7298), pp.606-608.

Schönbächler, M. and Fehr, M., 2014. Basics of Ion Exchange Chromatography for Selected Geological Applications. Treatise on Geochemistry, pp.123-146.

Schopf, J., Kitajima, K., Spicuzza, M., Kudryavtsev, A. and Valley, J., 2017. SIMS analyses of the oldest known assemblage of microfossils document their taxon-correlated carbon isotope compositions. *Proceedings of the National Academy of Sciences*, 115(1), pp.53-58.

Schroder, S., Lacassie, J. and Beukes, N., 2006. Stratigraphic and geochemical framework of the Agouron drill cores, Transvaal Supergroup (Neoarchean-Paleoproterozoic, South Africa). South African Journal of Geology, 109(1-2), pp.23-54.

Sclater, F., Boyle, E. and Edmond, J., 1976. On the marine geochemistry of nickel. Earth and Planetary Science Letters, 31(1), pp.119-128.

Semrau, J., DiSpirito, A. and Vuilleumier, S., 2011. Facultative methanotrophy: false leads, true results, and suggestions for future research. FEMS Microbiology Letters, 323(1), pp.1-12.

Semrau, J., DiSpirito, A. and Yoon, S., 2010. Methanotrophs and copper. FEMS Microbiology Reviews, 34(4), pp.496-531.

Semrau, J., DiSpirito, A., Gu, W. and Yoon, S., 2018. Metals and Methanotrophy. Applied and Environmental Microbiology, 84(6).

Sherry, A., Osborne, K., Sidgwick, F., Gray, N. and Talbot, H., 2016. A temperate river estuary is a sink for methanotrophs adapted to extremes of   pH   , temperature and salinity. Environmental Microbiology Reports, 8(1), pp.122-131.

Shields, W., Goldich, S., Garner, E. and Murphy, T., 1965. Natural variations in the abundance ratio and the atomic weight of copper. Journal of Geophysical Research, 70(2), pp.479-491.

Silva, J. and Williams, R., 2009. The biological chemistry of the elements. Oxford: Oxford University Press.

Sossi, P., Halverson, G., Nebel, O. and Eggins, S., 2014. Combined Separation of Cu, Fe and Zn from Rock Matrices and Improved Analytical Protocols for Stable Isotope Determination. Geostandards and Geoanalytical Research, 39(2), pp.129-149.

Spivak-Birndorf, L., Wang, S., Bish, D. and Wasylenki, L., 2018. Nickel isotope fractionation during continental weathering. Chemical Geology, 476, pp.316-326.

Steele, R., Coath, C., Regelous, M., Russell, S. and Elliott, T., 2012. NEUTRON-POOR NICKEL ISOTOPE ANOMALIES IN METEORITES. The Astrophysical Journal, 758(1), p.59.

Steele, R., Elliott, T., Coath, C. and Regelous, M., 2011. Confirmation of mass-independent Ni isotopic variability in iron meteorites. Geochimica et Cosmochimica Acta, 75(24), pp.7906-7925.

Strelow, F., Victor, A., Van Zyl, C. and Eloff, C., 1971. Distribution coefficients and cation exchange behavior of elements in hydrochloric acid-acetone. Analytical Chemistry, 43(7), pp.870-876.

Stueeken, E., 2021. Early evolution of environments and metabolism: insights from nitrogen, selenium and sulfur isotopes. [online] Hdl.handle.net. Available at: <http://hdl.handle.net/1773/27215> [Accessed 1 February 2021].

Stüeken, E. and Buick, R., 2018. Environmental control on microbial diversification and methane production in the Mesoarchean. Precambrian Research, 304, pp.64-72.

Stüeken, E., 2020. Hydrothermal vents and organic ligands sustained the Precambrian copper budget. Geochemical Perspectives Letters, pp.12-16.

Stüeken, E., Buick, R. and Schauer, A., 2015. Nitrogen isotope evidence for alkaline lakes on late Archean continents. Earth and Planetary Science Letters, 411, pp.1-10.

Stüeken, E., Buick, R., Anderson, R., Baross, J., Planavsky, N. and Lyons, T., 2017. Environmental niches and metabolic diversity in Neoarchean lakes. Geobiology, 15(6), pp.767-783.

Summons, R., Franzmann, P. and Nichols, P., 1998. Carbon isotopic fractionation associated with methylotrophic methanogenesis. Organic Geochemistry, 28(7-8), pp.465-475.

Sumner, D. and Bowring, S., 1996. U Pb geochronologic constraints on deposition of the Campbellrand Subgroup, Transvaal Supergroup, South Africa. Precambrian Research, 79(1-2), pp.25-35.

Sumner, D. and Grotzinger, J., 2004. Implications for Neoarchaean ocean chemistry from primary carbonate mineralogy of the Campbellrand-Malmani Platform, South Africa. Sedimentology, 51(6), pp.1273-1299.

Sumner, D., 2006. Sequence Stratigraphic Development of the Neoarchean Transvaal carbonate platform, Kaapvaal Craton, South Africa. South African Journal of Geology, 109(1-2), pp.11-22.

Sutherland, R., 2000. Bed sediment-associated trace metals in an urban stream, Oahu, Hawaii. Environmental Geology, 39(6), pp.611-627.

Tang, H. and Dauphas, N., 2012. Abundance, distribution, and origin of 60Fe in the solar protoplanetary disk. Earth and Planetary Science Letters, 359-360, pp.248-263.

Tang, M., Chen, K. and Rudnick, R., 2016. Archean upper crust transition from mafic to felsic marks the onset of plate tectonics. *Science*, 351(6271), pp.372-375.

Tashiro, T., Ishida, A., Hori, M., Igisu, M., Koike, M., Méjean, P., Takahata, N., Sano, Y. and Komiya, T., 2017. Early trace of life from 3.95 Ga sedimentary rocks in Labrador, Canada. Nature, 549(7673), pp.516-518.

Taupp, M., Constan, L. and Hallam, S., 2010. The Biochemistry of Anaerobic Methane Oxidation. Handbook of Hydrocarbon and Lipid Microbiology, pp.887-907.

Taylor, S. and McLennan, S., 1995. The geochemical evolution of the continental crust. Reviews of Geophysics, 33(2), p.241.

Taylor, S. and McLennan, S., 1995. The geochemical evolution of the continental crust. Reviews of Geophysics, 33(2), p.241.

Thibon, F., Blichert-Toft, J., Albarede, F., Foden, J. and Tsikos, H., 2019. A critical evaluation of copper isotopes in Precambrian Iron Formations as a paleoceanographic proxy. Geochimica et Cosmochimica Acta, 264, pp.130-140.

Thomas, R., 2004. Practical Guide to ICP-MS. 1st ed. Marcel Dekker, Inc.

Thomazo, C., Pinti, D., Busigny, V., Ader, M., Hashizume, K. and Philippot, P., 2009. Biological activity and the Earth's surface evolution: Insights from carbon, sulfur, nitrogen and iron stable isotopes in the rock record. Comptes Rendus Palevol, 8(7), pp.665-678.

Thorne, A. and Trendall, A., 2001. Geology of the Fortescue Group, Pilbara Craton, Western Australia. Perth: Geological Survey of Western Australia.

Tostevin, R., Shields, G., Tarbuck, G., He, T., Clarkson, M. and Wood, R., 2016. Effective use of cerium anomalies as a redox proxy in carbonate-dominated marine settings. Chemical Geology, 438, pp.146-162.

Trendall, A. and Blockley, J., 1970. The Iron-Formations of the Precambrian Hamersley Group, Western Australia, with Special Reference to the Associated Crocidolite. Western Australia Geological Survey Bulletin, 119, pp.1-365.

Trendall, A., 1983. Iron Formation Facts and Problems. Amsterdam: Elsevier, pp.69-129.

Trendall, A., Compston, W., Nelson, D., De Laeter, J. and Bennett, V., 2004. SHRIMP zircon ages constraining the depositional chronology of the Hamersley Group, Western Australia*. Australian Journal of Earth Sciences, 51(5), pp.621-644.

Tribovillard, N., Algeo, T., Lyons, T. and Riboulleau, A., 2006. Trace metals as paleoredox and paleoproductivity proxies: An update. Chemical Geology, 232(1-2), pp.12-32.

Tribovillard, N., Algeo, T., Lyons, T. and Riboulleau, A., 2006. Trace metals as paleoredox and paleoproductivity proxies: An update. Chemical Geology, 232(1-2), pp.12-32.

Tschugaeff, L., 1905. Ueber ein neues, empfindliches Reagens auf Nickel. Berichte der deutschen chemischen Gesellschaft, 38(3), pp.2520-2522.

Ueno, Y., Yamada, K., Yoshida, N., Maruyama, S. and Isozaki, Y., 2006. Evidence from fluid inclusions for microbial methanogenesis in the early Archaean era. Nature, 440(7083), pp.516-519.

Vance, D., Little, S., Archer, C., Cameron, V., Andersen, M., Rijkenberg, M. and Lyons, T., 2016. The oceanic budgets of nickel and zinc isotopes: the importance of sulfidic environments as illustrated by the Black Sea. Philosophical Transactions of the Royal Society A: Mathematical, Physical and Engineering Sciences, 374(2081), p.20150294.

Vanhaecke, F., 2012. Single-Collector Inductively Coupled Plasma Mass Spectrometry. Isotopic Analysis, pp.31-75.

Victor, A., 1985. Separation of cobalt from uranium(VI), manganese(II), and lithium on AG50W-X8 resin in hydrochloric acid-acetone. South African Journal of Chemistry, 38(1).

Wahlgren, M., Orlandini, K. and Korkisch, J., 1970. Specific cation-exchange separation of nickel. Analytica Chimica Acta, 52(3), pp.551-553.

Walker, E., Cuttitta, F. and Senftle, F., 1958. Some natural variations in the relative abundance of copper isotopes. Geochimica et Cosmochimica Acta, 15(3), pp.183-194.

Walt, T., Strelow, F. and Verheij, R., 1985. THE INFLUENCE OF CROSSLINKAGE ON THE DISTRIBUTION COEFFICIENTS AND ANION EXCHANGE BEHAVIOUR OF SOME ELEMENTS IN HYDROCHLORIC ACID. Solvent Extraction and Ion Exchange, 3(5), pp.723-740.

Wang, S., Rudnick, R., Gaschnig, R., Wang, H. and Wasylenki, L., 2019. Methanogenesis sustained by sulfide weathering during the Great Oxidation Event. Nature Geoscience, 12(4), pp.296-300.

Wang, Z., Park, J., Wang, X., Zou, Z., Kim, J., Zhang, P. and Li, M., 2019. Evolution of copper isotopes in arc systems: Insights from lavas and molten sulfur in Niuatahi volcano, Tonga rear arc. Geochimica et Cosmochimica Acta, 250, pp.18-33.

Warke, M., Di Rocco, T., Zerkle, A., Lepland, A., Prave, A., Martin, A., Ueno, Y., Condon, D. and Claire, M., 2020. The Great Oxidation Event preceded a Paleoproterozoic "snowball Earth". Proceedings of the National Academy of Sciences, 117(24), pp.13314-13320.

Warke, M., Edwards, N., Wogelius, R., Manning, P., Bergmann, U., Egerton, V., Kimball, K., Garwood, R., Beukes, N. and Schröder, S., 2019. Decimeter-scale mapping of carbonate-controlled trace element distribution in Neoarchean cuspate stromatolites. Geochimica et Cosmochimica Acta, 261, pp.56-75.

Warke, M., Schröder, S. and Strauss, H., 2018. Testing models of pre-GOE environmental oxidation: A Paleoproterozoic marine signal in platform dolomites of the Tongwane Formation (South Africa). Precambrian Research, 313, pp.205-220.

Wasylenki, L., Howe, H., Spivak-Birndorf, L. and Bish, D., 2015. Ni isotope fractionation during sorption to ferrihydrite: Implications for Ni in banded iron formations. Chemical Geology, 400, pp.56-64.

Weiss, M., Sousa, F., Mrnjavac, N., Neukirchen, S., Roettger, M., Nelson-Sathi, S. and Martin, W., 2016. The physiology and habitat of the last universal common ancestor. Nature Microbiology, 1(9).

Wiederhold, J., 2015. Metal Stable Isotope Signatures as Tracers in Environmental Geochemistry. Environmental Science & Technology, 49(5), pp.2606-2624.

Williamson, M. and Parnell, R., 1994. Partitioning of copper and zinc in the sediments and porewaters of a high-elevation alkaline lake, east-central Arizona, U.S.A. Applied Geochemistry, 9(5), pp.597-608.

Wilschefski, S. and Baxter, M., 2019. Inductively Coupled Plasma Mass Spectrometry: Introduction to Analytical Aspects. Clinical Biochemist Reviews, 40(3), pp.115-133.

Wolfe, J. and Fournier, G., 2018. Horizontal gene transfer constrains the timing of methanogen evolution. Nature Ecology & Evolution, 2(5), pp.897-903.

Wongnate, T. and Ragsdale, S., 2015. The Reaction Mechanism of Methyl-Coenzyme M Reductase. Journal of Biological Chemistry, 290(15), pp.9322-9334.

Wright, C., Kwadiba, M., Simon, R., Kgaswane, E. and Nguuri, T., 2004. Variations in the thickness of the crust of the Kaapvaal craton, and mantle structure below southern Africa. Earth, Planets and Space, 56(2), pp.125-137.

Wu, G., Zhu, J., Wang, X., Han, G., Tan, D. and Wang, S., 2019. A novel purification method for high precision measurement of Ni isotopes by double spike MC-ICP-MS. Journal of Analytical Atomic Spectrometry, 34(8), pp.1639-1651.

Xu, G., Hannah, J., Bingen, B., Georgiev, S. and Stein, H., 2012. Digestion methods for trace element measurements in shales: Paleoredox proxies examined. Chemical Geology, 324-325, pp.132-147.

Yang, J., Junium, C., Grassineau, N., Nisbet, E., Izon, G., Mettam, C., Martin, A. and Zerkle, A., 2019. Ammonium availability in the Late Archaean nitrogen cycle. Nature Geoscience, 12(7), pp.553-557.

Yang, S., Hawco, N., Pinedo-González, P., Bian, X., Huang, K., Zhang, R. and John, S., 2020. A new purification method for Ni and Cu stable isotopes in seawater provides evidence for widespread Ni isotope fractionation by phytoplankton in the North Pacific. Chemical Geology, 547, p.119662.

Yoon, S., Kraemer, S., DiSpirito, A. and Semrau, J., 2010. An assay for screening microbial cultures for chalkophore production. Environmental Microbiology Reports, 2(2), pp.295-303.

Yoshiya, K., Nishizawa, M., Sawaki, Y., Ueno, Y., Komiya, T., Yamada, K., Yoshida, N., Hirata, T., Wada, H. and Maruyama, S., 2012. In situ iron isotope analyses of pyrite and organic carbon isotope ratios in the Fortescue Group: Metabolic variations of a Late Archean ecosystem. Precambrian Research, 212-213, pp.169-193.

Zahnle, K., Schaefer, L. and Fegley, B., 2010. Earth's Earliest Atmospheres. Cold Spring Harbor Perspectives in Biology, 2(10), pp.a004895-a004895.

Zerkle, A., Claire, M., Domagal-Goldman, S., Farquhar, J. and Poulton, S., 2012. A bistable organic-rich atmosphere on the Neoarchaean Earth. Nature Geoscience, 5(5), pp.359-363.

Zerkle, A., House, C. and Brantley, S., 2005. Biogeochemical signatures through time as inferred from whole microbial genomes. American Journal of Science, 305(6-8), pp.467-502.

Zerkle, A., Scheiderich, K., Maresca, J., Liermann, L. and Brantley, S., 2010. Molybdenum isotope fractionation by cyanobacterial assimilation during nitrate utilization and N2fixation. Geobiology, 9(1), pp.94-106.

Zerkle, A., Yin, R., Chen, C., Li, X., Izon, G. and Grasby, S., 2020. Anomalous fractionation of mercury isotopes in the Late Archean atmosphere. Nature Communications, 11(1).

Zhang, W., Hu, Z., Liu, Y., Chen, H., Gao, S. and Gaschnig, R., 2012. Total Rock Dissolution Using Ammonium Bifluoride (NH4HF2) in Screw-Top Teflon Vials: A New Development in Open-Vessel Digestion. Analytical Chemistry, 84(24), pp.10686-10693.

Zhu, X., Guo, Y., Williams, R., O'Nions, R., Matthews, A., Belshaw, N., Canters, G., de Waal, E., Weser, U., Burgess, B. and Salvato, B., 2002. Mass fractionation processes of transition metal isotopes. Earth and Planetary Science Letters, 200(1-2), pp.47-62.